# SEARCHES FOR BEYOND THE STANDARD MODEL PHYSICS IN DIJET RESONANCES AND DEVELOPMENT OF A NEW B-TAGGING CALIBRATION ALGORITHM AT THE ATLAS EXPERIMENT AT CERN

By

WASIKUL ISLAM

Bachelor of Science in Physics
Aligarh Muslim University
Aligarh, UP, India
2013

Master of Science in Physics
Aligarh Muslim University
Aligarh, UP, India
2015

Submitted to the Faculty of the
Graduate College of the
Oklahoma State University
in partial fulfillment of
the requirements for
the Degree of
DOCTOR OF PHILOSOPHY
May, 2021

SEARCHES FOR BEYOND THE STANDARD MODEL PHYSICS IN DIJET RESONANCES AND DEVELOPMENT OF A NEW B-TAGGING CALIBRATION ALGORITHM AT THE ATLAS EXPERIMENT AT CERN

Dissertation Approved:

Dr. Alexander Khanov

Dissertation Advisor

Dr. K. S. Babu

Dr. Joseph Haley

Dr. Joe Cecil

## ACKNOWLEDGMENTS

I am extremely thankful to my Ph.D. advisor Prof. Alexander Khanov for his guidance in all my research projects. I can't thank him enough for the support which he provided throughout the years and for allowing me to participate in multiple projects and to explore opportunities in different laboratories including Argonne National Lab, Fermilab & at CERN. I have been inspired by the hard works which he does for his own research. I am thankful to our whole ATLAS-research-group of OSU, specially to Prof. Flera Rizatdinova who has extraordinary leadership skills in managing the group and has a lot of care for the group members. Thanks to the Research Assistantship provided by the OSU-ATLAS group, I could travel to different labs and conferences and conducted my research. Thanks to Dr. Joseph Haley who taught me a Particle Physics course and also has been a great colleague in the OSU-ATLAS group.

Sincere thanks to my Ph.D. advisory committee members Dr. Alexander Khanov, Dr. K. S. Babu, Dr. Joseph Haley and Dr. Joe Cecil for agreeing to serve in my committee to guide me towards my Ph.D. degree. Special thanks to Prof. Albert T. Rosenberger, who has been a great support as Graduate coordinator at Physics department and also taught me multiple graduate courses.

I am thankful to Physics Department of OSU and all its office staffs specially including Susan Cantrell, Alisha Chavez and Elizabeth Bridenstine. My colleagues with whom I have worked, collaborated on teaching duties contributed to some great memories. All the Chairs of our OSU Physics Department during last 5-6 years: Prof.

Acknowledgments reflect the views of the author and are not endorsed by committee members or Oklahoma State University.

John Mintmire, Prof. K.S. Babu & Prof. David N. McIlroy deserve praise for running the OSU Physics department so smoothly.

I am grateful to Argonne National Laboratory(ANL) for hosting me for around 1.5 years by supporting me through their 'ANL-ATLAS Graduate Fellowship' and a summer fellowship at the High Energy Physics Center for Computational Excellence (HEPCCE) at ANL. Thanks to the ATLAS Collaboration at CERN for not only allowing me to to work at CERN for one year, but also proving many services and tools developed by the collaboration through out the years.

For all the hardware studies, I will like to thank Dr. Jessica Metcalfe, who has been my supervisor at Argonne National lab for a year. I am also thankful to a few more collaborators: Dr. Vallary Bhopatkar (ANL), Dr. Dylan Frizzell, Mr. Joseph Lambert, Mr. Joe Muse from University of Oklahoma. Thanks to Dr. Taylor Childers for supervising me for a research project at ANL during Summer 2017.

For the dijet plus lepton analysis and for the multi-body analysis I will like to thank Dr. Sergei Chekanov from Argonne National Laboratory, Dr. Vincent Pascuzzi (Lawrence Berkeley National Laboratory), Mr. Henry Meng (University of Toronto), Dr. Smita Darmora (ANL) and the whole Dijet plus lepton analysis team. Dr. Sergei Chekanov has been an extra-ordinary support and guide. His enthusiasm in different Physics studies is truly inspiring. I owe a lot to Dr. Sergei Chekanov for teaching me much Physics and for being an outstanding collaborator in multiple Physics projects.

I owe a lot to Dr. Josu Cantero (OSU) for teaching me many aspects of Physics analysis. Sincere thanks to Dr. Alexander Khanov, who has taught me all the basics of flavor tagging. I am grateful to Dr. Giacinto Piacquadio (Stony Brook University), Dr. David Olivier Jamin (formerly at OSU), Dr. Andrea Coccaro (INFN, Italy) and the ATLAS Flavor tagging group. I wish all the best to Mr. Jacob Crosby for taking

Acknowledgments reflect the views of the author and are not endorsed by committee members or Oklahoma State University.

my Direct tag studies forward in the coming days.

I want to specially thank much to a scholarship program named Sir Syed Global Scholar Award (SSGSA) with whose mentorship and support I could dream to travel from India to the United States to pursue my Ph.D. in Physics. Thanks to all my mentors in SSGSA for their valuable guidance, care and friendship. Thanks to some of my great friends S.M. Isha, Ajaharul Islam, Sk Abdus Sayeed, Hafijul Islam and friends in Stillwater, Oklahoma including Sudip Jana, Dewan Russel, Dipendra Bhandari, Tajuddin Khan, Junaid etc. and to many more great friends from SSGSA, OSU, CERN, Aligarh and West Bengal, India for their support.

While writing this thesis, I frequently remember my first physics teacher Mr. Ahindranath Chatterjee from my high school Ramakrishna Mission at Sargachi, who taught me the subject with great love and passion and inspired to study Physics. I am thankful to all my teachers from my high school days, to all my Professors from my undergraduate university Aligarh Muslim University, India who guided and inspired me in my journey from a very small town in India to a distant land USA. Thanks to all those Professors who taught me graduate courses at OSU as well.

Most importantly I will like to thank my parents Mr. Saiful Islam and Mrs. Merina Khatun and also my dear sister Shayla Sarmin for their love, support, struggles and sacrifices without which this journey would never be possible.

The ongoing COVID-19 pandemic has made the job market difficult for early career researchers. I sincerely thank my collaborators who helped me in going through this phase of job search by providing their reference letters. As I move forward to a new phase of life by joining University of Wisconsin-Madison, USA as a Post-doctoral research associate, I do hope to be able to contribute to some good Physics in my research career as a Physicist in the coming days.

Acknowledgments reflect the views of the author and are not endorsed by committee members or Oklahoma State University.

Name: WASIKUL ISLAM

Date of Degree: MAY, 2021

Title of Study: SEARCHES FOR BEYOND THE STANDARD MODEL PHYSICS IN DIJET RESONANCES AND DEVELOPMENT OF A NEW B-TAGGING CALIBRATION ALGORITHM AT THE ATLAS EXPERIMENT AT CERN

Major Field: PHYSICS

Abstract:

This Ph.D. dissertation describes the development of a new b-tagging calibration algorithm which helps to correctly identify jets originated from b quarks at the ATLAS detector at European Organization for Nuclear Research (CERN). B-tagging has been crucial for physics programs at the ATLAS experiment and the newly developed technique aims to improve its performance.

The dissertation also addresses the R&D efforts for the upgrade of Internal Tracker (ITk) of the ATLAS detector for the upcoming High-Luminosity LHC.

Finally, the dissertation presents a search for dijet resonances in events with identified leptons, which has been performed using data collected in proton-proton collisions at $\sqrt{s} = 13$ TeV by the ATLAS experiment at CERN between 2015 and 2018, corresponding to an integrated luminosity of 139 fb$^{-1}$. The study investigated the possibilities of new physics beyond the standard model in the dijet invariant mass distributions in the range of $0.22 < m_{jj} < 6.3$ TeV. The analysis probes much lower $m_{jj}$ than traditional inclusive dijet searches and is sensitive to a wide range of new physics models with a final-state lepton. This dissertation summarizes the results of interpretation of dijet resonance search in terms of Charged Higgs boson decaying into top and bottom quarks. The dissertation also discusses possible extensions of scopes for similar dijet resonance searches using multi-body search techniques.

TABLE OF CONTENTS

Chapter Page

**I. Introduction** . . . . . **1**

I.1 The Standard Model . . . . . 3

I.1.1 Spontaneous Symmetry Breaking . . . . . 6

I.1.2 Some verification of the predictions in history . . . . . 9

I.1.3 The Higgs Boson . . . . . 9

I.1.4 The Top-Quark . . . . . 13

I.1.5 Top-Quark Pair Production . . . . . 14

I.1.6 Decay of the Top-Quark . . . . . 15

I.1.7 The Bottom-Quark . . . . . 17

I.1.8 SM production cross sections . . . . . 19

I.2 Beyond the Standard Model . . . . . 20

I.2.1 BSM Physics in dijet resonances along with a lepton . . . . 22

I.2.2 Charged Higgs Boson . . . . . 22

I.2.3 W' Boson . . . . . 24

**II. The Experiment** . . . . . **27**

II.1 Large Hadron Collider . . . . . 28

II.1.1 The LHC acceleration chain . . . . . 28

II.1.2 Beam structure and Luminosity . . . . . 29

II.1.3 LHC Run-2 performance . . . . . 32

II.1.4 Pileup . . . . . 33

II.2 ATLAS detector . . . . . 34

II.2.1 ATLAS coordinate system . . . . . 34
II.2.2 ATLAS magnet system . . . . . 36
II.2.3 The Inner Detector(ID) . . . . . 36
II.2.4 The ATLAS Calorimeters . . . . . 38
II.2.5 The muon spectrometer . . . . . 39
II.2.6 The trigger and data acquisition system . . . . . 40
II.2.7 Luminosity monitor of the ATLAS experiment . . . . . 42

**III. R & D studies : ITk Pixel upgrade studies for High Luminosity LHC . . . . . 44**

III.1 HL-LHC upgrades . . . . . 44
III.2 Pixel Module Assembly . . . . . 46
III.2.1 Peel test . . . . . 48
III.2.2 Glue deposition repeatability . . . . . 48
III.2.3 Rotational alignment . . . . . 48
III.2.4 Profile thickness . . . . . 49
III.2.5 Wire bond strength . . . . . 49
III.2.6 Wire bond yield . . . . . 49
III.2.7 Time estimate . . . . . 51
III.2.8 Comparative summary . . . . . 51
III.3 Argonne Telescope at Fermilab Test-beam . . . . . 52
III.4 Tool developments with 3D printer . . . . . 56
III.5 3D Visualization of the recorded test beam data . . . . . 58
III.6 Conclusions . . . . . 60

**IV. Development of Direct tag Lightjet Calibration method . . . . . 61**

IV.1 The method . . . . . 61
IV.1.1 Basics of light jet calibration . . . . . 62

IV.1.2 Description of Direct tag method . . . . . 63
IV.2 Data samples, Monte Carlo simulations and event selection . . . . . 64
IV.2.1 Reweighting while ntuple production . . . . . 65
IV.2.2 Systematic uncertainties in Direct tag . . . . . 65
IV.3 Direct tag Results . . . . . 66
IV.3.1 Early results in release 20.7 . . . . . 67
IV.3.2 Early results in release 20.7 and issues . . . . . 67
IV.3.3 Investigating dependencies of results on different taggers . . 71
IV.3.4 Investigating discriminators unaffected by track IP resolution 71
IV.3.5 Results with release 20.7 . . . . . 72
IV.3.6 First results with DL1 tagger . . . . . 72
IV.3.7 Results for FixedCut B efficiencies . . . . . 74
IV.3.8 Changing the binning of template fit from 7 to 5 . . . . . 75
IV.4 Alternative method : Verification of Direct tag results . . . . . 75
IV.4.1 Direct tag vs Negative tag rate method : A comparison . . . 78
IV.5 Analysis of early results . . . . . 78
IV.6 Further studies with high-pt samples . . . . . 81
IV.7 Studies on additional bins . . . . . 87
IV.8 Trigger studies . . . . . 89
IV.9 Summary . . . . . 89

**V. Search for Charged Higgs through Dijet plus lepton . . . . . 90**
V.1 Broad strategies . . . . . 90
V.1.1 Strategies for Model independent searches . . . . . 90
V.1.2 Strategies for the searches for Charged Higgs boson . . . . . 91
V.2 Monte Carlo simulations and physics modelling . . . . . 91
V.2.1 Heavy Charged Higgs MC description . . . . . 92
V.2.2 Background MC description . . . . . 93

V.3 Event selection and object definitions . . . 99
V.3.1 Electrons and muons : selection of events . . . 100
V.3.2 Jets : selection of events . . . 104
V.3.3 Efficiency of HLT triggers . . . 106
V.3.4 Overlap removal . . . 109
V.3.5 Minimum $m_{jj}$ . . . 110
V.4 Data-Monte Carlo comparison . . . 111
V.5 Analytic functions and statistical tests . . . 111
V.6 Control region studies . . . 116
V.6.1 MC based Control region . . . 116
V.6.2 Loose electron Control region(LE-CR) . . . 117
V.7 Tests on signals . . . 120
V.7.1 Signal injection test . . . 120
V.7.2 Spurious signal tests . . . 121
V.7.3 Tests for Charged Higgs signals . . . 123
V.8 Studies of signal region . . . 129
V.9 Additional studies for the Charged Higgs boson model . . . 133
V.9.1 Mass scan using likelihood fits . . . 133
V.9.2 Angle and $p_T$ for leading jet and top quarks . . . 135
V.9.3 Boosted topology for $H^+$ . . . 137
V.9.4 Zero-width approximation . . . 141
V.10 Systematic uncertainties . . . 143
V.10.1 Background estimate uncertainties . . . 143
V.10.2 Systematic uncertainties on signal . . . 143
V.10.3 Systematic uncertainties for Gaussian limits (Gaussian signal shape uncertainties) . . . 145
V.10.4 Model uncertainty . . . 147

V.11 Results . . . 148
V.11.1 Limit calculation for Charged Higgs . . . 148
V.11.2 Results on Charged Higgs . . . 149
V.11.3 Comparisons of the $H^+$ limits with published results . . . 153
V.12 Conclusion from the search . . . 155

**VI. Multi-body searches: Ideas for extension of Dijet resonance searches along with charged lepton . . . 156**
VI.1 Three body invariant masses . . . 157
VI.1.1 Case study : Radion Model . . . 158
VI.1.2 A hypothetical scenario . . . 159
VI.2 Four-body invariant masses . . . 160
VI.2.1 Case study : Composite lepton Model . . . 160
VI.2.2 A hypothetical scenario . . . 161
VI.3 Exclusion limits . . . 162
VI.4 Conclusion . . . 164

**VII.Summary and conclusions . . . 166**

**REFERENCES . . . 169**

**APPENDIX . . . 181**
A.1 A few additional studies . . . 181
A.1.1 Control plots of different reweightings . . . 181
A.1.2 Contribution of each systematic in SF . . . 195
A.1.3 Plots from investigations of different taggers . . . 207
A.1.4 Plots from investigations of discriminators unaffected by track IP resolution . . . 215
A.1.5 Alternative Fit/MC method . . . 222

LIST OF TABLES


| Table | | Page |
|---|---|---|
| I.1 | The table summarises the different Standard Model particles, gauge groups and their properties. The values against gauge groups $SU(2)_L$, $SU(3)_C$ indicate that the fields belong to singlet, doublet, triplet or octet representations for 1,2,3,8 values respectively. The values in the column of $U(1)_Y$ represent corresponding weak hyper-charges. | 5 |
| I.2 | Higgs boson decay modes and Branching Ratios [1]. | 10 |
| I.3 | Top quark decay modes and Branching Ratios [1]. | 17 |
| II.1 | Run 2 performance of LHC while using regular proton proton collisions. The emittance values for 2017 were for Batch Compression Merging and Splitting(BCMS) beam and for 2017, maximum number of bunches and train length values correspond to BCMS and 8b4e beams respectively [2]. | 32 |
| II.2 | Pseudorapidity $\eta$ coverage for measurement in different sub-detectors of ATLAS[3]. | 36 |
| III.1 | Measurements of the mass of the glue deposited for different trials while using rice paper method. The mean is quoted with the sample standard deviation [4]. | 48 |
| III.2 | Measurements of the relative alignment between the flex cable and the sensor hybrid for different trials have been shown. The uncertainty quoted is the sample standard deviation. The measurements were performed with an optical device with estimated resolution of 0.2 mrad [4]. | 49 |
| III.3 | Ratio of successfully wire bonded ASICs and origin of failures have been shown in table. Technician aid refers to either injecting small amounts of extra epoxy around the edges/corners or performing in-situ alignment corrections | 51 |
| III.4 | Comparative results of the three methods of module assembly[4]. | 51 |
| III.5 | A comparative table for 3D printing while printing PCB covers. | 57 |
| IV.1 | Comparing different taggers | 71 |
| IV.2 | Systematic uncertainties with 1d fit with 5 binning. It can be seen c-fraction uncertainty for large jet pT explodes | 83 |

IV.3 Systematic uncertainties with tag weight and SMT with 5 binning. It can be seen c-fraction uncertainties are under control, Light fraction uncertainties are significantly improved compared to 1d fit . 84
IV.4 Systematic uncertainties with tag weight and SV with 5 binning. Better results at high jet pT compared to tag weight and SMT.Light fraction uncertainties are significantly improved compared to 1d fit. 85

V.1 This table lists the information on Charged Higgs boson production in the 4FNS Monte Carlo for $\tan(\beta) = 1$ for the hMSSM model [5]. The luminosity for each mass (4th column) was calculated from the numbers of events and the predicted cross sections listed in this table. The last column shows the branching fractions. . . . . 93
V.2 This table lists the information on Charged Higgs boson production in the 4FNS Monte Carlo for $\tan(\beta) = 0.5$ for the hMSSM model [5]. The last column shows the branching fractions. . . . . 93
V.3 This table lists the Charged Higgs boson production cross sections in the 4FNS Monte Carlo for the $m_h^{\mathrm{mod}-}$ model used in this study. The branching ratios are included. . . . . 94
V.4 Background sources and their contribution percentage. . . . . 94
V.5 Background processes, number of events used in the analysis and their cross sections [6]. . . . . 98
V.6 Muon selection criteria . . . . . 101
V.7 Electron selection criteria . . . . . 101
V.8 Jet definitons and selections as used in the analysis. . . . . 104
V.9 Criteria for overlap removal . . . . . 109
V.10 Final selection cuts for objects . . . . . 110
V.11 Absolute values of mass shifts for different systematic uncertainties for several mass points. The systematic shifts marked with (*) are shown for the signal width. . . . . 145
V.12 Numbers of $H^+$ events generated, passed the acceptance cuts, fully reconstructed, and the visible cross sections. The final efficiency is given in the last column. Only statistically uncertainties on the acceptance and efficiencies are shown. . . . . 149

1 Comparing contribution of different systematics for pt1 in central eta . . . . . 196
2 Comparing contribution of different systematics for pt2 in central eta . . . . . 197
3 Comparing contribution of different systematics for pt3 in central eta . . . . . 198
4 Comparing contribution of different systematics for pt4 in central eta . . . . . 200
5 Comparing contribution of different systematics for pt5 in central eta . . . . . 201

6 Comparing contribution of different systematics for pt6 in central eta . . . . . 202
7 Comparing contribution of different systematics for pt7 in central eta . . . . . 203
8 Comparing contribution of different systematics for pt8 in central eta . . . . . 205
9 Comparing contribution of different systematics for pt1 in Forward eta . . . . . 206

LIST OF FIGURES


| Figure | | Page |
|---|---|---|
| I.1 | Standard Model of particle physics [7]. | 4 |
| I.2 | $\mathcal{V}(x)$ shape when $\mu^2 > 0$, $\lambda > 0$ | 7 |
| I.3 | $\mathcal{V}(x)$ shape when $\mu^2 < 0$, $\lambda > 0$. The dashed line at the bottom representing circle of absolute minima. | 7 |
| I.4 | Feynman diagrams of Higgs boson production processes [1]. | 11 |
| I.5 | Standard Model Higgs boson production cross sections as the function of center of mass energy $\sqrt{s}$ [8]. | 12 |
| I.6 | Combined measurement results from ATLAS and CMS experiments from $t\bar{t}$ production observables [9]. | 13 |
| I.7 | Feynman diagrams of $t\bar{t}$ pair production processes | 14 |
| I.8 | Summary of ATLAS and CMS measurements of the single top production cross-sections in different channels as a function of $\sqrt{s}$ (the center of mass energy).Theoretical calculations based on: NLO QCD, NLO QCD complemented with NNLL resummation and NNLO QCD (t-channel only) are also compared to the measurements [9]. | 15 |
| I.9 | Combined measurements of ttbar+W, ttbar+Z, ttbar+$\gamma$ production cross sections by ATLAS and CMS experiments at center of mass energy 13 TeV. The ttbar+W and ttbar+Z cross section measurements are compared to the NLO QCD and EW theoretical calculation complemented with NNLL resummation, while the ttbar+$\gamma$ cross section measurement is compared to the NLO QCD theoretical calculation. The theory band represents uncertainties due to renormalization and factorisation scales and parton density functions [9]. | 16 |
| I.10 | Diagrams for few dominant decays of b quarks [10]. | 18 |
| I.11 | Feynman diagram of Higgs boson decaying to pair of b and anti-b quarks [10]. | 18 |
| I.12 | Standard Model production cross sections of different Physics processes at different center of mass energies ($\sqrt{s}$ = 7, 8, and 13 TeV). | 19 |
| I.13 | Upper limits on cross sections for the interactions between spin independent Dark matter  nucleon as a function of mass of dark matter [1]. | 21 |

I.14 The Feynman diagrams show generic resonance X decaying into two partons producing two jets and leptons is also produced from the decay of W boson. In the first diagram X' is another resonance particle [11]. . . . . 23
I.15 The Feynman diagram for heavy charged Higgs boson being produced by gluon fusion, together with a top and bottom quark ($tbH^+$). 24
I.16 Feynman diagram of W prime decaying to a top and bottom quarks 25

II.1 A schematic view of LHC and its 4 biggest experiments at the Frenco-Swiss border at CERN. . . . . 29
II.2 A schematic view of LHC complex at CERN [12]. . . . . 30
II.3 A comparative plot of cumulative luminosity during different years of data taking by the LHC. . . . . 31
II.4 Number of Interactions per Crossing during Run 2 at the ATLAS detector. . . . . 33
II.5 A schematic view of ATLAS detector. . . . . 35
II.6 A schematic view of ATLAS Magnet systems. In the figure central solinoid is hidden. [13] . . . . . 37
II.7 A schematic view of ATLAS Inner tracking detector. . . . . 38
II.8 A sketch of ATLAS calorimeters. [14] . . . . . 39
II.9 A layout of ATLAS Muon spectrometers. [15] . . . . . 40
II.10 ATLAS Trigger and DAQ system in Run 2 shown using block diagram. . . . . 41
II.11 Comparison of the main luminosity algorithms to the LUCID hit-counting algorithm. The results are mostly within 1.3% of the LUCID measurements [16]. . . . . 42
II.12 A plot of cumulative luminosity during different years of data taking at the ATLAS detector at CERN. . . . . 43
II.13 Total integrated Luminosity during Run 2 at the ATLAS detector. 43

III.1 LHC timeline plan . . . . . 44
III.2 Schematic design of a hybrid pixel module [17]. . . . . 45
III.3 The rice paper assembly method uses a vacuum sealed bag to apply even pressure to the flex cable and sensor hybrid. A rice paper piece that has been cut to the correct dimensions and infused with adhesive is sandwiched between the two. The grid paper shown is a thick, clean room safe paper that is cut to align the sensor hybrid in place. . . . . 46
III.4 Paper cutter machine used for Rice paper method . . . . . 47
III.5 Three methods of module assembly used at Argonne . . . . . 47
III.6 Diagram of the profile thickness measurement locations. Each green square represents a measurement point, and the blue ovals represent the points used to construct a Z datum plane. The six rows of measurements nearest the edges are used to fill the histograms in next Figure . . . . . 50

III.7 Thickness distribution for rice paper method. . . . . 50
III.8 Design of Argonne telescope at Fermilab . . . . . 53
III.9 Wirebond connection between flexible PCB and Module. . . . . 54
III.10 PixX and PixY distribution in the raw data. . . . . 54
III.11 HSIO *II* and the RCE which are used for data acquisition. . . . . 55
III.12 Temperature and humidity distribution inside cold-box for DUTs. 55
III.13 Beam correlation between different planes while using FEI4 modules. 56
III.14 Beam spots with our experimental setup with three different pixel modules. The left plot is withFEI4 module, the middle plot is with ATLASPix module and the right plot is with the RD53A module. 56
III.15 Printing steps with 3D printer . . . . . 57
III.16 Examples of telescope plane development with 3D printer . . . . 58
III.17 Experimental setup with 3D printed covers and test stands . . . . 58
III.18 Development of a new method for module assemble with 3D printer 59
III.19 Example 3D visualization of 3 tracks passing though different planes 59
III.20 Example 3D visualization of ToTs with different planes . . . . . 60

IV.1 Example 3D visualization of 3 tracks passing though different planes 62
IV.2 Template fit of pdfs of *b*, *c* and light jets. . . . . 68
IV.3 Left to right :Flavor Fractions of b (left) and c jets (right) for central (left 2 plots) and forward eta (right two plots) with MV2c20 tagger while using ATLAS reconstruction software 20.7. . . . . 68
IV.4 Scale Factors bin by bin for Pythia in both release 20.7 and release 21 in central (left plots; for SF 85% and SF 77%) and forward (right plots for SF 85% and SF 77%) eta regions. . . . . 69
IV.5 Scale factors bin by bin at central eta region with both MV2c20 and MV2c10 taggers for SF 85% (left) and SF 77% (right). . . . . 70
IV.6 Left to right : Flavor Fractions for b jets and c jets central eta and for b jets and c jets for forward eta regions . . . . . 70
IV.7 ROC curves using different taggers . . . . . 73
IV.8 fit/MC ratio for c jets with masssvx discriminator excluding the underflow bins for central (left) and forward (right) eta regions . . 73
IV.9 Scale factor bin by bin for central (left 2 plots; for SF 85% and SF 77%) and forward (right 2 plots; for SF 85% and SF 77%) eta with DL1 tagger . . . . . 73
IV.10 Scale factor bin by bin for fixed cut B eff 85 in central (left 2 plots; for SF 85% and SF 77%) and forward (right 2 plots; for SF 85% and SF 77%) eta regions . . . . . 74
IV.11 Scale factor bin by bin for fixed cut B eff 77 in central (left 2 plots; for SF 85% and SF 77%) and forward (right 2 plots; for SF 85% and SF 77%) eta regions . . . . . 74
IV.12 FlavFractions for central (left two plots) and forward (right two plots) eta in 5 binning . . . . . 76

IV.13 Scale factor bin by bin for central (left 2 plots; for SF 85% and SF 77%) and forward (right 2 plots; for SF 85% and SF 77%) eta in 5 binning . . . . . 76
IV.14 Correlation matrices for 7 bin template fit for 1st and 2nd pt bins in 7 binning (left) and 5 binning(right) . . . . . 77
IV.15 Comparison of Scale factors bin by bin from 7 bin template fit (at the top) and 5 bin template fit (at bottom) respectively . . . . . 77
IV.16 Comparison of Scale factors for pseudo continuous b-efficiencies from Direct tag method (at the top) and Negative tag rate method (at bottom) . . . . . 79
IV.17 Comparison of Scale factors for pseudo Fixed-cut b-efficiencies from Direct tag method (at the top) and Negative tag rate method (at bottom) . . . . . 80
IV.18 Jet pT distribution in different JZ MC slices are shown in the left and right plots respectively. . . . . 81
IV.19 B-tagging efficiency in different JZ slices are shown in the left and right plots respectively. . . . . 82
IV.20 Template fit for JZ4 slice for r21. The plots have compared SMT and jet SV1 masssvx discriminators with 5 bins. . . . . 86
IV.21 Template fit for JZ4 slice for r21. The plots have compared SMT and jet SV1 masssvx discriminators with 7 bins. . . . . 87
IV.22 B-tagging efficiency for 5 binning(left plot) and 7 binning(right plot) 88
IV.23 Some Trigger studies with data of dijet samples for Direct tag can be observed in the plot. Leading JetpT with HLT triggers with 2018 data are seen in the plots. In the left plot 2018 data with period D and in the right plot 2018 data with period F can be seen. 89

V.1 Dijet invariant mass at the truth level. . . . . 95
V.2 Comparison of the $m_{jj}$ shapes at the detector and truth levels for Charged Higgs boson Monte Carlo for 600 GeV(top row left), 800 GeV (top row right), 1000 GeV (2nd row left), 1200 GeV (2nd row middle), 1600 GeV (2nd row right), 1800 GeV (3rd row left) and 2000 GeV (3rd row right). . . . . 96
V.3 Reconstructed $m_{jj}$ distribution for signal samples generated with $tbH^+$ model. The numbers of events for each mass are the predictions for the 139 fb$^{-1}$ luminosity. . . . . 97
V.4 Event rates for fired electron and muon triggers before selecting events. . . . . 100

V.5 Comparison of efficiencies due to lowest unprescaled single electron triggers in the years of 2015, 2016, 2017 and 2018 are shown in the plots as function of offline electron transverse energy $E_T$. FCTight isolation and tight offline identification are ensured for the offline electrons. Among 2015 triggers logical OR of HLT_e24_lhmedium_L1EM20VH, HLT_e60_lhmedium and HLT_e120_lhloose and among triggers of 2016-2018, logical OR of HLT_e26_lhtight_nod0_ivarloose, HLT_e60_lhmedium_no and HLT_e140_lhloose_nod0 are used [18]. . . . . 102
V.6 Efficiency of Level 1 (L1) MU20 trigger and absolute and relative efficiencies of the OR of mu26_ivarmedium with mu50 HLT plotted as a function of $p_T$ of offline muon candidates for different years (2015 year is similar to 2016 plot) [19] for three different years. The top plots is for year 2016, the second plot is for 2017 data and the bottom plot is for 2018 data. Offline isolated muon candidates and are required to pass "Medium" quality requirement. . . . . 103
V.7 $\eta$ distributions for leading (top) and sub-leading(bottom) in $p_T$ jets for signal and background Monte Carlo. The background MC (red line) includes all the different backgrounds combined with the expected cross sections for 139 fb$^{-1}$ luminosity. . . . . 105
V.8 Event rates for fired electron and muon triggers selecting events. . 106
V.9 Studies of the efficiency of the high-threshold electron trigger (e60) using 2015 data (top plot) and 2016-2018 data (bottom plot) with respect to $m_{jj}$. . . . . 107
V.10 Studies of the efficiency of the high-threshold muon trigger (mu50) using 2015 data (top plot) and 2016-2018 data (bottom plot) with respect to $m_{jj}$. . . . . 108
V.11 The distributions of $\Delta R(jet, electron)$ that defines a distance between leading jet and any electron above $p_T^l > 60$ GeV for for $> 190$ GeV (note this cut is lower than for the central analysis). . 109
V.12 Studies of the leading jet $p_T$ for different cuts of $p_T^{lepton}$ on electrons (top) and muons (bottom) respectively. . . . . 110
V.13 The distribution of transverse momentum distribution for selected muons(top left), electrons (top right), leading jets(bottom left) and sub-leading jets(bottom right) . . . . . 112
V.14 Dijet invariant mass $m_{jj}$ distributions comparing data and MC. Large differences of over 50% between data and MC appear due to limited statistics in multijet samples. These statistical fluctuations makes quantitative comparisons inappropriate.The left plot is for muons and the right plot is for electrons.Final analysis was done using a data-driven method, without relying on the background MC presented in this figure. . . . . 113
V.15 Jet $P_t$ distributions comparing data and MC. Differences of over 50% also appear here. Final analysis was done using a data-driven method, without relying on the background MC presented in this figure. . . . . 113

V.16 Example of using 5p fit hypothesis with different Monte Carlo simulations of background samples. The red line denotes the combined contribution of of all Standard Model backgrounds. Each contribution is also shown separately, without stacking the histograms. The observed large spikes in the MC is due to small statistics of the JZ0-JZ12 dijet samples after the lepton requirement. . . . . 115
V.17 The left plot shows the 5 parameter(Eq. V.5.1) fit in the 2+1 jet control region and the right plot shows the residuals of the 5p fit of the same MC based control region along with the statistical tests. The 3rd jet has $p_T(jet) > 60$ GeV. . . . . 116
V.18 The left plot shows the alternative 5p fit (Eq. V.5.2) fit in the 2+1 jet control region and the right plot shows the residuals of the 5p fit of the same MC based control region along with the statistical tests. The 3rd jet has $p_T(jet) > 60$ GeV. . . . . 117
V.19 The top plot shows the 5 parameter(Eq. V.5.1) fit of dijet mass spectra for $>$ 216 GeV in the Loose electron control region and the bottom plot shows the residuals of the 5p fit of the same LE control region along with the statistical tests. . . . . 118
V.20 The top plot shows the alternative function Eq. V.5.2 fit of dijet mass spectra for $>$ 216 GeV in the Loose electron control region and the bottom plot shows the residuals of the 5p fit of the same LE control region along with the statistical tests. . . . . 119
V.21 The plot shows calculated signal reconstruction efficiency using the 5p+Gaussian description while using different widths of the injected Gaussian signals. The number of observed events was calculated from the Gaussian component of the global 5p+Gauss fit using 100 pseudo-experiments. The uncertainties on the data points are the RMS values on the ratios. The peak and the width of the Gaussian function were fixed to the expected values to avoid instabilities in the 8-parameter fit. . . . . 121
V.22 The average values of events from the Gaussian amplitude (for 15% width) using the 5p+Gaussian fits applied to 100 random templates constructed using background-only hypothesis. For the top plot, the parameters of the 5p fit for 5p+Gaussian were fixed to the 5p-fit only. And for the bottom plot, parameters of the 5p fit were allowed to float (not fixed), though width of Gaussian and peak position are fixed.The vertical error bars shows the RMS values, which are used as additional contribution to systematic uncertainty. . . . . 122
V.23 Examples of the fit of the $m_{jj}$ distributions of the $H^+$ model (for two representative masses) using an asymmetric Gaussian function ("AGaus") for $H^+$ at 300 GeV, 600 GeV, 800 GeV, 1000 GeV, 1200 GeV and 1800 GeV respectively. The dots are the signal $H^+$ Monte Carlo, the solid lines are the fits of using the AGaus function used for the signal recovery. The fits have $\chi^2/ndf = 1 - 1.2$. . . . . 125

V.24 Signal reconstruction efficiency calculated using the 5p+AGauss description of the wide Gaussian signals, with $20\%/M$ symmetric Gaussian and $40-60\%/M$ (assuming the $H^+$ signal template). The number of observed events was calculated from the Gaussian component of the global 5p+AGauss fit using 100 pseudo-experiments. The number of injected events corresponds to the 3 for $5\sigma$ amplitudes The pseudo-data were created using the signal region of the data. The uncertainties on the data points are the RMS values on the ratios. The peak and the widths of the asymmetric Gaussian function were fixed to the expected values to avoid instabilities in the 9-parameter fit. . . . . 126
V.25 Signal injection test for $H^+$ signal at different masses for 5 $\sigma$ injected signals. . . . . 127
V.26 The average values of events from the Gaussian amplitude using the 5p+Gaussian fits applied to 100 random templates constructed using background-only hypothesis. The parameters of the 5p fit were allowed to float (not fixed to the parameters from background-fit only). The vertical error bars shows the RMS values. The pseudo-data were created using the signal region of the data. . . 128
V.27 With the presence of an isolated muon, dijet mass spectra data for $m_{jj} > 216$ GeV after the fit with the 5p background function using the Likelihood method can be found in the top plot. The corresponding distribution of residuals from the same fit can be found in the second plot. Local statistical significance in each mass interval showing the local probability that the background fluctuates to the observed number of events (or higher) can be seen in the bottom plot. The positions of the local excesses indicated using the solid (smoothed) lines. . . . . 130
V.28 With the presence of an isolated electron, dijet mass spectra data for $> 216$ GeV after the fit with the 5p background function using the Likelihood method can be found in the top plot. The corresponding distribution of residuals from the same fit can be found in the second plot. Local statistical significance in each mass interval showing the local probability that the background fluctuates to the observed number of events (or higher) can be seen in the bottom plot. The positions of the local excesses indicated using the solid (smoothed) lines. . . . . 131

V.29 With the presence of an isolated electron or muon, dijet mass spectra data for $> 216$ GeV after the fit with the 5p background function using the Likelihood method can be found in the top plot. The corresponding distribution of residuals from the same fit can be found in the second plot. Local statistical significance in each mass interval showing the local probability that the background fluctuates to the observed number of events (or higher) can be seen in the bottom plot. The positions of the local excesses indicated using the solid (smoothed) lines. . . . . 132
V.30 $Z$ values from the global likelihood fits of the $m_{jj}$ distribution assuming the 5p function (background only) and 5p+signal, where signal was either the $H^+$ shape or a Gaussian with the widths of 5% and 30%. . . . . 134
V.31 The distributions of the opening angle between the leading jet that forms $m_{jj}$ and the direction of the top quark from the $H^+$ decays. The plots show the distributions for different $H^+$ masses. . . . . 135
V.32 Correlation between the $p_T$ of the leading jet and the the top quark from the $H^+$ decays. The plots show the distributions for different $H^+$ masses. . . . . 136
V.33 Correlations between $m_{jj}$ masses at the reconstructed and truth levels for two representative $H^+$ mass points (lowest and where the largest deviations by BumpHunter is reported). . . . . 137
V.34 Comparisons between $m_{jj}$ generated with MG5 at NLO QCD using the default PDF (NNPDF23NLO) and the alternative PDF (CT10nlo). . . . . 138
V.35 Comparisons between $m_{jj}$ (at the truth level) generated with MG5 at LO QCD with and without including MadSpin. Also, comparison with an alternative PDF (CTEQ6L) is shown. . . . . 140
V.36 Comparisons between $m_{jj}$ shapes before and after 4% ($\tan\beta = 1$) and 18% ($\tan\beta = 0.5$) Breit-Wigner smearing of the original MG5 distribution that assumes the zero-width approximation. . . . . 142
V.37 Comparison of the default 5p and the alternative fit function given by Eq. V.5.2. The yellow area on the ratio shows $\pm 1\sigma$ statistical uncertainties on the default function, while the red curve shows the behaviour of the alternative fit function. . . . . 144
V.38 Shapes of the Gaussian "signals" with different values of the width (detector resolution, 5%, 10%, 15%) together with systematic uncertainties after using the second order polynomials that parameterize shifts for the peaks and widths. The red color shows the nominal values, the black histogram shows signals due to systematic variation. . . . . 146
V.39 Observed (filled circles) and expected 95% credibility-level upper limits (dotted line) on the on the cross-section times acceptance ($A$), efficiency ($\epsilon$) and branching ratio (BR) for for the $H^+t$ model for the $m_h^{\mathrm{mod}-}$ benchmark scenario [20]. . . . . 150

V.40 Observed (filled circles) and expected 95% credibility-level upper limits (dotted line) on the on the cross-section times acceptance ($A$), efficiency ($\epsilon$) and branching ratio (BR) for for the $H^+t$ model for the $m_h^{\text{mod}-}$ benchmark scenario [20]. The limits are shown for $e$ and $\mu$ channels separately. . . . . 151
V.41 Observed (filled circles) and expected 95% credibility-level upper limits (dotted line) on the cross-section times acceptance ($A$) and branching ratio (BR) for for the $H^+t$ model for the $m_h^{\text{mod}-}$ benchmark scenario [20]. . . . . 152
V.42 Observed (filled circles) and expected 95% credibility-level upper limits (dotted line) on the cross-section times branching ratio (BR) for for the $H^+t$ model for the $m_h^{\text{mod}-}$ benchmark scenario [20]. . . 152
V.43 This figure compares the expected and observed limits from the Run 2 paper [21] (without indicating the 1 and 2 $\sigma$ bands). . . . 153
V.44 This figure compares the expected and observed limits from the Run 2 paper [21] with indicating the 1 and 2 $\sigma$ bands. . . . . 154

VI.1 A representative diagram of the decay a heavy particle A to two other particles B and C [22]. . . . . 157
VI.2 A Feynman diagram describing decay in Radion model . . . . . 158
VI.3 Comparisons between $m_{jj}$ and $m_{jjl}$ distributions for the 3 TeV $W_{kk}$ mass for $M_{Wkk} - M_{Rad} = 250$ GeV [22]. . . . . 159
VI.4 The invariant masses of two jets ( $m_{jj}$) and two jets and a lepton ($m_{jjl}$) in events $A \to B\,C$ simulated with Pythia with the settings described earlier. . . . . 160
VI.5 A representative Feynman diagram for the composite lepton model[23].161
VI.6 Invariant masses for a $Z'E$ model [23] constructed from 2 jets, 2 jets plus a lepton and 2 jets + 2 leptons. The $Z'$ mass was generated at 3 TeV, while $M(E) = 2$ TeV. The simulations are performed using MG5 with Pythia 8 showering. . . . . 162
VI.7 The invariant masses of two jets ( $m_{jj}$), two jets and a lepton ($m_{jjl}$) and two jets and two leptons $m_{jjll}$ in events $A \to B\,C$ simulated with Pythia with the settings described earlier. . . . . 163
VI.8 Expectations for $m_{jjl}$ invariant mass distributions for 140 $fb^{-1}$, 440 $fb^{-1}$ and 3 $ab^{-1}$(14 TeV) using the Pythia 8 generator for events having at least one isolated lepton with $p_T^l > 60$ GeV. Contributions from $W/Z/H^0$ -boson processes and top-quark processes are shown separately [22]. . . . . 164
VI.9 The 95% CL upper limits obtained from the $m_{jjl}$ distribution on cross-section times acceptance ($A$), efficiency ($\epsilon$) and branching ratio (BR), for a BSM signal with a cross-section that produces a Gaussian contribution to the particle-level $m_{jjl}$ distribution, as a function of the mean of the Gaussian mass distribution. The limits are calculated assuming 15% width [22]. . . . . 165

1 Illustration of the reweighting of the MC to data in each bin of the LF mistag rate measurement ($p_{jet}/|\eta_{jet}|$) for the leading (left) and sub-leading jet (right) as a function of the jet transverse momentum and eta for he Pythia multijet sample in release 20.7 data after pt/$\eta$ reweighting. . . . . 182
2 Illustration of the reweighting of the MC to data in each bin of the LF mistag rate measurement ($p_{jet}/|\eta_{jet}|$) for the leading (left) and subleading jet (right) as a function of the jet transverse momentum and eta for HERWIG++ sample in release 20.7 data after pt/$\eta$ reweighting. . . . . 183
3 Jet multiplicity distributions in data and in the Pythia and HERWIG++ samples in release 20.7 data after pt/$\eta$ reweighting. . . . 184
4 Illustration of the reweighting of the MC to data in each bin of Njet, $IP3D_{Neg}/p_{jet}$ for the leading (top) subleading (bottom) jet as a function of the jet track multiplicity, Njet, IP3DNeg. The Pythia multijet sample is shown in the left and the HERWIG++ sample is shown in the right in release 20.7 data after pt/$\eta$ reweighting. . 185
5 Data/MC comparison in jet MV2c10 Output(left) and in jet MV2c10Flip Output(right) for the leading (left) and subleading jet (right) as a function of the jet transverse momentum and eta for the Pythia multijet sample in release 20.7 data after pt/$\eta$ reweighting. . . . . 186
6 Data/MC comparison in jet MV2c10 Output(left) and in jet MV2c10Flip Output(right) for the leading (left) and subleading jet (right) as a function of the jet transverse momentum and eta for the HERWIG++ multijet sample in release 20.7 data after pt/$\eta$ reweighting.187
7 Illustration of the reweighting of the MC to data in each bin of the LF mistag rate measurement ($p_{jet}/|\eta_{jet}|$)for the leading (left) and subleading jet (right) as a function of the jet transverse momentum and eta for he Pythia multijet sample in release 21 data after pt/$\eta$ reweighting. . . . . 189
8 Illustration of the reweighting of the MC to data in each bin of the LF mistag rate measurement ($p_{jet}/|\eta_{jet}|$) for the leading (left) and subleading jet (right) as a function of the jet transverse momentum and eta for HERWIG++ sample in release 21 data after pt/$\eta$ reweighting. . . . . 190
9 Jet multiplicity distributions in data and in the Pythia and HERWIG++ samples in release 21 data after pt/$\eta$ reweighting. . . . . 191
10 Illustration of the reweighting of the MC to data in each bin of Njet, $IP3D_{Neg}$/pjet for the leading (top) subleading (bottom) jet as a function of the jet track multiplicity, $N_{jet}$, $IP3D_{Neg}$. The Pythia multijet sample is shown in the left and the HERWIG++ sample is shown in the right in release 21 data after pt/$\eta$ reweighting. . . 192

11 Data/MC comparison in jet MV2c10 Output(left) and in jet MV2c10Flip Output(right) for the leading (left) and subleading jet (right) as a function of the jet transverse momentum and eta for the Pythia multijet sample in release 21 data after pt/$\eta$ reweighting. . . . . 193
12 Data/MC comparison in jet MV2c10 Output(left) and in jet MV2c10Flip Output(right) for the leading (left) and subleading jet (right) as a function of the jet transverse momentum and eta for the HERWIG++ multijet sample in release 21 data after pt/$\eta$ reweighting. 194
13 Fit/MC ratio for b jets for central and forward eta using MV2c20 tagger . . . . . 208
14 Fit/MC ratio for c jets for central and forward eta using MV2c20 tagger . . . . . 208
15 Fit/MC ratio for b jets for central and forward eta using MV2c10 tagger . . . . . 208
16 Fit/MC ratio for c jets for central and forward eta using MV2c10 tagger . . . . . 209
17 Fitting of b, c and light jet templates for central eta using IP2D tagger . . . . . 209
18 Fitting of b, c and light jet templates for forward eta using IP2D tagger . . . . . 210
19 Fit/MC ratio for b jets for central and forward eta using IP2D tagger210
20 Fit/MC ratio for c jets for central and forward eta using IP2D tagger210
21 Fitting of b, c and light jet templates for central eta using IP3D tagger . . . . . 211
22 Fitting of b, c and light jet templates for forward eta using IP3D tagger . . . . . 211
23 Fit/MC ratio for b jets for central and forward eta using IP3D tagger212
24 Fit/MC ratio for c jets for central and forward eta using IP3D tagger212
25 Fitting of b, c and light jet templates for central eta using SV1 tagger . . . . . 213
26 Fitting of b, c and light jet templates for forward eta using SV1 tagger . . . . . 213
27 Fit/MC ratio for b jets for central and forward eta using SV1 tagger214
28 Fit/MC ratio for c jets for central and forward eta using SV1 tagger214
29 b, c and light jet efficiencies using different discriminators including underflow bins. b, c and light jet tagging efficiencies are calculated for each discriminator. . . . . 216
30 b, c and light jet efficiencies using different discriminators excluding underflow bins. b, c and light jet tagging efficiencies are calculated for each discriminator. . . . . 217
31 fit/MC ratio for b, c jets with masssvx discriminator including the underflow bins . . . . . 218
32 fit/MC ratio for b, c jets with masssvx discriminator excluding the underflow bins . . . . . 219

33 b, c and light jet efficiencies using different discriminators in release 20.7 data with reweighting. . . . . 220
34 b, c and light jet efficiencies using different discriminators in release 21 data. . . . . 221
35 Alternative fit/MC procedure for Pythia in 7 bin template fit. . 223
36 Prefit plots by Alternative fit/MC procedure for Pythia in 7 bin template fit.In the top row: leftmost plot is for pt bin 1 in central eta, second plot is for pt bin 1 for forward eta, third plot is for pt bin 2 in central eta and rightmost plot is for pt bin 2 for forward eta. In the Second row: leftmost plot is for pt bin 3 in central eta, second plot is for pt bin 3 for forward eta, third plot is for pt bin 4 in central eta and rightmost plot is for pt bin 4 for forward eta.In the third row: leftmost plot is for pt bin 5 in central eta, second plot is for pt bin 5 for forward eta, third plot is for pt bin 6 in central eta and rightmost plot is for pt bin 6 for forward eta. In the 4th/bottom row: leftmost plot is for pt bin 7 in central eta, second plot is for pt bin 7 for forward eta, third plot is for pt bin 8 in central eta and rightmost plot is for pt bin 8 for forward eta. 224
37 Postfit plots after Alternative fit/MC procedure for Pythia in 7 bin template fit.In the top row: leftmost plot is for pt bin 1 in central eta, second plot is for pt bin 1 for forward eta, third plot is for pt bin 2 in central eta and rightmost plot is for pt bin 2 for forward eta. In the Second row: leftmost plot is for pt bin 3 in central eta, second plot is for pt bin 3 for forward eta, third plot is for pt bin 4 in central eta and rightmost plot is for pt bin 4 for forward eta.In the third row: leftmost plot is for pt bin 5 in central eta, second plot is for pt bin 5 for forward eta, third plot is for pt bin 6 in central eta and rightmost plot is for pt bin 6 for forward eta. In the 4th/bottom row: leftmost plot is for pt bin 7 in central eta, second plot is for pt bin 7 for forward eta, third plot is for pt bin 8 in central eta and rightmost plot is for pt bin 8 for forward eta. 225

# CHAPTER I

## Introduction

> I wish we could derive the rest of the phenomena of nature by the same kind of reasoning from mechanical principles; for I am induced by many reasons to suspect that they may all depend upon certain forces
>
> *Isaac Newton in Philosophiæ Naturalis Principia Mathematica (1686)*

One of the main qualities of human beings which distinguishes itself from many other animals is the the ability to think. Deep thinking brings more questions than answers along the way often. The quest for knowledge never stops. To find solutions and answers to the difficult questions about the universe, substantial collective efforts are needed often, as a result team efforts and collaborations are formed to understand the big universe and nature around.

The history of Physics or Physical sciences goes back to the time immemorial. Since last thousands of years, humans have tried to figure out how our physical universe works or what are the ingredients of nature. 5th century BC Greek philosopher Empedocles predicted the four ultimate elements which are the constituents of everything which he could think of. And his four elements were: fire, air, water, earth [24]. Later on as human's quest for knowledge continued, understanding about nature continued to be fine-tuned gradually. The confidence graph of humans as an intelligent species has mostly seen a sharp rise over the time. Thanks to the development of communications between scholars, philosophers throughout the world which have helped to develop the knowledge further standing on each others' shoulders. The discovery of zero in India, or the developments of algorithms by Arab polymath Muammad ibn Mūsā al-Khwārizmī are simply one among innumerable massive scientific developments which took place all over the world. 20th century Physicist Abdus Salam has rightly said : "The creation of Physics is the shared heritage of all mankind. East and West, North and South have equally participated in it".

Sir Isaac Newton's revolutionary contributions in mathematics and Physics in 17th century set the new directions for human knowledge. After solving many problems with his innovative ideas, he inspired others on how with reasons and mechanical principles many other problems related to the understanding of the universe can be

solved.

In 19th century amid many developments in Physics, for few decades there has been a time where many had a sense of saturation of knowledge. Often a saying by a famous Physicist William Thompson in the year 1900 is quoted as "There is nothing new to be discovered in physics. All that remains is more and more precise measurement".

But as the history of science has been unpredictable over time, very soon discovery of X-rays by Wilhelm Conrad Röntgen and dramatic development of quantum mechanics shook the Physics world. Quantum mechanics' non-classically-explainable ideas raised eyebrows for sure, but it gave the world new ways of looking at things of day to-day life. Many problems which were difficult to solve with classical physics earlier got solved by Quantum physics , but that introduced more uncertainties and probabilistic interpretations in life. Only after many experimental confirmations of quantum mechanical phenomena, more confidence grew on the theories and Physicists kept on building more robust theories towards generalization of outstanding ideas to explain the happenings of our universe in a new language of quantum physics. Gradually merging of Electricity and Magnetism into Electromagnetism, advent of special and general relativities also made Physics world very exciting. Modern Physics finally could have 4 different fundamental forces of nature and also a world of Particle Physics. Particle Physics as a new and broad field of study offered new ways of exploring nature at the fundamental scale. From the Empedocles's four elements to the modern Physics' four forces efforts towards their unification has been a long and remarkable journey so far.

Though Physicist community have successfully answered many deep questions about our universe, there are long lists of unanswered mysteries which are arguably waiting to be solved. To solve some specific mysteries, often bigger scientific instruments , bigger scientific laboratories and facilities are needed. The Large Hadron Collider is surely one of the those facilities which helps in the collective attempts of human beings to solve many of them. The prospects of new Physics at the LHC are pushing the boundaries of human knowledge and understanding of how universe works.

Through this doctoral thesis works, I explore possibilities of finding new physics beyond the Standard Model of particle physics and shed light on the development of an algorithm which shows promise to help in some specific explorations of experimental high energy collider physics as a tool.

## I.1 The Standard Model

The Standard Model of particle physics is a successful theory based on the concepts of symmetries which describes the fundamental building blocks of nature and interactions at the elementary scale. Standard Model categorizes most physical phenomena by mainly 4 type of interactions or forces. Those four fundamental forces of nature are : Gravitational force, Electromagnetic force, Strong force and Weak force. These interactions bind together the fundamental building blocks named as 'elementary particles', which are subatomic particles with no sub-structures inside.

Gravitational force being the weakest among 4 forces doesn't have much relevance in the understanding of particle interactions. Though while studying massive objects like planets, stars, galaxies Gravitational forces become crucial and it can be studied well with the help of General Theory of Relativity. On the other hand, Electromagnetism, Weak  Strong forces are quantum in nature. Many properties of Electromagnetism are well experienced and recognized by people. But the other short range forces Weak force and Strong force also play key role to many very basic happenings of the universe. Radioactive decays, nuclear fission processes at the core of Sun due to Weak interactions are crucial processes of nature. Strong force which holds neutrons and protons together inside a nucleus is the strongest forces among all others.

The Standard Model of particle physics is basically a quantum field theory which describe different elementary particles, their properties and three fundamental forces of nature : strong, weak and electromagnetic interactions excluding the Gravity.

According to the Standard Model, elementary particles can be divided into two categories : matter particles and force particles. Matter particles make up the class named 'Fermions' consisting of 6 type of quarks (up, down, top, bottom, charm, strange), 3 leptons (electron, muon, tau), 3 neutrinos (electron neutrino, muon neutrino and tau neutrino) and their anti-particles. On the other hand, force particles are another class of particles named bosons (gauge bosons: W, Z boson, gluon, photon and Higgs boson) which act as mediators in the different interactions. W, Z bosons mediate in the weak interactions, photon mediates electromagnetic interactions, gluon mediates strong interactions and Higgs boson gives masses to elementary particles through Higgs mechanism. Other particles can be constructed out of the elementary particles. For example a proton (two up and a down) and a neutron (two down and an up) are complex particles consisting of three quarks.

Noether Theorem [25] has been one of the highly celebrated theorems which predict existence of conservation laws or conserved quantities while due to continuous symmetry. Standard model has also been constructed on the basis of some gauge symmetries (symmetry groups).

Mathematically Standard model is represented by the gauge groups :
$SU(3)_c \times SU(2)_L \times U(1)_Y$.

where Color, Isospin and hyper-charge are conserved charges respectively under the three gauge groups. The local symmetry group $SU(3)$ describes the strong force

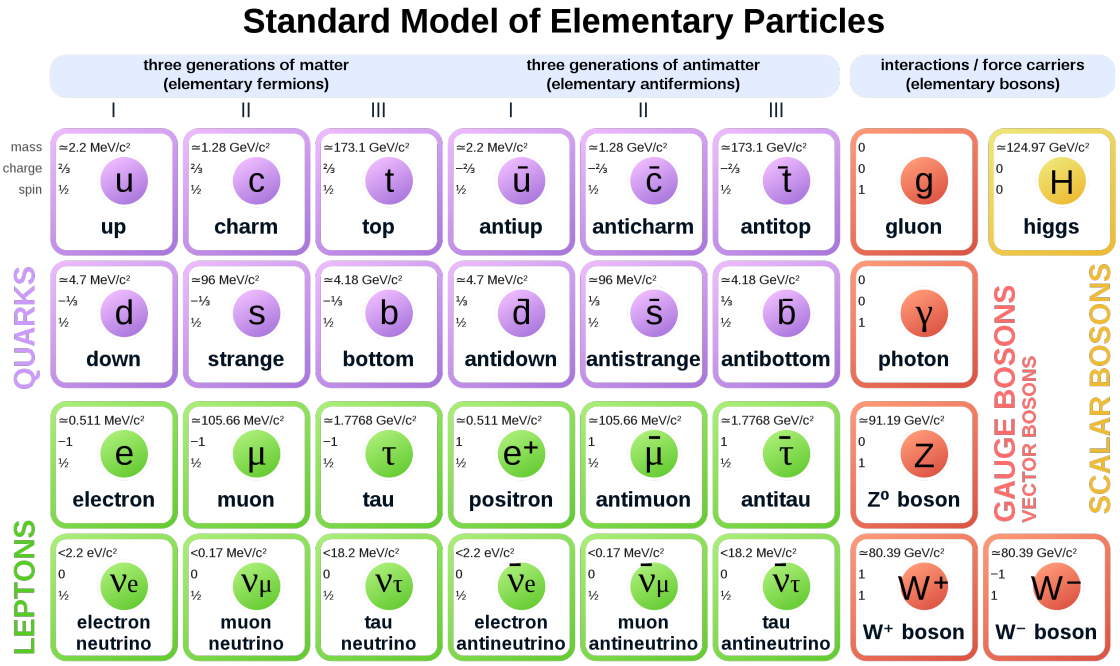


Figure I.1: Standard Model of particle physics [7].

acting on elementary particles with color charges. $SU(3)_c \times SU(2)_L$ gauge groups represent electroweak interactions. Interestingly symmetry group SU(2) in this case are obeyed by left-handed chiral particles only.

The Standard model Lagrangian is written as :

$$\mathcal{L}_{SM} = -\frac{1}{4}\sum_{gauge} F_{i\mu\nu}F^{i\mu\nu} - \sum_{f} \bar{f}\gamma^{\mu}D_{\mu}f + (D_{\mu}\phi)^{\dagger}(D^{\mu}\phi) - \mu^2\phi^{\dagger}\phi - \lambda(\phi^{\dagger}\phi)^2 \quad \text{(I.1.1)}$$

Where,

$$F^{a}_{\mu\nu} = \partial_{\mu}A^{a}_{\nu} - \partial_{\nu}A^{a}_{\mu} + gf^{abc}A^{b}_{\mu}A^{c}_{\nu} \quad \text{(I.1.2)}$$

Here $A_\mu$ represents a gauge field, $\phi$ represents scalar field, f represents fermionic field, g represents a parameter for gauge coupling and $f^{abc}$ represents structure contacts of gauge group. 2nd term of equation I.1.1 describes the interaction of quarks and leptons with gauge fields.

$$D_{\mu} = \partial_{\mu} - igA^{a}_{\mu}t^{a}_{r} \quad \text{(I.1.3)}$$

$D_\mu$ represents gauge covariant derivative which has gauge coupling constants in its extended expressions. $t^a_r$ is representative matrix.

The last two terms in equation I.1.1, $-\mu^2\phi^{\dagger}\phi - \lambda(\phi^{\dagger}\phi)^2$ represents the scalar potential which takes part into Higgs mechanism and contribute to the process of spontaneous symmetry breaking.

Standard model beautifully combines the 3 basic interactions of nature and consists of mediating boson particles of those interactions: Gluons, photon, $W^{\pm}, Z^0$, Higgs and also fermions including 6 quarks, 6 leptons. All these interactions emerge out of symmetries as described by different symmetry groups. Different particles which participate in different interactions often carry special charges : electrical charge, weak charge and color charges due to strong interactions. Red(r), Green (g) and Blue (b) are the three color labels used to study these special interactions mediated by Gluon particles. Non-abelian gauge group of strong interaction and non-zero value of structure constant of the gauge group allow gluons to have self interactions.

| Categories | Particles | Charge | Spin | $SU(2)_L$ | $SU(3)_C$ | $U(1)_Y$ |
|---|---|---|---|---|---|---|
| Leptons | $(\nu_l, l)_L; [l = e, \mu, \tau]$ | (0,-1) | 1/2 | **2** | **1** | -1 |
| | $l_R$ | -1 | 1/2 | **1** | **1** | -2 |
| Quarks | $(u, d)_{i,L}$ [i: 3 generations] | (2/3, -1/3) | 1/2 | **2** | **3** | 1/3 |
| | $u_{i,R}$ | 2/3 | 1/2 | **1** | $\overline{\mathbf{3}}$ | 4/3 |
| | $d_{i,R}$ | -1/3 | 1/2 | **1** | $\overline{\mathbf{3}}$ | -2/3 |
| Gauge fields | Gluons (g) | 0 | 1 | **1** | **8** | 0 |
| | W, Z bosons ($W^{\pm}, Z^0$) | $\pm$1, 0 | 1 | **3** | **1** | 0 |
| | Photon ($\gamma$) | 0 | 1 | **1** | **1** | 0 |
| Higgs field | $\phi^+, \phi^0$ | 0 | 0 | **2** | **1** | 1 |

Table I.1: The table summarises the different Standard Model particles, gauge groups and their properties. The values against gauge groups $SU(2)_L$, $SU(3)_C$ indicate that the fields belong to singlet, doublet, triplet or octet representations for 1,2,3,8 values respectively. The values in the column of $U(1)_Y$ represent corresponding weak hypercharges.

It is also interesting to note Standard Model is also invariant of combined symmetries of to Charge Conjugation(C), Parity (P) and Time reversal (T). Though there has been cases of CP violations, but CPT violation has been never been observed. Since in the visible universe, matter particles are way more in abundance than the anti-matters, such symmetries and violations become crucial for understanding. Matter-antimatter asymmetry is still an open ended problem, which has not been solved yet.

The matter particles of the Standard model are not observed as free particles, but they form bound states. Quarks form hadronic bound states. And hadrons like protons, neutrons help to form atomic nucleus later on resulting visible structures of our universe.

Initial credits goes to Sheldon Glashow, Steven Weinberg and Abdus Salam for playing significant roles in shaping the Standard Model, specially by providing a theory of unified weak and electromagnetic interactions between elementary particles which landed them Nobel Prize of Physics in 1979 [26, 27, 28]. Standard Model was confirmed by experimental discovery of neutral weak currents caused by Z boson exchange at CERN in 1973. And in a continuous journey, Standard Model has been developed over the last half of the century observed and confirmed by many experimental discoveries of new elementary particles, many precise measurements in

different decades. The discovery of elusive least interacting particles neutrinos of different kinds, or the discoveries of three different generation of quarks, confirmation of properties of gauge (W and Z) bosons as predicted by Standard Model, the discovery of most recent particle Higgs boson made the Standard Model a very successful theory. But at the same time, there are many mysteries of nature which Standard Model can't describe properly. Those include baryon asymmetry in the universe, dark matter, dark energy, neutrino oscillations and their non-zero masses.

### I.1.1 Spontaneous Symmetry Breaking

The gauge symmetries $SU(3)_c, SU(2)_L, U(1)_Y$ has been successful in predicting interactions. They work very well when there is no reference of mass terms. But historically a new mechanism was needed which could allow generation of masses while having the interactions unaffected. Brout-Englert-Higgs Mechanism is the mechanism which allow $SU(2)_L \times U(1)_Y$ gauge symmetry breaking into $U(1)_{EM}$.

With the mechanisms of Spontaneous Symmetry breaking, the Physical laws based on symmetries result into asymmetric solutions. As a result, many different possible vacua exist instead of a unique lowest energy solution and any of those choices breaks the symmetry.

During the historical developments, the simplest models or field theory which exhibited the spontaneous symmetry breaking has been the Goldstone model.

Its Lagrangian density had the following expression :

$$\mathcal{L}(x) = [\partial^\mu \phi^*(x)][\partial_\mu \phi(x)] - \mu^2 \phi^\dagger \phi - \lambda(\phi^\dagger \phi)^2 \tag{I.1.4}$$

where $\mu^2 and \lambda$ are arbitrary real parameters and

$$\phi(x) = \frac{1}{\sqrt{2}}[\phi_1(x) + i\phi_2(x)] \tag{I.1.5}$$

The Lagrangian density of equation I.1.4 is invariant under global phase transformations due to symmetry group U(1). The Hamiltonian density from the same equations can be derived as :

$$\mathcal{H}(x) = [\partial^0 \phi^*(x)][\partial_0 \phi(x)] + [\Delta \phi^*(x)][\Delta \phi(x)] + \mathcal{V}(x) \tag{I.1.6}$$

with potential energy density of the field $\mathcal{V}(x)$ :

$$\mathcal{V}(x) = \mu^2 |\phi(x)|^2 - \lambda |\phi(x)|^4 \tag{I.1.7}$$

If we want to have the energy should be bounded, the value of $\lambda$ should be positive. Now depending on the values of $\mu^2$, there can be two scenarios :

**Case 1 - When the value of $\mu^2$ is greater than zero :**

In that case the potential energy density $\mathcal{V}(x)$ of equation I.1.7 will have positive definite value. For a unique value of $\phi(x) = 0$, $\mathcal{V}(x)$ will have absolute minima. As a result, spontaneous symmetry breaking will not be possible in that case.

**Case 2 - When the value of $\mu^2$ is less than zero :**

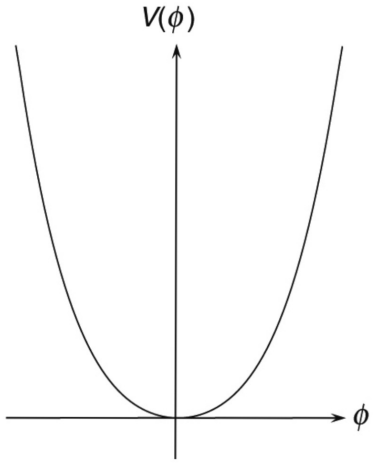


Figure I.2: $\mathcal{V}(x)$ shape when $\mu^2 > 0$, $\lambda > 0$

In this specific case, potential energy surface will have a local maxima at $\phi(x) = 0$ and will result a circle of absolute minima at

$$\phi(x) = \phi_0 = (\frac{\mu^2}{2\lambda})^{1/2} e^{i\theta} \tag{I.1.8}$$

for the the values of phase angle $\theta : 0 \leq \theta < 2\pi$. With some assumptions it can be shown that $\phi_0$ is not any imaginary, but a real quantity.

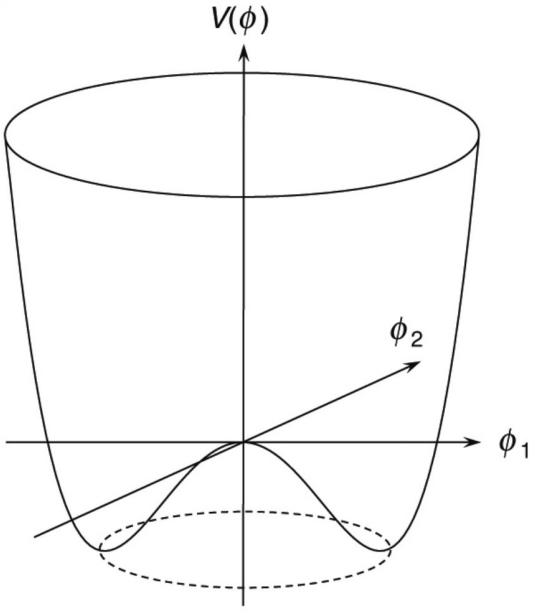


Figure I.3: $\mathcal{V}(x)$ shape when $\mu^2 < 0$, $\lambda > 0$. The dashed line at the bottom representing circle of absolute minima.

Now if $\phi(x)$ is redefined as

$$\phi(x) = \frac{1}{\sqrt{2}}[v + \sigma(x) + i\eta(x)] \tag{I.1.9}$$

The Lagrangian density of equation I.1.4 will become the following :

$$\begin{aligned}\mathcal{L}(x) = &\frac{1}{2}[\partial^\mu \sigma(x)][\partial_\mu \sigma(x)] - \frac{1}{2}(2\lambda v^2)\sigma^2(x) \\ &+ \frac{1}{2}[\partial^\mu \eta(x)][\partial_\mu \eta(x)] \\ &- \lambda v \sigma(x)[\lambda^2(x) + \eta^2(x)] \\ &- \frac{1}{4}[\lambda^2(x) + \eta^2(x)]^2\end{aligned} \tag{I.1.10}$$

In equation I.1.10, the first, second and third terms are the quadratic terms and if compared to Lagrangian density of Klein Gordon fields, it can be found that both $\sigma(x)$ and $\eta(x)$ are Klein Gordon fields which lead to spin zero neutral particles. From equation I.1.10, it can be also concluded that though $\sigma$ boson gets the mass of $\sqrt{2\lambda v^2}$, the $\eta$ boson particle remains massless. Such massless bosons which occur through spontaneous symmetry breaking are called the Goldstone bosons.

Higgs mechanism provided further developments on Goldstone models resulting in Lagrangian density which can be split into a free field Lagrangian density term and higher order interaction terms.

$$\begin{aligned}\mathcal{L}(x) = &\frac{1}{2}[\partial^\mu \sigma(x)][\partial_\mu \sigma(x)] - \frac{1}{2}(2\lambda v^2)\sigma^2(x) - \frac{1}{4}F_{\mu\nu}(x)F^{\mu\nu}(x) + \frac{1}{2}(qv)^2 A_\mu(x)A^\mu(x) \\ &- \lambda v \sigma^3(x) - \frac{1}{4}\lambda\sigma^4(x) + \frac{1}{2}(q)^2 A_\mu(x)A^\mu(x)[2v\sigma(x) + \sigma^2(x)]\end{aligned} \tag{I.1.11}$$

where the first four terms from the first line is free field Lagrangian density and terms on the second line are the higher order interaction terms.

In this Higgs mechanism, Goldstone bosons are not produced and through quantization, real massive scalar field ($\sigma$) and a massive real vector field ($A_\mu$) are obtained. Through this phenomena, while having gauge invariance of Lagrangian density vector boson can acquire mass! That makes the Higgs mechanism an incredible development in the journey of developing The Standard Model.

Next step in the journey was to apply Higgs mechanism in generating non vanishing masses for the Vector boson particles such $W^\pm, Z^0$ bosons while having spontaneous symmetry breaking. Starting from a simple weak isospin doublet, through transformations of SU(2) and U(1), through some assumptions and choices and also by adding some new terms of Higgs field and terms representing interactions between leptons and Higgs fields it is possible to formulate a Lagrangian density which is invariant under SU(2) $\times$ U(1) gauge transformations. The vacuum expectation value of Higgs field can be represented as :

$$\langle 0|\, \phi(x)\, |0\rangle = \phi_0 = \begin{pmatrix} 0 \\ \frac{v}{\sqrt{2}} \end{pmatrix} \tag{I.1.12}$$

where

$$v = (-\frac{\mu^2}{\lambda})^{1/2} \tag{I.1.13}$$

### I.1.2 Some verification of the predictions in history

The Standard model theory started on the basis of $SU(3)_C \times SU(2)_L \times U(1)_Y$ symmetry and the developments of spontaneous symmetry breaking theories from the gauge invariance gave it a solid foundation. The fascinating part of the Standard Electroweak theory is it perfectly described the interactions occurred by Electromagnetic and Weak interactions and gauge bosons $W^{\pm}$ and $Z^0$ bosons, photons, charged and neutral leptons and Higgs Boson. The electro-weak unification at the high energies are the outstanding ideas. Quantum chromodynamics (QCD) also described the strong interactions very successfully.

Standard Model had many predictions about new particles and their interactions. And significant experimental efforts have been made to verify those predictions. The important aspect of Standard Model is it has been developed over decades and experimental verification hugely contributed to the developments and its form has been updated after each discovery. For example, in the year of 1974, when two different experiments at Brookhaven National Laboratory(BNL) [29] and Stanford Linear Accelerator Laboratory(SLAC) [30] discovered the J/$\Psi$ particle which is bound state of Charm(c) and anti-Charm ($\overline{c}$) quarks, particle physics found a new quark through "November Revolution"! During 1974-1977, at the SPEAR collider at SLAC, Tao ($\tau$) lepton was observed [31], in 1977 at the E288 experiment at Fermilab, Bottom quark was discovered [32], In 1979 at the TASSO detector of DESY, Gluon was discovered [33], at the UA1 Experiment of CERN's SPS the W and Z bosons were discovered [34] and in 1995 at the DØ [35] and CDF [36] detectors at Fermilab , Top quark was discovered, and in 2012 by the ATLASc̃iteAad:2012tfa and CMS [37] experiments, Higgs Boson was discovered in 2012.

Each of these discoveries, experimental verification often suggested new generations of particles and resulted in new symmetries and gauge invariances for the models. The experimental verification of many predictions had very good precision of matching with the theoretical predictions. And with the discovery of Higgs Boson all the known members of the standard model's elementary particle family have been discovered.

### I.1.3 The Higgs Boson

The discovery of Higgs Boson has been one of greatest discoveries of Particle Physics as over decades experiments around the world have been searching for it. At the same time, the discovery opened new areas of study involving Higgs boson, which can be called as Higgs Physics. The couplings of different standard particles with Higgs is still a topic of current studies and its production processes and decay modes has potential to explore new Physics addressing the current limitations of the Standard Model.

The Higgs boson has the following properties :

In Standard Model of Particle Physics, Spin of Higgs Boson S = 0, Parity = +1 and charge conjugation C = +1. Standard model Higgs is a CP-even particle (as $J^P = 0^+$). Weak hyper-charge of Higgs is +1 and weak isospin number is : $+1_{\frac{-}{2.}}$

The combined ATLAS-CMS measurement while combining $\gamma\gamma$, ZZ $\rightarrow 4l$ channels from LHC RUN1, provided the following mass value for the Higgs Boson:

$M_H = 125.09 \pm 0.24(\pm 0.21[Stat.] \pm 0.15[Syst])$ GeV.

**Production Mechanisms of the Higgs Boson:**

Higgs boson can be created in many different processes. Some prominent production processes are : Gluon-Gluon-Fusion (ggF) where gluons fusion takes place by the mediation of a fermion loop and produces a Higgs Boson, Vector Boson Fusion (VVF) where pair of Vector bosons ($W^+W^- or ZZ$ produces Higgs boson, Associated production of Higgs with Vector boson (VH) where Higgs boson is produced along with a Vector bosons while being radiated from an off-shell vector boson and Associated production of Higgs with quark pairs for example ttH, bbH, associated production with a single Top quark, associated production with Gauge boson from gluon-gluon interactions etc.

The plot I.5 from the LHC working group report on Higgs boson production shows how different processes have varying cross sections from proton proton collisions.

**Higgs Boson Decays:**

Higgs boson decays into different decay channels and processes. A summary of decay modes and their branching ratios can be found in the table below :

| Decay channel | Branching Ratio | Relative uncertainties |
|---|---|---|
| $H \rightarrow \gamma\gamma$ | $2.27\ 10^{-3}$ | 2.1% |
| $H \rightarrow ZZ$ | $2.62\ 10^{-2}$ | $\pm$1.5% |
| $H \rightarrow W^+W^-$ | $2.14\ 10^{-1}$ | $\pm$1.5% |
| $H \rightarrow^+ {}^-$ | $6.27\ 10^{-2}$ | $\pm$1.6% |
| $H \rightarrow b\bar{b}$ | $5.82\ 10^{-1}$ | $^{+1.2\%}_{-1.3\%}$ |
| $H \rightarrow c\bar{c}$ | $2.89\ 10^{-2}$ | $^{+5.5\%}_{-2.0\%}$ |
| $H \rightarrow Z\gamma$ | $1.5310^{-3}$ | $\pm$5.8% |
| $H \rightarrow \mu^+\mu^-$ | $2.1810^{-4}$ | $\pm$1.7% |

Table I.2: Higgs boson decay modes and Branching Ratios [1].

It is evident from Table 2 that $H \rightarrow b\bar{b}$ is the most dominant decay mode for Higgs Boson with having around 58% branching ratio.

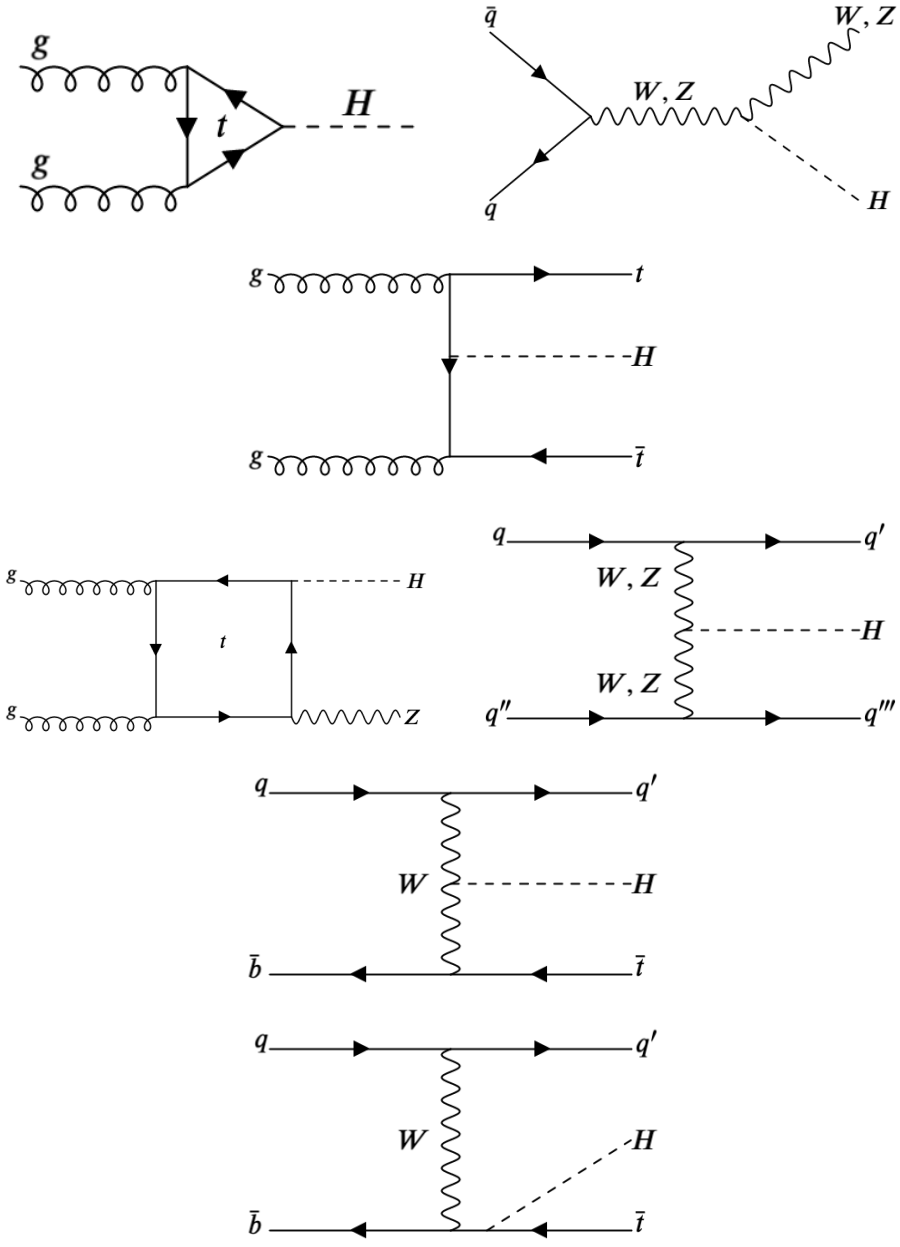


Figure I.4: Feynman diagrams of Higgs boson production processes [1].

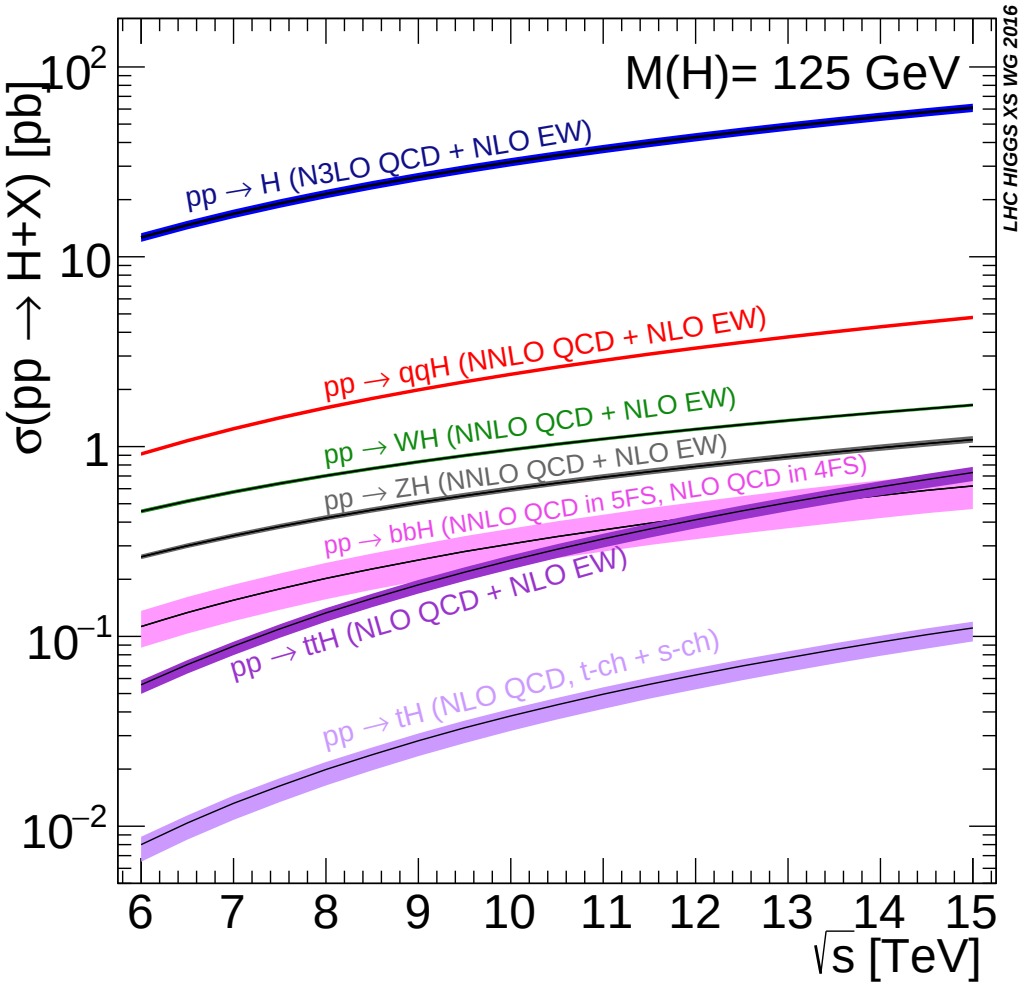


Figure I.5: Standard Model Higgs boson production cross sections as the function of center of mass energy $\sqrt{s}$ [8].

### I.1.4 The Top-Quark

The Top quark is the heaviest particle in the Standard Model of particle Physics with its mass of $173.2 \pm 0.9$ GeV. Top quark was discovered at Fermilab by the DØ [35] and CDF [36] collaborations.

The Top quark forms the third generation of quarks and has charge $\frac{2}{3}$ of electron. Since it is a Fermion, spin of Top is $\frac{1}{2}$. Due to its very large mass and width, it decays very quickly and its lifetime is only $5.0 \times 10^{25}$ seconds.

Top quark has been a topic of many ongoing studies specially due to its properties. The high mass value of Top quark also indicate very strong Yukawa coupling with the Higgs Boson. At the LHC also, its mass has been measured by both ATLAS and CMS experiments with great precision.

Top quark is heavier than a proton by 190 times. Due to its large mass, Top quark also contributes to interesting physics signatures at the colliders and and special techniques are needed for its detection.

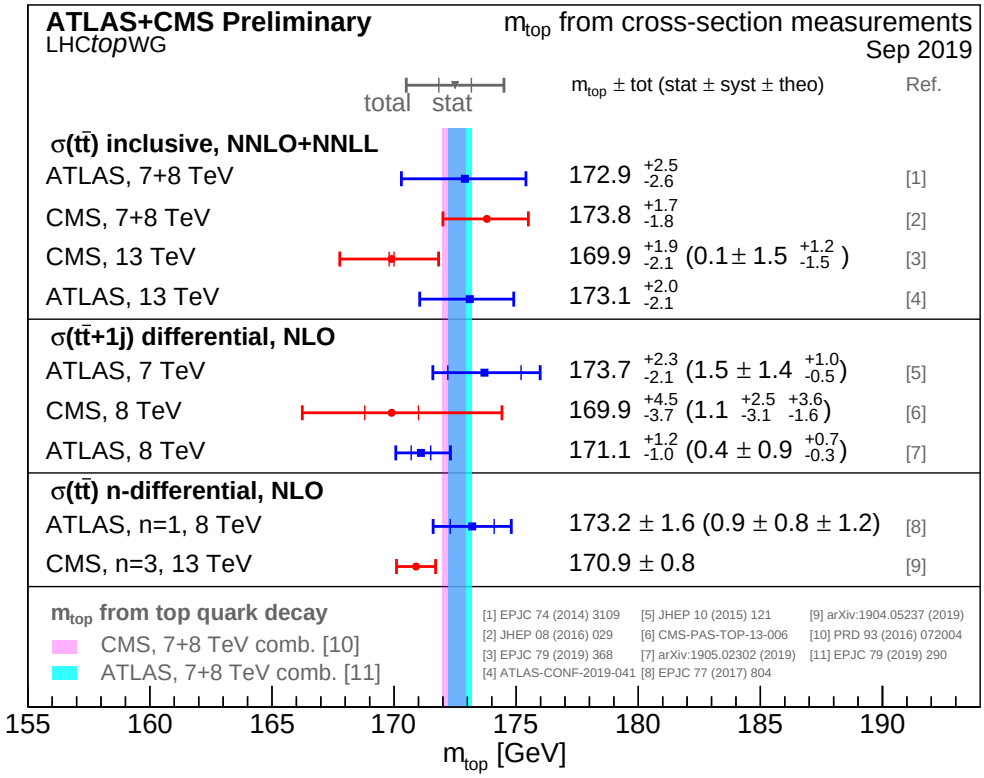


Figure I.6: Combined measurement results from ATLAS and CMS experiments from $t\bar{t}$ production observables [9].

The figure I.6 summarizes the attempts by ATLAS and CMS experiments of CERN to measure the mass of the Top quark at different center of mass energies ($\sqrt{s}$ = 7, 8 and 13 TeVs).

### I.1.5 Top-Quark Pair Production

Among the production processes of Top quark, $t\bar{t}$ production is the most common one at the collider experiments. At the Large Hadron collider, gluon-gluon fusion processes are the dominant production mode for $t\bar{t}$ and accounts for 80 to 90 % of the production processes, whereas at the Tevatron experiments at Fermilab, annihilation of quarks contributed to the most production processes.

Few leading order dominant $t\bar{t}$ production processes are shown below using Feynman diagrams :

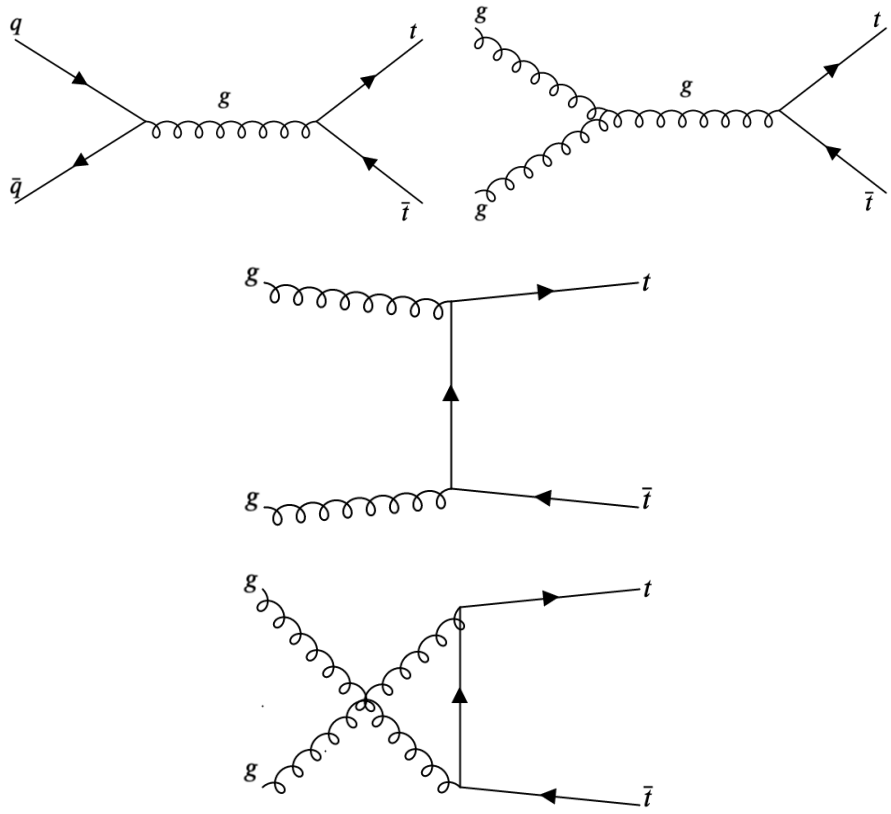


Figure I.7: Feynman diagrams of $t\bar{t}$ pair production processes

In the gluon fusion processes, gluons fuse and produce pair of a top and anti-top quarks or it creates another gluon with high energy which decays to $t\bar{t}$ pair. The first Feynman diagram in I.7 shows two quarks annihilate and produces a gluon which decays to $t\bar{t}$ pair subsequently. Apart from these processes, there can be possible processes, where intermediate Z boson or photon are produced and they decay to produce $t\bar{t}$, but those processes are rare at the Large hadron collider.

Apart from $t\bar{t}$ productions, Single-Top production and also associated production of $t\bar{t}$+W, $t\bar{t}$+Z, $t\bar{t} + \gamma$ are the other important processes for the production of Top quarks. In single Top production processes, a top and a anti-bottom quark can be produced from the decay of an intermediate W boson, or from an initial state bottom quark, a top quark and a W boson can be produced and also in t-channel processes, a bottom quark while exchanging a W boson, can produce top quark.

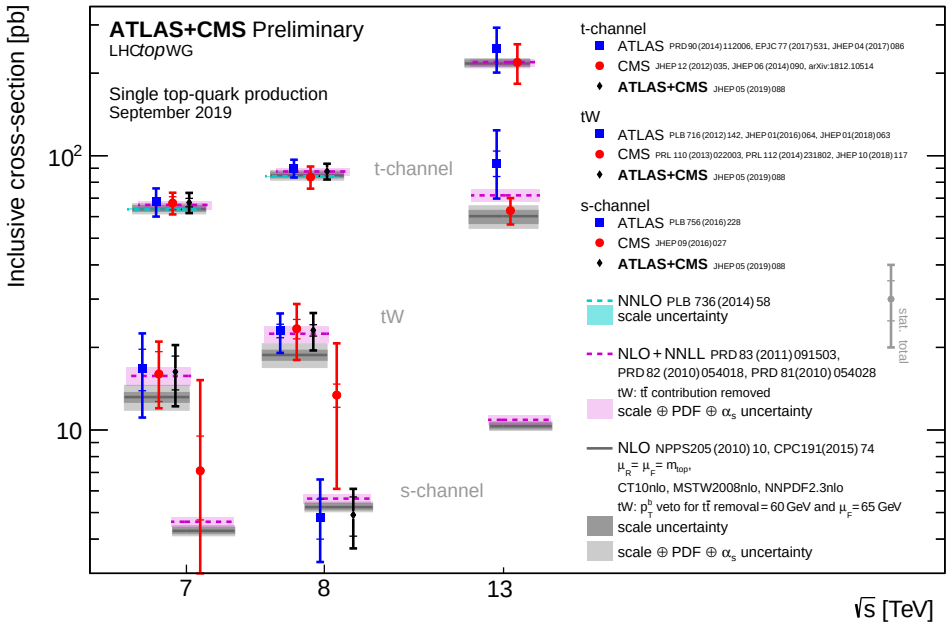


Figure I.8: Summary of ATLAS and CMS measurements of the single top production cross-sections in different channels as a function of $\sqrt{s}$ (the center of mass energy).Theoretical calculations based on: NLO QCD, NLO QCD complemented with NNLL resummation and NNLO QCD (t-channel only) are also compared to the measurements [9].

### I.1.6 Decay of the Top-Quark

Top Quark being the heaviest quark doesn't form any Top-bound state and decays very fast to lighter particles while having its lifetime 5.0 $10^{25}$ seconds as mentioned earlier.

Top quark decays to a W boson and a bottom quarks most of the times. CKM matrix is a powerful tool to understand the quark mixing processes and the values of square of the elements for example $|V_{td}|^2, |V_{ts}|^2, |V_{tb}|^2$ etc. indicates the probabilities of the processes.

$$V_{CKM} = \begin{bmatrix} |V_{ud}| & |V_{us}| & |V_{ub}| \\ |V_{cd}| & |V_{cs}| & |V_{cb}| \\ |V_{td}| & |V_{ts}| & |V_{tb}| \end{bmatrix} = \begin{bmatrix} 0.97401 \pm 0.0001 & 0.22650 \pm 0.0004 & 0.00361^{+0.0001}_{-0.0000} \\ 0.22636 \pm 0.0004 & 0.97320 \pm 0.0001 & 0.0405^{3+0.0008}_{0.0006} \\ 0.0085^{4+0.0002}_{0.0001} & 0.0397^{+0.0008}_{0.0006} & 0.99912^{+0.00002}_{0.00003} \end{bmatrix} \tag{I.1.14}$$

In the above CKM matrix [1], it can be seen that $|V_{td}|^2$, $|V_{ts}|^2$ values are close to zero, which indicates the suppression of possible decay modes of Top quark into d quark or s quark. AT the same time the value of $|V_{tb}|^2$ to close to 1, which indicates Top quark decays to B quark via $T \to Wb$ most of the times.

After $T \to Wb$, W boson can decay either leptonically producing a lepton and a neutrino or it can decay hadronically by decaying into a quark pair.

Some decay modes of Top quarks and their branching ratios are given in the

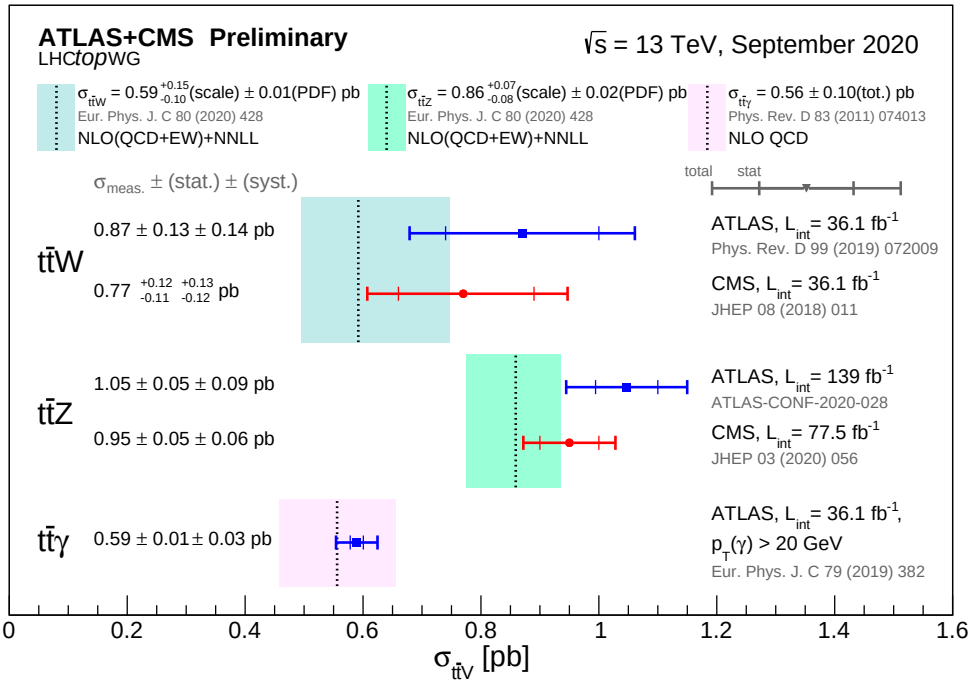


Figure I.9: Combined measurements of ttbar+W, ttbar+Z, ttbar+$\gamma$ production cross sections by ATLAS and CMS experiments at center of mass energy 13 TeV. The ttbar+W and ttbar+Z cross section measurements are compared to the NLO QCD and EW theoretical calculation complemented with NNLL resummation, while the ttbar+$\gamma$ cross section measurement is compared to the NLO QCD theoretical calculation. The theory band represents uncertainties due to renormalization and factorisation scales and parton density functions [9].

following table :

Its evident from the I.3 that when $t\bar{t}$ decay into $b\bar{b}W^+W^-$, in the leptonic decay modes will include $b\bar{b}$ two opposite sign leptons and two neutrinos coming from the W bosons. But at the same time, instead of dileptons , it can decay semi-leptonically while producing a single lepton and a neutrino along with $q\bar{q}$. In such cases, in the collider after hadronization lepton jets are observed. From $t\bar{t}$ around 46% of times fully hadronic decays, around 45% of the times semileptonic (single lepton + jets) decays and around 9% of the times dileptonic decays are found.

Search for Yukawa coupling between the Higgs boson and the top quark have also been investigated by both ATLAS and CMS experiments at different center of mass energies. In 2018, ATLAS observed production of Higgs boson in association with a top quark pair with a significance of 6.3 standard deviations [38] and the observation set the direct observation of the Yukawa coupling between Top quark and the Higgs.

In recent developments CMS [39] and ATLAS [40] experiments have also observed Single top quark production in association with a Z boson (tZq).

Top quark decays provide many interesting physics prospects in the searches for new BSM Physics. It many different decay modes as proposed by BSM theories are constantly probed by collider experiments at the LHC. In the following sections of

| Decay channel | Branching Ratio |
|---|---|
| $T \to Wb \to e\nu_e b$ | 11.10 $\pm$0.30 |
| $T \to Wb \to \mu\nu_\mu b$ | 11.40 $\pm$0.20 |
| $T \to Wb \to \tau\nu_\tau b$ | 11.10 $\pm$0.9 |
| $T \to Wb \to q\bar{q}b$ | 66.5 $\pm$1.4 |
| $T \to \gamma q (q = u, c)$ | $< 1.8\ 10^{-4}$ |

Table I.3: Top quark decay modes and Branching Ratios [1].

this PhD thesis some of those Physics prospects related to Top quarks have been explored.

### I.1.7 The Bottom-Quark

Bottom quark, one of the six members of the Standard Model quark family and plays very crucial roles both in the Physics of standard model and in many different BSM Physics. Its known as 'Beauty quark' often as well.

After being discovered at Fermilab in 1977 as the fifth quark at that time, its was placed in the third generation of quarks which was joined by Top quark later on as the weak-doublet partner. Bottom quark has spin quantum number $\frac{1}{2}$ and it processes charge of $\frac{1}{3}$ of electron. Before the discovery of Top Quark, Bottom quark used to be the heaviest known quark!

Bottom quark's mass have been measured using the minimal subtraction scheme as : $M_B = 4.18^{+0.03}_{0.02} GeV$ [1].

As we have seen from equation I.1.14 of CKM matrix, that Top quark decays to a bottom quark along with a W boson most of the times. Bottom quark, which is second most heavy quark in the quark family, decays into Charm quark and into other lighter quarks after travelling some distance inside the detector. The lifetime os a b-hadron is typically around 1.5 pico-seconds.

The decay of bottom quark provide experiments scopes to measure parameters of the CKM matrix. The bound state of b-quarks : B-mesons and B-hadrons have been studied by many different experiments of $e^+e^-$ colliders such as ARGUS,CLEO, Belle, BaBar, SLC, LEP etc. and also in the pp collider experiments of Tevatron and at the LHC. Specially LHCb experiment studies the decays, mixing of B mesons extensively.

From the figure I.10, one can see few different decay channels of bottom quarks through Weak interactions. Decay of b quark to processes to u quark is negligible compared to decays into charm quarks. Processes of $b \to cl^-\overline{\nu}$, $b \to c\overline{u}d$, $b \to c\bar{c}s$ are the significant ones.

In the search of Higgs boson, b quark played crucial role as now its well known fact that Higgs boson decays to pair of bottom and anti-bottom quarks 58% of the times [41]. That makes bottom quarks very important tool to explore Physics of the Higgs Boson in the near future.

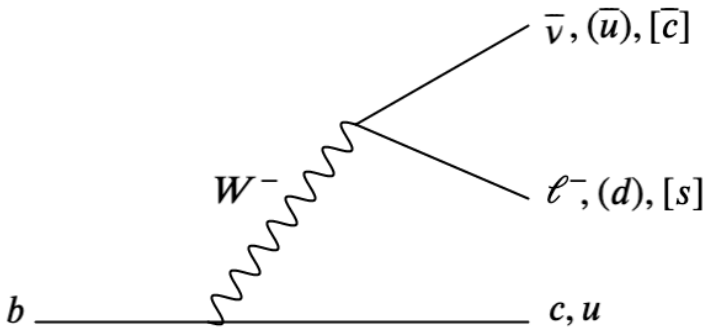


Figure I.10: Diagrams for few dominant decays of b quarks [10].

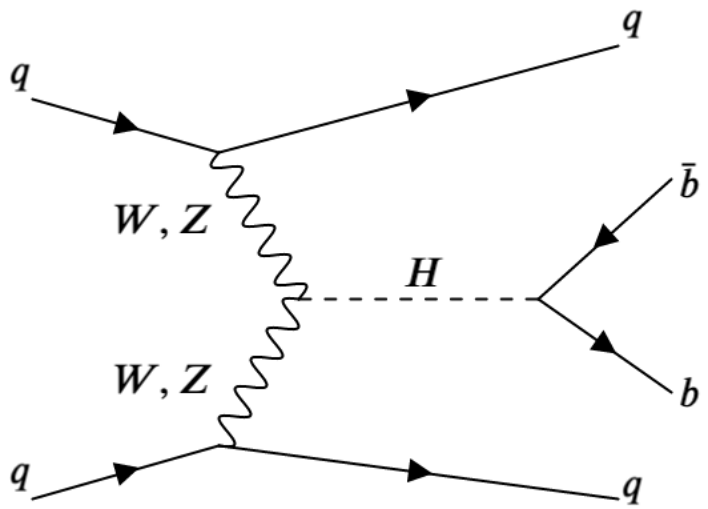


Figure I.11: Feynman diagram of Higgs boson decaying to pair of b and anti-b quarks [10].

The distinct properties of decay topology and signatures of longer life time of b-jets which are formed though hadronization provides experimentalists with ample opportunities of developing different techniques to identify a b-jet in the detectors. The fact that b-jets produces distinguishable secondary vertices before decaying to lighter quarks leaves special signature inside the detector. The identification techniques of b-jets are also known as b-tagging which contribute to the Physics analysis and searches if there are b-jets in the final state of the Physics processes. If there are multiple b-jets, that also needs dedicated strategies. In the process of identification of b-jets, a very important aspect of possibilities of mis-identification which is known as 'mistags'. In the later section, I have been discussed mistags, and its calibrations in details.

### I.1.8 SM production cross sections

Standard Model's physics processes are not always equally probable to take place. Some of them take place very easily, while some of them are suppressed in the collider experiments. Experiments put significant efforts in measuring the cross sections of different processes. One of such summary plots on measurements are given below :

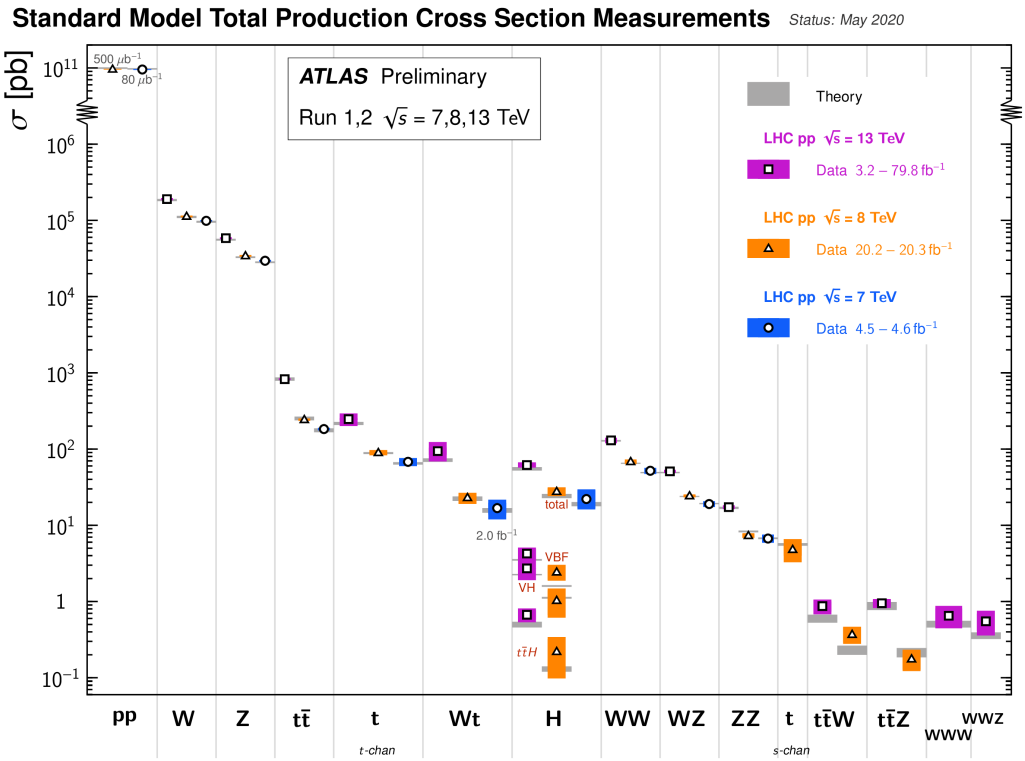


Figure I.12: Standard Model production cross sections of different Physics processes at different center of mass energies ($\sqrt{s}$ = 7, 8, and 13 TeV).

The figure I.12 summarizes how the different production processes in Standard Model have different cross sections vary. It also shows the comparative production probabilities among different processes. For example higher cross sections of W, Z, $t\bar{t}$ with higher cross section values indicate they are produced way more often than $t\bar{t}H$, $t\bar{t}Z$ etc.

## I.2 Beyond the Standard Model

Though Standard Model of particle Physics has been a very successful theory in explaining basic interactions of elementary particles due to Electromagnetic, Strong and Weak forces, but there are many unsolved questions which Standard Model can't answer properly and there are phenomena which can't be explained by Standard Model processes.

The biggest discrepancy of the current Standard Model theory is it excludes on the four forces Gravitational interactions completely. The three quantum forces couldn't be unified with Gravity and also the hypothetical mediating particle for Gravitational interactions Graviton is also not experimentally found yet. The incompatibility of current framework of Standard Model with General Theory of Relativity which explains Gravity provides scopes for Physics Beyond the standard model.

Neutrino Physics is another big motivation for BSM Physics as Standard Model cannot describe why Neutrino Oscillation phenomena takes place and neutrino of one flavor converts into a neutrino of other flavor. The mass of neutrino and its hierarchy also provides a set of some open questions. A Majorana fermion is a hypothetical particles which is its own anti-particle. Regarding neutrinos, it has not been confirmed yet, whether a neutrino is a Majorana particle or not. Possibilities that a Neutrino is a Majarana particle may bring interesting Physics processes where they could annihilate. But Standard Model doesn't provide a clear answer to that question.

Experimental measurements of many Physical parameters often motivates for new BSM models. One of such examples is the anomalous magnetic moment of muons. Though in case of electrons, the anomalous magnetic moment value from the experiments matches with Standard Model predictions, but in case of muons for decades there has been discrepancy between experimental measurements and theoretical predictions [42].

Muon magnetic moment anomaly is often described by the term $a_\mu = (g-2)/2$ and the Standard model predicted value $a_\mu^{SM}$ has been lying 3.7 $\sigma$ below the experimental results from Brookhaven National Lab $a_\mu^{Exp}$ [43]. Some latest results from Muon g-2 collaboration at Fermilab indicates that the combined results of BNL and Fermilab provides 4.2 $\sigma$ deviations from the standard model predictions [44, 45, 46]. Since Standard Model can't describe this, it has become a limitation for SM.

According to $\lambda CDM$ cosmological model, Dark matter contribute to the 26.4% of the critical density of the Universes, yet Dark matter is not explained by the Standard Model. Standard Model doesn't have any candidate particle which could be the building blocks of dark matter. The interactions of dark matter is completely unknown till date. But from the galactic rotation curve studies by Vera Rubin in 1970s [47] and from many other direct-indirect astrophysical phenomena, existence of Dark matter is an accepted fact. Huge number of BSM models have been built to explain Dark matter, though none of them have been experimentally verified so far.

The figure I.13 shows how many different experiments are searching for DM-

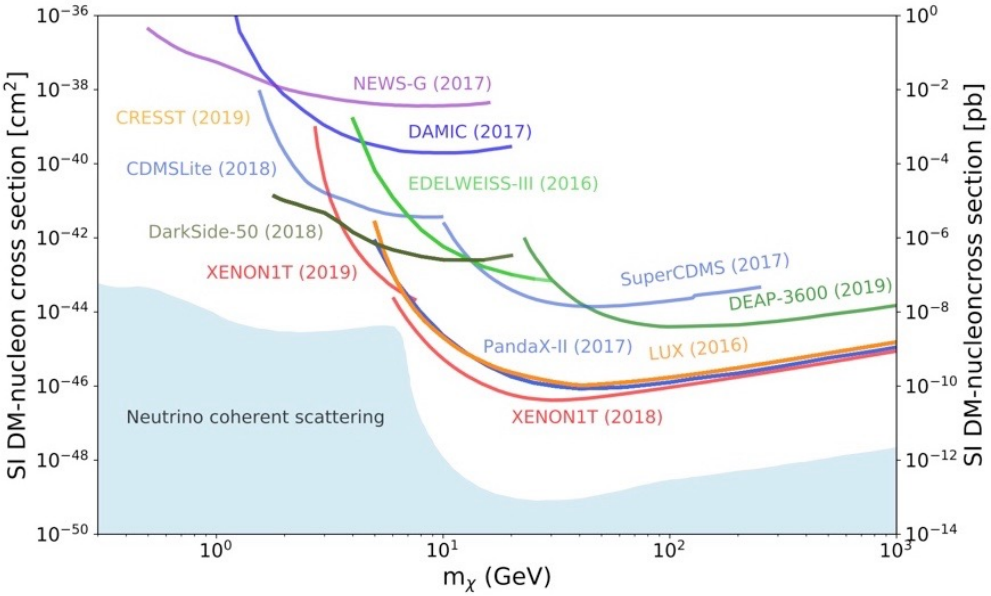


Figure I.13: Upper limits on cross sections for the interactions between spin independent Dark matter  nucleon as a function of mass of dark matter [1].

nucleon interactions and setting limits on the cross section values. The extreme low values in cross sections show, how unlikely a Dark matter would interact with standard model particles.

Baryon asymmetry in the universe has been another aspect which cannot be explained by Standard Model. It is an evident from the known visible universe that number of matter particles has been way more than the number of anti-matter particles, but there has not been any good explanation on the mechanism which could have led to tiny imbalance between matter and anti-matter during early formation days of the universe.

Standard Model of particle Physics also doesn't say anything about the acceleration in the expansion of the universe or cosmological inflation and also about the Dark Energy which constitutes of around 73% of total energy of the universe.

Apart from these many limitations of Standard Model, many BSM models provide prospects of Grand Unification (GUT) of forces, Proton Decay, Super Symmetry, Extra-dimensions, String-unification etc. After the discovery of standard model Higgs boson in 2012, many new theories have been emerged proposing new Higgs bosons like Charged Higgs bosons, two-Higgs-doublets, Higgs-triplets etc. One of the many motivations for Two-Higgs-doublet models is that it can introduce Flavor-changing neutral currents, which have not been experimentally observed so far. Presence of additional Charged Higgs boson or new heavy gauge bosons would surely give new insights about many new new physics.

Over the decades many different BSM models have been built to provide alternative to the Standard Model while explaining New Physics and experimental exploration has been continuing for the same.

Beyond the standard model is a vast field of possibilities which can open new av-

enues for new insights on elementary particles and their interactions. In the following sections, three specific cases of BSM theories have been mentioned briefly.

### I.2.1 BSM Physics in dijet resonances along with a lepton

Beyond the Standard Model Physics is proposed by many theories in different sectors and provide motivation for many resonance searches at the collider experiments. In many BSM theories heavy particles decay into two partons which go through hadronization processes and form jets. From experimental point of view the two partons form, two jets and experiments can look for dijet resonances to probe for such BSM theories. Apart from different BSM model motivated studies, there have been many model independent studies on the dijet resonance searches as well.

ATLAS [48, 49, 50], CMS [51, 52, 53] have performed many searches for such dijet heavy resonances by probing dijet mass distributions and set limits on many BSM theory models.

There have been also many BSM models which predict dijet resonances and presence of a charged lepton in the final state of the decay process along with the resonance.

The representative diagrams at Figure I.14 represent many different BSM processes where two jets and a charged lepton can be found in the final state. In few Dark matter models [54], in Sequential Standard Model [55] where new gauge bosons $W' \rightarrow WZ' \rightarrow l\nu q\bar{q}$ and also in few charged Higgs models ($b\bar{b} \rightarrow W^{\pm}H^{\mp} \rightarrow l\nu q\bar{q}$) [56], $H^{+} \rightarrow tb$ can provide similar signatures.

The advantage for probing BSM models in dijet resonances along with a charged lepton is, usage of lepton as triggering or spectator objects reduces the backgrounds generated from QCD multijet events and also it helps to overcome the limitation of minimum single jet $p_T$ trigger threshold (of 450 GeV) as with single lepton triggers (with $p_T$ trigger threshold of 24 GeV) much lower mass range can be probed for possible resonances predicted by the BSM models.

For the dijet and lepton processes, reconstruction of 3 body of 4 body objects in the final state also provide wide ranges of scopes for the searches for new physics [22, 57, 23].

### I.2.2 Charged Higgs Boson

In the searches for new Physics, models predicting Charged Higgs Boson provide good motivation to be investigated at the collider experiments. After the discovery of Higgs Boson [58, 37, 59] at the LHC [60], there has been renewed interests to probe the possibility of more Higgses apart from the discovered Standard Model Higgs. Many Beyond Standard model theories including two-Higgs-doublet models (2HDM) [61, 56], [62, 63], [64] and models containing Higgs triplets [65, 66, 66, 67, 68] predict more Higgs bosons including singly charged Higgs bosons coming from an extended Higgs sector.

Among the different production and decay processes, in some BSM 2HDM models, Charged Higgs is produced along with a top quark and a bottom quark from the fusion

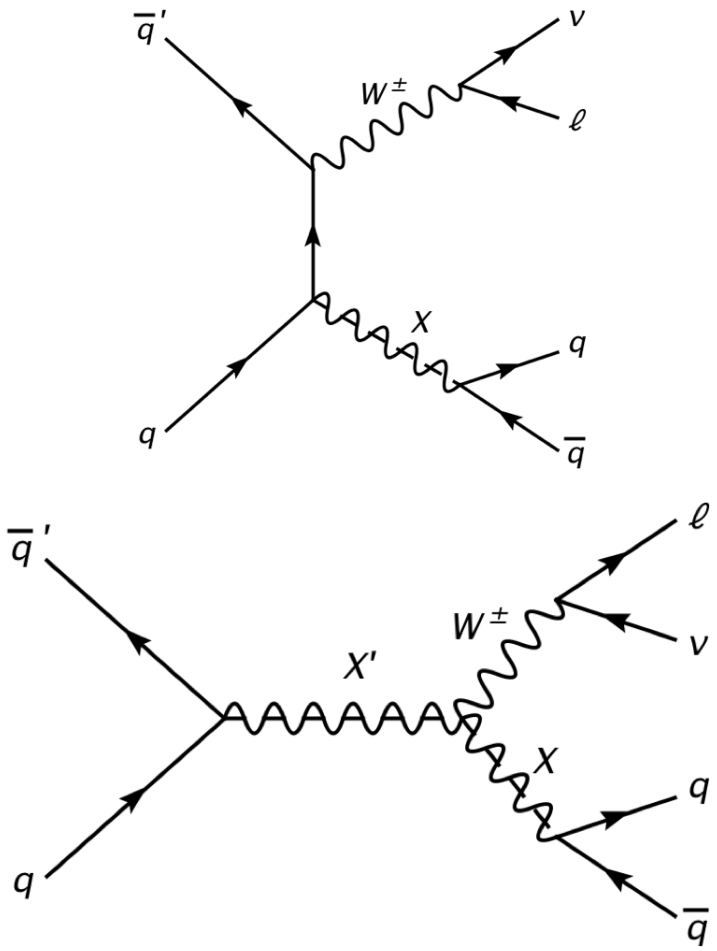


Figure I.14: The Feynman diagrams show generic resonance X decaying into two partons producing two jets and leptons is also produced from the decay of W boson. In the first diagram X' is another resonance particle [11].

of gluons and decays into a top and bottom quarks [69, 70].

$$qq \to tbH^+; H^+ \to tb \tag{I.2.1}$$

The 2HDM, being one of the simplest low-energy effective Higgs models, can be described in terms of different physical parameters including masses of Higgs bosons, the ratio of the two vacuum expectation values ($\tan\beta$ ) and the mixing angle ($\alpha$) which diagonalizes the mass matrix of the neutral CP even Higgses. In MSSM Higgs sector [71], the searches for such BSM signatures include studies with different values of ($\tan\beta$) [72].

Different colliders have been searching for Charged Higgs for long and limits on charged Higgs boson production have been obtained by many experiments. LEP at CERN set the upper limits on $H^+$ production in the mass range 40–100 GeV [73], and CDF and DØ at the Tevatron set upper limits on the branching ratio $B(t \to bH^+$ ) for 80 GeV $< mH^+ <$ 150 GeV [74, 75].

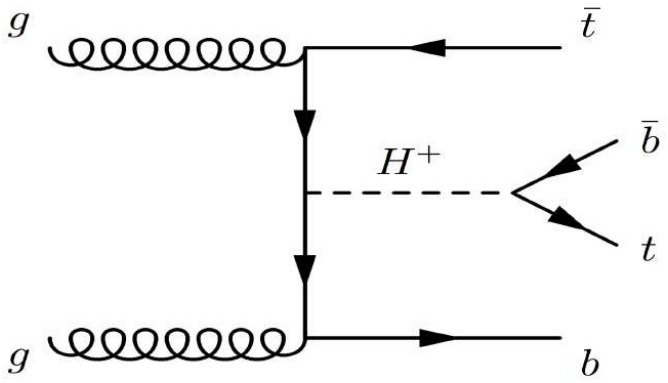


Figure I.15: The Feynman diagram for heavy charged Higgs boson being produced by gluon fusion, together with a top and bottom quark ($tbH^+$).

The CMS Collaboration has performed direct searches for heavy charged Higgs bosons in 8 TeV proton–proton (pp) collisions. By assuming the branching ratio $B(H^+ \to tb) = 1$, CMS set an upper limit of 2.0–0.13 pb for the production cross-section $\sigma(pp \to tbH^+)$ for 180 GeV $< mH^+ <$ 600 GeV [76].

The ATLAS Collaboration has also searched for similar heavy charged Higgs boson production in the $H^+ \to$ tb decay channel at 8 TeV, and 13 TeV and at the 8 TeV set upper limits on the production cross-section times the $H^+ \to tb$ branching ratio at 6–0.2 pb for 200 GeV $< mH^+ <$ 600 GeV [77].

At 13 TeV [21], ATLAS also excluded a range of masses in hMSSM scenario of the MSSM for values of $\tan\beta$ in the range 0.5–1.91 (0.5–1.95) and the $H^+$ masses of 200–920 (200–965) GeV. For the $H^+$ masses between 200 GeV and 520 GeV (220 and 540 GeV), high values of $\tan\beta$ are excluded, for example $\tan\beta > 36$ is excluded at 300 GeV.

Some combined flavour-physics results [78] also set a lower limit at 95% confidence level on the charged Higgs boson mass of $mH^+ > 600$ GeV for $\tan\beta > 1$ and $mH^+ > 650$ GeV for lower $\tan\beta$ values, assuming a Type-II Two Higgs Doublet Model (2HDM).

The process of $H^+t$ decaying to Top and bottom quarks are interesting for the prospects of dijet resonance searches along with charged lepton if the associated top quarks decays into a lepton and the decay products of Charged Higgs boson in boosted regime form two jets in the final state inside detector.

### I.2.3 W' Boson

While exploring the possibilities of new Physics beyond standard model, many popular theories predict new gauge bosons as the result of the enhanced symmetries.

Some of the prominent models which predicted about new massive gauge boson W' are Kaluza-Klein excitation models, Left-Right Symmetric models [79], Sequential Standard Model (SSM) [80], Little Higgs model [81, 82], composite Higgs model [83], extra-dimension models [84], models with strong dynamics [85, 86, 87, 88] etc. Many of these models predict charged current interactions and coupling of W prime with

different particles [83, 89, 90, 91, 92].

W' boson being a very massive particle as proposed can decay into the heaviest quark, the top quark along with a b quark. In such decay processes, top quark subsequently decays into a W boson and another b quarks. And then the W boson can decay both leptonically or hadronically into pair of two quarks. Figure I.16 shows the hadronic decay of a W boson into a pair of quarks.

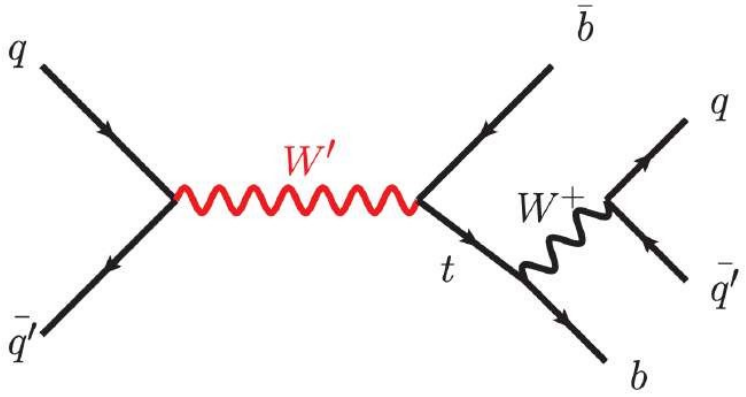


Figure I.16: Feynman diagram of W prime decaying to a top and bottom quarks

Sequential Standard Model (SSM) [80] predicts W prime boson with properties such that the coupling strength of W prime boson to the fermions are the exactly same as the coupling strength a W boson has with the fermions of the Standard Model [93, 94]. By the theories, both left handed and right handed W prime bosons have been predicted.

A model independent Lorentz invariant Lagrangian of lowest order using the ZTOP model can be seen below [95, 96] :

$$\mathcal{L} = \frac{V'_{ij}}{2\sqrt{2}}\overline{f_i}\gamma_\mu(g'^R_{1,j}(1+\gamma^5) + g'^L_{1,j}(1-\gamma^5))W'^\mu f_i + h.c. \tag{I.2.2}$$

Where $g'^R_{1,j}$ is the gauge coupling of right handed W prime boson with the fermions $f_i$ and $g'^L_{1,j}$ is the gauge coupling of left handed W prime boson with the fermions. $\gamma^5$ is the operator for chirality and the $V'_{ij}$ represented the values of quark mixing and it is assumed that its values are exactly the same with the values of CKM matrix components.

When the W prime boson is left handed, the coupling between a left handed W' and quarks are assumed to be the same as Standard Model and the coupling between right handed W prime and quarks are assumed to be zero. Similarly for the right handed W prime boson, the coupling between a right handed W' and quarks are assumed to be the same as Standard Model and the coupling between left handed W prime and quarks are assumed to be zero.

Both Tevatron experiments [97, 98] and the experiments at LHC including CMS experiment at 13 TeV [99], ATLAS at 8 TeV [100] and ATLAS at 13 TeV [101] have been searching for W prime boson in the same channel. ATLAS experiment at $\sqrt{s} =$

13 TeV using 36.1 $fb^{-1}$ data, excluded right-handed W' bosons with masses below 3.0 TeV and left-handed W prime bosons with masses below 2.9 TeV are excluded. But improved detector technologies and better object identification techniques, larger amount of datasets and explorations of high mass regions are always motivating to perform new searches of beyond the standard Model Physics.

Among the many new physics beyond the Standard Model, in this thesis some of the experimental efforts have been discussed on the searches for Charged Higgs Boson though Dijet resonances, searches for hypothetical gauge boson W' boson and some new resonances by Radion particles and Kaluza Klein excitation (Boson) [102] and lepton flavor violating composite resonances [23]. Also while searching those new physics, a few R&D studies on experimental apparatus and technologies which have been crucial for the success of the experiments have also been discussed.

# CHAPTER II

## The Experiment

> It doesn't matter how beautiful your theory is, it doesn't matter how smart you are. If it doesn't agree with the experiment, it's wrong
>
> Richard Feynman

For scientific knowledge experiments play crucial roles. An experiment can provide confirmation on theoretical hypothesis and at the same time experimental results can also inspire new theoretical ideas. In Science, experiments are generally designed to find answers to scientific questions and often motivated by theories. Size, nature and methodologies vary according to the problems involved. A scientific Experiment generally deals with variables which act as tunable parameters while maintaining control over the explorations and conclusions are made based on empirical data and reasoning. Experimental apparatus are the means for scientists to test ideas and to search for truth.

Ancient Greek Scientist and Philosopher Aristotle has significantly pioneered some of the scientific methods including importance of empirical evidence. 11th century Arab polymath Ibn al-Haytham, who is considered the father of modern scientific methodology also helped to establish a method where theoretical hypothesis must be supported by experimental and logical evidence.[103]. 16th century physicist Galileo Galilei, the father of observational astronomy also greatly promoted the ideas of experiment based evidence in scientific practice and methodologies. Another Physicist who revolutionised the idea of an experiment was 16th century British Physicist Francis Bacon,often referred as father of Experimental philosophy [104] wrote:"Experimentation is essential to discovering the truths of Nature" [105].

Over the years, as modern Science and Physics continued to develop and complexity of ideas, theories continued to increase, the experiments and the experimental techniques also developed at the same pace.

Small table-top laboratory experiments experiments are useful for many scientific investigations. But depending on the science and limitations of experimental approach bigger experiments have also been designed. In human history, the biggest machine and biggest experiments for scientific explorations ever designed till date is the giant experimental facility at the Large Hadron Collider(LHC) and its associated experiments at European Organization of Nuclear Research (CERN) laboratory. Human civilization has come a long way from the times of Galileo Galilei's experiments on pendulums to the times of Large Hadron Collider.

One short trip for a proton, but one giant leap for mankind!

Nigel Lockyer, Director of Fermilab, on the first successful proton beam at the Large Hadron Collider in 2008

## II.1 Large Hadron Collider

The Large Hadron Collider (LHC)[106] is the biggest machine of the world and also the most powerful particle accelerator at the European Organization of Nuclear Research (CERN) laboratory near the border of France and Switzerland. It consists of a 27 kilometer long gigantic tunnel where extremely high energy proton beams travel at speed of very close value to the speed of light and collide from the opposite directions producing huge amounts of energy. Those billions of collisions give physicists enough scopes to study elementary particles, their interactions at that extremely high energy frontier. These interactions give insight about the stages of creation of our universe, about different particles which may have been produced during those stages and later on got frozen while the temperature of our universe went down due to cooling off with time.

The Large Hadron Collider complex is one of the most complicated experimental complexes of the world as well, as proton beam starting from a simple bottle of hydrogen gradually passed through extremely complex phases of LINACS[107], Proton Synchrotron (PS), Super Proton Synchrotron (SPS)[108] and then it goes into the biggest collision ring after going through systematic accelerations in different stages using electro-magnets and many cutting-edge technologies.

In the gigantic tunnel of LHC, there are 4 collision points and at those 4 points , 4 big experimental detectors are located. Four of those underground detectors at the collision points are : ATLAS[3], CMS[109], LHCb[110] and ALICE[111].

ATLAS and CMS experiments are the two general purpose detectors, where LHCb focuses on studies of b-physics, matter-anti matter asymmetry and ALICE experiment explores the conditions, during and after the Big Bang and other problems in nuclear physics through heavy ion collisions.

The center of mass energy of the LHC collisions was 7 TeV during Run 1 of the LHC in 2010-2011. Later on the energy got upgraded to 8 TeV in 2012 and for the Run 2 of LHC, the center of mass energy has been 13 TeV during 2015-2018. Run 2 has ended in 2018 and LHC has started its long shutdown 2 for 2-3 years, during which it went through major upgrades to prepare for its Run 3 starting in later 2021 or in early 2022.

### II.1.1 The LHC acceleration chain

The LHC acceleration chain is complex. A schematic view of that can be seen in the figure II.2. The journey of protons of the LHC ring starts from bottle of hydrogen

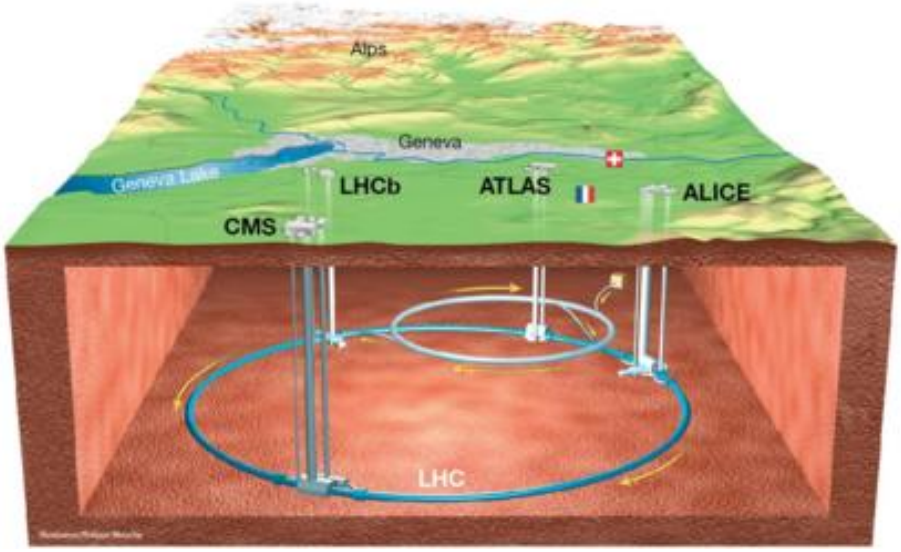


Figure II.1: A schematic view of LHC and its 4 biggest experiments at the Franco-Swiss border at CERN.

where at first its ionized and they are accelerated by the electric field inside the Linear Accelerator LINAC-2 and gradually the bunches of around $1.1510^{11}$ protons are accelerated up to one third of speed of light. In the next phase, the protons enter Proton Synchrotron Booster where with the help of pulsating electric field and magnetic field protons are accelerated and the proton beams are bent around the circle due to the magnetic field before entering Proton Synchrotron and during this journey proton beams are accelerated from 50 MeV to to 1.4 GeV. After circulating around Proton Synchrotron, protons reach a mass of 25 GeV and they enter the bigger ring of 7 km circumference the Super Proton Synchrotron (SPS). After travelling around 7 km long ring protons accelerate more and gain more kinetic energy of 450 GeV before passing into the gigantic 27 km long ring of the Large Hadron Collider. While travelling through the LHC ring, protons reach the energy of 6.5 TeV and Using the sophisticated vacuum pipe technologies, two beam pipes are aligned in such a way, two opposite bunch of protons collide in 4 different points at the 4 detectors on the collider ring while producing energy of 13 TeV. The collisions take place in every 25 nanoseconds with the frequency of 40 MHz.

### II.1.2 Beam structure and Luminosity

The proton beams which travel at the LHC ring consist of 2808 bunches per beam during its full intensity which each bunch contain $1.15 * 10^{11}$ protons at the start of the journey. While passing through the LHC, the beams get squeezed to 16 $\mu m$ only.

In particle physics the cross section $\sigma$ defines the probability of interactions or events. If the number of events per second is denoted by N, it can be written as :

$$N = \sigma L = \sigma \int_t \mathcal{L} dt \tag{II.1.1}$$

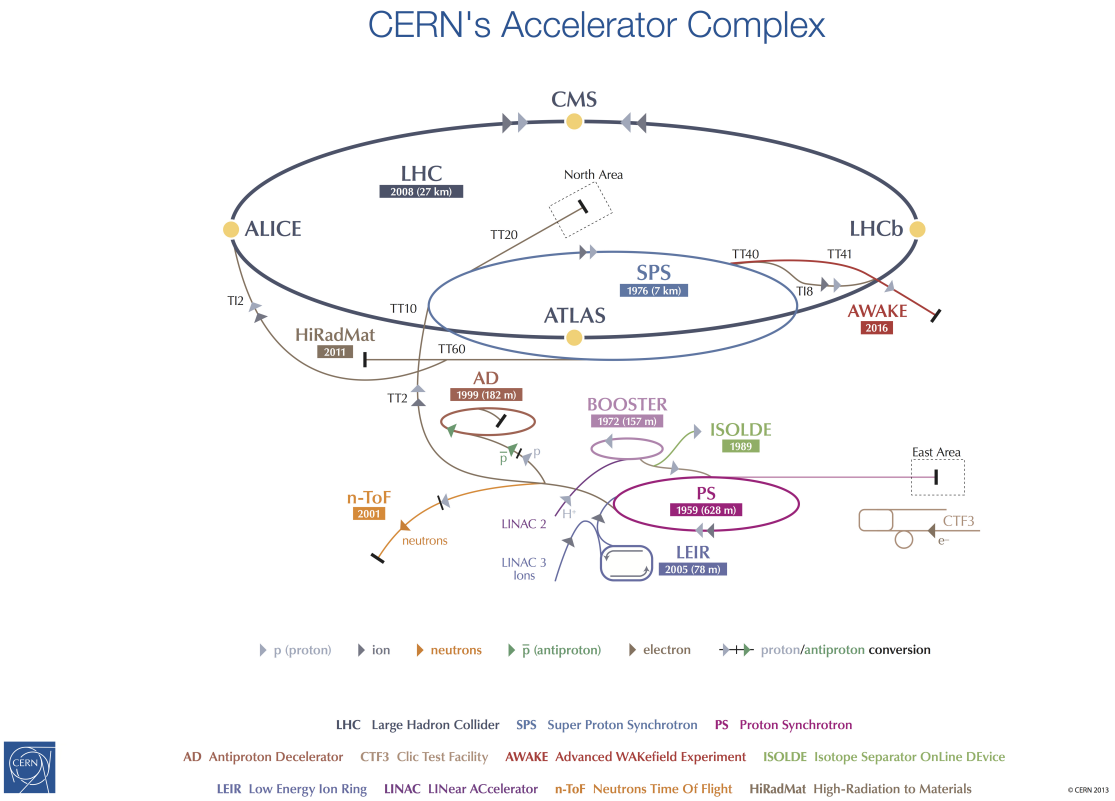


Figure II.2: A schematic view of LHC complex at CERN [12].

where $\mathcal{L}$ is called the luminosity. In beam physics, specially for two colliding beams at the LHC, the definition of luminosity becomes more complicated.

If the two colliding beams have have $N_1$ and $N_2$ numbers of particles(protons in this case) in each bunch respectively and if there are $N_{bunch}$ number of bunches which are released per each revolution by the LHC, if f represents LHC's revolution frequency and $\sigma_x$ and $\sigma_y$ characterize rms transverse beam sizes horizontally and vertically respectively (the Gaussian widths of the beams horizontally and vertically respectively), luminosity can be defined as[112] :

$$\mathcal{L} = \frac{N_1 N_2 f N_{bunch} \mathcal{F}}{4\pi\sigma_x\sigma_y} \tag{II.1.2}$$

The factor $\mathcal{F}$ takes care of geometric effects including mutual focusing of two beams, finite bunch length, crossing angle etc. $\mathcal{F}$ has the value in the order of 1.

The luminosity over time can be integrated to calculated integrated or total luminosity. Integrated luminosity reflects the total amount of data collected by the any detector.

$$L = \int_t \mathcal{L} dt \tag{II.1.3}$$

For the Large Hadron Collider, during Run 2 the $\mathcal{L}$(instantaneous luminosity) has

reached the value of $2.1410^{34} cm^{-2} s^{-1}$ and the total integrated (delivered) luminosity by the LHC was $158 fb^{-1}$.

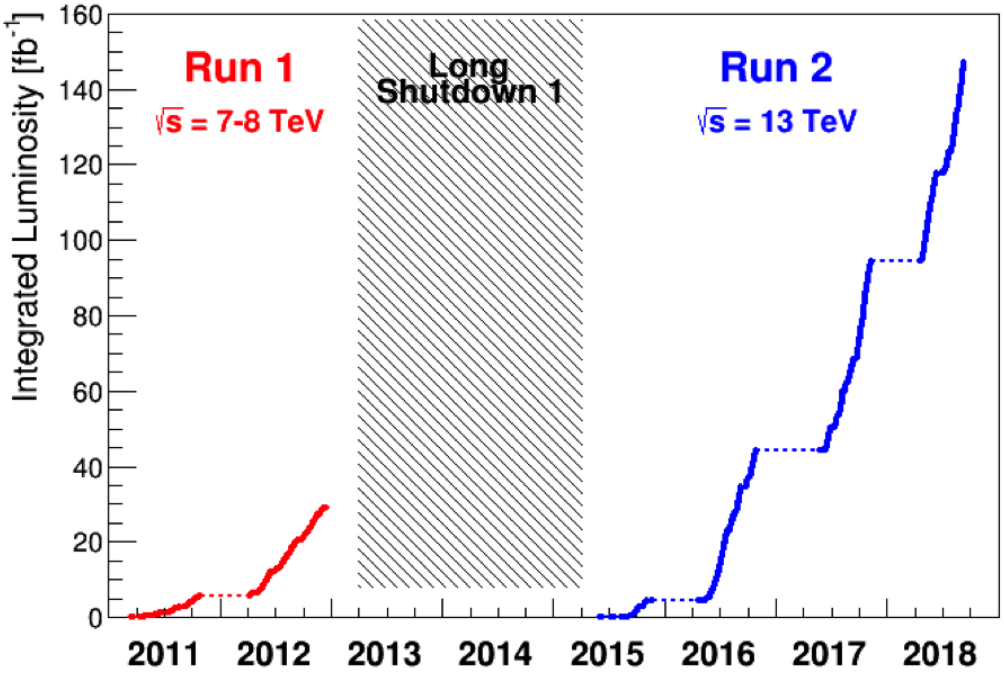


Figure II.3: A comparative plot of cumulative luminosity during different years of data taking by the LHC.

In summary, with the current infrastructure of LHC, 450 GeV beams are injected inside LHC ring and it can be accelerated up to 7 TeV beams, the nominal luminosity at the LHC is $110^{34} cm^{-2} s^{-1}$, but it can reach maximum $2.510^{34} cm^{-2} s^{-1}$, bunch spacing between two different beams is 24.95 nanosecond. The nominal number of protons with each bunch is $1.1510^{11}$, though it can reach a maximum value of $1.7010^{11}$. The nominal Beam current at the LHC is 0.58 Ampere and its capable of reaching 0.86 Ampere in its ultimate capability [113].

### II.1.3 LHC Run-2 performance

After the Long shutdown 1, LHC had a very successful Run 2 during 2015-2018. During Run 1, ATLAS Experiment recorded proton proton collision data of 25 $fb^{-1}$ and during Run 2, it recorded proton proton collision data of 150 $fb^{-1}$. That speaks volume of the success of data taking.

| Parameter | 2015 | 2016 | 2017 | 2018 |
|---|---|---|---|---|
| IR1/IR5 Peak L ($10^{34} cm^{-2} s^{-1}$ ) | 0.5 | 1.4 | 2.1 | 2.1 |
| Average pile-up $<\mu>$ | 13 | 25 | 38 | 37 |
| Max. no bunches | 2244 | 2220 | 2556 / 1868 | 2556 |
| Max. train length (bunches) | 144 | 96 | 144 / 128 | 144 |
| Emittance injection ($\mu$m) | 3.0 | 1.6 | 1.6 | 1.4 |
| Bunch pop. start of stable beams (($10^{11}$) | 1.0-1.25 | 1.0-1.25 | 1.0-1.25 | 1.0-1.25 |
| Emittance start of stable beams ($\mu$m) | 3.5 | 2.2 | 2.2 | 1.9 |
| RF Voltage injection (MV) | 6 | 6 | 6 | 6 / 4 |
| RF Voltage collisions (MV) | 12 | 12 | 10 | 10 |
| $\beta$* IR1/5 (cm) | 80 | 40 | 40-30 | 30-25 |
| Half crossing angle IR1/5 (cm) | 145 | 185 / 140 | 150-120 | 160-130 |
| IR1 crossing sign | -1 | -1 | +1 | +1 |
| Max. stored energy (MJ) | 280 | 270 | 330 | 320 |
| IR1/IR5 integrated L ($fb^1$) | 4.2 | 39.7 | 50.6 | 66 |
| IR8 integrated L ($fb^1$) | 0.36 | 1.87 | 1.98 | 2.46 |
| IR2 integrated. L ($pb^{-1}$) | 9 | 13 | 19 | 27 |
| Commissioning duration (days) | 58 | 28 | 24 | 17 |
| Average length of stable beams (hours) | 6.8 | 11.2 | 8.2 | 8.3 |
| No. days of physics operation | 88 | 146 | 140 | 145 |
| Machine availability (%) | 69 | 76 | 83 | 79 |
| Average turnaround time - with faults(h) | | 7.1 | 6.2 | 6.0 |
| Average turnaround time - excluding faults(h) | | 4.3 | 3.5 | 3.5 |
| Stable beams efficiency (%) | 35 | 49 | 49 | 49 |

Table II.1: Run 2 performance of LHC while using regular proton proton collisions. The emittance values for 2017 were for Batch Compression Merging and Splitting(BCMS) beam and for 2017, maximum number of bunches and train length values correspond to BCMS and 8b4e beams respectively [2].

The table II.1 shows the comparison between different years of runs during Run 2 for many different parameters.

### II.1.4 Pileup

The term Pileup is defined as the no. of interactions in bunch crossing or $<\mu>$.

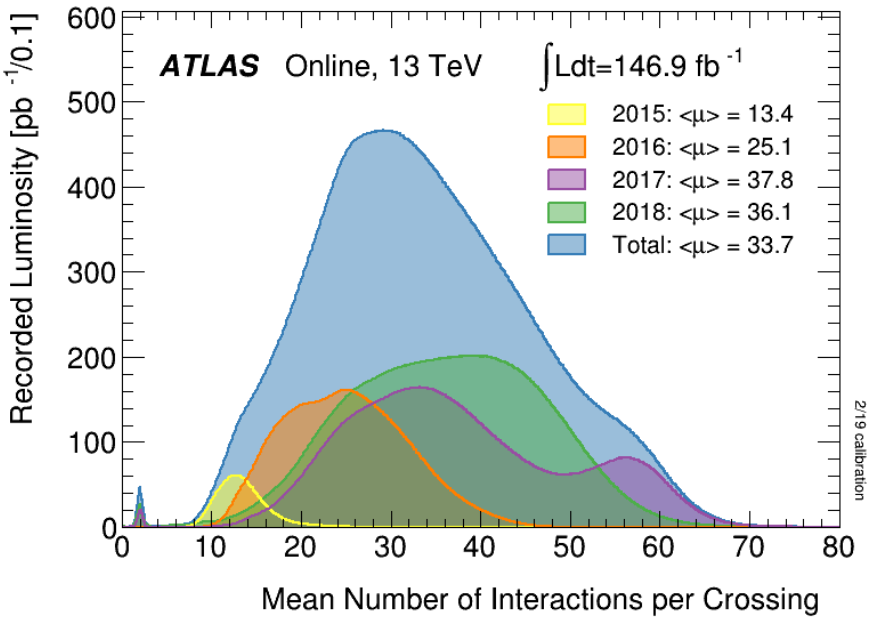


Figure II.4: Number of Interactions per Crossing during Run 2 at the ATLAS detector.

Figure II.4 shows the number of interactions per Crossing during 2015-2018 (Run 2) at the ATLAS detector. It can seen as over the years, ATLAS recorded data with more luminosity, the mean no. of interactions in bunch crossing $<\mu>$ value has also increased. Pileup beyond than detector's capacity can affect the reconstruction efficiency of Physics objects. So proper pileup mitigation techniques are applied so minimize the bad effects due to pileup.

$$< \mu >= \frac{\sigma_{inelastic}\mathcal{L}}{n_c f_{rev}} \tag{II.1.4}$$

Here $n_c$ is the Number of colliding bunch pairs and $f_{rev}$ is the machine revolution frequency of LHC. The above equation give expression for $in-time$ pile-up and also there can be another kind of pile up where signals from the different bunch crossing overlaps and that kind of pile-up is called $out-time$ pile-up.

> Detectors are really the way you express yourself. To say somehow what you have in your guts. In the case of painters, it's painting. In the case of sculptors, it's sculpture. In the case of experimental physicists, its detectors. The detector is the image of the guy who designed it
>
> *Carlo Rubbia ( p44, Nobel Dreams by Gary Taubes)*

## II.2 ATLAS detector

ATLAS(A Toroidal LHC ApparatuS) [3] is a general-purpose particle physics experiment placed at one of the four collision points of the Large Hadron Collider (LHC) ring and it is designed to explore the Physics opportunities of the Large Hadron Collider.

Dimension wise, ATLAS detector is 46-meter-long, 25-meter-high and 25-meter-wide and its weight is 7000-tonne, which makes the ATLAS detector the largest volume particle detector among LHC experiments. It sits in a cavern 100 meter below ground near the main CERN site at point P1 on the LHC ring, close to the village of Meyrin in Switzerland.

Unlike another LHC detector LHCb, ATLAS detector is symmetric in its cylindrical geometry in both forward and backward direction while providing a coverage of $4\pi$ solid angle.

ATLAS detector consists of different sub-detectors namely an inner tracking detector, electromagnetic and hadron calorimeters, and a muon spectrometer. The inner detector is surrounded by a thin superconducting solenoid which provides axial magnetic field of 2 T.

ATLAS detector has a wide range of Physics prospects. Searching for Higgs boson was one of the many important motivations for the Experiment. From the searches for SuperSymmetry, dark matter to studies on heavy ion physics or B-Physics or the measurements of Standard Model processes, studies on different leptonic, hadronic, semi leptonic decay processes etc. all have been part of ATLAS experiment's activity. For all those studies, ATLAS detector possess some of the good qualities of having fast and radiation hard electronics, large coverage in pseudorapidity and azimuthal angle, good particle identification techniques and good reconstruction efficiency.

### II.2.1 ATLAS coordinate system

ATLAS detector use multiple coordinate systems for its measurements including both Cartesian and cylindrical coordinate systems. The beam pipes who goes through the detector and the collision point where interactions take place become important

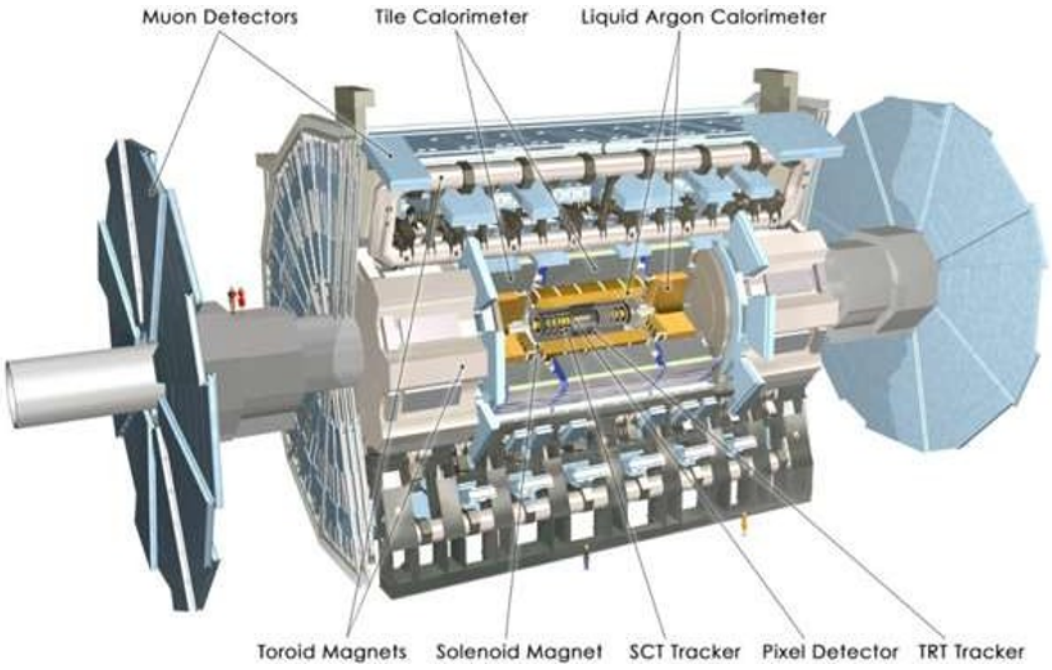

Figure II.5: A schematic view of ATLAS detector.

parameters and reference for the coordinate system. Generally $Z$ axis is pointed to the direction of beam pipe, $x$ axis points to the center of the collider ring from the interaction point in transverse plane and $y$ axis is directed towards the up. In the transverse plane, while using cylindrical coordinate systems (r, $\phi$) ,the azimuthal angle around beam pipe is denoted by $\phi$. The polar angle is denoted the $\theta$, which express the angle between the particle three momentum $p$ and the positive axis of beam axis. To describe the angle of a particle relative to beam axis, another popular variable pseudorapidity $|\eta|$ is used. By definition :

$$|\eta| = -\ln[\tan(\theta/2)] \tag{II.2.1}$$

The variable rapidity is defined by :

$$y = \frac{1}{2}\ln[\frac{E+p_z}{E-p_z}] \tag{II.2.2}$$

The distance $\Delta$R is defined by :

$$\Delta R = \sqrt{(\Delta\eta)^2 + (\Delta\phi)^2} \tag{II.2.3}$$

In summary all the different sub-detectors have the following pseudorapidity coverage as seen in the table II.2.

After the particle beams collide at the interaction points, the registered particles pass through different sections of the detectors and different particles end up in different sub-detectors, while some pass out of the detectors.

| Sub-detector name | Pseudorapidity $\eta$ coverage |
|---|---|
| Inner Tracker | $\pm$ 2.5 |
| Electromagnetic calorimeter | $\pm$ 3.2 |
| Hadronic calorimeter<br>Barrel and end-cap<br>Forward calorimeter | <br>$\pm$ 3.2<br>$3.1 < \|\eta\| < 4.9$ |
| Muon Spectrometer | $\pm$ 2.7 |

Table II.2: Pseudorapidity $\eta$ coverage for measurement in different sub-detectors of ATLAS[3].

Electronics and trigger systems gather information about the particle tracks and their different properties. The collected raw data goes through multiple processing stages before it is ready to be analyzed by thousands of physicists across the globe.

### II.2.2 ATLAS magnet system

ATLAS magnet system is 26 meters long and has a diameter of 20 meters. The magnetic system plays a crucial role by helping to bend the particles while they pass through various sub-detectors. The magnet system can be divided into three parts :

1. Central Solenoid Magnet
2. Barrel Toroid
3. End-cap Toroids

The barrel toroid and end-cap toroid provide magnetic field of 4 Tesla on superconductors and the central solenoid magnet provides 2 Tesla magnetic field. Both of the Barrel toroid and end-cap toroid consist of 8 different coils.

Both Barrel Toroid and End-cap toroid needs to maintain -269.15 degree Celsius or 4 Kelvin temperature for normal operations. All these subsystems are connected with wires with lengths kilometers. For example the Barrel toroid is connected with 100 km long superconducting wires, where Central Solenoid magnet has 9 km long superconducting wiring.

For the Muon systems, Barrel toroid bends the particles inside sub-detectors when $|\eta| < 1.4$. The end-cap toroids help to bend the particles when $1.6 < |\eta| < 2.7$ and in the transition region ($1.4 < |\eta| < 1.6$), with the combined effect of barrel toroids and end-cap toroids, particles are bent due to magnetic field [3].

### II.2.3 The Inner Detector(ID)

The inner tracking detector (ID)[114, 115] as evident from its name is the inner most sub-detector and it consists of silicon pixel detector ,silicon micro-strip detector and transition radiation tracker. In terms of pseudorapidity, the inner tracking detector covers a range of $|\eta| < 2.5$.

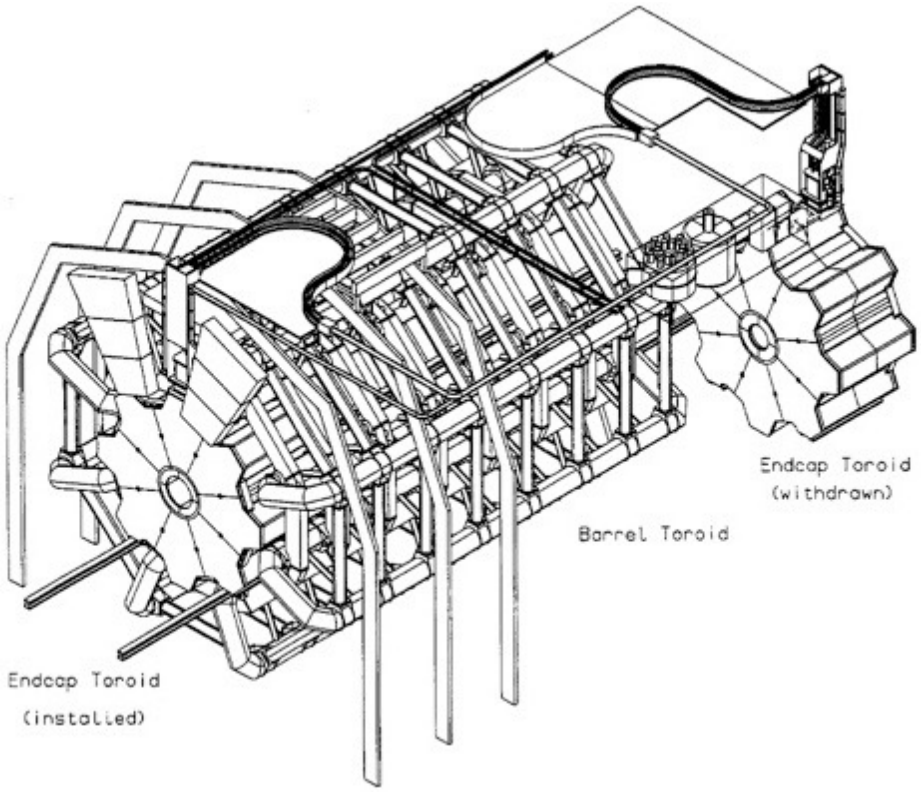


Figure II.6: A schematic view of ATLAS Magnet systems. In the figure central solinoid is hidden. [13]

ATLAS inner detector is 6.2 meters long and 2.1 meter wide and is the nearest sub-detector around beam pipe. Its innermost part is the Pixel detectors which consist of 92 million pixels and it contains 4 barrel layers with 1736 sensor modules. Each of its end cap is also connected with 288 modules. Pixel detector is very crucial for b-tagging or b-jet identifications. Insertable B-layer(IBL)[116] was added at a mean sensor radius of 3.2 cm from beam pipe during long shutdown 1 , to improve performance of b-tagging by pixel detectors during Run 2.

Semiconductor tracker which surrounds the Pixel detector consist of 4,088 modules, each of them are two-sided. The sub-detector also consist of 6 millions readout channels/strips of large numbers which help to record the position of charged particles which pass through the inner detector.

Transition radiation tracker is the outer most part of the Inner detector and consist of straw tubes where 50000 straws are inside the barrel and 250000 straws are placed in both endcaps. The sub-detector has electronics to read total 350000 channels to reconstruct the tracks of charged particle and to identify particles which passed through the detector.

Figure II.9 provides a view of different layers of ATLAS inner detector.

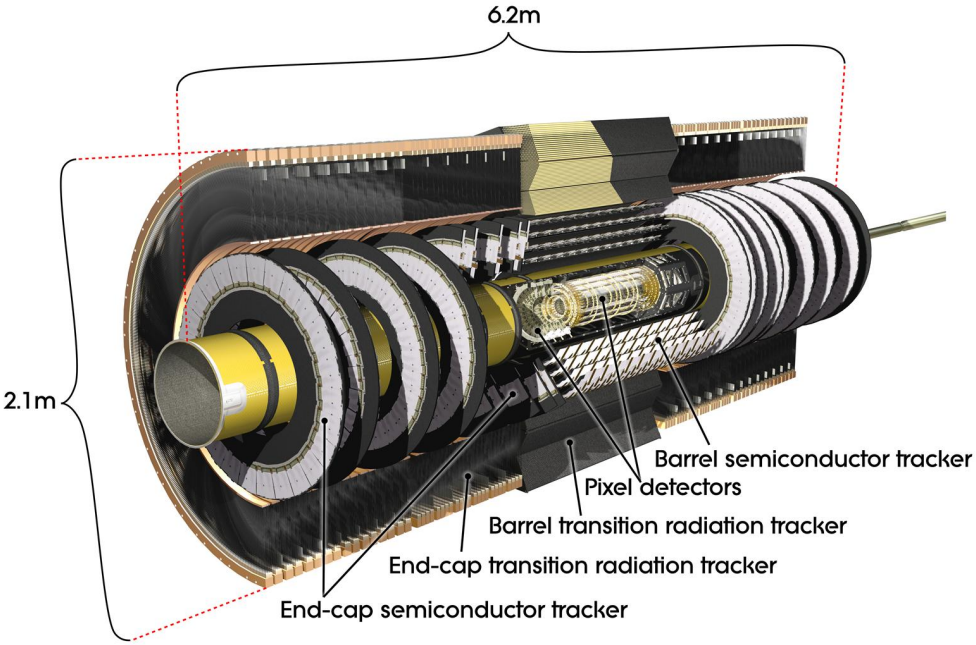


Figure II.7: A schematic view of ATLAS Inner tracking detector.

### II.2.4 The ATLAS Calorimeters

The ATLAS calorimeter system consists of two parts : The Electromagnetic Calorimeter and the Hadronic Calorimeter.Electromagnetic calorimeter is also known as Liquid Argon (LAr) Calorimeter. A calorimeter is sub-detector designed to stop the particles generated from the collision point and to measure their energies.

**The Electromagnetic Calorimeter:**

The second sub-detector surrounding the Inner detector is the Electro-magnatic calorimeter[117] made out of liquid-argon (LAr) which helps in measuring the electromagnetic energy deposited by the generated particles like electrons and photons with high granularity. The electromagnetic calorimeter covers pseudo-rapidity region with ($|\eta| < 3.2$). The liquid Argon is operated at the temperature of -183 degree Celsius, so the calorimeter maintains the low temperatures.

Lead material is also used in the calorimeter to act as absorber and from the interactions of electrons it help to generate photons through bremsstrahlung processes. Photons generate showers and liquid Argon measures the energy of the showers.

The EM calorimeter barrel has total 110,000 channels and its endcaps is connected to three different layers : 1. Forward calorimeter, 2. Electromagnetic (EM) and Hadronic endcaps.

**The Hadronic Calorimeter:**

A hadronic calorimeter is the next sub-detector after Electromagnetic calorimeter where hadrons(protons, neutrons) deposit their energy. The hadronic showers often produced by strong interactions generate large number of pions which decay into

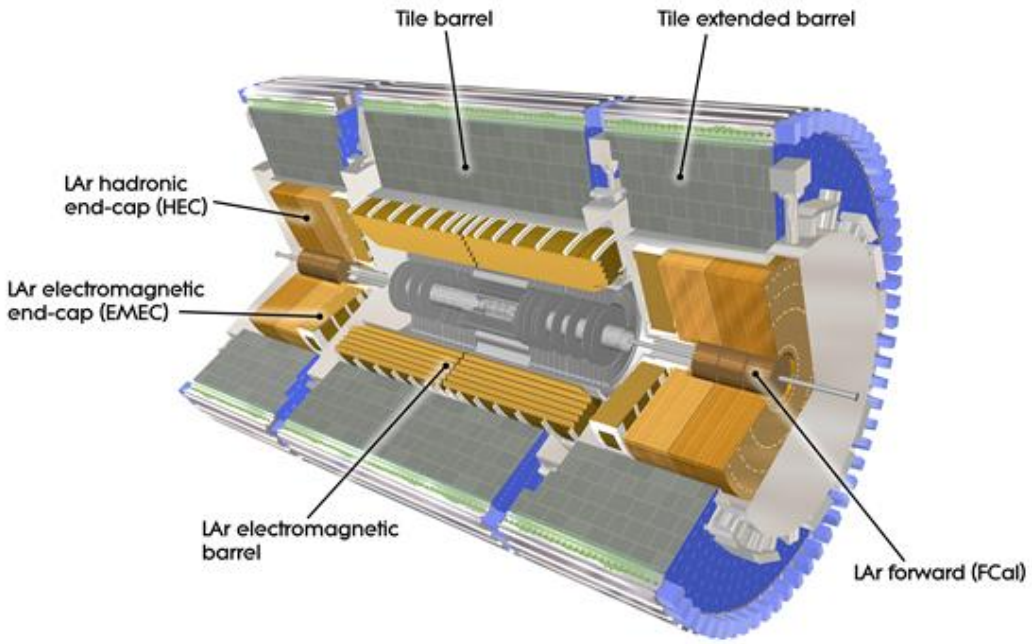


Figure II.8: A sketch of ATLAS calorimeters. [14]

other particles later on.

Tile Calorimeter surrounds the EM calorimeter. It consists of three layers in barrel ($|\eta| < 1.7$) and endcap consisting of two wheels. The hadronic calorimeters consist of 500,000 plastic scintillator tiles. A central pseudorapidity range of ($|\eta| < 1.7$) is covered by the hadronic calorimeter and by construction, its end-cap and the forward regions are instrumented with LAr calorimeters for both EM and hadronic energy measurements up to $|\eta| < 4.9$. The forward calorimeter (FCal) while working in the forward region($3.2 < |\eta| < 4.9$) not only optimize the measurements of hadrons, but also reduces background levels at the Muon spectrometer.

### II.2.5 The muon spectrometer

The muon spectrometer[118, 119] is the biggest sub-detector in size and the spectrometer is based on three large air-core toroid superconducting magnets, while each of them have eight coils. It includes a system of precision tracking chambers and fast detectors for triggering purposes.

Muon spectrometer is a combination of 4,000 individual muon chambers and have broadly 4 different sections :

1. Thin Gap Chambers (TGCs)
2. Resistive Plate Chambers (RPCs)
3. Monitored Drift Tubes (MDTs)
4. Cathode Strip Chambers (CSCs)

Monitored Drift Tubes (MDTs) are used significantly to fill the layers inside the barrel region of muon spectrometer. Both Thin Gap Chambers (TGCs) and Resistive Plate Chambers (RPCs) have very good efficiency in triggering muons, where Monitored Drift Tubes (MDTs) help in tracking.

Muons after being generated at the collision point, passes through Inner detector, calorimeters and the Muon spectrometer, but it cannot be stopped in any part of the detector. Muons take part into very important physics and carries away energy from the collision point. Toroids from the ATLAS magnetic system help to bend the muons while passing through muon spectrometer. To measure the properties of the passing muons, the Muon spectrometer with the 4 different technologies calculate the momentum of the muons with high precision and provide crucial information for the analyzers.

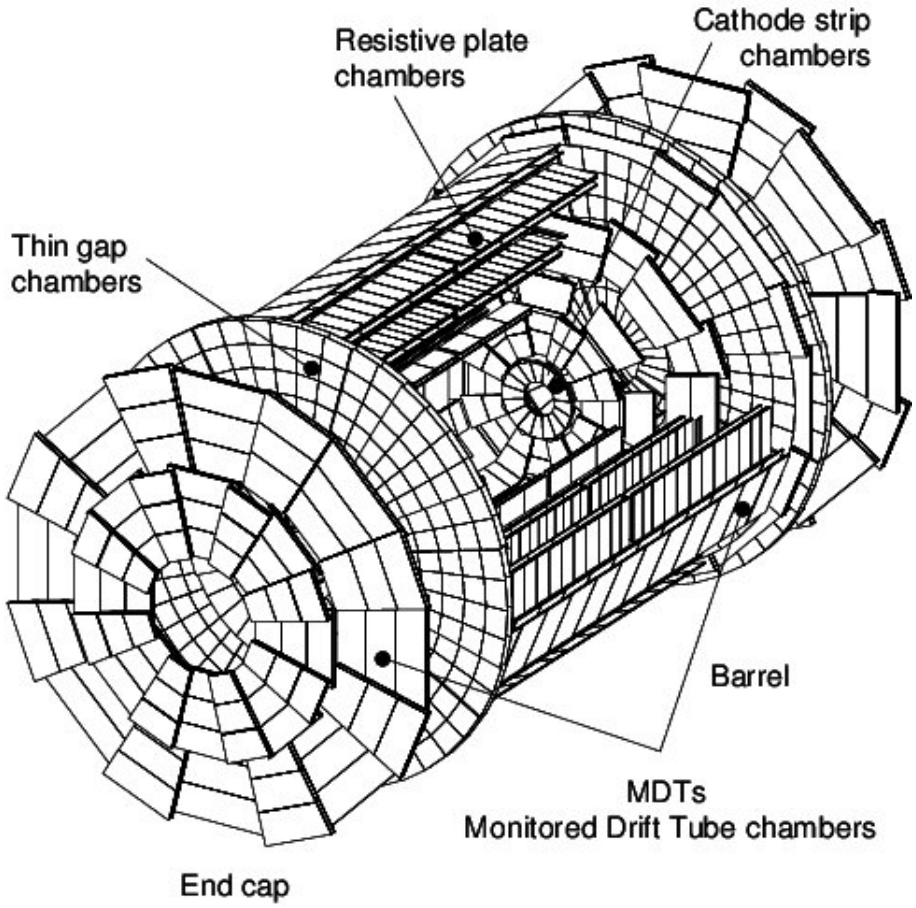


Figure II.9: A layout of ATLAS Muon spectrometers. [15]

### II.2.6 The trigger and data acquisition system

The ATLAS detector is capable of observing 1.7 collisions in each second at its interaction point. Particles generated from the collisions travel through the detector and and with the help of electronics the information of hits or other signatures of the passing particles are collected. Collecting all these information as data from 1.7

billion collisions account for 60 million MB data per second, all of whom may not be useful to explore the new and interesting physics. So, ATLAS uses its trigger systems to select only around 1000 collisions per second which are interesting for physics purposes.

The ATLAS trigger system consist of Level-1 (L1), Level-2 (L2), and event filter where the L2 and the event filter form the High Level Trigger(HLT) [3].

The first trigger system L1 rely on the electronics and different parts of the hardware detectors and collect the information from different sub-detectors including the momenta of different particles (quarks, leptons, gluons etc.)and also missing energy $E_T$. L1 read out system is capable of accepting the information at the rate of 75 kHz and withing 2.5$\mu$s, decisions are made on the selection cuts and 100000 events are selected per second.

The software based High Level Trigger(HLT) uses the inputs from the Level 1 trigger as all information on the selected events by L1 are fully stored. Analyzing those data with the help of large computation power, HLT performs detailed analysis of the events in different sections of the detectors and selects the most interesting data of 1000 events per second. In terms of frequency, it can be summarized that starting from the 20 millions events per second, the Level 1 trigger selects events with 75000 Hz frequency. Level 2 trigger reduces the 75000 Hz frequency to $\tilde{5}$000 Hz frequency after its further selections. And then another component of HLT, the event filter reduces the rate upto 1000 Hz.

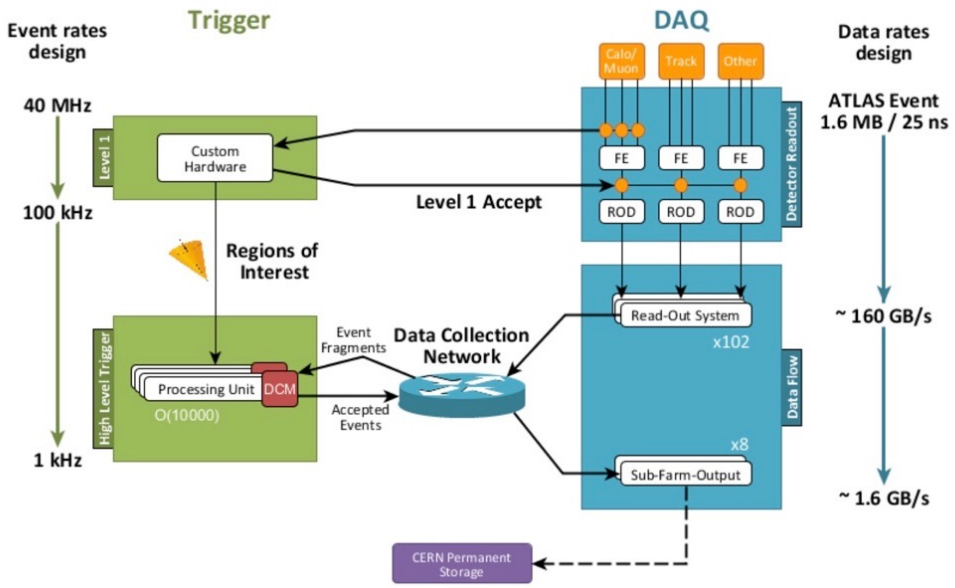


Figure II.10: ATLAS Trigger and DAQ system in Run 2 shown using block diagram.

Figure II.10 provides a good high level layout for Run 2 how TDAQ system works and the L1 triggers with its readout devices collect the data and then for the Region of interests (ROI), transfers the information to L2 trigger system and then through multi-layered data network, HLT makes decision to select very few interesting events for storage [120].

### II.2.7 Luminosity monitor of the ATLAS experiment

To monitor the luminosity at the ATLAS experiment, there is a dedicated sub-detector named LUCID or LUminosity Cherenkov Integrating Detector[121, 122]. The purpose of the sub-detector is to provide luminosity information of every bunch for while data taking and also for later offline studies. The luminosity monitor is important as luminosity information contribute as systematic uncertainty while performing searches and Physics measurements.

LUCID detector is designed to measure and identify if there are more number of interactions in bunch crossing $<\mu>$ which is the probable case as LHC moves towards higher luminosity.

LUCID detector has two modules and consists of 16 Photo multiplier(PMT) tubes and placed at a distance of 17 meters from the collision point along +z axis. When charged particles pass through the PMTs, cherenkov light is produced and detected through the read out systems of PMTs. The information received by different PMTs are combined to calculate the number of interactions per bunch crossing. Calibrations and correction factors are also applied to determine the correct luminosity.

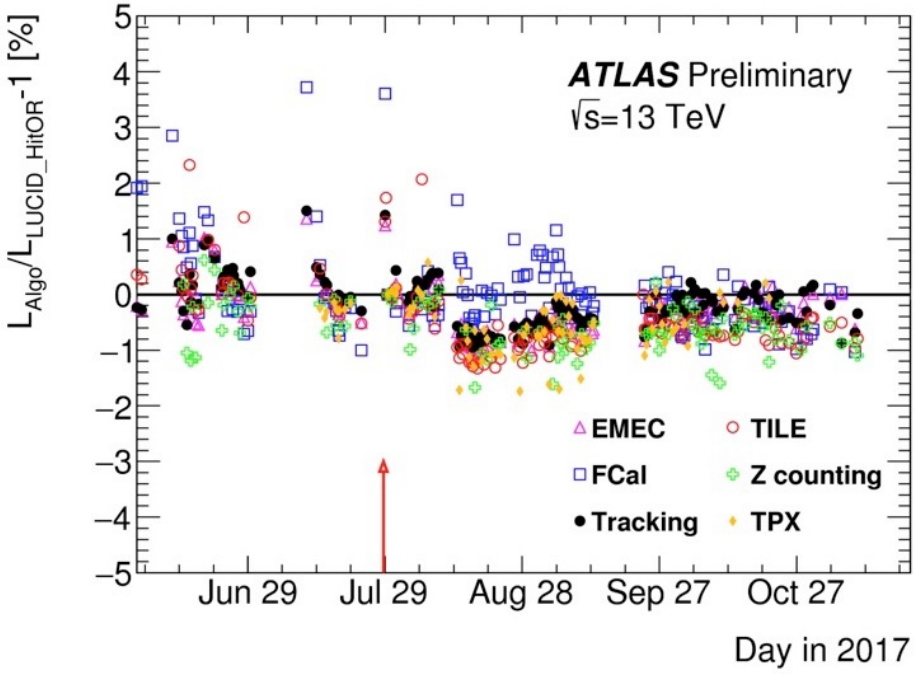


Figure II.11: Comparison of the main luminosity algorithms to the LUCID hit-counting algorithm. The results are mostly within 1.3% of the LUCID measurements [16].

During Run 1 with 22 $fb^{-1}$ of data, there was 1.9% uncertainty[123] and during Run 2, while collecting 139 $fb^{-1}$, there has been 1.7 % uncertainties[124].

Figures II.12 and II.13 show the cumulative luminosity in Run 1-2 and in Run 2 respectively. Figure II.13 also reflects the small difference between LHC-delivered

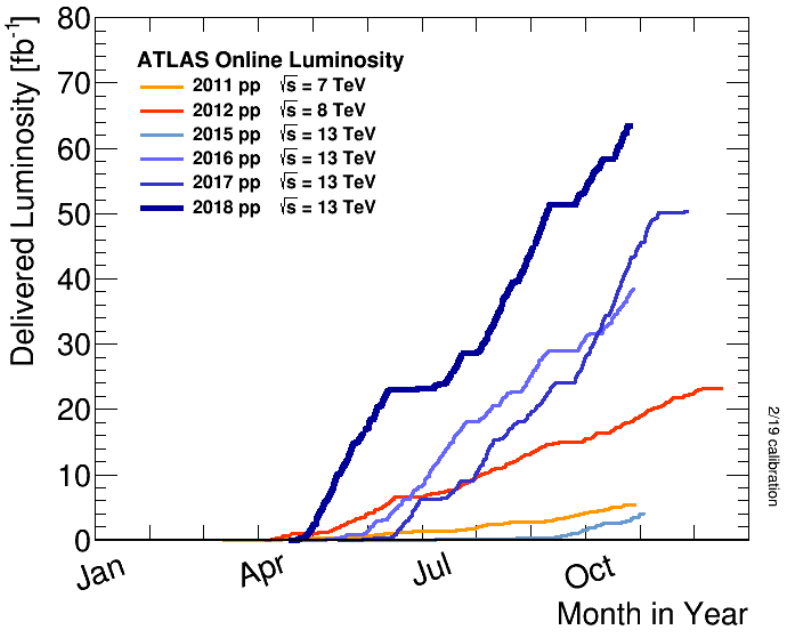


Figure II.12: A plot of cumulative luminosity during different years of data taking at the ATLAS detector at CERN.

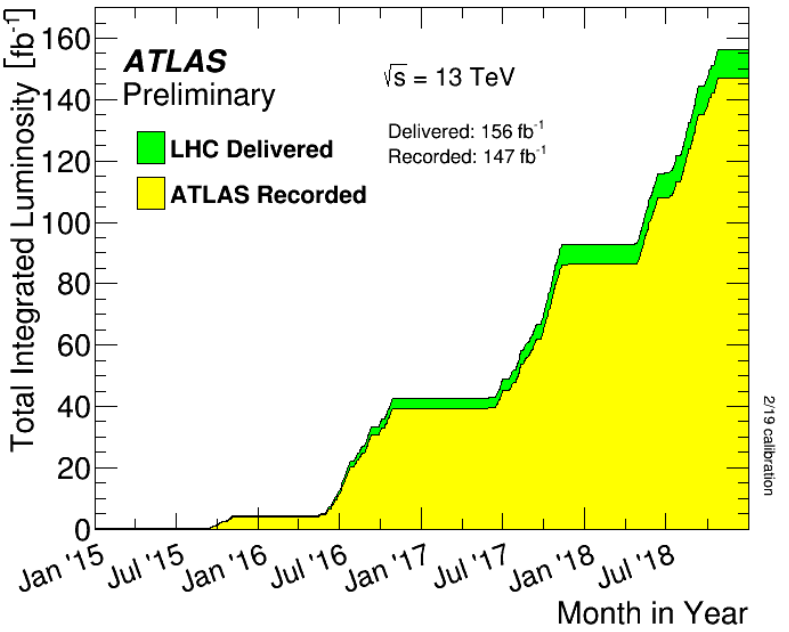


Figure II.13: Total integrated Luminosity during Run 2 at the ATLAS detector.

luminosity and the luminosity recorded by ATLAS.

# CHAPTER III

## R & D studies : ITk Pixel upgrade studies for High Luminosity LHC

> Astonishing how great the precautions that are needed in these delicate experiments. Patience. Patience.
>
> *Michael Faraday*

Behind every every successful experiment there lies years of preparation, years of research and development studies before it starts. For the Large Hadron Collider, such upgrade and R&D studies is more crucial due to huge size and logistics of the experiment. Before every major upgrade at the LHC or at the detectors, multi-step preparations including design study, production of prototype samples, significant efforts on testing, constructions, installations etc. take place. High Luminosity LHC upgrade is also no exception. This section describes some of my works which I did to contribute to the ITk pixel upgrade studies for the HL-LHC.

### III.1 HL-LHC upgrades

High Luminosity LHC (HL-LHC) upgrade is planned to be a very major upgrade for the Large Hadron Collider and the instantaneous luminosity at the collider will increase from $2 \times 10^{34} cm^{-2} s^{-1}$ to $5 - 7 \times 10^{34} cm^{-2} s^{-1}$. Because of such luminosity, HL-LHC will lead to very high detector occupancy, with a hit rate of 3 $GHz/cm^2$.


Figure III.1: LHC timeline plan

ATLAS Pixel subsystem is the innermost part of the ATLAS detector surrounding beam pipe. It has 4 barrel layers and 3 endcap disks on each side, providing coverage for $|\eta| < 2.5$. Insertable-B-layer (IBL)[116] added in Run 2 provides excellent spatial

resolution for tracking and vertex reconstruction, and its radiation hardness matches the LHC requirements. The current ATLAS Inner Detector (ID) works excellently to provide precision charged particle trajectories and vertices reconstruction with high efficiency, but these characteristics don't match the requirements for High Luminosity LHC which is scheduled to start after long shutdown 3 in 2024. In terms of the radiation damage current ID PIX is designed for 400 $fb^{-1}$ , ID SCT is designed for $700fb^{-1}$ , IBL is designed for $850fb^{-1}$ , but HL-LHC should deliver 4000 $fb^{-1}$. For bandwidth saturation, ID is designed to accommodate average number of pile-up interactions per bunch crossing $< \mu > \sim 50$ at $2 \times 10^{34}$ $cm^{-2}s^{-1}$ . But the HL-LHC goes to $< \mu > \sim 200$ at $7.5 \times 10^{34}$ $cm^{-2}s^{-1}$. For detector occupancy, finer granularity is required to keep ITk performance at the same level as current ID. Fluences will go up to $2 \times 10^{16}$ MeV $n_{eq}/cm^2$ and new sensor and Front-end design requires more radiation hardness. Also, faster readout and more storage needed to support Level1 track trigger. For these reasons, a lot of dedicated studies are needed for Internal Tracker (ITk) upgrade.

To cope up with the situation, ATLAS inner detector will undergo a major upgrade and it will be replaced with an all silicon tracking detector during the long shutdown 3. The 5 innermost layers of the Inner Tracker (ITk) will be comprised entirely of silicon pixel sensors.

Out of many different pixel technologies, we have been interested in two technologies: hybrid pixel modules (baseline), and monolithic pixel modules (option for the outer barrel layer).

The basic unit of the pixel detector is a module. A module is a rectangular active device with thousands of pixels in it. The two main ITk pixel prototype modules under study are based on two different types of chips: FEI4 and RD53A.

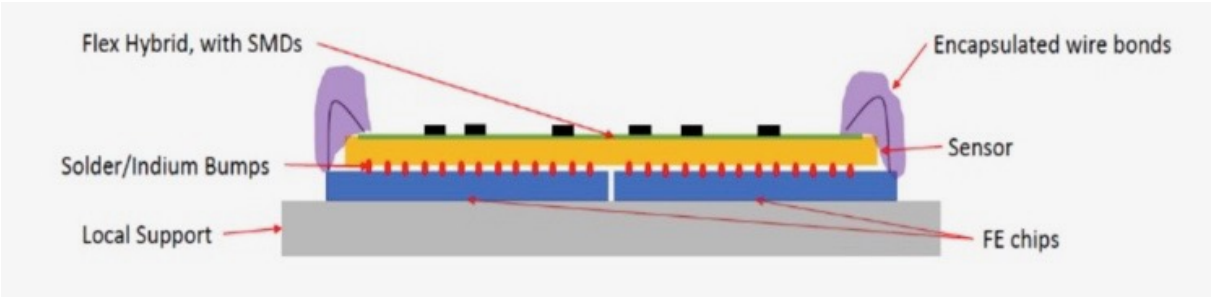


Figure III.2: Schematic design of a hybrid pixel module [17].

The FEI4 modules have been used in ATLAS IBL[116]. The FE-I4 integrated circuit consists of a readout circuit with 26880 hybrid pixels arranged in 336 rows and 80 columns on $50\mu m$ pitch and $250\mu m$ pitch respectively [125].

In FEI4 design, Sensors are DC coupled to FE-I4 with negative charge collection. Each FE-I4 includes an independent, free running amplification circuit with adjustable shaping, followed by a discriminator with independently adjustable threshold.

The RD53A modules[126] have also been designed and produced recently by joint ATLAS-CMS effort (RD53A collaboration). RD53A modules have pixel size of 50 ×

$50\mu m^2$ ($25\times100\mu m^2$) and three different front-ends: 1. Synchronous FE (128 Columns from 0 to 127), 2. Linear FE (136 Columns from 128 to 263) and 3. Differential FE (136 Columns from 264 to 399). RD53A will be used in the ATLAS ITk detector. Many different studies have been done with these two kinds of ITk-pixel modules.

### III.2 Pixel Module Assembly

The pixel module assembly, the efficient technique of joining a flex hybrid and pixel sensor has been one of the important tasks for ITk pixel upgrade. Both ATLAS collaboration and Argonne National laboratory have investigated various module assembly methods, including 1. Robotic glue dispenser, 2. Stamp method, 3. Rice paper method. I was involved in the studies with the 'Rice paper method'.

Figure III.3: The rice paper assembly method uses a vacuum sealed bag to apply even pressure to the flex cable and sensor hybrid. A rice paper piece that has been cut to the correct dimensions and infused with adhesive is sandwiched between the two. The grid paper shown is a thick, clean room safe paper that is cut to align the sensor hybrid in place.

Rice paper method developed by Iliya Tsurin at the University of Liverpool uses a high precision automated paper cutter to cut $50\mu m$ thick Amplitude C6-99 rice paper pieces that are infused with epoxy, positioned in between the flex and the sensor. The three layers are compressed together inside a vacuum sealer bag.

The precision paper cutter is used to cut pieces that are used to align the sensor for assembly. Applying the epoxy to the rice paper is done with a small foam roller with

Figure III.4: Paper cutter machine used for Rice paper method

another dry roller to remove any excess. The entire assembly process takes less than 1 min to assemble and vacuum seal a module, and preparing the paper cutouts requires an additional 2 minutes per module after the required patterns have been developed. The price of the paper cutter and vacuum sealer combined with required accessories is less than $400. An alignment tool machined from aluminum was required for each module assembled in parallel which cost $300 each.

We repeated this assembly procedure at Argonne National lab and the results looked similar to other two methods.

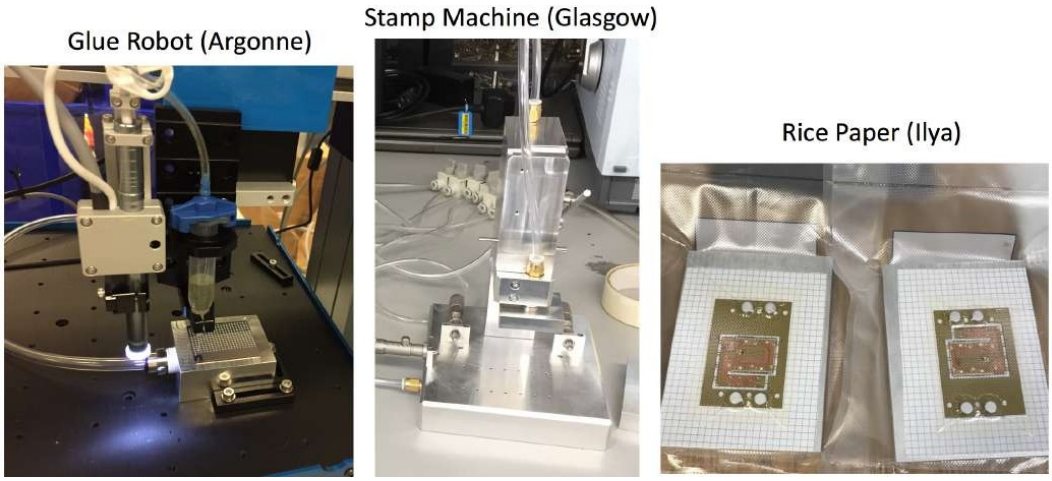


Figure III.5: Three methods of module assembly used at Argonne

| | Rice Paper Method |
|---|---|
| Trial 1 | 80 mg |
| Trial 2 | 90 mg |
| Trial 3 | 70 mg |
| Trial 4 | 80 mg |
| Mean | 80 ± 7 mg |

Table III.1: Measurements of the mass of the glue deposited for different trials while using rice paper method. The mean is quoted with the sample standard deviation [4].

### III.2.1 Peel test

This study addressed the properties of adhesives of epoxy used for the module assembly. To examine the strength of different assembly methods, peel tests have been performed with a device typically used to test tensile strength of metals by pulling test units apart at a constant rate and monitoring the force exerted with an electromechanical load cell. For each assembly method two proxy samples were made using glass cut to the same size as a quad module to simulate the sensor and kapton to simulate the flex cable. These two materials are assumed to be similar in properties to the materials adhered together in an actual module, thus giving a good proxy for performing meaningful peel tests. The peel tests are performed by pulling the kapton at a 90 degree angle to the glass at a constant rate of 1 inch per minute. The three methods gave very similar results with strengths in a range from 0.14 N/mm to 0.17 N/mm.

### III.2.2 Glue deposition repeatability

The amount and repeatability of glue deposition is an important metric to consider during module assembly to ensure uniformity across all units. To quantify it, the difference of the mass before and after glue deposition was measured for four modules of each method. The results of these measurements are compiled in Table III.1 along with rice paper method's mean and sample standard deviation. The measurements were performed using a balance with ±5 mg resolution.

### III.2.3 Rotational alignment

In order for wire bonding to be performed autonomously the relative rotation between the flex cable and sensor hybrid should be minimized as much as possible. Initially a tolerance goal of 1.25 mrad was pursued and achieved, but during optimization it was found that alignments of less than 2.50 mrad was also bondable due to fiducial in-situ correction of the wire bonder. The measurements were performed using the mounted camera on the EFD nordson fluid dispenser. An estimated systematic uncertainty of 0.2 mrad is estimated from the camera resolution for each datum. Table III.2 compiles the results of each measurement along with the mean and sample standard deviation for each assembly method.

| | Rice Paper Method |
|---|---|
| Trial 1 | 0.30 mrad |
| Trial 2 | 0.50 mrad |
| Trial 3 | 0.48 mrad |
| Trial 4 | 1.55 mrad |
| Mean | 0.71 ± 0.49 mrad |

Table III.2: Measurements of the relative alignment between the flex cable and the sensor hybrid for different trials have been shown. The uncertainty quoted is the sample standard deviation. The measurements were performed with an optical device with estimated resolution of 0.2 mrad [4].

### III.2.4 Profile thickness

One of the most critical measures of module assembly, along with relative rotation of the flex cable and sensor hybrid, is a uniform and repeatable thickness of the adhesive layer. Large variations in module thickness can make wire bonding the flex cable to the ASICs difficult and fully automated wire bonding impossible. For this comparison study four modules of each method were measured with a non-contact visual measurement tool with a precision of ±2 µm. Each module was measured by first constructing a Z datum plane level with the top of the ASICs, and then measuring a series of 40 points spaced 1 mm apart along each of the six wire bond rails along the flex cable edges for a total of 240 thickness measurements per module located preferentially where wire bonds will be made. The measurement locations are shown visually in Figure III.6 below, and the distributions for all measurements of each method are shown in Figure III.7 below. Each method was found to have fairly equivalent adhesive thickness of approximately 25 µm with a standard deviation of 33 µm after accounting for the 350 µm flex cable and 100 µm sensor dummy.

### III.2.5 Wire bond strength

Wire bond pull strength was measured for each assembly method using a counter-weight driven wire bond pull test device. All wire bonds exhibited a pull strength of (7 ± 0.2) g which is consistent with the resolution of the measurement device. The wire bond pull strength was more of a function of the quality of flex cable used than the method of gluing the sub assembly together. Earlier tests with a lower quality flex cable showed wire bond pull strengths of $< 5$ g.

### III.2.6 Wire bond yield

After each of the quantitative measurements have been completed, wire bonding is performed for each assembled module. This is the critical process that electrically joins the flex cable with the ASIC. This process is challenging as the module thickness is non uniform and contains localized bumps of greater thickness, the adhesive can become pushed out from between the flex cable and sensor and cover the bond pads of the ASICs, the flex cable is not securely held down to the sensor in certain areas, and

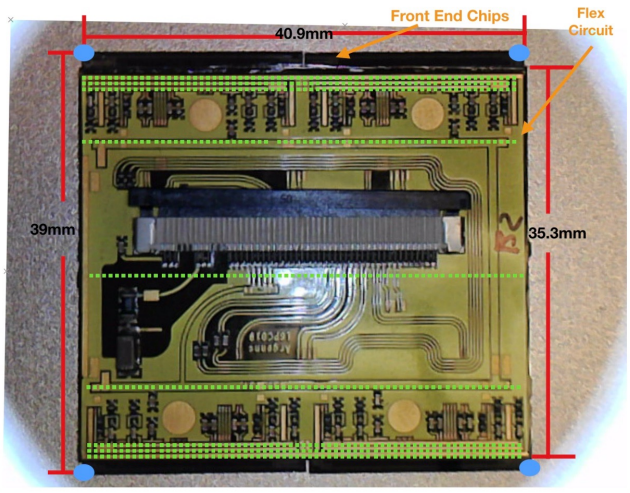


Figure III.6: Diagram of the profile thickness measurement locations. Each green square represents a measurement point, and the blue ovals represent the points used to construct a Z datum plane. The six rows of measurements nearest the edges are used to fill the histograms in next Figure .

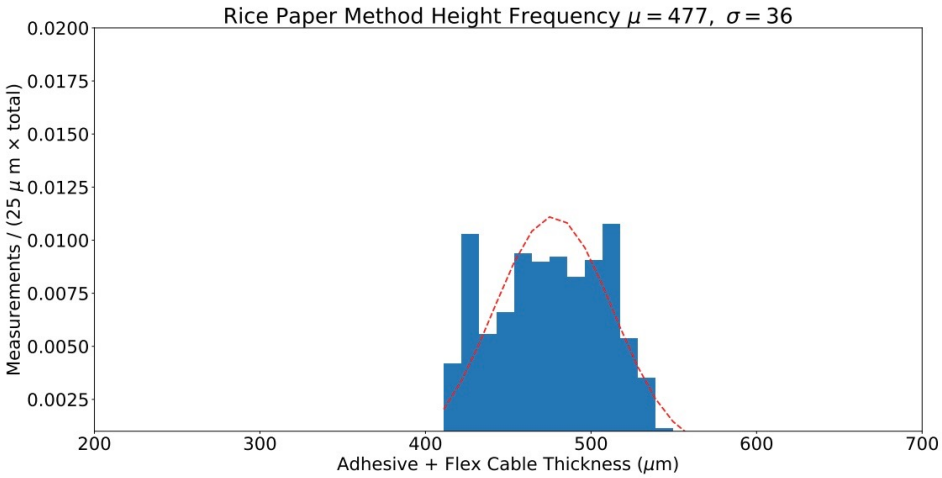


Figure III.7: Thickness distribution for rice paper method.

misalignment between the flex cable and sensor hybrid. The yield of the wire bonding process, calculated as ratio of successfully bonded ASIC chips to those attempted, is shown in table III.3 below for rice paper method. In total, wire bonding was attempted on five modules built with the robotic method, three with the stamp machine method, and six with the rice paper method. The most likely cause of failure in terms of number of ASICs unable to wire bond is also tabulated. There exists clear areas of optimization for each method that will increase wire bonding yield.

| | Rice Paper Method |
|---|---|
| ASIC bonding yield ratio | 22/24 |
| Bonded fully automatically | 12 |
| Bonded with technician aid | 10 |
| Failures due to epoxy on ASICs | 0 |
| Failures due to insufficient epoxy | 2 |

Table III.3: Ratio of successfully wire bonded ASICs and origin of failures have been shown in table. Technician aid refers to either injecting small amounts of extra epoxy around the edges/corners or performing in-situ alignment corrections

| | Stamp Method | Rice Paper Method | Robotic Method |
|---|---|---|---|
| Peel strength | 0.155 ± 0.005 N/mm | 0.155 ± 0.015 N/mm | 0.17 N/mm |
| Glue mass | 35.0 ± 5 mg | 80 ± 7 mg | 90 mg |
| Rotational alignment | 1.69 ± 1.09 mrad | 0.71 ± 0.49 mrad | 0.96 ± 0.70 mrad |
| Profile thickness | 475 ± 31 µm | 474 ± 34 µm | 477 ± 36 µm |
| Wire bond strength | 7.0 g | 7.0 g | 7.0 g |
| Relative difficulty (1-5) | 3 | 1 | 3 |
| Time estimate | 5 min / module | 1 min / module | 6 min / module |
| Setup cost | $ 6,200 | $ 400 | $ 18,166 |
| Cost per modules assembled in parallel | $ 6,200 | $ 300 | $ 1000 |
| ASICs successfully wire bonded | 6/12 | 20/24 | 16/24 |

Table III.4: Comparative results of the three methods of module assembly[4].

### III.2.7 Time estimate

The setup time is estimated to be approximately equal across each method and less than one hour. The time spent per module for each method is on the order of minutes. For this study the epoxy was allowed to dry for 14 hours, which by comparison leaves the time spent for each assembly technique negligible by comparison.

### III.2.8 Comparative summary

The summary of different quantitative measurements are shown below in tabular form:

We can conclude that while rice paper method is very cheap, it has some disadvantages. Since it is not known how paper will behave inside the detector, we don't want to put paper inside. Also, frayed paper and dust particles near edges of the sensors may cause problems.

The rice paper method currently uses a clean-room safe construction paper for the alignment of the sensor. This may still be a little too thin and the method may benefit from a thicker paper used for sensor alignment.

The statistics of the study were low, especially for the measurement of the rotational alignment of the flex cable to the sensor hybrid where the measured values are close to the estimated maximum allowed specification. Modules should continue to be assembled and measured in order to learn more about this vital characteristic of the process[4].

### III.3 Argonne Telescope at Fermilab Test-beam

Tracking telescopes are very useful to perform test beam studies. By following the design of a similar beam telescope developed by University of Geneva[127], Argonne National Lab's group also installed a new pixel telescope in section 1B of Fermilab test beam facility (FTBF) as a permanent setup. The purpose of the telescope is to do research and development of ATLAS pixel data acquisition systems. In the experimental setup we have tested different types of pixel sensors. High voltage CMOS sensors, a candidate technology for the ATLAS Phase-II ITk Pixel Upgrade and a top candidate for future experiments has been the first device under test (DUT).

A standard CMOS process is modified to provide a deep n-well with high resistivity that can be biased to form an active region sensitive to charged particles. The ATLASPix1 CMOS sensor is a fully monolithic pixel module as shown in Figure III.8. It requires an independent DAQ system and was thoroughly evaluated for the first time at the Fermilab Test Beam Facility. The baseline pixel module for the ATLAS Phase-II ITk Pixel Upgrade uses a newly designed front-end read-out chip. The first prototype version, the RD53A, was fabricated in late 2017 and the first modules available in the spring. These modules were used to develop the DAQ system in order to integrate with the telescope.

I was involved in installation of a new beam telescope 'APOLLO' at the Test beam facility at Fermi National laboratory. in site MTest 1B. That's a FE-I4 telescope for particle tracking in test beam experiments. The purpose of setting up this experiment at Fermilab has been to be able to do many different tests for the High Luminosity LHC upgrades for ITk-pixels. The only other such facility to do such tests in the United States is located in Stanford Linear Accelerator Laboratory (SLAC).

The beam at Fermilab has 120 GeV protons; 8-60 GeV pions ; 1-32 GeV pions, kaons, electrons, muons etc. Rate is around 100kHz, 4.2 second spills every minute and up to 3 Million particles per spill. Beam spot size varies from 1 cm to 4 cm.

Some of the characteristics of the experimental setup of the ANL telescope are : 1. The telescope contains 6 Si pixel sensor planes; same modules have been used in Insertable B Layers; 2. The six planes of planar silicon sensors have 250 $\times 50\mu\ m^2$ pitch, read out by ATLAS FE-I4 chips; 3. It uses front and back planes coincidence for a trigger; 4. It also uses HSIO RCE, cosmicGUI for DAQ etc.; 5. The telescope also uses a DUT box (cold box); 6. Relatively easy to integrate any sample mount into the system Cold Box; 7. Chiller fluid flows at -50 $^0$ C (potentially it can go up to -70 $^0$ C if needed); 8. Continuously dry air is supplied. We also have remote monitoring system to control temperature and humidity.

Telescopes two arms in the front and back has three FE-I4B AC-coupled pixel modules. Each module is made of planar silicon pixel sensor[116] readout by four FE-I4 chips.

Each sensor is read out by two FE-I4 chips, of which only one is active for data taking. For processing data, thresholds are set globally with local corrections applied per pixel by Digital to Analogue Converters (DACs). The deposited charge is stored as a 4-bit Time over Threshold (ToT) signal clocked at 40MHz, the nominal bunch crossing frequency of the LHC. Detected hits and 8-bit timestamps are stored in

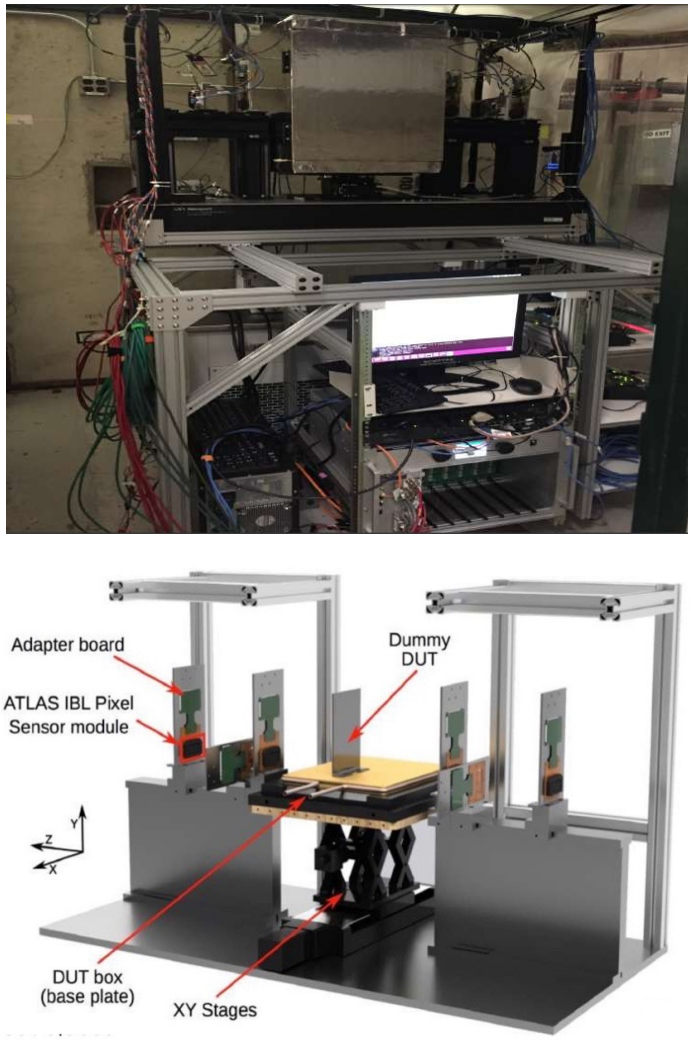


Figure III.8: Design of Argonne telescope at Fermilab

memory cells shared by four pixels, that are read out following a trigger signal. This design allows for a hit rate of up to 400MHz/$cm^2$ . While recording raw data, it records very basic variables like the number of hits in the pixel module, time over threshold, hit distribution along X and Y axis of pixel, charge etc. Later on they are processed using complicated software that reconstructs the data so that it is possible to analyze and to evaluate the performance of the modules, chips etc.

For the data acquisition system, a telescope plane consists of high speed input output *II* (HSIO *II*) [128] board with reconfigurable cluster elements (RCE) and an additional DAQ computer.The HSIO with its front-end electronics receives the data from the telescope planes and is also able to use triggers and clock. The data received by HSIO are stored in the DAQ computer in a form of histograms. Graphical GUI at the DAQ computer helps to visualize the data and also helps to tune different parameters while taking data.

Figure III.10 shows the PixX and PixY distributions in the raw data recorded by telescope planes. Right plot PixX provides the distribution of hits along the X axis

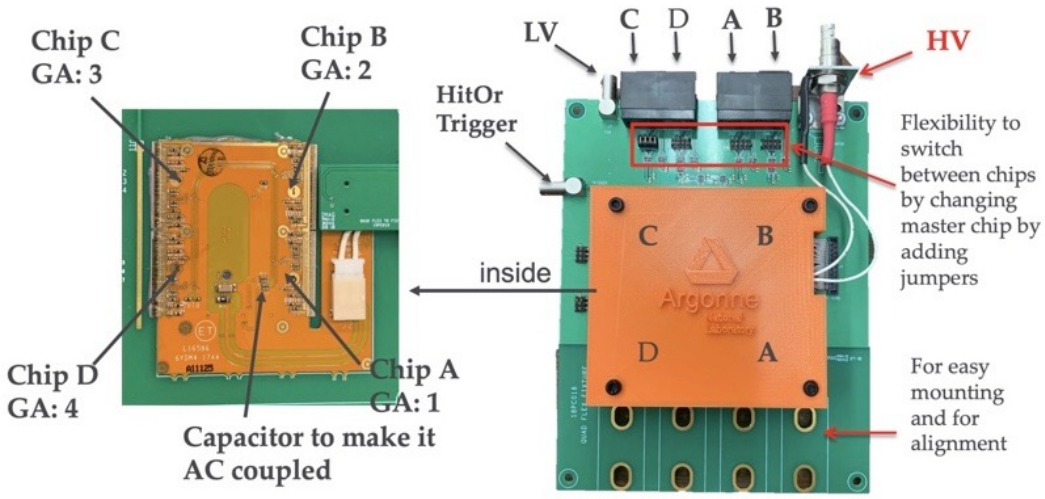


Figure III.9: Wirebond connection between flexible PCB and Module.

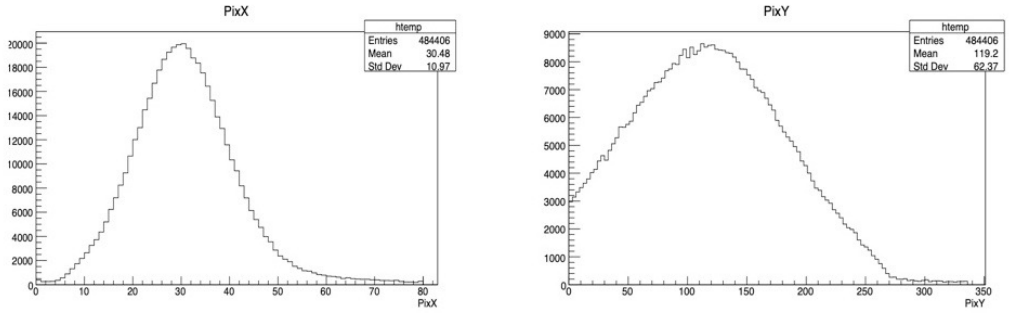


Figure III.10: PixX and PixY distribution in the raw data.

of the pixel. It also tells at which value of X we get maximum hits. Similarly PixY provides the distribution of hits along the Y axis of the pixel. It also tells at which value of Y we get maximum hits.

For testing any module in the telescope, the irradiated sample (device under test, DUT) needs proper cooling. For this, DUT is placed in a special cold box where temperature of -15 degree Celsius has been reached. At the same time the humidity inside the cold box should also be checked as it needs to be very low.

While data taking it is important to ensure all the six planes are properly aligned. To check alignment one of the methods is producing correlation plots between the subsequent planes. First and the sixth planes are also connected. So, it is important to check correlation between them as well. Linear relationship will ensure, beam is going through all of them properly.

In III.13, it can be seen that between all the different subsequent planes and among first and last planes there are linear correlations which ensure good alignments of the planes of the telescope.

Three different pixel modules were tested at the Fermilab test beam facility with proton beams of 120 GeV. FEI4, Monolithic CMS- ATLASPix[129] and RD53A mod-

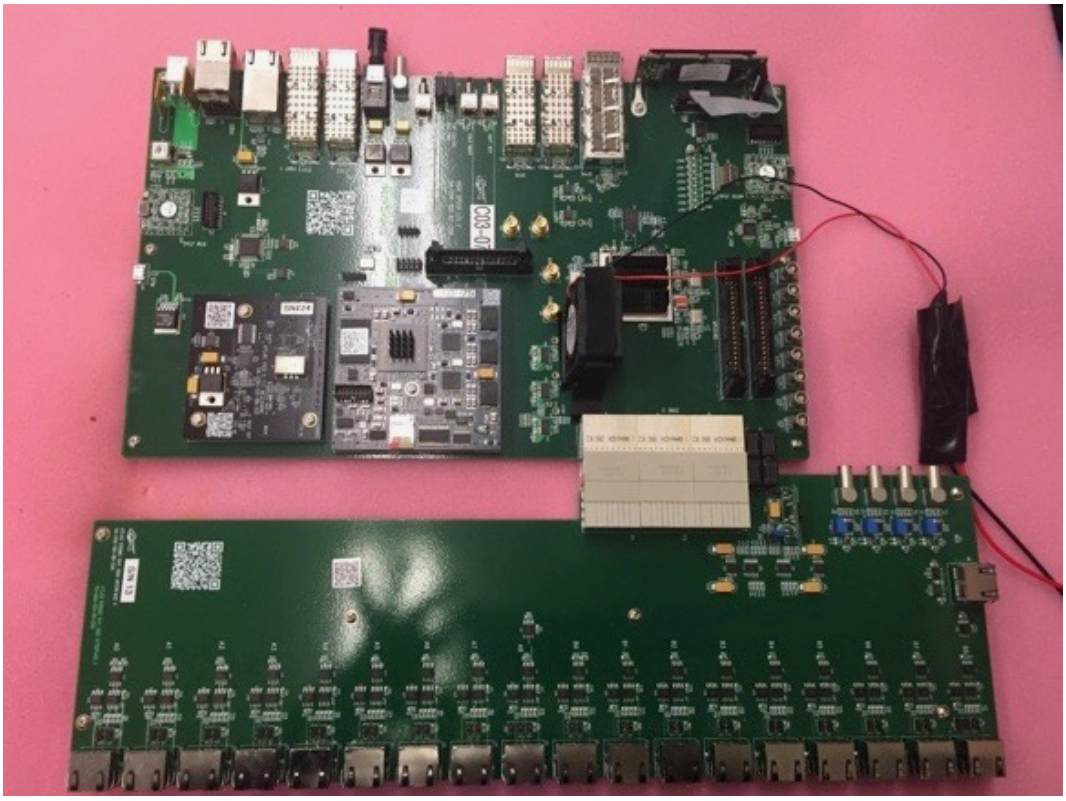

Figure III.11: HSIO *II* and the RCE which are used for data acquisition.

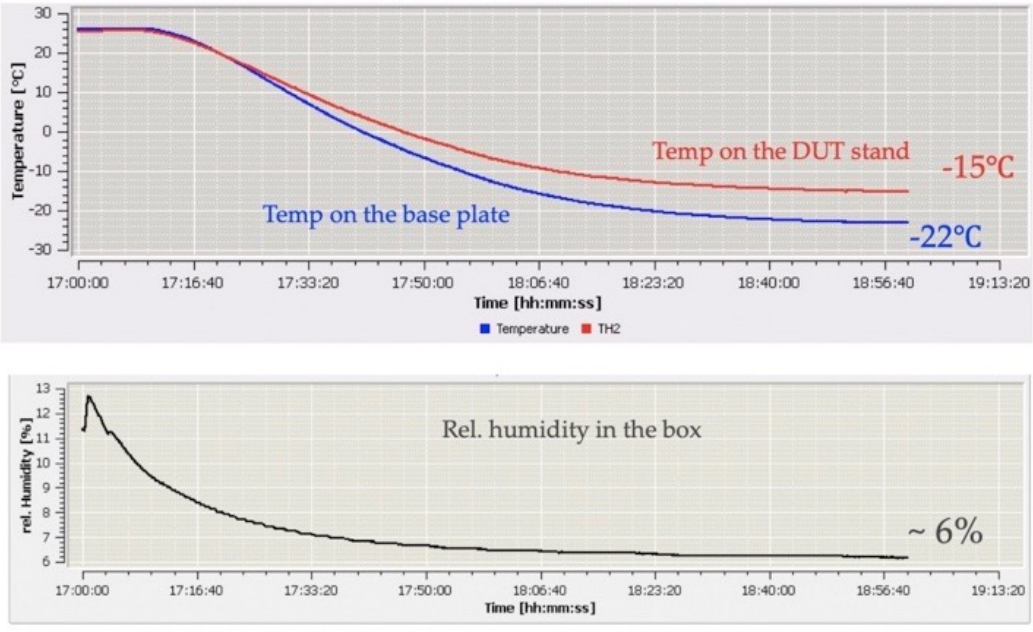


Figure III.12: Temperature and humidity distribution inside cold-box for DUTs.

ules have been studied extensively.

The studies are still ongoing at Fermilab and results will be published as research

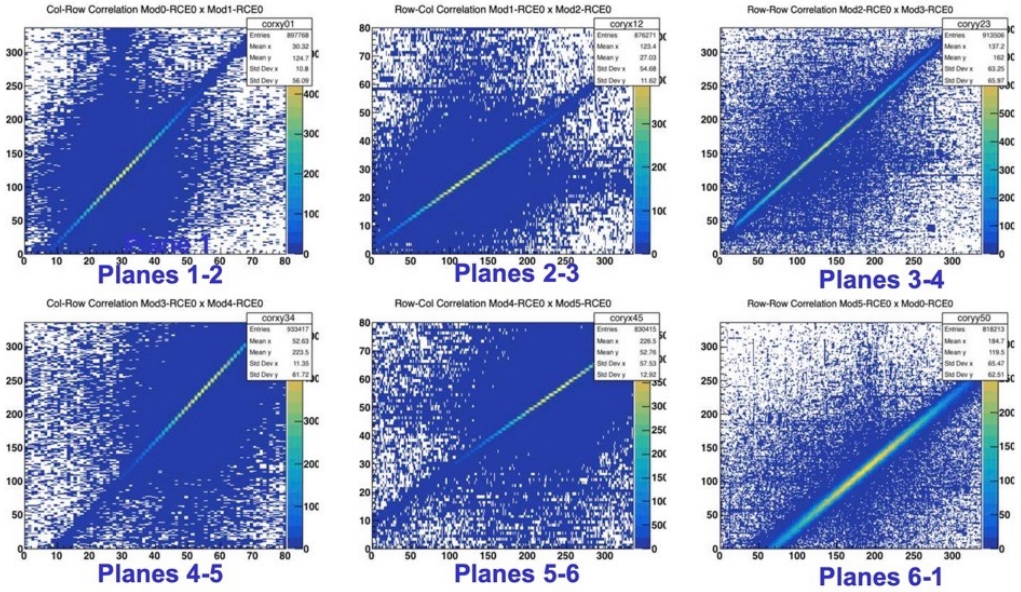


Figure III.13: Beam correlation between different planes while using FEI4 modules.

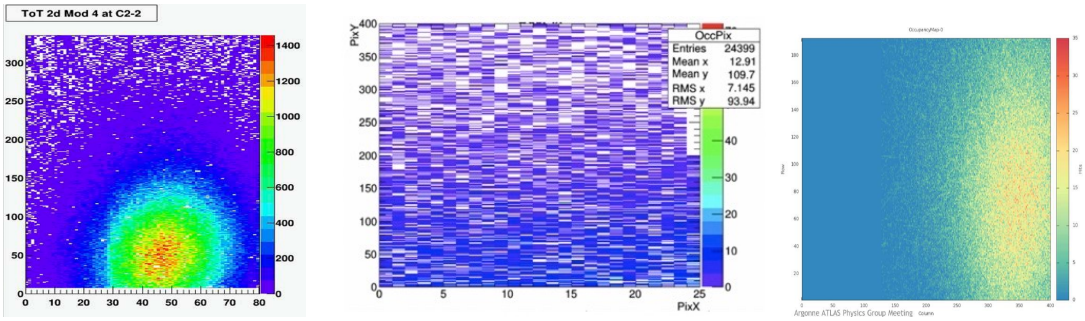


Figure III.14: Beam spots with our experimental setup with three different pixel modules. The left plot is withFEI4 module, the middle plot is with ATLASPix module and the right plot is with the RD53A module.

papers once more tuning with alignments are done and data analysis is complete.

We have been running experiment T1224 at Fermilab Test beam facility with the purpose of preparing the ATLAS Inner Tracker (ITk) for Pixel Phase II Upgrade [130, 131, 132].

### III.4 Tool developments with 3D printer

3D printer gives us more freedom to design various construction elements and to print them in the lab at very low cost. For our experiment at Fermilab, with the Argonne national lab's 3D printer (Raise 3D N2 plus), I developed different components of our experimental setup. For 3D printing, first step is to make proper designs of the complicated systems, then processing the designs through proper softwares and do the printing.

Figure III.15: Printing steps with 3D printer

| Filament type | Diameter | Temperature(in Celsius) | Printing time of PCB cover | Cost(in $) |
|---|---|---|---|---|
| PETG | 1.75 mm | 220-250 | 11 hours 20 min | 5.2 |
| PLA | 1.75 mm | 180-210 | 11 hours 23 min | 1.82 |
| Polymaker | 1.75 mm | 190-235 | 9 hours 41 min | 5.67 |

Table III.5: A comparative table for 3D printing while printing PCB covers.

Proper choice of printing filaments among PETG, PLA, Poly Maker (PC Plus, PC Max, Poly MAX PLA, Poly plus, PolyFlex, Poly Wood, Ply Smooth etc.) is important with different materials have different temperature range and different behavior.

There have been many issues which needed to be dealt properly as observed from my studies. For example: 1. Nozzles of the 3D printer get clogged many times; 2. The temperature difference between filament and print board makes the printed object lose and move, resulting in a mess. So, temperature of the board should be chosen properly; 3. Filaments are broken sometimes, one needs to be careful while changing; 4. Sometimes it needs proper support system to be printed in particular alignment; 5. While removing the printed objects, proper technique should be applied, otherwise they may break.

Over the year, I designed and printed different test stands for our telescope planes at Fermilab, see Figure III.16.

Also, I deigned covers for the telescope planes for different designs of PCB boards to protect the sensors from dust particles, heating etc., as shown in Figure III.17.

Another work I did with 3D printing was to develop a new method for module-assembly other than the three previously discussed traditional methods. The idea was to follow the robotic glue dispenser procedure, but use vacuum pump to pick up the flex by the pick-up tool and put it on the sensor hybrid precisely.

For this development, different models/designs of pick-up tool have been investigated and models were printed using 3D printer (Figure III.18).

Using the vacuum, the pick up tool was able to pick up flex and sensors successfully. But it was not able to hold it for long. More work needs to be done to minimize leakage or to have better vacuum system so that automation can be done for picking up and doing module assembly on large scale by the machine.

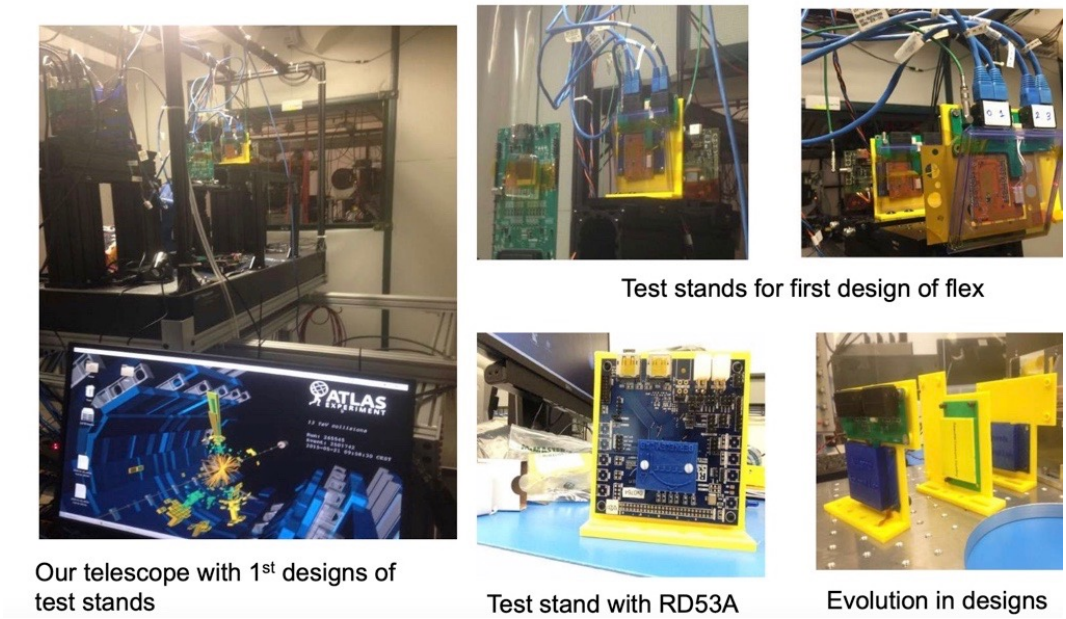


Figure III.16: Examples of telescope plane development with 3D printer

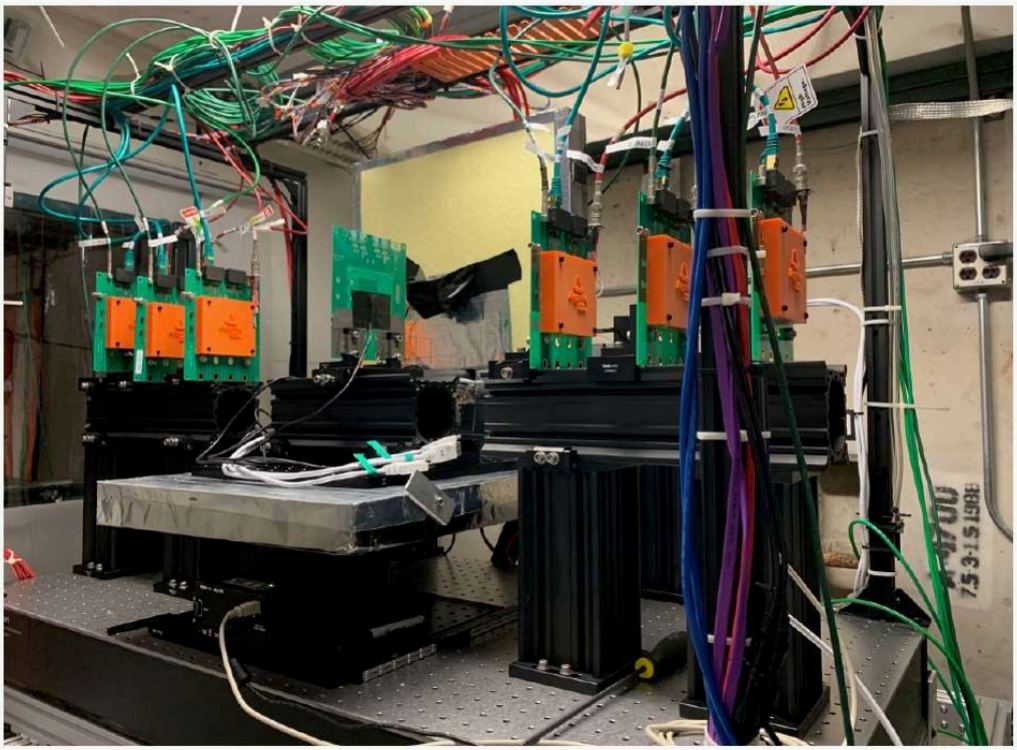

Figure III.17: Experimental setup with 3D printed covers and test stands

### III.5 3D Visualization of the recorded test beam data

At our experiment at Fermilab when we record data with 120 GeV proton beam, it has been our desire to enable 3D visualization of the recorded data. So, there has

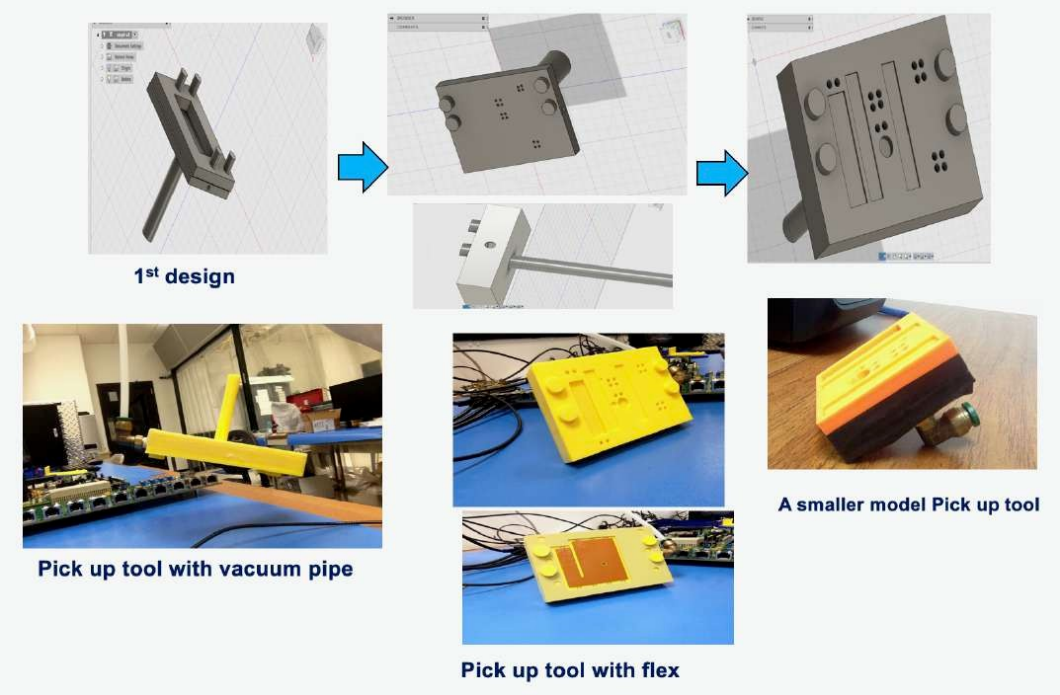


Figure III.18: Development of a new method for module assemble with 3D printer

been effort by a previous undergrad student Evan Cheng (Univ. of Michigan) to enable 3D visualization of particle tracks at different telescope planes of our setup. I further developed the 3D visualization codes to add more features.

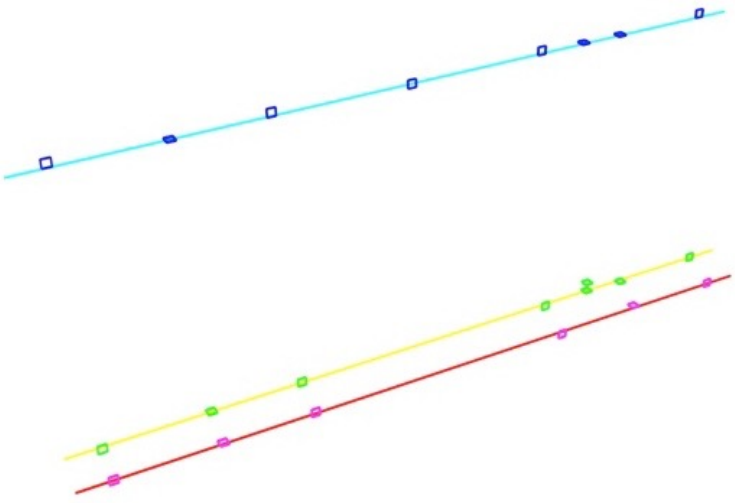

Figure III.19: Example 3D visualization of 3 tracks passing though different planes

In Figure III.19, rectangles are representing different planes and different colors represent different tracks which are passing through the telescope planes.

Since time over threshold (ToT) gives scopes to do comparative studies with different energies, it has been our interest to do 3D visualization with ToT for different planes.

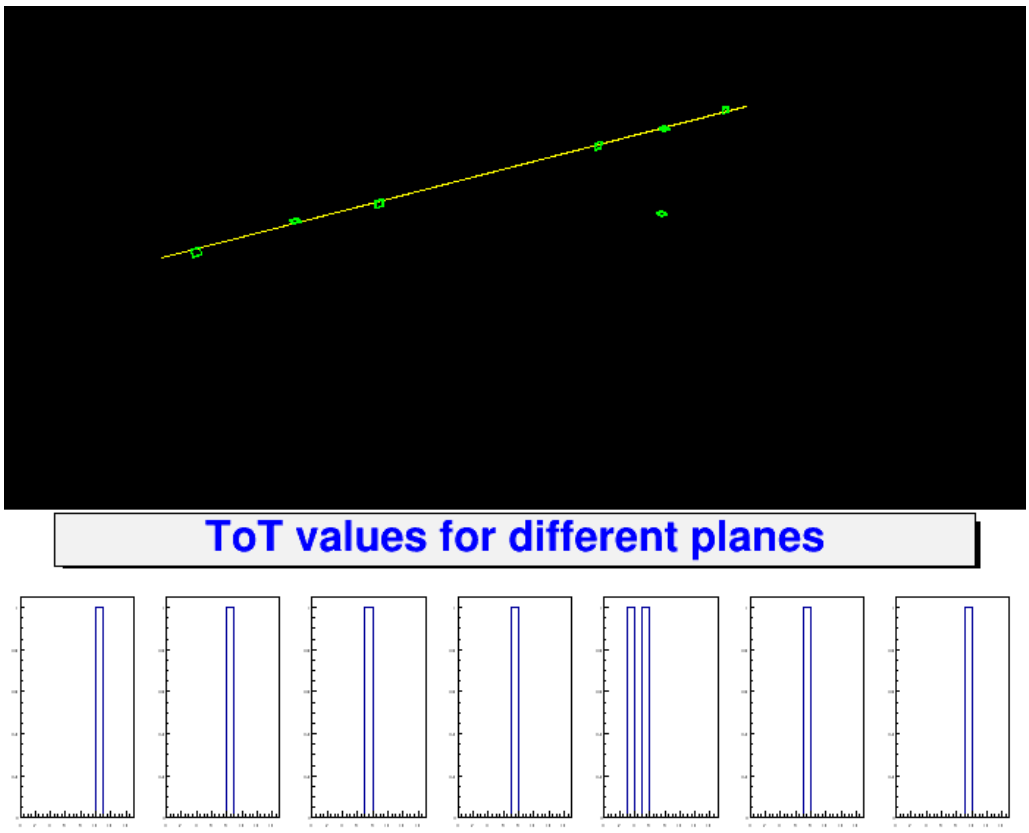


Figure III.20: Example 3D visualization of ToTs with different planes

Figure III.20 provides a good example for 3D visualization of ToTs with different planes.

### III.6 Conclusions

This section summarizes the work on ITk pixel upgrade R&D studies which I performed along with Argonne National Lab group. I investigated different techniques for Pixel-Module assembly, which is important for mass production and assembly of pixel modules before the start of the HL-LHC. ANL beam telescope at Fermilab, which I helped to install and commission throughout one year using 120 GeV proton proton collision, provides opportunities to test the performance of different pixel sensors to understand their possible performance at the LHC. It should be noted that the studies I participated in are part of continuous R&D effort to be prepared for the HL-LHC upgrade. The upgraded pixel detector at the HL-LHC is supposed to provide better performance in tracking and reconstruction of collision events, so that the physics results including the different searches and measurements can be done smoothly at high luminosity in high pileup environment.

# CHAPTER IV

## Development of Direct tag Lightjet Calibration method

> A programmer is ideally an essayist who works with traditional aesthetic and literary forms as well as mathematical concepts, to communicate the way that an algorithm works and to convince a reader that the results will be correct.
>
> Donald E. Knuth

### IV.1 The method

The efficient identification of jets from bottom quarks ($b$-jets) is one of the most important techniques for many physics analyses at the Large Hadron Collider, including studies of the Higgs boson, the top quark, and searches beyond the Standard Model. For example, Top quarks decay into W bosons and $b$-quarks about 100 percent of time, Standard Model Higgs boson predominantly decays into $b$-anti $b$-quark pairs and many searches for new physics, e.g. supersymmetry, involve final states with $b$-quarks. The developments of b-tagging techniques aims to improve the performance which impacts the Physics results at the LHC. The main physics analysis presented in this dissertation also involves b quarks where Charged Higgs boson decays into a top and bottom quarks. Though some analysis strategies may not require b-tagging, but b-tagging performance studies [133] provide new insights of the analysis.

The $b$-tagging performance is characterized by $b$-tagging efficiency (the probability to correctly identify a $b$-jet) and mistag rate (the probability to misidentify a jet not originating from a B-hadron as a $b$-jet). As the effects causing mistags can be different between the experimental data and Monte Carlo (MC) simulation, it is important to measure the $b$-tagging performance in data and derive the MC correction factors. The $b$-tagging calibration works on the connection of $b$-tagging efficiency and mistag rate for discrepancies between Monte Carlo simulation and data.

How b-tagging works: The long lifetime of hadrons with b-quarks ($1.510^{-12}s$), compared to other particles (e.g. Higgs boson lives for $10^{-22}s$) results in a typical decay topology with at least one vertex displaced from the primary vertex from the hard-scattering collision.

Identification of the b-quark jets is based on distinct strategies encoded in three basic algorithms: An impact parameter based algorithm (IP), an inclusive secondary vertex reconstruction algorithm (SV) and a decay chain multi-vertex reconstruction

algorithm (JetFitter).

The outputs of these algorithms are combined in a multivariate discriminant (MV2) which provides the best separation between the different jet flavors.

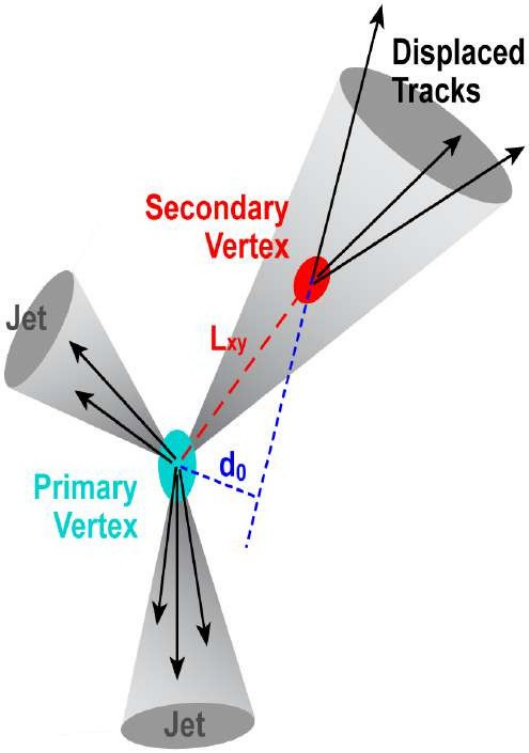


Figure IV.1: Example 3D visualization of 3 tracks passing though different planes

### IV.1.1 Basics of light jet calibration

Mistags occur due to IP and SV resolution, and long lived particles, fakes, interactions in material etc. Mistags due to IP and SV resolution prevails mainly at loose working points and mistags due to long lived particles, fakes, interactions in material etc. prevails at tight working points. The prevalent methods of mistag rate calibration[134] include Negative tag method, MC based method and Direct tag method. Negative tag rate method can only directly measure and calibrate loose working points. But Negative tag rate method is not that much effective at tight working points as they are dominated by MC driven systematic uncertainties.

The light jet calibration performed by the method is done using binned distributions of tag weights for light, c, and b jets (templates). The boundaries between the bins of the templates are chosen to correspond to certain cumulative b-tagging efficiencies obtained on the t samples used for b-tagging efficiency calibration. The reference b-tagging efficiencies are taken to be 0.85, 0.77, 0.70, 0.60, 0.50, and 0.30. Consequently, there are 7 tag weight bins referred to as 100-85, 85-77, 77-70, 77-60, 60-50, 50-30, and 30-0. The light jet tagging scale factors are derived for each of these bins and are assumed to stay constant within the bins. This type of calibration is known as pseudo-continuous, as opposed to truly continuous calibration where the

scale factors are smooth functions of a tag weight. It allows fairly straightforward conversion to and from the fixed cut calibration, provided the bin-by-bin correlations are properly taken into account.

The tag weight binning in direct tag method is chosen in the same way as it is done for b and c calibration. This allows us to use the scale factors for b and c tagging efficiency obtained by other analyses. The b and c templates used in the direct tag fit are corrected for these scale factors as provided by the standard b-tagging calibration data interface (CDI).

In Direct tag method for fitting, at first b and c templates are obtained from Monte Carlo (MC) simulations. And for the start, light templates are obtained from MC as well to fix the last four bins of lower working points (b tag efficiencies) which correspond to 70-60,60-50, 50-30, 30-0. The first three bins (100-85, 85-77, 77-70) of the light template float in the fit. Data is fitted to a weighted sum of three MC templates (b, c, and light). In Direct tag method, fractions of b/c/light jets are also extracted and the mistag rate and data/MC scale factors are calculated.

For each bin corresponding to different working points, both bin contents and bin Integrals are calculated for both Data and MC where bin Integral is the summation of bin content of that particular bin and the bin contents of all the bins having lower working points. By calculating the ratio of bin content of Data and MC, Scale Factor is calculated for every bin by bin and similarly by calculating the ratio of bin Integral coming from Data and MC respectively, cumulative Scale factor is calculated for any bin of particular working point.

### IV.1.2 Description of Direct tag method

The light jet calibration performed by the method is done using binned distributions of tag weights for light, $c$, and $b$ jets (templates). The boundaries between the bins of the templates are chosen to correspond to certain cumulative $b$-tagging efficiencies obtained on the $t\bar{t}$ samples used for $b$-tagging efficiency calibration. The reference $b$-tagging efficiencies are taken to be 0.85, 0.77, 0.70, 0.60, 0.50, and 0.30. Consequently, there are 7 tag weight bins referred to as 100-85, 85-77, 77-70, 77-60, 60-50, 50-30, and 30-0. The light jet tagging scale factors are derived for each of these bins and are assumed to stay constant within the bins. This type of calibration is known as pseudo-continuous, as opposed to truely continuous calibration where the scale factors are smooth functions of a tag weight. It allows fairly straightforward conversion to and from the fixed cut calibration, provided the bin-by-bin correlations are properly taken into account.

The tag weight binning in direct tag method is chosen in the same way as it is done for $b$ and $c$ calibration. This allows us to use the scale factors for $b$ and $c$ tagging efficiency obtained by other analyses. The $b$ and $c$ templates used in the direct tag fit are corrected for these scale factors as provided by the standard $b$-tagging calibration data interface (CDI).

In Direct tag method for fitting,at first $b$ and $c$ templates are obtained from Monte Carlo (MC) simulations. And for the start, light templates are obtained from MC as well to fix the last four bins of lower working points ($b$ tag efficiencies) which

correspond to 70-60,60-50, 50-30, 30-0. The first three bins (100-85, 85-77, 77-70) of the light template float in the fit. Data is fitted to a weighted sum of three MC templates ($b$, $c$, and light). In Direct tag method, fractions of $b/c$/light jets are also extracted and the mistag rate and data/MC scale factors are calculated.

For each bin corresponding to different working points, both bin contents and bin Integrals are calculated for both Data and MC where bin Integral is the summation of bin content of that particular bin and the bin contents of all the bins having lower working points.By calculating the ratio of bin content of Data and MC, Scale Factor is calculated for every bin by bin and similarly by calculating the ratio of binIntegral coming from Data and MC respectively, cumulative Scale factor is calculated for any bin of particular working point.

In Direct Tag method, MV2 distribution is directly used and b and c jet MV2 PDFs are obtained from the monte carlo simulations and fixed in the fit. After that the last four bins for the light jet PDF from the Monte Carlo are also fixed.

For example, in Figure IV.2, in the right side three PDFs of b, c and light jets for a particular pt bin can be seen. They have been obtained from the Monte Carlo simulations. And all these PDFs fitted at first to produce a weighted sum of these templates. And after that data is fitted with that weighted sum of templates. The fitting of data and MC can be seen in the top right plot for that particular pt bin. Here 0-1 bin corresponds to 100-85 percent b tag efficiencies, 1-2 bin corresponds to 85-77 percent b tag efficiencies and 2-3 bin corresponds to the b tag efficiencies ranging from 77-70 percent. In these three bins, light jet templates float in the fit. But in the consecutive bins after that, which corresponds to 70-60, 60-50, 50-30 and 30-0 b tag efficiencies light jets are obtained simply from MC, as this Direct method aims to provide light jet calibration mainly for higher working points. At bottom right plot, for different working points the perfection of the fit between Data and MC has been shown. That plot has been obtained by calculating the ration of Data and MC and then subtracting 1 from it.

Starting from the similar process of data production like default negative tag method, several different steps are taken to get the best data to be used by Direct tag method. Proper Calibration Data Interface(CDI) of ATLAS is used, proper reweightings are also applied in $P_T$ and $\eta$ to minimize the discrepancies between data and Monte Carlo.

In Direct Tag method, MV2 distribution is directly used and $b$ and $c$ jet MV2 PDFs are obtained from the monte carlo simulations and fixed in the fit. After that the last four bins for the light jet PDF from the Monte Carlo are also fixed.

## IV.2 Data samples, Monte Carlo simulations and event selection

The data sample used in the negative-tag analysis was recorded using an 'OR' between several prescaled and unprescaled HLT inclusive jet trigger during the year 2015 and 2016.The analysis makes use of the Pythia 8 and Herwig++ multi-jet samples. Once the basic ntuples from btag derivations are obtained, the framework of Negative tag rate method is used to process the ntuples to be used by Direct tag method. The framework includes the steps of dumping the basic ntuples, then applying pt-$\eta$

rewighting, n-track reweighting, and a step which provides readable ntuple for Direct tag. According to previous modelling the data was rewighted due to prescales. And as a part of our study, the rewighting in data was removed later on.

For the version of ATLAS reconstruction software 20.7, adopted in 2016, the Calibration Data Interface(CDI) from 2016 and 2017 recommendations have been used and for the version of ATLAS reconstruction software 21, adopted in 2017, the CDI recommendations from 2017 and 2018 have been used.

### IV.2.1 Reweighting while ntuple production

Discrepancies among data and monte carlo are supposed to have few important reasons. Firstly inside data mixture of triggers are present and those triggers are prescaled for low pt jet. Secomdy inside monte carlo samples, mixture of different samples are present, where the samples are generated for different production cuts. Thirdly the MC doesn't describe the data very well, as in the tracking efficiency, there have been differences in distribution (of number of tracks in jet).

Now to fix thsese issues, while producing the ntuples for Direct tag, some reweighting procedures have been applied. To deal with the first two issues, pt-eta reweighting is applied and to fix the third issue, ntrack reweighting has been applied.

While development of Direct tag analysis, at some point of time reweighting in data due to trigger prescales was introduced. But later on, due to some bad behaviour of results, data reweighting was removed. Some of the control plots after pt-eta reweighting and after both pt-eta and ntrack reweighting can be found in the Appendix section. The control plots before and after removing data reweighting can also be found in the Appendix section.

### IV.2.2 Systematic uncertainties in Direct tag

The systematic uncertainties of Direct tag method are composed of 49 systematic variations. Among those 49 systematics, there has been 3 major categories. The first 30 systematics have been b jet systematics, the next 14 systematics have been c jet systematics. Dominant systematic uncertainty is from right tail of light-jet template (last 5 systematics). Contribution of each systematic toward uncertainty have been extracted in different pt-eta bins with Pythia monte carlo generators.

Following systematics have been used while producing the monte carlo simulations for Direct tag method :

1. FlavourTagging-Nominal, 2. FlavourTagging-JET-EffectiveNP-1-1down, 3. FlavourTagging-JET-EffectiveNP-1-1up, 4. FlavourTagging-JET-EffectiveNP-2-1down, 5. FlavourTagging-JET-EffectiveNP-2-1up, 6. FlavourTagging-JET-EffectiveNP-3-1down, 7. FlavourTagging-JET-EffectiveNP-3-1up, 8. FlavourTagging-JET-EffectiveNP-4-1down, 9. FlavourTagging-JET-EffectiveNP-4-1up, 10. FlavourTagging-JET-EffectiveNP-5-1down, 11. FlavourTagging-JET-EffectiveNP-5-1up, 12. FlavourTagging-JET-EffectiveNP-6-1down, 13. FlavourTagging-JET-EffectiveNP-6-1up, 14. FlavourTagging-JET-EffectiveNP-7-1down, 15. FlavourTagging-JET-EffectiveNP-7-1up, 16. FlavourTagging-JET-EffectiveNP-8restTerm-1down, 17. FlavourTagging-JET-EffectiveNP-8restTerm-

1up, 18. FlavourTagging-JET-EtaIntercalibration-Modelling-1down, 19. FlavourTagging-JET-EtaIntercalibration-Modelling-1up, 20. FlavourTagging-JET-EtaIntercalibration-TotalStat-1down, 21. FlavourTagging-JET-EtaIntercalibration-TotalStat-1up, 22. FlavourTagging-JET-EtaIntercalibration-NonClosure-1down, 23. FlavourTagging-JET-EtaIntercalibration-NonClosure-1up, 24. FlavourTagging-JET-Pileup-OffsetMu-1down, 25. FlavourTagging-JET-Pileup-OffsetMu-1up, 26. FlavourTagging-JET-Pileup-OffsetNPV-1down, 27. FlavourTagging-JET-Pileup-OffsetNPV-1up, 28. FlavourTagging-JET-Pileup-PtTerm-1down, 29. FlavourTagging-JET-Pileup-PtTerm-1up, 30. FlavourTagging-JET-Pileup-RhoTopology-1down, 31. FlavourTagging-JET-Pileup-RhoTopology-1up, 32. FlavourTagging-JET-Flavor-Composition-1down, 33. FlavourTagging-JET-Flavor-Composition-1up, 34. FlavourTagging-JET-Flavor-Response-1down, 35. FlavourTagging-JET-Flavor-Response-1up, 36. FlavourTagging-JET-PunchThrough-MC15-1down, 37. FlavourTagging-JET-PunchThrough-MC15-1up, 38. FlavourTagging-JET-SingleParticle-HighPt-1down, 39. FlavourTagging-JET-SingleParticle-HighPt-1up, 40. FlavourTagging-JET-BJES-Response-1down, 41. FlavourTagging-JET-BJES-Response-1up, 42. FlavourTagging-JET-JER-SINGLE-NP-1up, 43. FlavourTagging-PRW-DATASF-1down, 44. FlavourTagging-PRW-DATASF-1up, 45. FlavourTagging-JVT-effSF-1down, 46. FlavourTagging-JVT-effSF-1up, 47. conversions-1down, 48. conversions-1up, 49. hadronic-1down, 50. hadronic-1up, 51. longlivedparticles.

Contribution of each systematic toward uncertainty have been extracted in different pt-eta bins with Pythia monte carlo generators. The exact contribution of those each sytematics for different working points can be found in the Appendix section.

### IV.3 Direct tag Results

Early studies were done to compare different b-taggers and different working points where MV2c10 (C10 stands for c-jet fraction is of 10 percent) tagger performed better than that of MV2c20 (C20 stands for c-jet fraction is of 20 percent) tagger. In the early results, scale factors deviated significantly from the value 1. Many investigations were done to find out the reason and it was found that some of the bins were affected by track IP resolution. Removal of those bins improved the results. Comparative studies were done with different taggers like BDT based MV2c10 and Deep neural Net based DL1 tagger for different operating points. Template fitting was changed from 7 binning to 5 binning as well, but 7 binning fit still gave better results. Alternative codes have been developed to verify the results of Direct tag method. Results were produced fir different event generators : Pythia, Herwig, Sherpa. Among three of them, results with Pythia turned out to be better than others. Most importantly results were compared to the default method Negative tag, and results were found comparable or better.

The results of Direct tag method can be broken down into different subsections as following :

### IV.3.1 Early results in release 20.7

Early results were produced with the version of ATLAS reconstruction software 20.7 dataset. The results consist of light jet scale factors for different working points, flavor fractions of b and c jets, and tag weight functions in different working points. The scale factors found out to be reasonable and flavor fractions could also be found for b and c jets.

Figure IV.3 shows the distributions which describes the flavor fractions for both b and c jets and it can be see, in ATLAS reconstruction software 20.7, the b jet flavor fraction is competitively better and the simulation explains the distribution well, but in case of c-jets the=re has been some discrepancies between data and simulation.

Figure IV.4 shows the that the bin by bin scale factor improved while using release version of 21. For this comparison, Monte Carlo samples were simulated using Pythia generator. Similar studies have also been done using other event generators such as Herwig and Sherpa and similar improvement in release 21 was reported.

#### Early results : Comparison between MV2c20 and MV2c10

It has been important to verify the performance of Direct tag light jet calibrations on versions of MV2 algorithm trained on different c fractions. Comparisons between MV2c10 and MV2c20 have been made for Direct tag performance.

From the figure IV.5, the comparison between two taggers MV2c20 and Mv2c10 indicate that MV2c20 tagger has way more systematic uncertainties than that of MV2c10. So, it has been decided to move to MV2c10 tagger completely for the further analysis.

### IV.3.2 Early results in release 20.7 and issues

Early results of Direct tag method indicates that Direct tag method is working. But the scale factors were not exactly 1 and specially the Flavor factions of c jets are not good, though flavor fractions of b jets are close to 1.

The flavor fractions produced by Direct tag method has been one of the challenging issues. It can been seen that in case of c jets, the flavor fractions is around 2 and sometimes its even bigger than that.

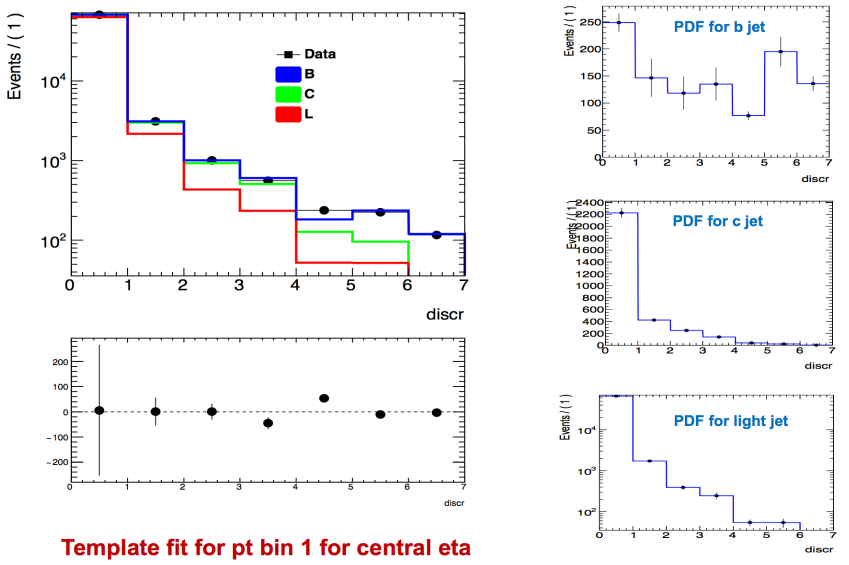


Figure IV.2: Template fit of pdfs of $b$, $c$ and light jets.

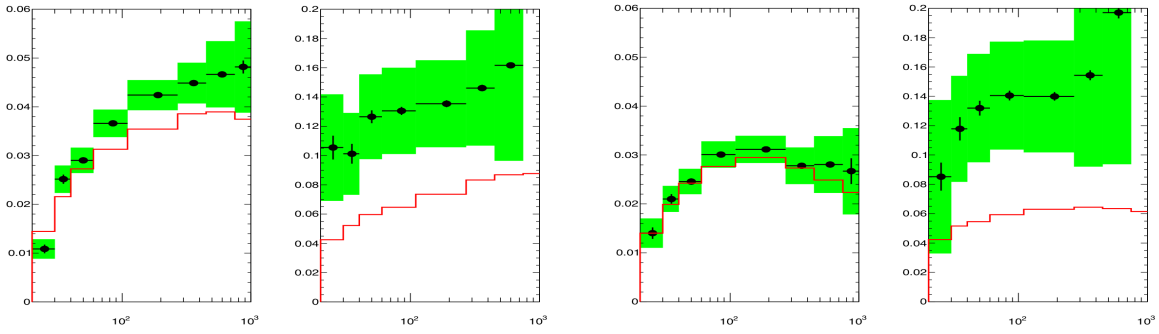

Figure IV.3: Left to right :Flavor Fractions of b (left) and c jets (right) for central (left 2 plots) and forward eta (right two plots) with MV2c20 tagger while using ATLAS reconstruction software 20.7.

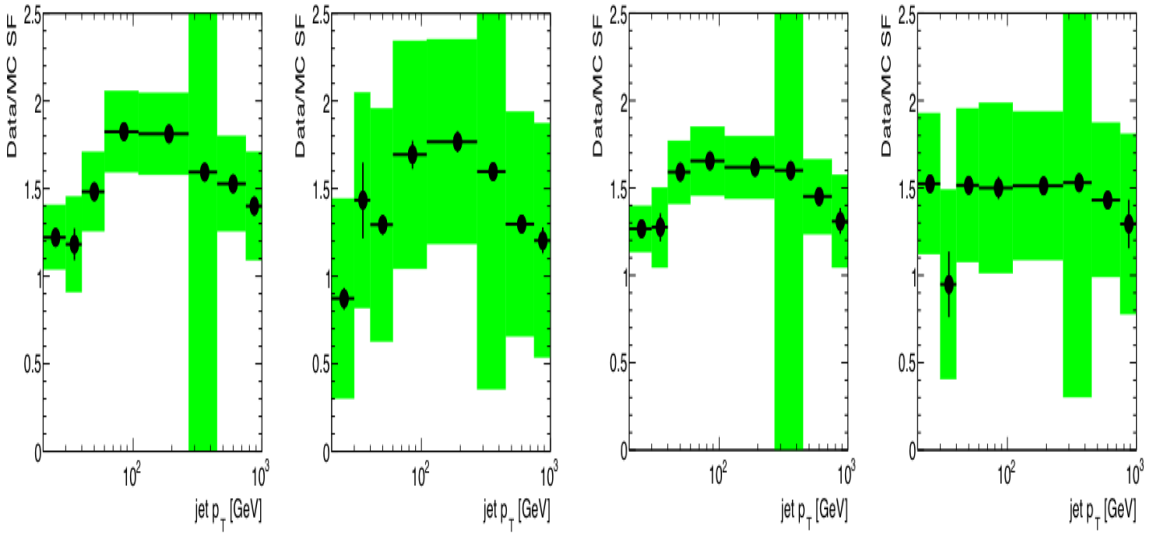


(a) SF 85% with release 20.7

(b) SF 77% with release 20.7

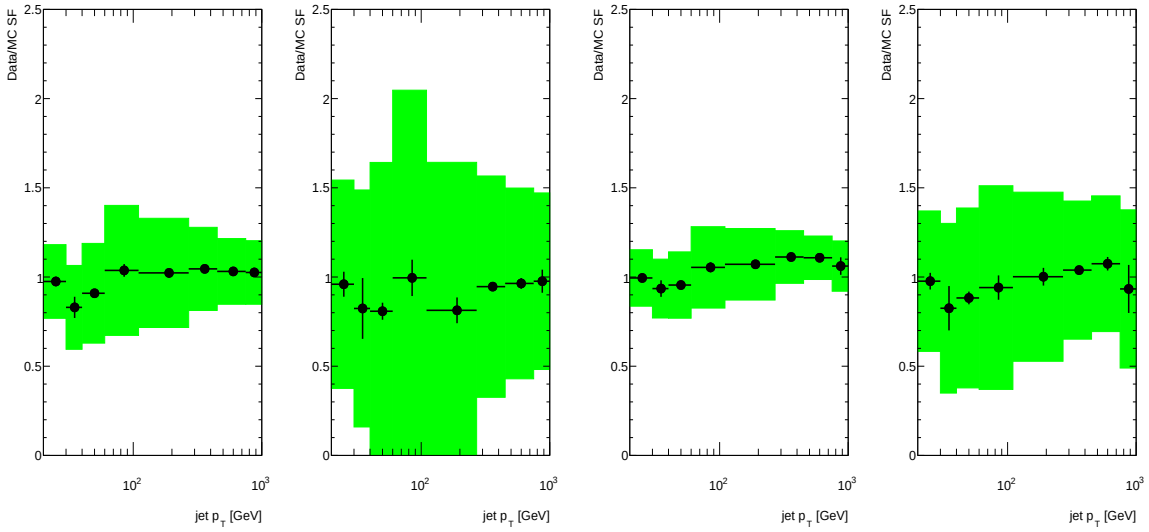


(c) SF 85% with release 21

(d) SF 77% with release 21

Figure IV.4: Scale Factors bin by bin for Pythia in both release 20.7 and release 21 in central (left plots; for SF 85% and SF 77%) and forward (right plots for SF 85% and SF 77%) eta regions.

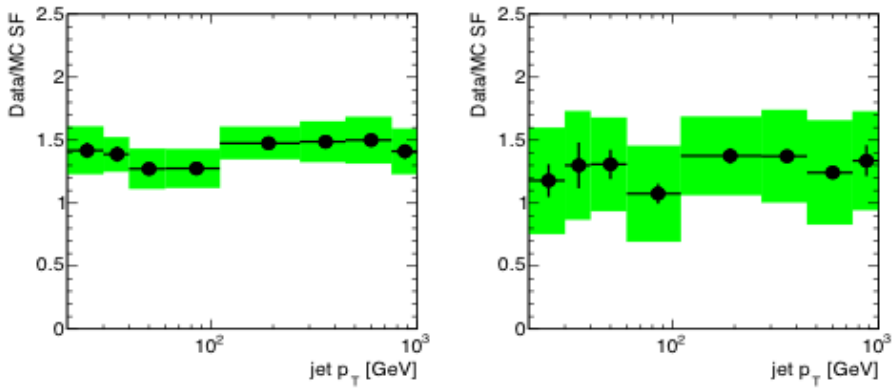


(a) With MV2c20 tagger

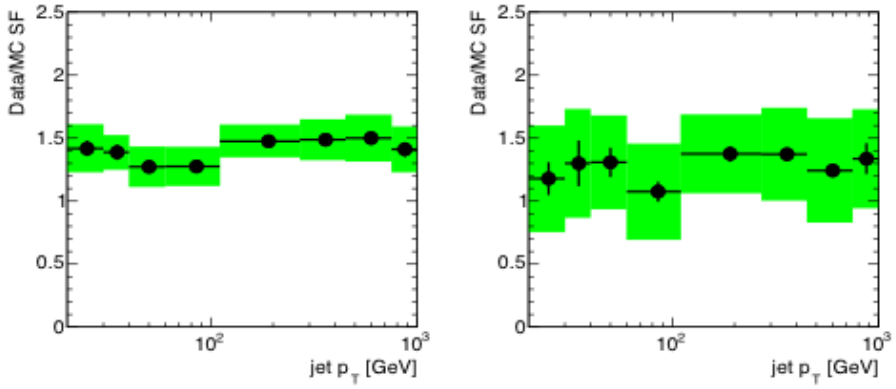


(b) With MV2c10 tagger

Figure IV.5: Scale factors bin by bin at central eta region with both MV2c20 and MV2c10 taggers for SF 85% (left) and SF 77% (right).

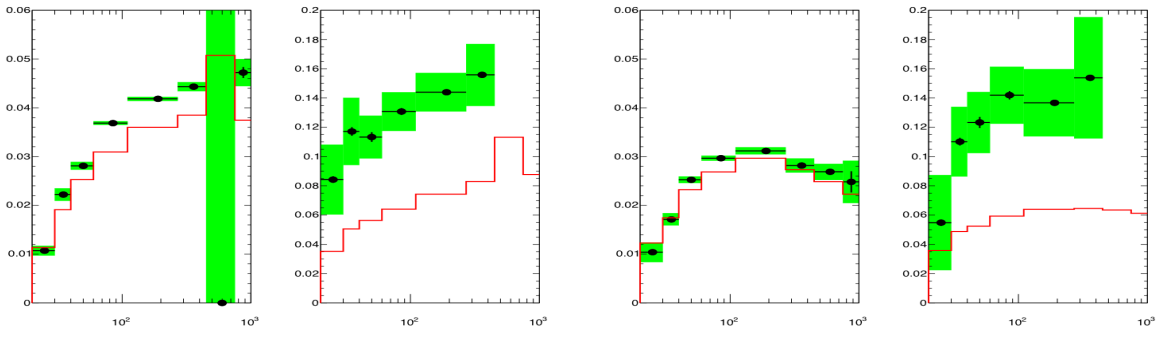

Figure IV.6: Left to right : Flavor Fractions for b jets and c jets central eta and for b jets and c jets for forward eta regions

| weight cuts based on b-tagging efficiencies in reweighed samples | | | | | | |
|---|---|---|---|---|---|---|
| Tagger | 30% | 50% | 60% | 70% | 77% | 85% |
| MV2c20 | -0.160 | 0.472 | 0.744 | 0.904 | 0.964 | 0.996 |
| MV2c10 | -0.240 | 0.312 | 0.624 | 0.848 | 0.940 | 0.992 |
| IP2D | -1.400 | 0.000 | 1.200 | 2.800 | 4.400 | 8.200 |
| IP3D | -1.200 | 0.200 | 1.600 | 3.400 | 5.400 | 9.400 |
| SV1 | -1.400 | -1.100 | 1.700 | 3.700 | 5.150 | 7.350 |

Table IV.1: Comparing different taggers

### IV.3.3 Investigating dependencies of results on different taggers

Unsatisfactory flavor fractions led the questions that whether the discrepancies between MC and data are due to the specific tagger in use or the performance is independent of tagger. To have the answer to that question, 5 different taggers (MV2c20, MV2c10, IP2D, IP3D and SV1) have been investigated.

It has been observed that in case of all the different (above mentioned) taggers, the data/MC ratio is different from 1, and the discrepancies are consistent between various taggers. For b-jet fractions, Data/MC is about 1 at higher jet pT, but below100 GeV it gets very large. For c-jet fractions, Data/MC is about 2 or it goes for even higher values for higher and lower energies.Improper reweighting could be a reason for distortion at low $p_T$. The scale factor plots using different taggers can be found at Appendix section.

### IV.3.4 Investigating discriminators unaffected by track IP resolution

The conclusion from the above exercises was that c fraction is affected by discrepancy in 'track IP resolution' between data and monte carlo. I tried to find discriminators (for b,c and light jets) which are not affected by 'track IP resolution'. There has been good motivations to investigate the low level parameters and inputs for the Multivariate discriminant such as variables associated with JetFitter algorithm and few other variables associated with mass of secondary vertex. The variables which have been studied are the following: JetFitter_N2Tpair , JetFitter_dRFlightDir, JetFitter_energyFraction, JetFitter_mass, JetFitter_nSingleTracks, JetFitter_nTracksAtVtx, JetFitter_nVTX, SV1_N2Tpair, SV1_L3d, SV1_Lxy, SV1_deltaR, SV1_efracsvx, SV1_NGTinSvx, SV1_masssvx, JetFitter_significance3d etc.

From the comparisons of different discriminators, it was found that 'masssvx' or the invariant mass of secondary vertex tracks gives better discrimination with respect to all the above mentioned variables. With only 'masssvx' the ratio of data and monte carlo for all the three b, c and light jets were observed to be 1 or close to 1. So, 'masssvx'has been chosen to be a good candidate.

The study of calculating b, c flavor fractions were repeated for two cases: 1. Including underflow bins (bins affected by bad track IP resolution) 2. Excluding underflow bins. The results of the investigating discriminators unaffected by track

IP resolution and also the results of b, c flavor fractions including and excluding underflow bins can be obtained in Appendix section.

Calculations of b, c flavor fractions were repeated with updated reweighting procedure as well and it has been observed that with proper jet-pt-eta reweighting problems at low-pt were gone; C fraction comes closer to 1 (around 2) compared to MV2c10 fit . And the underflow bin i.e; first bin in the fit (first bin represents jets without secondary vertices, which is still affected by track IP resolution) is excluded, c fraction becomes almost 1.

To deal with some other investigations later on the reweighting procedure for ntuple production has been updated. There has been motivations to see whether those updated reweighting provides better data-monte carlo agreement with different dicriminators. So, with the updated rweighting the same variables were tested again for both the version of ATLAS reconstruction software 20.7 data and release 21 data. Two additional variables IP2D_logpbpu and IP3D_logpbpu are also included this time.

It has also been found that still 'SV1_masssvx' is the best discriminator for this purpose and with the updated reweighting, particular pt bins don't get influenced by the track-IP resolution any more. so, Unlike the previous cases, good discrimination between b, c and light jets can be achieved with 'SV1_masssvx' without excluding any particular pt bins.

### IV.3.5 Results with release 20.7

There has been many exercises to fix many issues with Direct tag while using the version of ATLAS reconstruction software 20.7 data. Final results with release 20.7 looked reasonable.The template fitting plots can be found in Appendix.

From the results obtained with the version of ATLAS reconstruction software 20.7 data, it has been clear that scale factors were reasonable, though for some particular pt-bins there has been huge systematic uncertainties. The development of these results included some steps of updating reweighting procedure while ntuple production and also using proper Calibration data interface (CDI file).

### IV.3.6 First results with DL1 tagger

First time, DL1 tagger has been used for Direct Tag method and the results/ scale factors using DL1 tagger also looks good. The plots are the following :

Figure IV.9 shows, DL1 tagger provides very good results with the Direct tag light jet calibration framework and the bin by bin scale factor values are close to 1. Though in the case of 77% working point, uncertainties are higher compared to 85% working point.

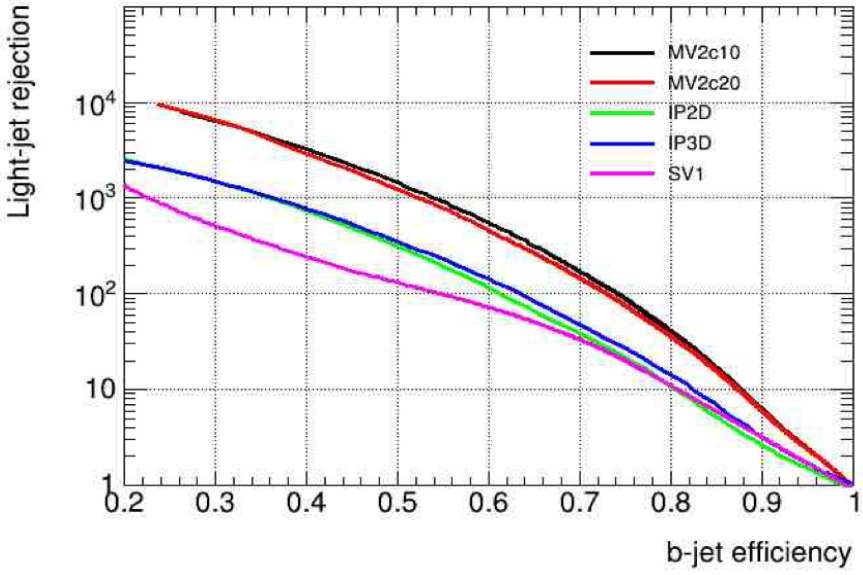


Figure IV.7: ROC curves using different taggers

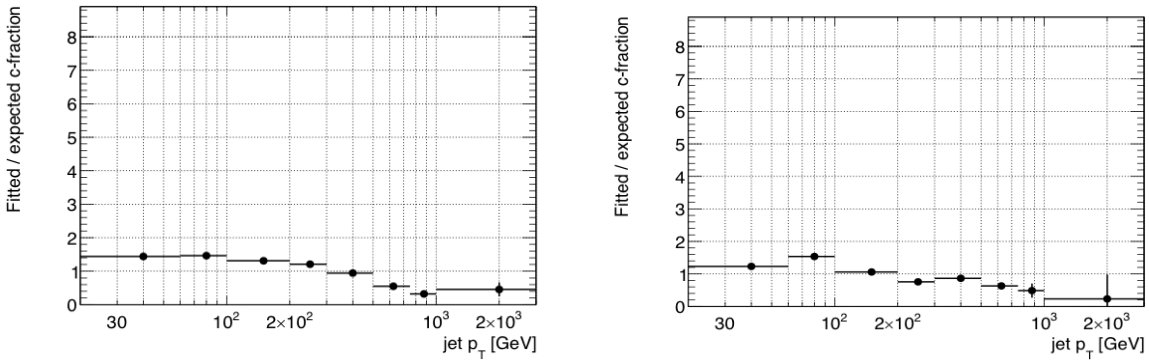


Figure IV.8: fit/MC ratio for c jets with masssvx discriminator excluding the underflow bins for central (left) and forward (right) eta regions

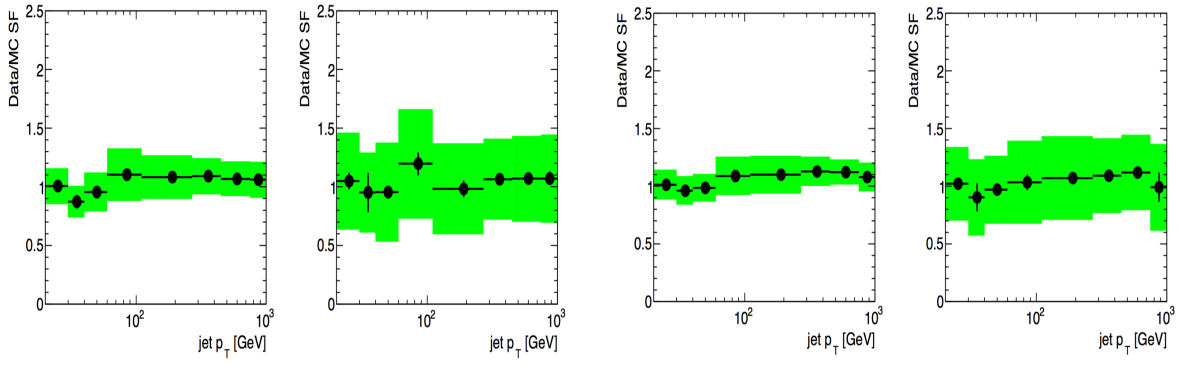


Figure IV.9: Scale factor bin by bin for central (left 2 plots; for SF 85% and SF 77%) and forward (right 2 plots; for SF 85% and SF 77%) eta with DL1 tagger

### IV.3.7 Results for FixedCut B efficiencies

Even though Direct tag runs in the "pseudo-continuous" mode, it can obtain the light-jet calibration for the fixed working points (85% and 77%). But it requires input from c and light-jets which are pseudo-continuous. Some of the results with fixed-cut 85% and fixed-cut 77% are shown in the figures IV.10 and IV.11 below.

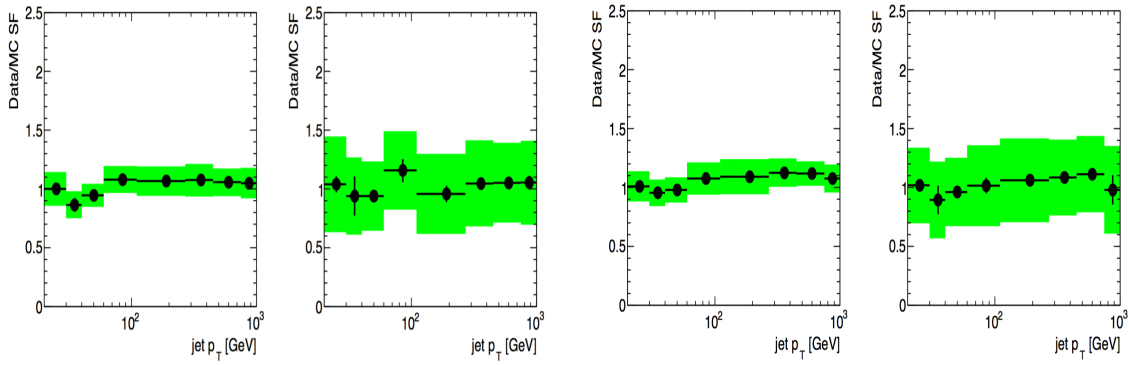


Figure IV.10: Scale factor bin by bin for fixed cut B eff 85 in central (left 2 plots; for SF 85% and SF 77%) and forward (right 2 plots; for SF 85% and SF 77%) eta regions

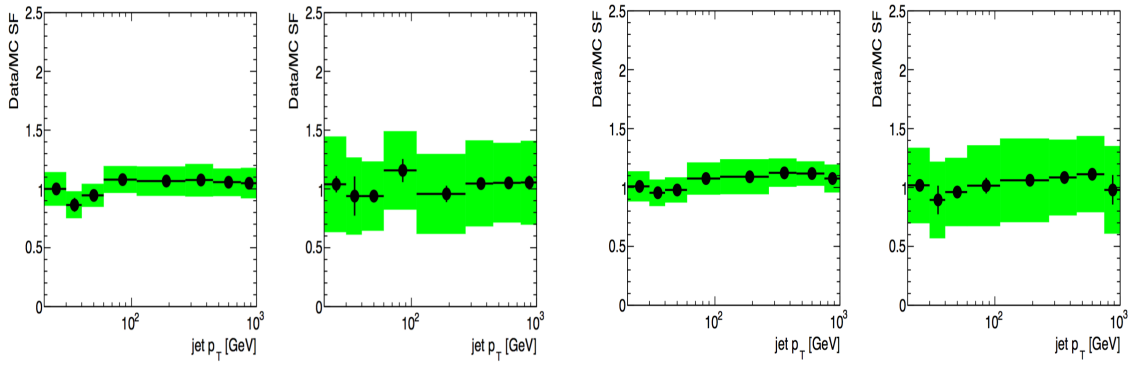


Figure IV.11: Scale factor bin by bin for fixed cut B eff 77 in central (left 2 plots; for SF 85% and SF 77%) and forward (right 2 plots; for SF 85% and SF 77%) eta regions

Figures IV.10 and IV.11 show that for fixed-cut working points, Direct tag light jet calibrations provide scale factors close to 1, though the uncertainties seems to be higher in the case of fixed-Cut 85%.

### IV.3.8 Changing the binning of template fit from 7 to 5

In the template fit procedure, seven bins of tagger output are for : 100-85, 85-77, 77-70, 70-60, 60-50, 50-30, 30-0 efficiencies.But there has been a notion that pseodo continuous scale factors may not support 7 binning template fit any more. The binning of the template fit were changed from 7 to 5. So the five bins of tagger output became for : 100-85, 85-77, 77-70, 70-60, 60-0 efficiencies. Also the scale factors are compared below. The correlation matrix for 5 binning template fit is looking good. Plots are the following :

More plots from the exercises of changing template fit from 7 bin to 5 bin can be found in Appendix section. The comparison between correlation matrices of the fit parameters in case of both 7 binning template fit and 5 binning template fit yield the following results:

The correlation matrices suggest that though there has been correlation between fit parameters in 5 binning template fit, still there has been scopes for optimization. In its current shape, the template fit in 7 binning has been better than that of 5 binning. Correlation matrices of fit parameters for all the pt-eta bins can be found in Appendix.

## IV.4 Alternative method : Verification of Direct tag results

An alternative code has been developed to cross check the results obtained by Direct tag method. That Alternative method works similarly to the Direct Tag package and takes the same data and monte carlo ntuples as inputs and take b, c and some of the light scale factors from the CDI file and provides the flavor fractions and scale factors for light jets in tight working points. Using this new method, for all the different monte carlo generators Pythia, Herwig and sherpa, flavor fractions and light jet scale factors in 85% and 77% working points were calculated. Plots have been obtained for both prefit and postfit. And it has been found that after post fit, the plots are looking very similar to the plots obtained by Direct tag method. And all those plots were generated for both 7 binning template ft and 5 binning template fit as well. The comparison betwen those two sets of plots, implies that the template fit plots due to 7 binning are looking better than the others. All those plots generated by the Alternative method can be found in Appendix section.

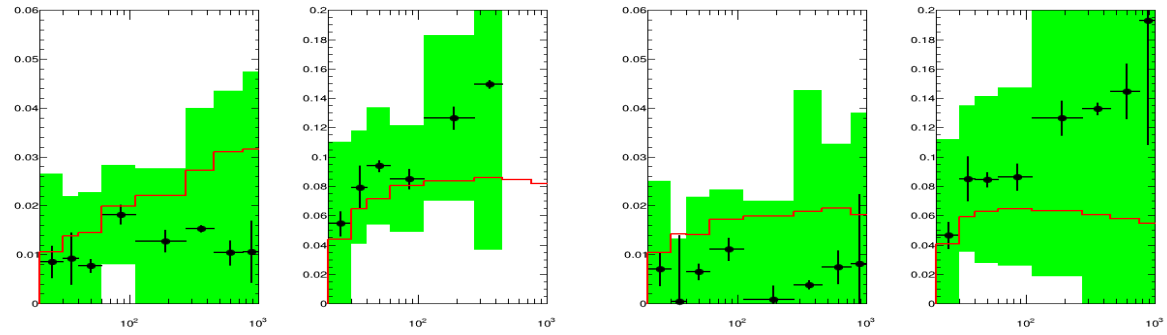

Figure IV.12: FlavFractions for central (left two plots) and forward (right two plots) eta in 5 binning

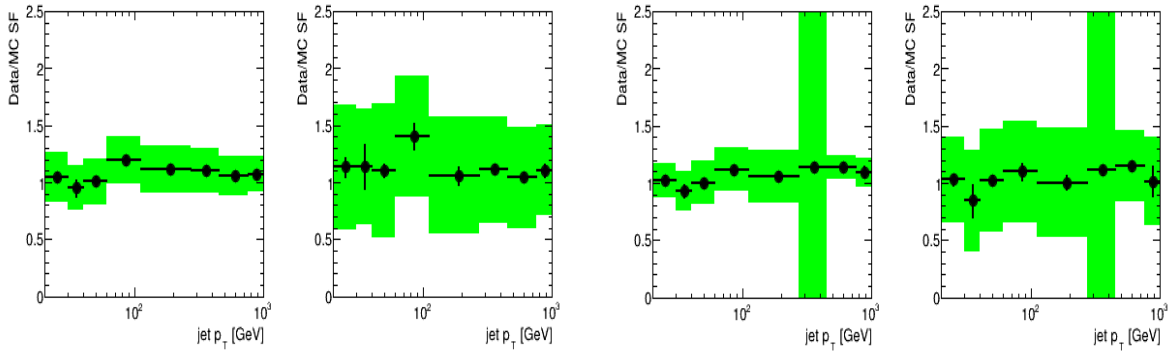


Figure IV.13: Scale factor bin by bin for central (left 2 plots; for SF 85% and SF 77%) and forward (right 2 plots; for SF 85% and SF 77%) eta in 5 binning

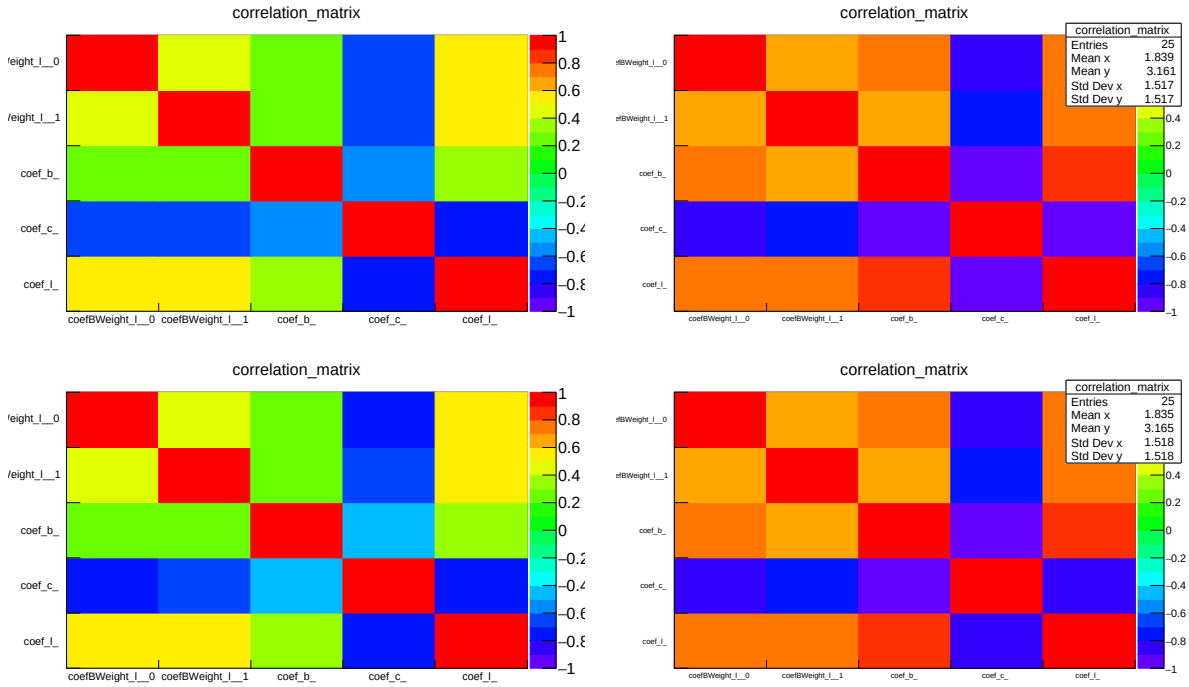


Figure IV.14: Correlation matrices for 7 bin template fit for 1st and 2nd pt bins in 7 binning (left) and 5 binning(right)

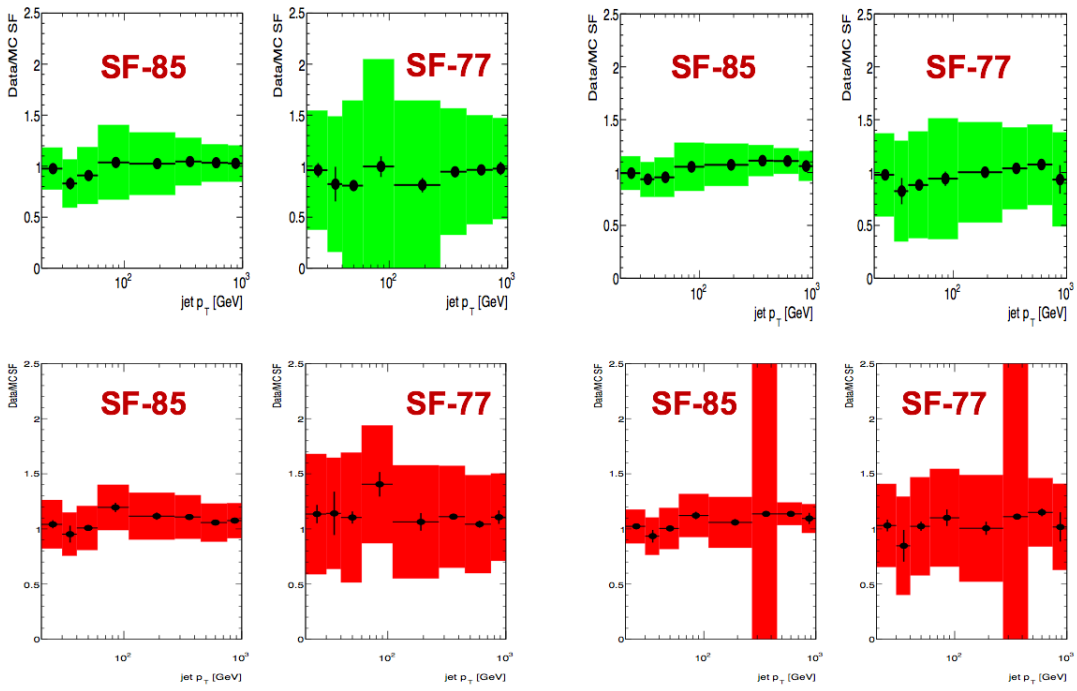


Figure IV.15: Comparison of Scale factors bin by bin from 7 bin template fit (at the top) and 5 bin template fit (at bottom) respectively

### IV.4.1 Direct tag vs Negative tag rate method : A comparison

The results(scale factors) coming from the Negative tag rate method and Direct tag method are compared for continuous, fixedCut and Hybrid b tagging efficiencies. The comparison plots are shown below.

## IV.5 Analysis of early results

Results of Direct tag method on Light Jet calibration is very promising. With newly processed data, the scale factors started to look much better than that of previous release. The comparison plots between negative tag and Direct tag gives insight that for tighter working points, the performance of Direct tag method seems to be better than Negative tag rate method. The Alternative cross-verification method for Direct tag results is also working very well. Though Direct tag method has been originally designed for continuous b tagging, but for FixedCut b tagging efficiencies, the method can be used for providing light jet calibration as well. More things can be done for further development of Direct tag : 1. With upcoming CDI, it can be checked whether c jet flavor fraction becomes closer to 1 or not. 2. Binning in negative tag can be modified so that inputs for Direct tag do not need to be transformed 3. 5 bin fitting code can be modified for better correlation of fit parameters 4. Variables like 'masssvx' can be included in Direct tag package to have better results (flavor fractions).

It can be concluded that Direct tag method has the potential to emerge as substitute to the standard light jet calibration method in ATLAS. My detailed work on this Direct tag is documented as an "Internal Note" of ATLAS collaboration [135] and this work made me an author of the ATLAS collaboration. In the coming years, the mothod has scopes to become an official method for ATLAS physics results.

Direct tag method's results on Light Jet calibration is very promising. With relaese 21 data, the scale factors started to look much better than taht of previous release. The comparison plots between negative tag and Direct tag gives insight that for tigher working points, the performance of Direct tag method seems to be better than Negative tag rate method. The Alternative method for Direct tag method's result verification is also working very well. Though Direct tag method has been originally designed for continuous b tagging, but for FixedCut b tagging efficiencies, the method can be used for providing light jet calibration as well. Few things can be done for further development of Direct tag : 1. With upcoming CDI, it can be checked whether c jet flavor fraction gets better or not 2. Binning in negative tag can be modified so that inputs for Direct tag don't need to be transformed 3. 5 bin fitting code can be modified for better correlation of fit parameters 4. Variables like 'masssvx' can be included in Direct tag package to have better results (flavor fractions).

Analyzing the early results, it can be concluded that Direct tag method has the potential to emerge as substitute to the standard light jet calibration method.

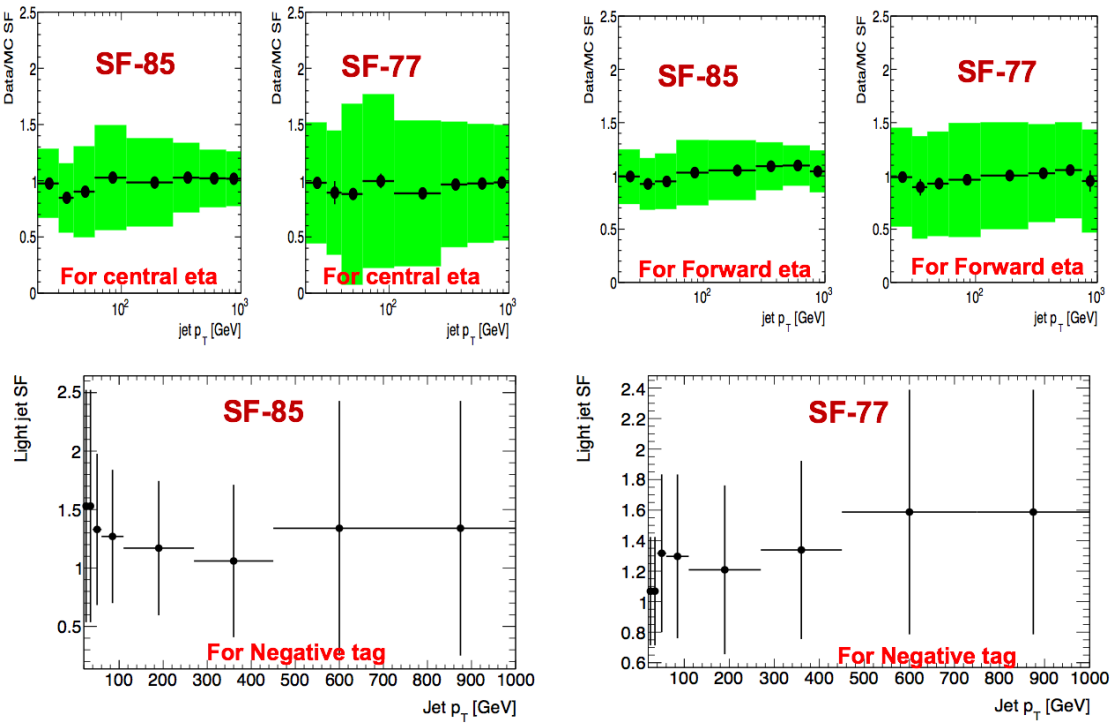


Figure IV.16: Comparison of Scale factors for pseudo continuous b-efficiencies from Direct tag method (at the top) and Negative tag rate method (at bottom)

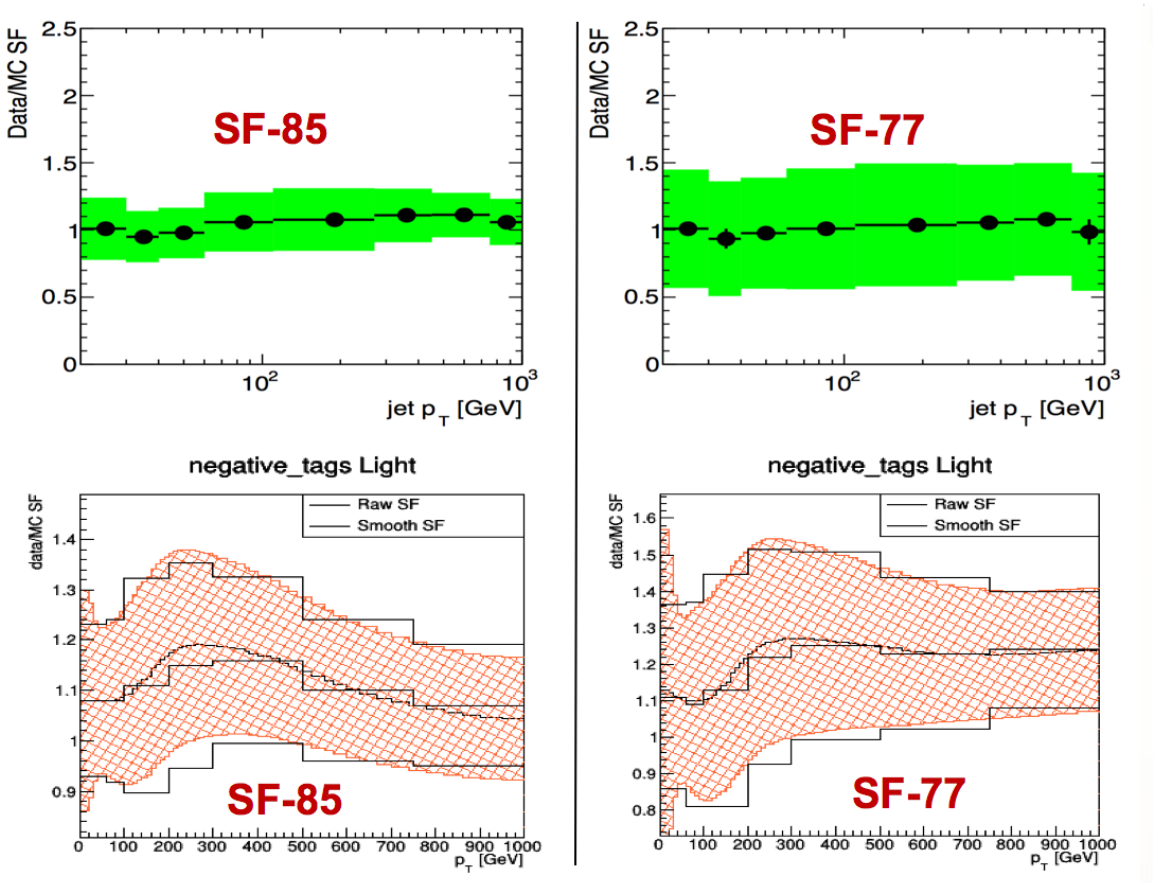


Figure IV.17: Comparison of Scale factors for pseudo Fixed-cut b-efficiencies from Direct tag method (at the top) and Negative tag rate method (at bottom)

### IV.6 Further studies with high-pt samples

As further development on the method, dijet-data based-high-pt samples were produced. Derivation samples were produced with ATLAS software release 21.2.78. The samples using Dijet Calibration framework the following samples :364702 (JZ2W), 364703 (JZ3W), 364704 (JZ4W), 364705 (JZ5W), 364706 (JZ6W), 364707 (JZ7W), 364708 (JZ8W), 364709 (JZ9W), 364710 (JZ10W), 364711 (JZ11W), 364712 (JZ12W).

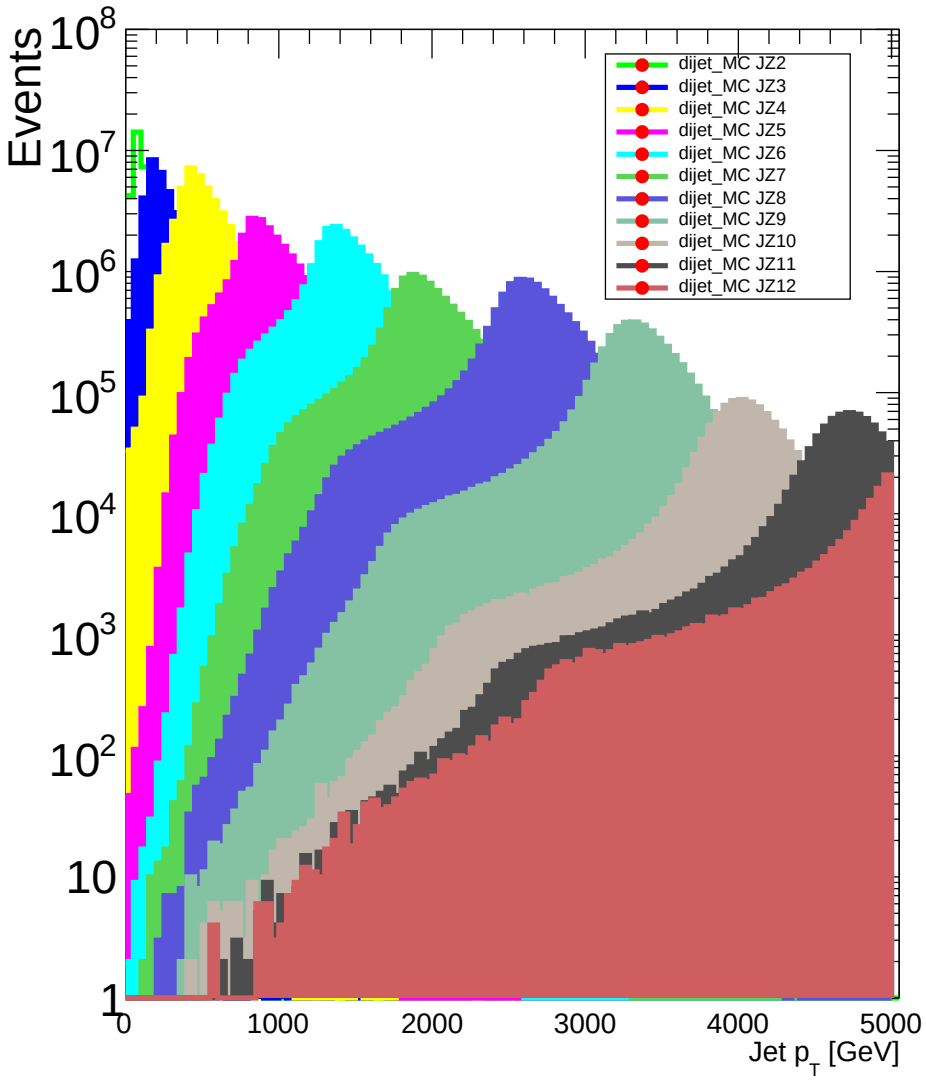


Figure IV.18: Jet pT distribution in different JZ MC slices are shown in the left and right plots respectively.

Figure IV.18 shows the $Jetp_T$ of the sample goes distributions of the monte carlo simulations used. The $Jetp_T$ of the sample goes up to 5000 GeV.

As was shown in previous studies, the dominant uncertainty of the light jet calibration method comes from normalization of light jets in tight Working Point bins. To evaluate the effect of fixed light jet fraction in tight WP bins, the number of light jets in bins 70-60, 60-0 is modified by ±50% and then the effect as a function of jet pT and look at uncertainties for each JZ slice are observed. It should be noted that, since the tag weight cuts are fixed, the corresponding b-tagging efficiencies are not the same for each slice. Studies have been performed on fits with 5 bins in this section.

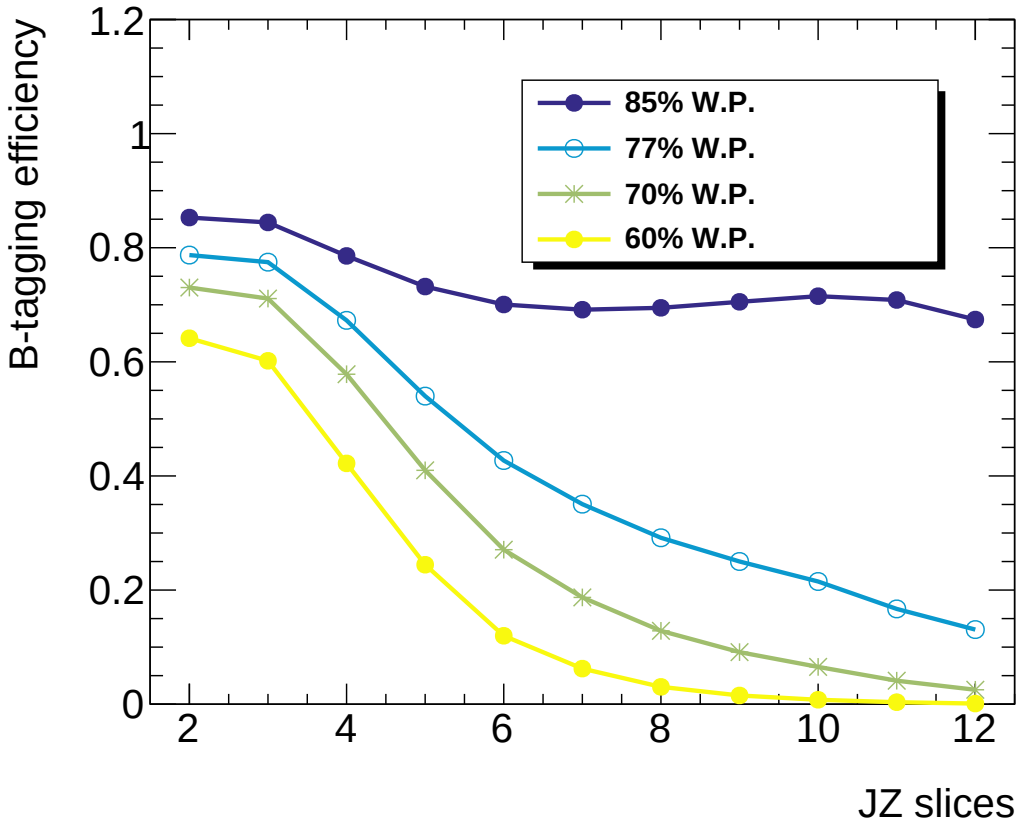


Figure IV.19: B-tagging efficiency in different JZ slices are shown in the left and right plots respectively.

In the figure IV.19, it can be seen how b-tagging efficiency varies among different JZ slices, Specially at the higher JZ slices, the b-tagging efficiency drops as observed in the plot.

Total three different fits have been used for the studies : 1D fit, fit with Soft Muon Tagger(SMT) discriminant and fits with Secondary Vertex(SV) discriminant. Following three tables show if there are changes in the light jets bins by ± 50% how systematic uncertainties and scale factors due to b and C jets $SF_b$ , $SF_c$ values change. The uncertainty values generally seem to be large for the high jet $p_T$ of higher slices than the lower one.

| JZ Slice | $l_{4,5}$ | $l_3$ | $l_2$ | $l_3$ | $SF_c$ | $SF_b$ |
|---|---|---|---|---|---|---|
| 2 | +0.5 | -0.019 | -0.100 | -0.264 | +0.310 | -0.041 |
| | -0.5 | +0.019 | +0.100 | +0.265 | -0.311 | +0.042 |
| 3 | +0.5 | -0.028 | -0.118 | -0.271 | +0.337 | -0.048 |
| | -0.5 | +0.028 | +0.118 | +0.272 | -0.337 | +0.049 |
| 4 | +0.5 | -0.115 | -0.162 | -0.332 | +0.837 | -0.074 |
| | -0.5 | +0.115 | +0.162 | +0.332 | -0.838 | +0.075 |
| 5 | +0.5 | -0.146 | -0.231 | -0.384 | +1.706 | -0.142 |
| | -0.5 | +0.146 | +0.231 | +0.385 | -1.708 | +0.143 |
| 6 | +0.5 | -0.184 | -0.230 | -0.373 | +2.017 | -0.172 |
| | -0.5 | +0.184 | +0.231 | +0.374 | -2.019 | +0.172 |
| 7 | +0.5 | -0.175 | -0.208 | -0.335 | +1.918 | -0.155 |
| | -0.5 | +0.175 | +0.208 | +0.335 | -1.920 | +0.156 |
| 8 | +0.5 | -0.153 | -0.182 | -0.314 | +1.747 | -0.136 |
| | -0.5 | +0.154 | +0.184 | +0.316 | -1.764 | +0.141 |
| 9 | +0.5 | -0.145 | -0.176 | -0.312 | +1.724 | -0.106 |
| | -0.5 | +0.145 | +0.177 | +0.313 | -1.732 | +0.109 |
| 10 | +0.5 | -0.135 | -0.180 | -0.339 | +1.684 | -0.039 |
| | -0.5 | +0.136 | +0.181 | +0.341 | -1.693 | +0.041 |
| 11 | +0.5 | -0.122 | -0.159 | -0.310 | +1.479 | -0.006 |
| | -0.5 | +0.122 | +0.160 | +0.311 | -1.487 | +0.009 |
| 12 | +0.5 | -0.269 | -0.314 | -0.485 | +3.185 | -0.579 |
| | -0.5 | +0.357 | +0.412 | +0.600 | -4.297 | +1.019 |

Table IV.2: Systematic uncertainties with 1d fit with 5 binning. It can be seen c-fraction uncertainty for large jet pT explodes

| JZ Slice | $l_{4,5}$ | $l_3$ | $l_2$ | $l_3$ | $SF_c$ | $SF_b$ |
|---|---|---|---|---|---|---|
| 2 | +0.5 | -0.013 | -0.066 | -0.173 | +0.214 | -0.018 |
| | -0.5 | +0.011 | +0.060 | +0.158 | -0.194 | +0.013 |
| 3 | +0.5 | -0.017 | -0.074 | -0.171 | +0.224 | -0.020 |
| | -0.5 | +0.016 | +0.067 | +0.155 | -0.201 | +0.015 |
| 4 | +0.5 | -0.055 | -0.090 | -0.186 | +0.472 | +0.003 |
| | -0.5 | +0.045 | +0.075 | +0.156 | -0.384 | -0.017 |
| 5 | +0.5 | -0.058 | -0.097 | -0.173 | +0.665 | +0.094 |
| | -0.5 | +0.047 | +0.079 | +0.143 | -0.521 | -0.101 |
| 6 | +0.5 | -0.060 | -0.082 | -0.152 | +0.621 | +0.157 |
| | -0.5 | +0.051 | +0.069 | +0.130 | -0.518 | -0.138 |
| 7 | +0.5 | -0.043 | -0.058 | -0.120 | +0.411 | +0.225 |
| | -0.5 | +0.038 | +0.052 | +0.106 | -0.374 | -0.181 |
| 8 | +0.5 | -0.021 | -0.033 | -0.094 | +0.171 | +0.300 |
| | -0.5 | +0.023 | +0.033 | +0.088 | -0.201 | -0.238 |
| 9 | +0.5 | -0.009 | -0.019 | -0.088 | +0.007 | +0.408 |
| | -0.5 | +0.012 | +0.022 | +0.083 | -0.066 | -0.329 |
| 10 | +0.5 | +0.001 | -0.008 | -0.091 | -0.150 | +0.547 |
| | -0.5 | +0.003 | +0.012 | +0.088 | +0.077 | -0.463 |
| 11 | +0.5 | +0.003 | -0.005 | -0.095 | -0.186 | +0.565 |
| | -0.5 | -0.000 | +0.008 | +0.090 | +0.130 | -0.491 |
| 12 | +0.5 | +0.018 | +0.009 | -0.097 | -0.419 | +0.779 |
| | -0.5 | -0.015 | -0.006 | +0.093 | +0.363 | -0.706 |

Table IV.3: Systematic uncertainties with tag weight and SMT with 5 binning. It can be seen c-fraction uncertainties are under control, Light fraction uncertainties are significantly improved compared to 1d fit

| JZ Slice | $l_{4,5}$ | $l_3$ | $l_2$ | $l_3$ | $SF_c$ | $SF_b$ |
|---|---|---|---|---|---|---|
| 2 | +0.5 | -0.013 | -0.066 | -0.166 | +0.212 | -0.013 |
| | -0.5 | +0.012 | +0.064 | +0.163 | -0.202 | +0.012 |
| 3 | +0.5 | -0.020 | -0.085 | -0.187 | +0.247 | -0.022 |
| | -0.5 | +0.019 | +0.083 | +0.187 | -0.239 | +0.021 |
| 4 | +0.5 | -0.057 | -0.090 | -0.190 | +0.479 | +0.013 |
| | -0.5 | +0.053 | +0.086 | +0.182 | -0.439 | -0.018 |
| 5 | +0.5 | -0.046 | -0.077 | -0.148 | +0.502 | +0.158 |
| | -0.5 | +0.038 | +0.066 | +0.129 | -0.411 | -0.151 |
| 6 | +0.5 | -0.043 | -0.062 | -0.128 | +0.420 | +0.233 |
| | -0.5 | +0.038 | +0.055 | +0.112 | -0.370 | -0.193 |
| 7 | +0.5 | -0.031 | -0.045 | -0.104 | +0.268 | +0.281 |
| | -0.5 | +0.030 | +0.042 | +0.095 | -0.271 | -0.221 |
| 8 | +0.5 | -0.010 | -0.020 | -0.075 | +0.036 | +0.341 |
| | -0.5 | +0.013 | +0.022 | +0.070 | -0.081 | -0.269 |
| 9 | +0.5 | +0.005 | -0.004 | -0.066 | -0.165 | +0.468 |
| | -0.5 | +0.002 | +0.009 | +0.065 | +0.067 | -0.367 |
| 10 | +0.5 | +0.017 | +0.011 | -0.064 | -0.358 | +0.622 |
| | -0.5 | -0.008 | -0.001 | +0.066 | +0.218 | -0.498 |
| 11 | +0.5 | +0.024 | +0.019 | -0.068 | -0.471 | +0.701 |
| | -0.5 | -0.015 | -0.010 | +0.068 | +0.329 | -0.572 |
| 12 | +0.5 | +0.043 | +0.037 | -0.073 | -0.753 | +0.951 |
| | -0.5 | -0.037 | -0.031 | +0.069 | +0.651 | -0.846 |

Table IV.4: Systematic uncertainties with tag weight and SV with 5 binning. Better results at high jet pT compared to tag weight and SMT.Light fraction uncertainties are significantly improved compared to 1d fit.

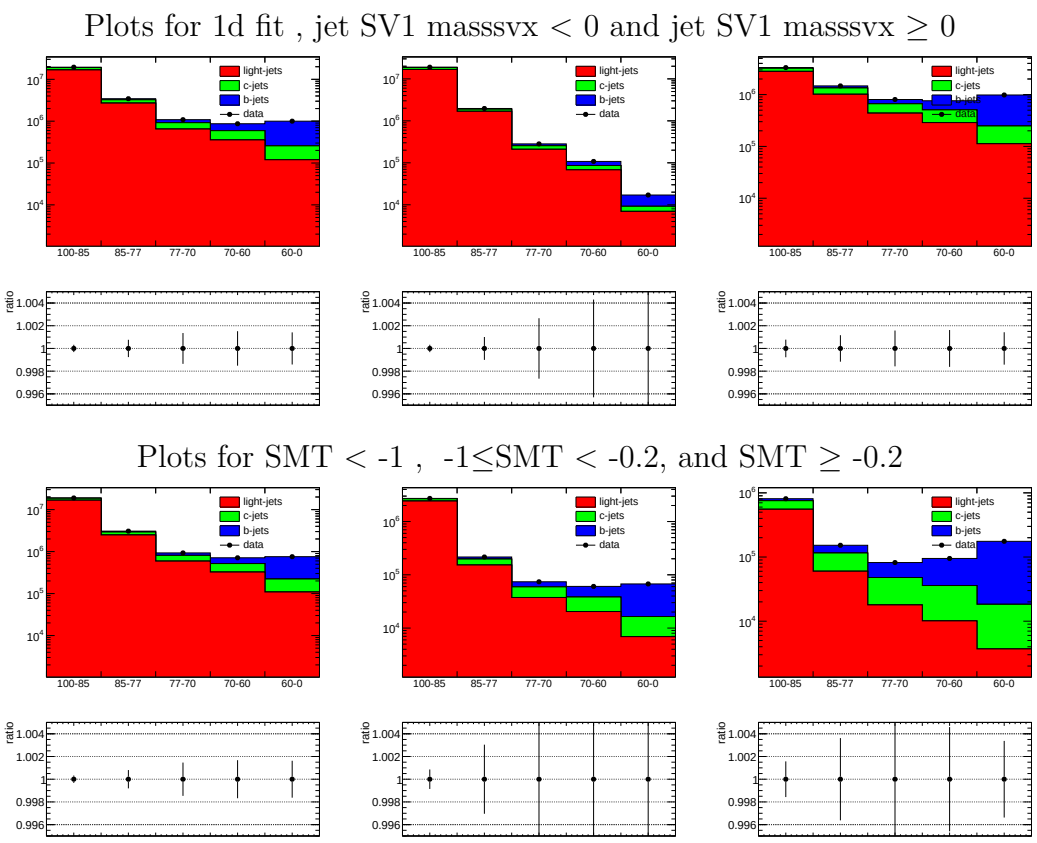


Figure IV.20: Template fit for JZ4 slice for r21. The plots have compared SMT and jet SV1 masssvx discriminators with 5 bins.

Table IV.2, IV.3 and IV.4 provides the variation of Systematic uncertainties using 1D fit, SMT and SV masssvx discriminators respectively for 5 binning.

The variation of different releases may also affect the fits of the templates used in the Direct tag studies. To check that two different releases r21.2.40 and r21.2.78 have been used and their 1 dimensional fits have been compared. Comparisons show that there has not been much difference between the two fits.

Using Release 21, different plots have been made with SMT discriminators for different JZ slices of monte carlo simulation which represent different jet $p_T$. Similar studies have been performed using SV1 masssvx discriminant as well. Comparison between plots using SMT and jet SV1 masssvx discriminators have also been made while using different JZ slices of monte carlo simulation which represent different jet $p_T$.

Figures IV.20 shows a comparison between 1d fit, SMT and SV1 discriminants while performing template fit of b , c and light jets.

The figures show good fitting using different discriminators, but they have scopes for improvement. One idea to improve the methods is to increase binning of of Direct tag to have better template fit. The strategy for that can be using b/c efficiency scale factors for the additional bins. The original version of negative tag rate with dijet samples used separate single jet triggers for each jet pT bin, so another approach is

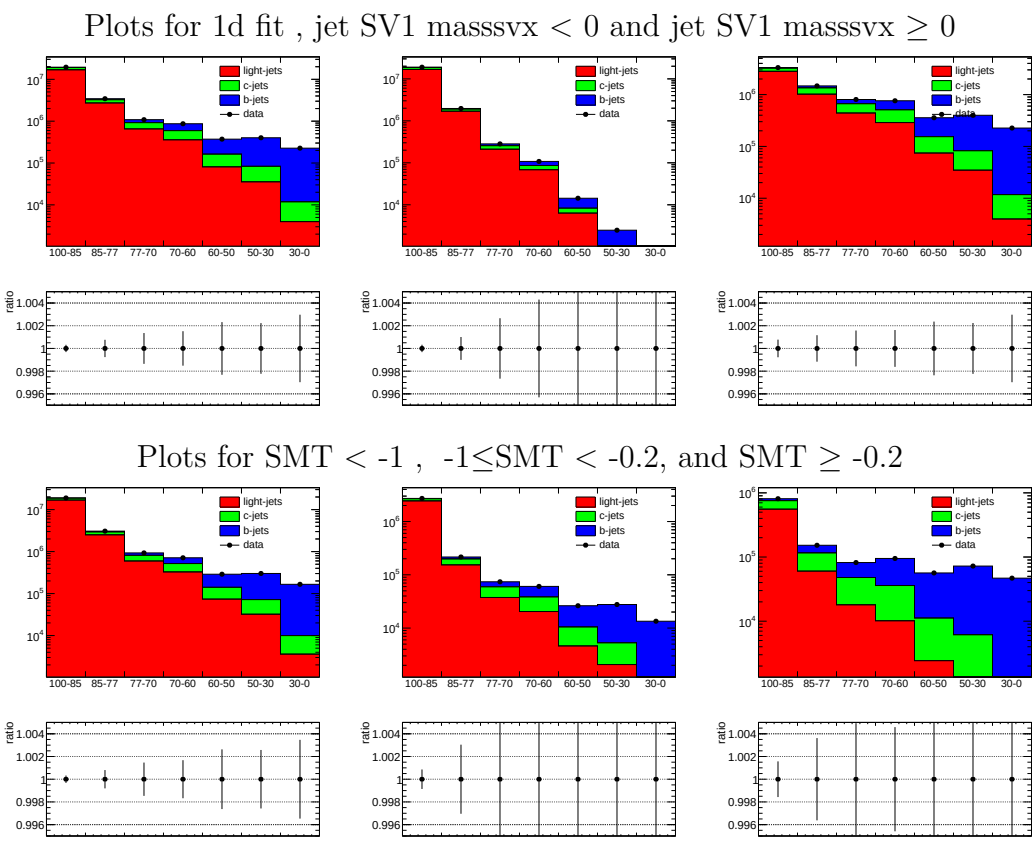


Figure IV.21: Template fit for JZ4 slice for r21. The plots have compared SMT and jet SV1 masssvx discriminators with 7 bins.

to perform dedicated studies on different triggers.

## IV.7 Studies on additional bins

While performing fits with 5 bins, the following cuts are provided by ATLAS : -1,0.11, 0.64,0.83,0.94,1. For further studies using 7 bins, some additional points for 50% and 30% Working points have been considered and the following working points have been used for 7 bin studies : -1,0.11,0.64,0.83,0.94,0.97,0.99,1.

Figure IV.21 shows the comparative fitting plots with 7 bins while using different discriminators Soft Muon tagger, SV1 masssvx, 1D fit etc for JZ4 monte carlo slice.

If B-tagging efficiencies also vary in between 5 binning and 7 binning. Figure IV.22 provides a comparative view on b-tagging efficiency changes for different working points and for different MC JZ slices of different jet $p_T$.

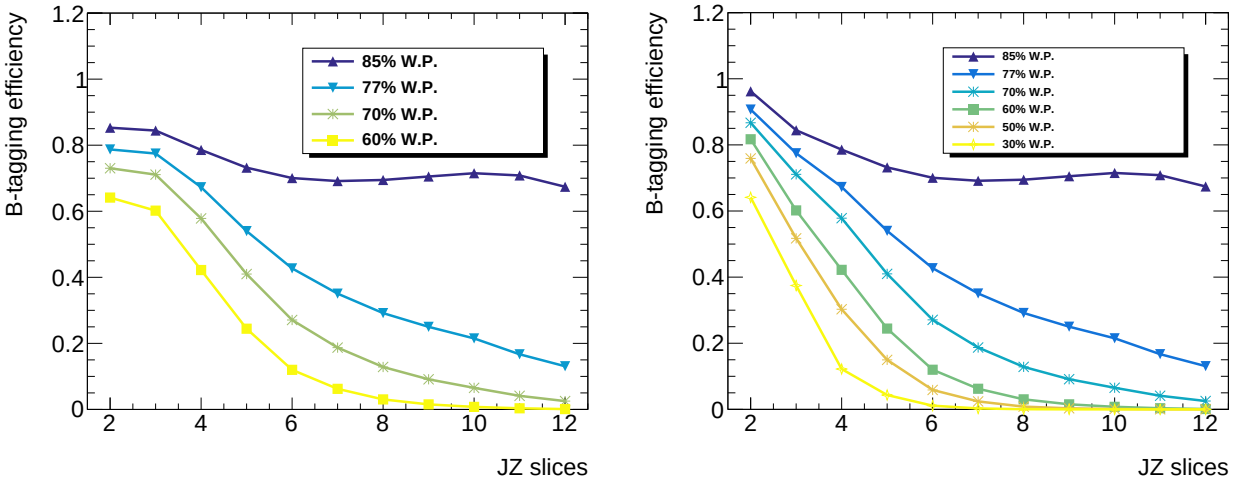


Figure IV.22: B-tagging efficiency for 5 binning(left plot) and 7 binning(right plot)


Figure IV.23: Some Trigger studies with data of dijet samples for Direct tag can be observed in the plot. Leading JetpT with HLT triggers with 2018 data are seen in the plots. In the left plot 2018 data with period D and in the right plot 2018 data with period F can be seen.

## IV.8 Trigger studies

In the development of Direct Tag light jet calibration method, another important aspect has been doing studies on triggers while being motivated by the Negative tag rate method. Data samples of 2016, 2017, 2018 have been studied and they contain different high level triggers. For example, Data 2016 has following triggers: HLT j260, HLT j150, HLT j320 HLT j380 and has Periods A, B, C, D, E, F, G, I, K, L. Similarly Data 2017 has following triggers: HLT j260, HLT j150, HLT j320 HLT j380 and has Periods B, C, D, E, F, H, I, K. Data 2018 has following triggers: HLT j175 HLT j110. HLT j360 HLT j420 and has Periods B, C, D, F, I, K, L, M, O, Q.

An example plot with triggers in 2018 data of period D and F can be found below :

In figure IV.23, the leading jet $p_T$ distribution can be well observed and accordingly best possible single jet triggers can be used for further development of the light jet calibration method.

## IV.9 Summary

In this chapter, the development of Direct tag light jet calibrations have been explained along with its challenges, scopes of improvement and motivation behind the development of such a new algorithm for B-tagging. I have worked on the method significantly and early results shows that the method has good potential of becoming a standard calibration method and in providing good calibrations for ATLAS physics results in near future.

# CHAPTER V

## Search for Charged Higgs through Dijet plus lepton

> This summer I have discovered
> something totally useless.
>
> Peter Higgs (1964)

The Searches for Dijet resonance is very common at the Large Hadron Collider specially at the ATLAS and CMS experiments. The theory section of Chapter 1 mentions the examples of many such searches. Requiring a charged lepton along with the dijet resonance not only reduces QCD multijet backgrounds and overcome some trigger limitations, but such processes are also sensitive to many different BSM models. Searches for Charged Higgs boson has also been popular through different channels

In this section, searches for model independent search and the search for Charged Higgs Boson through this channel has been described. The analysis was published as the first peer-reviewed ATLAS analysis of dijet resonance searches which used leptons for triggering purposes.

### V.1 Broad strategies

#### V.1.1 Strategies for Model independent searches

Different BSM models require different search strategies. But at the same time there are scopes of performing the searches in model independent ways by having generic event selections and by not having any specific bias towards any BSM model. This analysis also follows the same rules. If the decay process involve a W boson or top quark, often it has neutrinos in the final state. And for many such analysis, missing transverse momentum are taken into account. since the recent ATLAS result of dijet resonance searches along with a lepton and missing transverse momentum didn't find significant deviation from the Standard Model [136], for this analysis missing transverse momentum has not been included in the study and only the presence of a charged lepton along with dijet resonance has been considered.

The strategy for the analysis includes the following steps:

1. Performance-based object selection; 2. Estimating search range in the spectrum of dijet invariant mass $m_{jj}$ distribution; 3. Defining control region (CR) for the analysis; 4. Determining fit method for background estimation; 5 Performing bump searches; and 6. Follow-up analysis or setting exclusion limits depending on the outcome of the bump searches.

Even though the search is a model independent search, for signals realistic $m_{jj}$ signal shape and studies on lepton kinematics modelling is required. At the same time, many different studies on the different Physics objects involved have also been part of the strategy. Since the study also involve some model dependent searches, some systematic uncertainties derived from the BSM models are used for the model-independent studies.

### V.1.2 Strategies for the searches for Charged Higgs boson

For the model dependant search for Charged Higgs Boson through dijet resonance along with isolated charged lepton also follows similar strategies for the model independent search phase. The specific Charged Higgs model considered for the study predicts the production of Charged Higgs boson along with a top and a bottom quarks. The decays $H^+t$ are characterized by several jets from the top decays.

$$qq \rightarrow tbH^+; H^+ \rightarrow tb \tag{V.1.1}$$

In a very boosted regime, with $H^+$ masses being above 1 TeV, the decay products of top ($t$) and bottom ($b$) from $H^+$ form two jets travelling to the opposite direction, which can be reconstructed using the dijet invariant mass distributions($m_{jj}$). For lower masses of Charged Higgs boson, two leading jets are typically a jet from the top decay and a $b$ quark from $H^+$. The invariant masses of the leading jets approximate the mass of $H^+$, but the width of $m_{jj}$ is rather broad due to incomplete reconstruction of the decay products.

The $m_{jj}$ distributions follow the mass of the $H^+$, though it should be noted that the natural width of $H^+$ is smaller than the detector resolution, so the width of the $m_{jj}$ is entirely due to exploration of two leading jets, ignoring other jet activity associated with the $H^+$ decays.

For this analysis, different values of ($tan\beta$) have been explored and for different values of ($tan\beta$), the searches have been performed at the $m_h^{mod-}$ scenario[20] of the Minimal Supersymmetric Standard Model (MSSM) Higgs sector. $m_h^{mod}$ scenario is the modified version of $m_h^{max}$ which was derived for the Higgs boson searches and exclusion limits with respect to different values of ($tan\beta$) in the MSSM model [137]. For two important parameters of MSSM sector $X_t$ and $M_{SUSY}$, depending on the signs of $X_t/M_{SUSY}$, $m_h^{mod+}$ and $m_h^{mod-}$ scenarios differ. And for this analysis, $m_h^{mod-}$ benchmark scenario has been considered.

Dominant backgrounds for the processes have been the same as model independent searches including multijet, top quark, W+jets etc.

## V.2 Monte Carlo simulations and physics modelling

For performing any analysis, it is important to simulate events not only for the background hypothesis, but also for BSM models, which are being studied. It should be noted that for the generation of Monte Carlo samples, specially for the background events, standard model descriptions are used.

For the model independent studies, dijet mass distributions for different widths and peak positions were generated by a random-generators with Gaussian density function, to be used for different scenarios of Gaussian approximated signal shapes. The four different widths that have been considered are $\sigma_X/m_X$ = detector resolution, 0.05, 0.10, 0.15 %.

In the following sections the Monte Carlo simulations for Background events, Model specific Charged Higgs signal samples events and descriptions for model independent simulations are described.

### V.2.1 Heavy Charged Higgs MC description

For the modelling of $tbH^+$ process, `MadGraph5_aMC@NLO (MG5_aMC)` at next-to-leading order (NLO) in QCD while using a four-flavour scheme (4FS) formalism with `NNPDF2.3` parton distribution function (PDF).

Pythia 8.186 and the A14 tune were used for the parton showering and harmonization modelling processes. Another important aspect of $tbH^+$ simulation has been, the narrow-width approximation has been used for the simulation, though the the approximation has a negligible effect on the studies due to large experimental resolution than the natural width of the $m_{H^+}$ . For example, the dijet invariant mass distribution has a relative half width at half maximum (HWHM) of about 30% of the peak position. For the Charged Higgs, interference with the SM $t\bar{t} + b\bar{b}$ background has also not been considered.

The different mass hypothesis who have been used for the study are $m_{H^+}$ = 250 GeV, 275 GeV, 300 GeV, 600 GeV, 800 GeV, 1000 GeV, 1200 GeV, 1600 GeV, 1800 GeV and 2000 GeV, which have been used for another recent dedicated searches for Charged Higgs by the ATLAS Collaboration. [21]. Some truth level studied sowed that only above 600 GeV, the two highest $p_T$ jets form well defined peaks, so for the studies masses above 600 GeV have been considered. The samples production process included fast simulation ATLFASTII[138] with ATLAS and the cross sections of the signal events has been set to 1 pb.

The cross-sections for different masses and other information about those samples for $\tan(\beta) = 1$ are given in the Table V.1. The cross sections were calculated using the hMSSM model [5]. Note that the 2nd column is the production cross section, which needs to be multiplied by the branching ratio (the last column) to calculate the production cross section with $H^\pm \to tb$ decays.

Table V.2 lists the $H^+$ cross sections for $\tan(\beta) = 0.5$ for the hMSSM model [5].

The cross sections used in this note were calculated for the $m_h^{\mathrm{mod}-}$ scenario [20], as for Fig. 8 of the published ATLAS paper [21]. These cross sections are about 6% lower than those for the hMSSM scenario. Table V.4 shows such cross sections. The cross sections include the branching ratios.

For the truth level analysis, the main selection cut is $p_T^l > 60$ GeV and the two highest $p_T$ jets which were selected to calculate the invariant mass of dijets.

For detector-level Monte Carlo samples of Charged Higgs boson decaying into top and bottom quark have been used. Figure V.1 shows the dijet invariant mass for different masses of Heavy Charged Higgs boson at the truth level.

| $m_{H^\pm}$ [GeV] | $\sigma$ [pb] | No. of events | Luminosity [fb$^-$1] | $H^\pm \to tb$ |
|---|---|---|---|---|
| 225 | 5.36469 | 51581 | 9.61 | 0.9857 |
| 250 | 4.32031 | 52147 | 12.07 | 0.9811 |
| 275 | 3.50344 | 53550 | 15.28 | 0.98175 |
| 300 | 2.84478 | 54656 | 19.21 | 0.9834 |
| 600 | 0.349742 | 80318 | 22.96 | 0.9939 |
| 800 | 0.11198 | 80318 | 189.96 | 0.9959 |
| 1000 | 0.0408974 | 20000 | 2290.96 | 0.9989 |
| 1200 | 0.0164467 | 20000 | 6806.96 | 0.997 |
| 1800 | 0.00154663 | 127251 | 82276.30 | 0.9977 |

Table V.1: This table lists the information on Charged Higgs boson production in the 4FNS Monte Carlo for $\tan(\beta) = 1$ for the hMSSM model [5]. The luminosity for each mass (4th column) was calculated from the numbers of events and the predicted cross sections listed in this table. The last column shows the branching fractions.

| $m_{H^\pm}$ [GeV] | $\sigma$ [pb] | No. of events | $H^\pm \to tb$ |
|---|---|---|---|
| 225 | 21.4533 | 30000 | 0.9857 |
| 250 | 17.2768 | 30000 | 0.9811 |
| 275 | 14.0102 | 20000 | 0.98175 |
| 300 | 11.3763 | 20000 | 0.9834 |
| 600 | 1.39862 | 20000 | 0.9939 |
| 800 | 0.44782 | 20000 | 0.9959 |
| 1000 | 0.163551 | 20000 | 0.9989 |
| 1200 | 0.065771 | 20000 | 0.997 |
| 1800 | 0.00618506 | 20000 | 0.9977 |

Table V.2: This table lists the information on Charged Higgs boson production in the 4FNS Monte Carlo for $\tan(\beta) = 0.5$ for the hMSSM model [5]. The last column shows the branching fractions.

The comparison between dijet invariant mass plots at the truth and reconstructed level can be found in Fig. V.2. Note that all limit calculations in later section are obtained at the reconstruction level, thus the features seen at the truth level cannot directly affect them. The truth-level was only used to estimate acceptance correction due to the lepton selection.

The distribution in Figure V.3 is expressed in the terms of the number of events expected from these models for the luminosity of 139 fb$^{-1}$ using the final cuts of this analysis. The distribution has been shown in the range (peak±RMS).

### V.2.2 Background MC description

The dominant backgrounds in the analysis are top-anti top quark pair production ($t\bar{t}$), QCD multijets, and W+jets. Table V.4 shows relative contributions of those

| $m_{H^{\pm}}$ [GeV] | $\tan(\beta) = 1$ $\sigma$ x BR [pb] | $\tan(\beta) = 0.5$ $\sigma$ x BR [pb] |
|---|---|---|
| 225 | 5.1647 | 21.2679 |
| 250 | 4.1933 | 17.1413 |
| 275 | 3.3977 | 13.8974 |
| 300 | 2.7625 | 11.2841 |
| 600 | 0.2900 | 1.3318 |
| 800 | 0.0900 | 0.4224 |
| 1000 | 0.0323 | 0.1535 |
| 1200 | 0.0128 | 0.0615 |
| 1400 | 0.0055 | 0.02650 |
| 1600 | 0.00251 | 0.0121 |
| 1800 | 0.00118 | 0.0057 |
| 2000 | 0.000548 | 0.00305 |

Table V.3: This table lists the Charged Higgs boson production cross sections in the 4FNS Monte Carlo for the $m_h^{\text{mod}-}$ model used in this study. The branching ratios are included.

backgrounds.

| Background source | Contribution % |
|---|---|
| QCD multi-jets | 90 % |
| ttbar ($t\bar{t}$) | 1-10 % |
| W+ jets | 1-10 % |

Table V.4: Background sources and their contribution percentage.

When there are more than two jets, generally the events are called Multi-jet events. Mis-identification of leptons or production of non-prompt leptons can contribute to multi-jet events. In this analysis, the multi-jet production is the most prominent source of background events. Different data driven methods including matrix method are often used to model such backgrounds. For the production of QCD multi-jets samples, Pythia8 generator[139] and NNPDF23 along with A14 tune have been used.

Another prominent source of background is the $t\bar{t}$ process. As top quarks decay into W bosons, if the W boson decays leptonically, the leptons may create confusion in the analysis as the final state of the signal also requires an isolated charged lepton. Similarly, W+jets events for the exact same reason of leptonic decays of W boson, contribute to the background.

For the production of W+jets and $t\bar{t}$ events, Powheg generator[140] was used, while being interfaced with Pythia8 and using CT10 NLO PDF and AZNLO tune. Table V.5 shows the different background processes and corresponding number of events simulated in two Monte Carlo production campaigns (MC16a and MC16d) and also their production cross section values. It can be seen from the table that the QCD multi-jet processes have high cross section values.

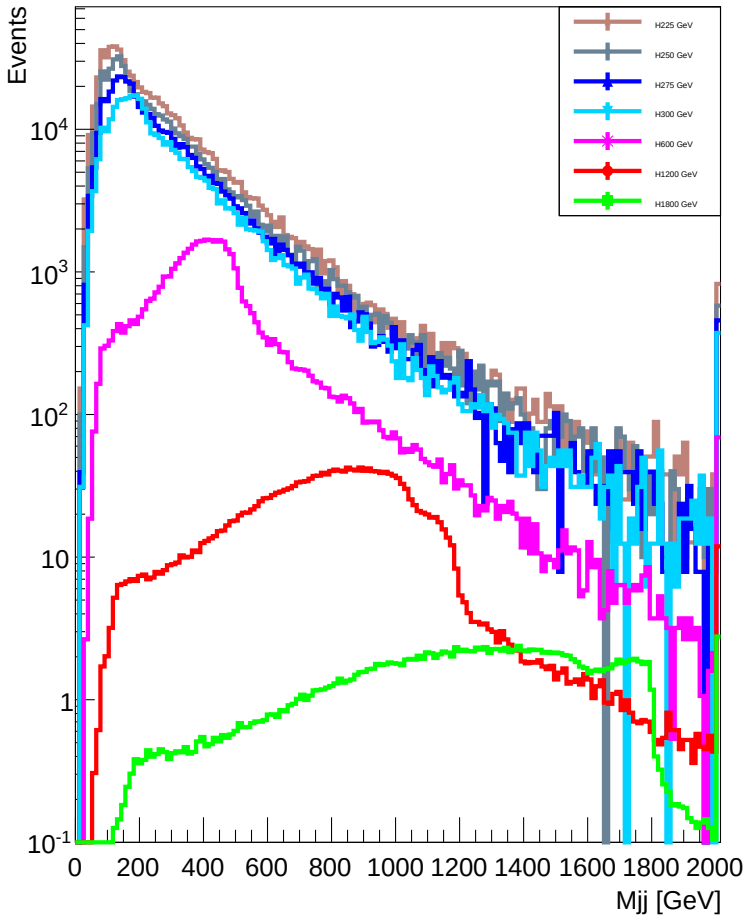


Figure V.1: Dijet invariant mass at the truth level.

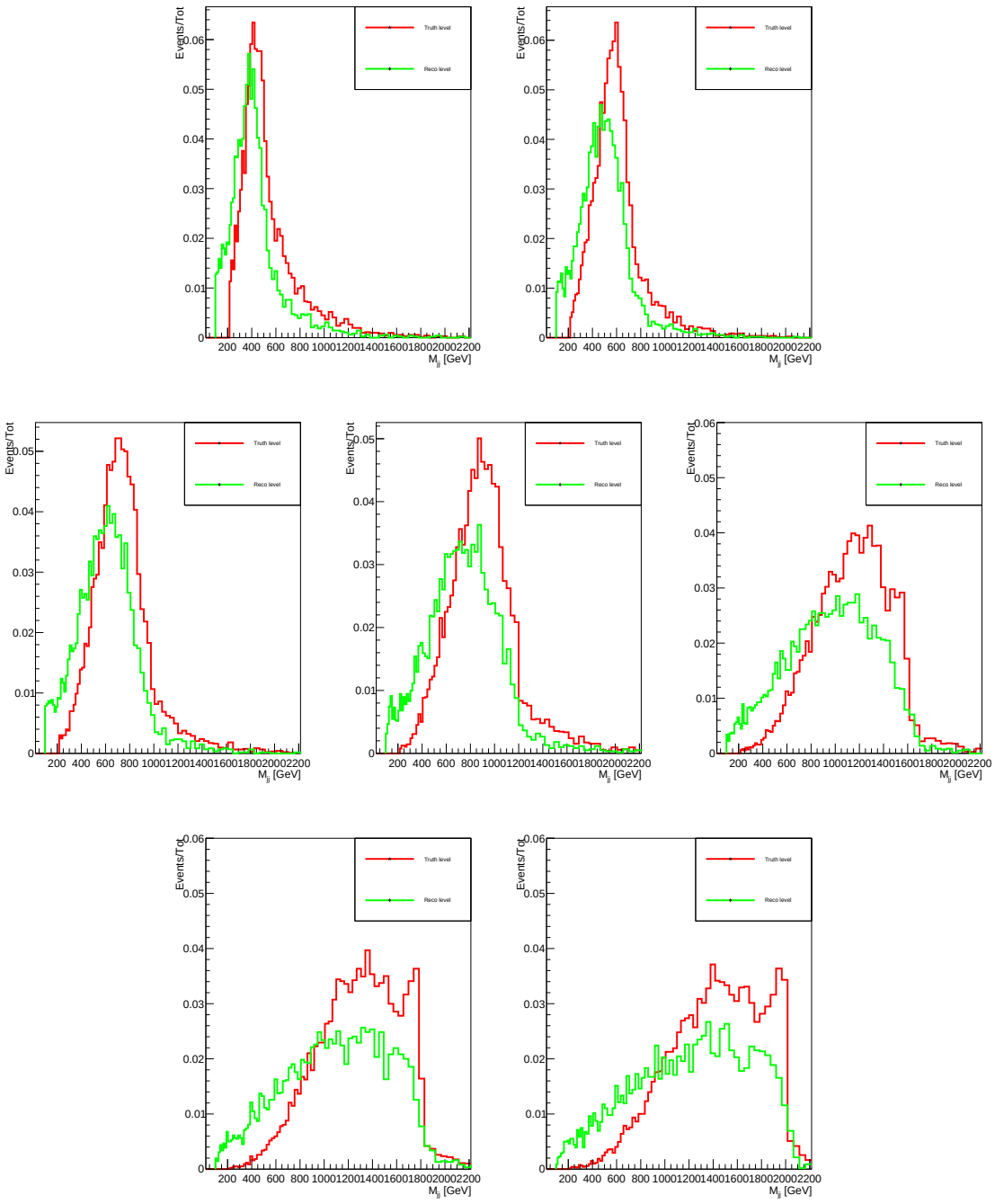


Figure V.2: Comparison of the $m_{jj}$ shapes at the detector and truth levels for Charged Higgs boson Monte Carlo for 600 GeV(top row left), 800 GeV (top row right), 1000 GeV (2nd row left), 1200 GeV (2nd row middle), 1600 GeV (2nd row right), 1800 GeV (3rd row left) and 2000 GeV (3rd row right).

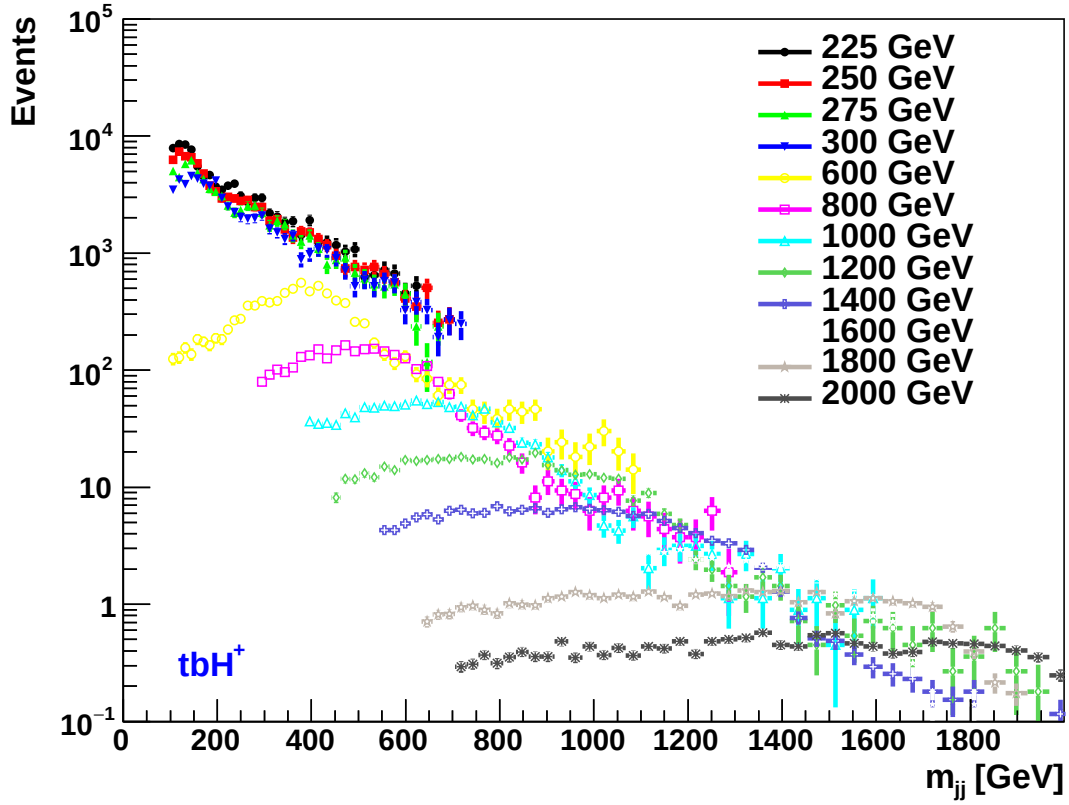


Figure V.3: Reconstructed $m_{jj}$ distribution for signal samples generated with $tbH^+$ model. The numbers of events for each mass are the predictions for the 139 fb$^{-1}$ luminosity.

| Background process | Number of events (MC16a, MC16d) | cross section [nb] |
|---|---|---|
| QCD Multijets (JZ0W slice) | 16000000, 15987000 | $7.8420 \times 10^{7}$ |
| QCD Multijets (JZ1W slice) | 15998000, 15997000 | $7.8420 \times 10^{7}$ |
| QCD Multijets (JZ2W slice) | 15989500, 15981000 | $2.4332 \times 10^{6}$ |
| QCD Multijets (JZ3W slice) | 15879500, 15878500 | $2.6454 \times 10^{4}$ |
| QCD Multijets (JZ4W slice) | 15925500, 15974500 | $2.5463 \times 10^{2}$ |
| QCD Multijets (JZ5W slice) | 15993500, 15991500 | 4.5535 |
| QCD Multijets (JZ6W slice) | 17834000, 17880400 | $2.5753 \times 10^{-1}$ |
| QCD Multijets (JZ7W slice) | 15983000, 15116500 | $1.6215 \times 10^{-2}$ |
| QCD Multijets (JZ8W slice) | 15999000, 15987000 | $6.2503 \times 10^{-4}$ |
| QCD Multijets (JZ9W slice) | 13995500, 14511500 | $1.9617 \times 10^{-5}$ |
| QCD Multijets (JZ10W slice) | 13985000, 15988000 | $1.1962 \times 10^{-6}$ |
| QCD Multijets (JZ11W slice) | 15948000, 15993000 | $4.2259 \times 10^{-8}$ |
| QCD Multijets (JZ12W slice) | 15815600, 15640000 | $1.0367 \times 10^{-9}$ |
| $t\bar{t}$ (inclusive) | 119432000, 74486000 | $7.2935 \times 10^{-1}$ |
| W+jets ($W \rightarrow \mu^{-}\nu$) | 19101695, 24015767 | 8.2831 |
| W+jets ($W \rightarrow e^{-}\nu$) | 24916639, 31348039 | 8.2831 |
| W+jets ($W \rightarrow \mu^{+}\nu$) | 24997577, 31375307 | $1.1263 \times 10^{1}$ |
| W+jets ($W \rightarrow e^{+}\nu$) | 20710568, 25836680 | $1.1300 \times 10^{1}$ |

Table V.5: Background processes, number of events used in the analysis and their cross sections [6].

### V.3 Event selection and object definitions

Selection requiring high-quality objects has been one of the very important strategies of the analysis. So, proper event selections and object definitions are very important aspects for the study. The analysis used full Run 2 data with 139 $fb^{-1}$ luminosity.

The events are selected with the help of single lepton (electron or muon) trigger. The lowest transverse momenta $p_T$ threshold without trigger presclaing is 24 GeV and the lowest transverse energy $E_T$ without trigger prescaling is 26 GeV for lepton triggers.

For the electron triggers, the following High level triggers (HLTs) have been used for the studies :

`HLT_e26_lhtight_nod0_ivarloose, HLT_e24_lhmedium_nod0_ivarloose, HLT_e60_medium, HLT_e60_lhmedium_nod0`

For the Muon triggers, the following High level triggers(HLTs) have been used for the studies :

`HLT_mu24_iloose, HLT_mu24_ivarloose, HLT_mu24_ivarmedium, HLT_mu26_ivarmedium, HLT_mu24_imedium, HLT_mu26_imedium, HLT_mu40, HLT_mu50`

The triggers operate in inclusive OR nature and the naming convention of the triggers is: `HLT_eN_idInfo[_lhinfo][_isolationInfo]` where N represents numbers and denote the $p_T$ cuts for the triggers. The suffix after the number denoted the identification info including the info on likelihood calculation and the isolation information for the trigger. loose, medium, tight denote the loose isolation, medium isolation and the tight isolation. The triggers whose name only contain the number and doesn't contain identification or isolation suffixes, are the triggers which don't have identification or isolation requirements. Such triggers are often useful and added to recover from the low efficiency at the high momenta.

Comparative studies on the different triggers based on quality, id, isolation and $p_T$ cuts have been done for the selected events using those triggers.

Figure V.4 shows that `HLT_e26_lhtinght_nod0_ivarloose` electron HLT trigger and `HLT_mu26_ivarmedium` triggers with $p_T \geq 26$ GeV cuts select maximum number of events. Trigger `HLT_e26_lhtinght_nod0_ivarloose` denote a trigger without d0, the transverse impact parameter, tight identification likelihood and loose isolation whereas `HLT_mu26_ivarmedium` denote a trigger with medium isolation without any identification requirements. It should be noted that the event rates with triggers change before and after applying final set of event selection criteria.

The dijet + lepton analysis deals with different Physics objects including the leptons and jets. To select events with leptons and jets for the dijet resonance searches, dedicated studies are needed to compare the selection cuts, identifications and isolation criteria. In this section, some of those comparisons are shown and the criteria for selection of leptons and jets are summarized briefly.

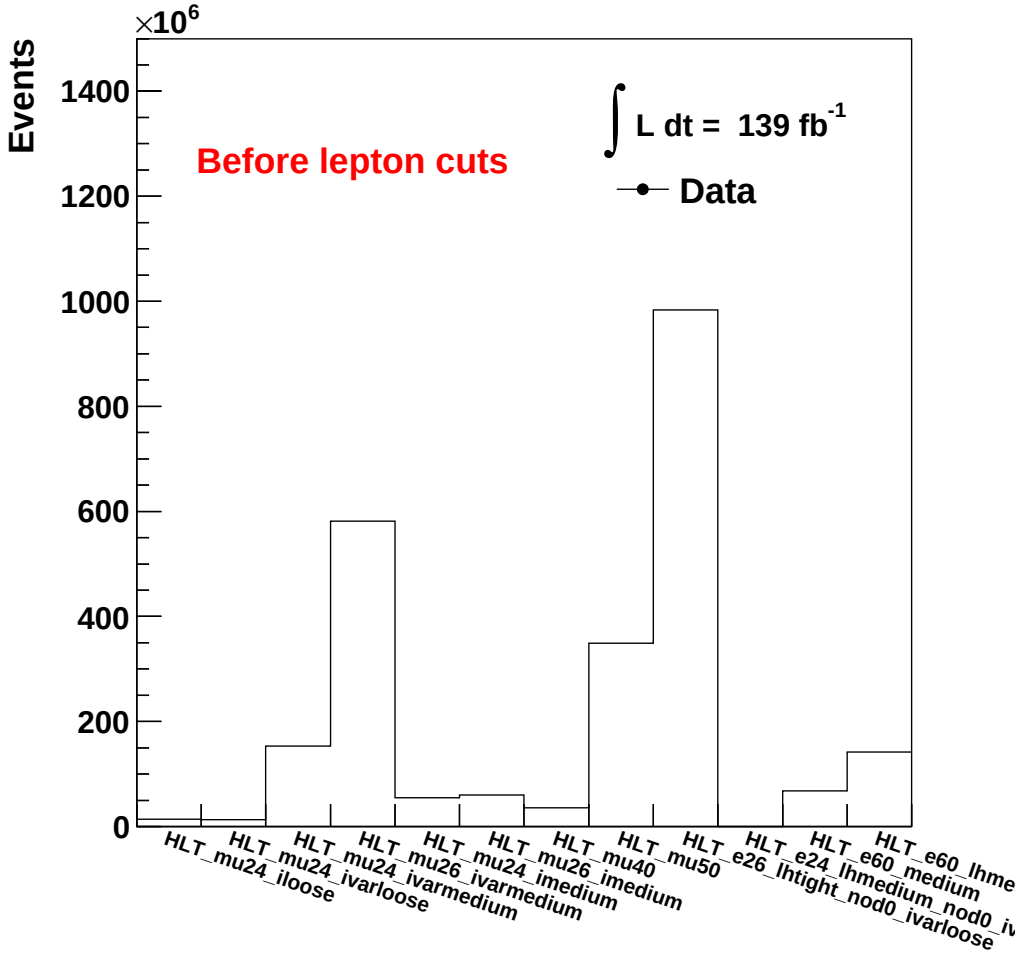


Figure V.4: Event rates for fired electron and muon triggers before selecting events.

### V.3.1 Electrons and muons : selection of events

As discussed in Chapter 2, muons are the particles with interesting feature as they can't be stopped by the detector. But Muon spectrometer can measure the momenta of the passing muons. By combining the information from the inner detector and the muon spectrometer, it is possible to reconstruct the tracks of muons. For that there are some criteria for examples, the transverse momenta should be more than 7 GeV and eta of muon should be within 2.5 values. While combining the information from the Muon spectrometer and the Inner detector, the significance of difference of the ratio of charge and momenta (q/$p_{MS}$-q/$p_{ID}$ between the two sub-detectors are also applied on the tracks. After qualifying few additional requirements of transverse impact parameters and longitudinal positions, a muon is selected as with 'Loose' isolation criteria if it fulfils the following criteria as described in the table V.6

Electrons after passing through the inner detector deposits its energy in the Electromagnetic (EM) calorimeter. As a result, the identification of electrons are done by combining information from the track information from inner detector and the en-

ergy information at the EM calorimeter. Except the barrel-endcap transition region, electrons are selected as 'Loose' if it fulfils the criteria as mentioned in the table V.7

| Muon selection | |
|---|---|
| Criteria | Value |
| Selection Working Point | Tight |
| Isolation Working Point | FCtight |
| Momentum Calibration | Sagitta Correction Not Used |
| $p_T$ Cut | $> 20$ GeV |
| $\eta$ Cut | $< 2.7$ |
| $d_0$ Significance Cut | $< 3$ |
| $z_0$ Cut | $< 0.5$ mm |

Table V.6: Muon selection criteria

The trigger efficiency for both muons and electrons change over time as it can been seen from figure V.5 where for different years of 2015 to 2018 of run 2, the trigger efficiency varies specially for the low regions of electron transverse energy $E_T$.

Similarly, figure V.6 shows that, trigger efficiency for muons for different years of 2015 to 2018 of run 2, for different values of muon's transverse momenta $p_T$.

The trigger efficiency for electron is 97% as measured through Z tag-and-probe method [141] and 72 % for muons [19] while measured separately, but while combining electrons and muons, the combined trigger efficiency is of 88%.

| Electron selection | |
|---|---|
| *Feature* | *Criteria* |
| Pseudorapidity range | $(\lvert\eta\rvert < 1.37)$ \|\| $(1.52 < \lvert\eta\rvert < 2.47)$ |
| Energy calibration | "es2017_R21_v1" (ESModel) |
| Transverse momentum | $> 20$ GeV |
| 2*Object quality | Not from a bad calorimeter cluster (BADCLUSELECTRON) |
| | Remove clusters from regions with EMEC bad HV (2016 data only) |
| 2*Track-to-vertex association | $\lvert d_0^{BL}(\sigma)\rvert < 5$ |
| | $\lvert\Delta z_0^{BL} \sin\theta\rvert < 0.5$ mm |
| Identification | TightLH |
| Isolation | FCTight |

Table V.7: Electron selection criteria

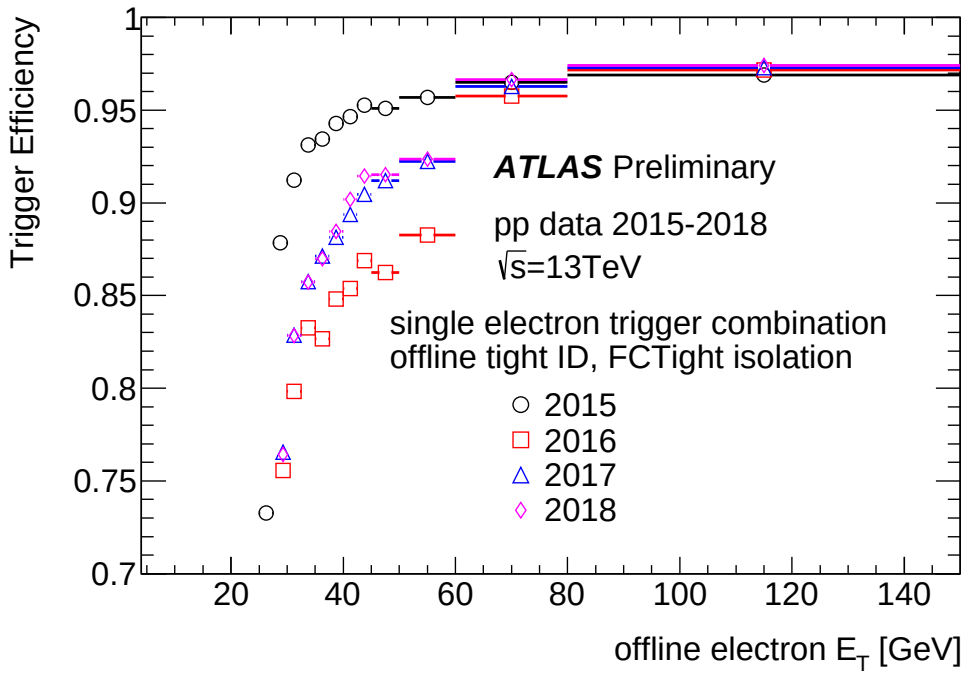


Figure V.5: Comparison of efficiencies due to lowest unprescaled single electron triggers in the years of 2015, 2016, 2017 and 2018 are shown in the plots as function of offline electron transverse energy $E_T$. FCTight isolation and tight offline identification are ensured for the offline electrons. Among 2015 triggers logical OR of HLT_e24_lhmedium_L1EM20VH, HLT_e60_lhmedium and HLT_e120_lhloose and among triggers of 2016-2018, logical OR of HLT_e26_lhtight_nod0_ivarloose, HLT_e60_lhmedium_nod0 and HLT_e140_lhloose_nod0 are used [18].

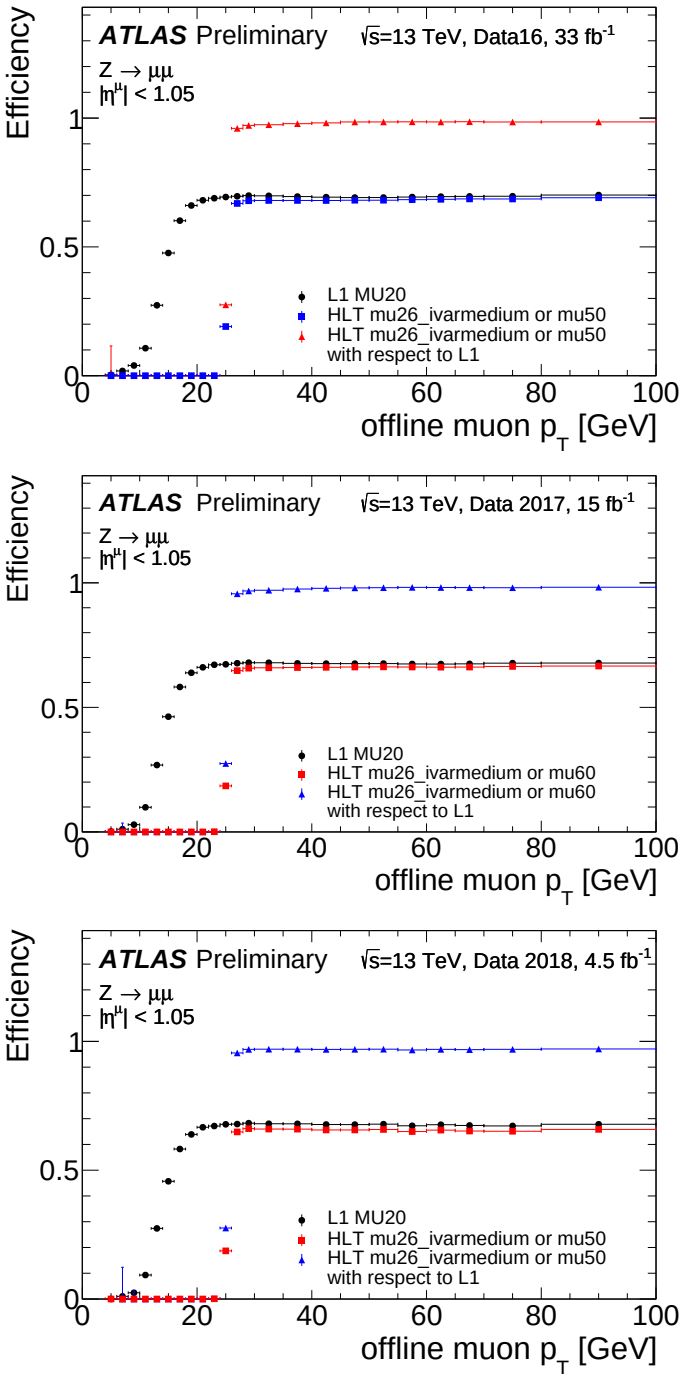


Figure V.6: Efficiency of Level 1 (L1) MU20 trigger and absolute and relative efficiencies of the OR of mu26_ivarmedium with mu50 HLT plotted as a function of $p_T$ of offline muon candidates for different years (2015 year is similar to 2016 plot) [19] for three different years. The top plots is for year 2016, the second plot is for 2017 data and the bottom plot is for 2018 data. Offline isolated muon candidates and are required to pass "Medium" quality requirement.

### V.3.2 Jets : selection of events

Jets are formed through hadronization of particles in the detector. Using anti-$k_T$ algorithm [142] within FastJet package [143], jets are constructed from topological clusters. Jet-vertex-tagging (JVT) algorithm [144] is implemented to avoid pileup due to jets from different collision events. For pileup mitigation, JVT algorithm puts a condition that 60% of the tracks' total momentum must come from the primary vertex. Also, the jets are selected if they have transverse momenta more than 20 GeV and $|\eta| < 2.4$. Though it can be seen in the figure V.7 that jets are mostly distributed in the central eta region fir the Charged Higgs model.

Table V.8 summarizes the definition and the selection criteria of a jet.

| Jet reconstruction parameters | |
|---|---|
| Parameter | Value |
| algorithm | anti-k$_T$ |
| R-parameter | 0.4 |
| input constituent | EMTopo |
| Analysis Release Number | |
| CalibArea tag | CalibArea-05 |
| Calibration configuration | JES_data2017_2016_2015_Consolidated_EMTopo_2018_Rel21.config |
| Calibration sequence (Data) | JetArea_Residual_EtaJES_GSC_Insitu |
| Calibration sequence (MC) | JetArea_Residual_EtaJES_GSC_Smear |
| Selection requirements | |
| Observable | Requirement |
| Jet cleaning | LooseBad |
| BatMan cleaning | No |
| | $>$ 20 GeV |
| $\|\eta\|$ | $<$ 2.47 |
| JVT | $>$0.59 for $<$60 GeV , $\|\eta\|<$2.4 |

Table V.8: Jet definitons and selections as used in the analysis.

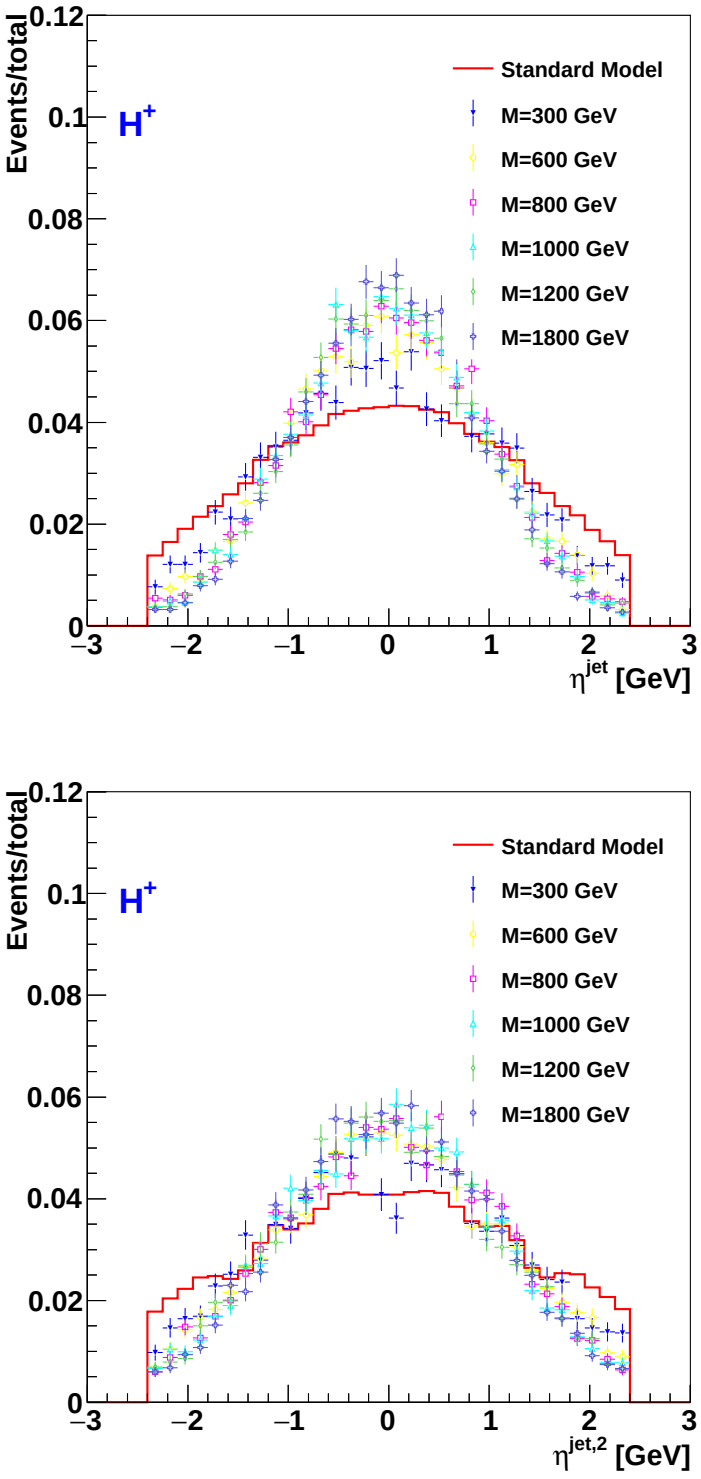


Figure V.7: $\eta$ distributions for leading (top) and sub-leading(bottom) in $p_T$ jets for signal and background Monte Carlo. The background MC (red line) includes all the different backgrounds combined with the expected cross sections for 139 fb$^{-1}$ luminosity.

### V.3.3 Efficiency of HLT triggers

As discussed in the previous sections, the trigger efficiency changes before and after selections. The figure V.8 is a good example of that if compared to figure V.4. It can be observed that after selections, the most prominent triggers with highest event rate are e60 and mu50 triggers which represent electron trigger for $E_T \geq 60GeV$ for electrons and $p_T \geq 50GeV$ for muons respectively. The combined event rate due to these two triggers is around 95.2%.

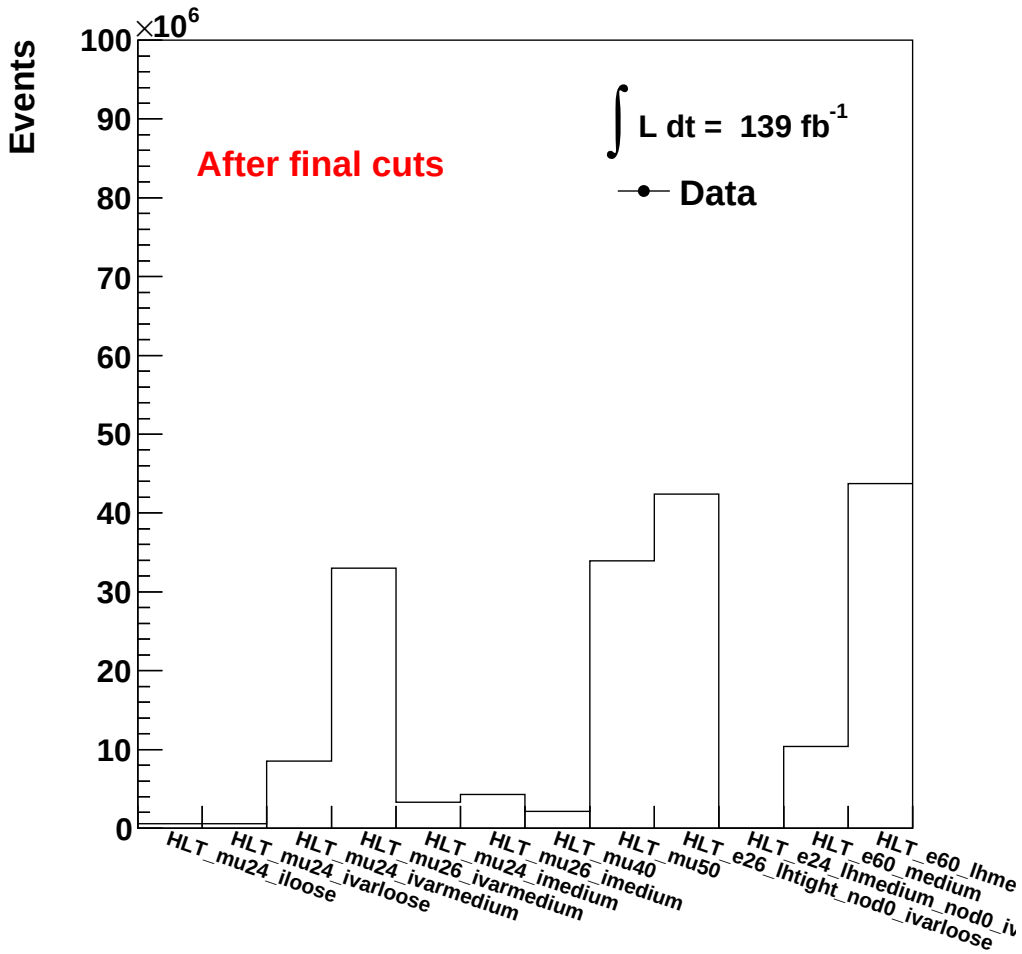


Figure V.8: Event rates for fired electron and muon triggers selecting events.

Using bootstrap method, comparative studies have been done for these two HLT triggers along with triggers associated with lowest $p_T$ thresholds. If $L$ represents all the low $p_T$ triggers and $L\&H$ represents high $p_T$ threshold triggers while passing the low threshold trigger chains and it can be described as :

$L\&H$ = (mu50 ||e60) &&(all low $p_T$ triggers)

For the whole run 2 data from 2015-2018 for both theses electron and muon triggers, efficiency comparisons have been done. Comparisons on the value of $m_{jj}$

have been done and it has been found with the increase in $m_{jj}$, the efficiency also smoothly as with around $m_{jj} = 200$ GeV, the global efficiency is around 98% which is higher than the case when $m_{jj} = 100$ GeV.

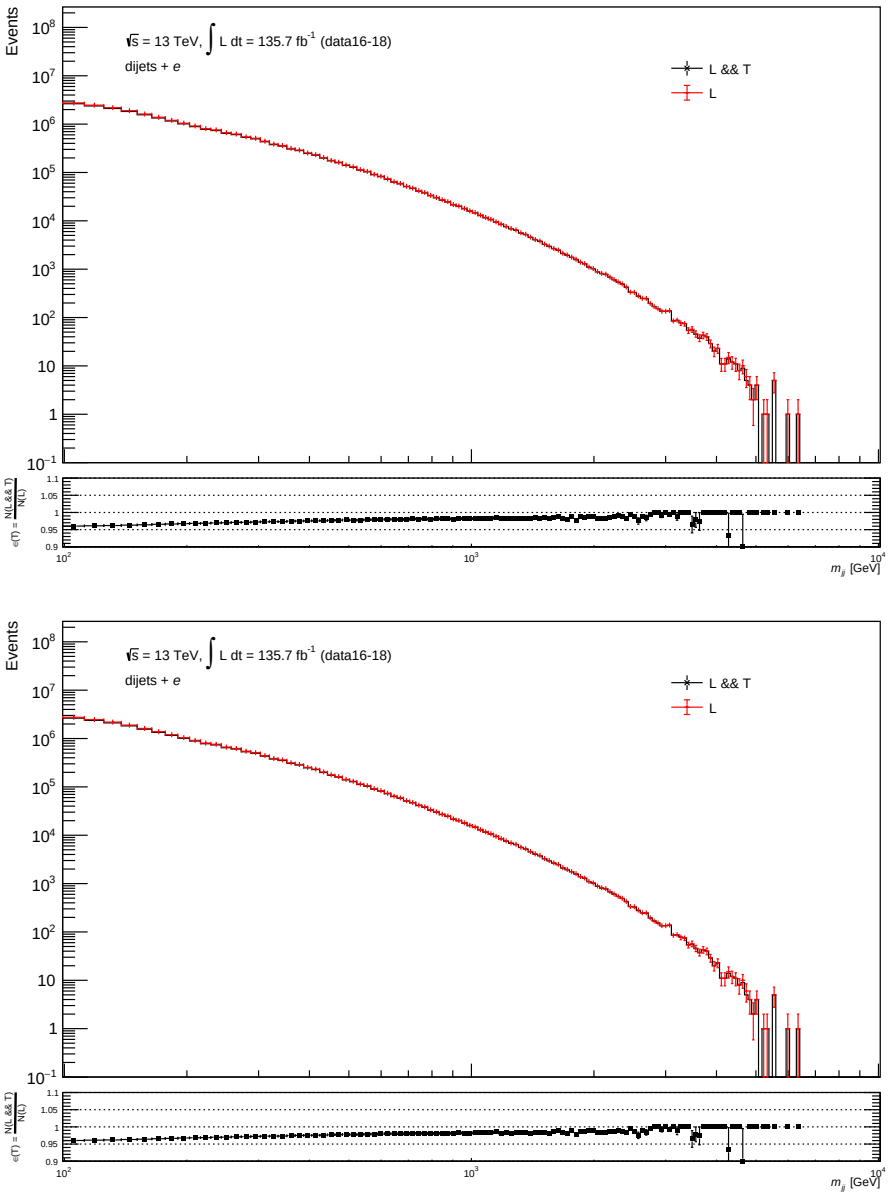


Figure V.9: Studies of the efficiency of the high-threshold electron trigger (e60) using 2015 data (top plot) and 2016-2018 data (bottom plot) with respect to $m_{jj}$.

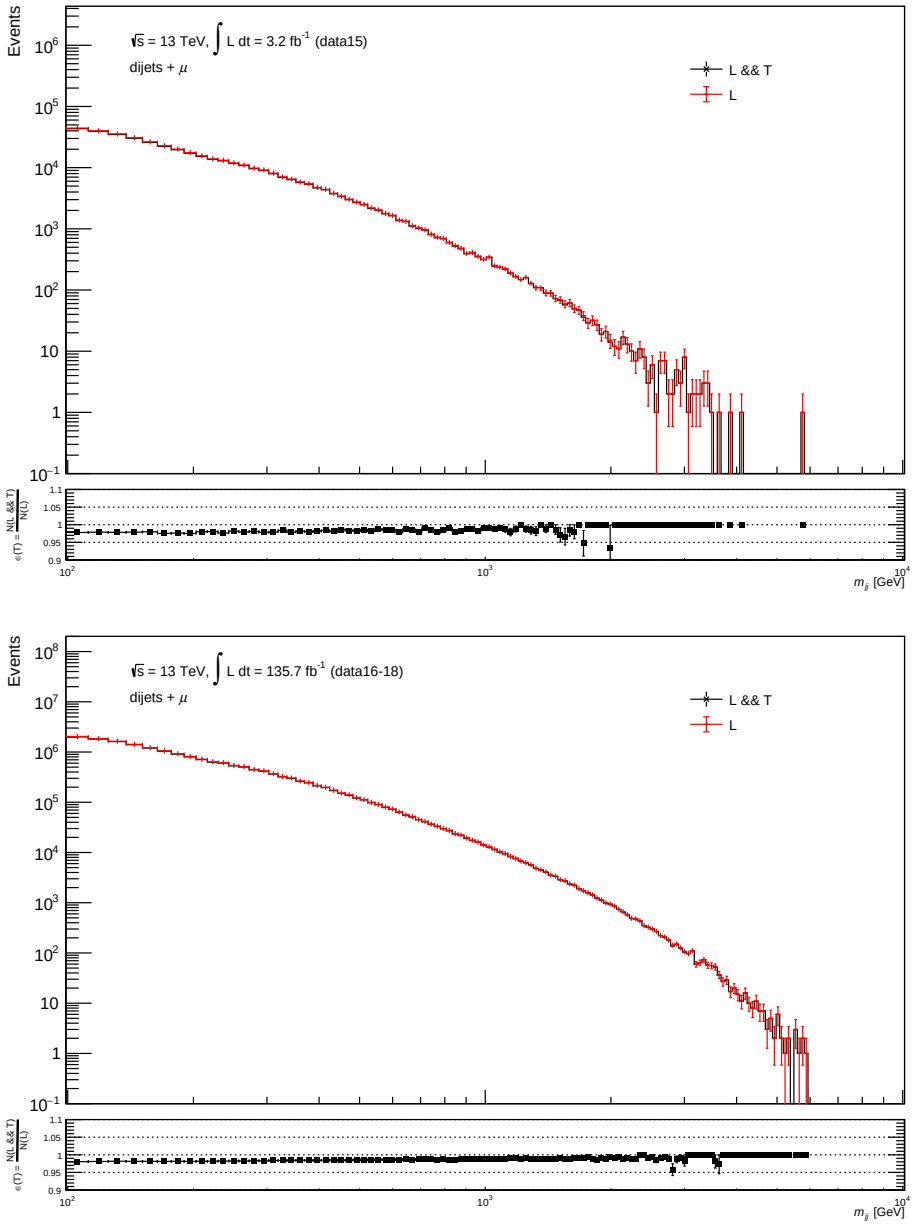


Figure V.10: Studies of the efficiency of the high-threshold muon trigger (mu50) using 2015 data (top plot) and 2016-2018 data (bottom plot) with respect to $m_{jj}$.

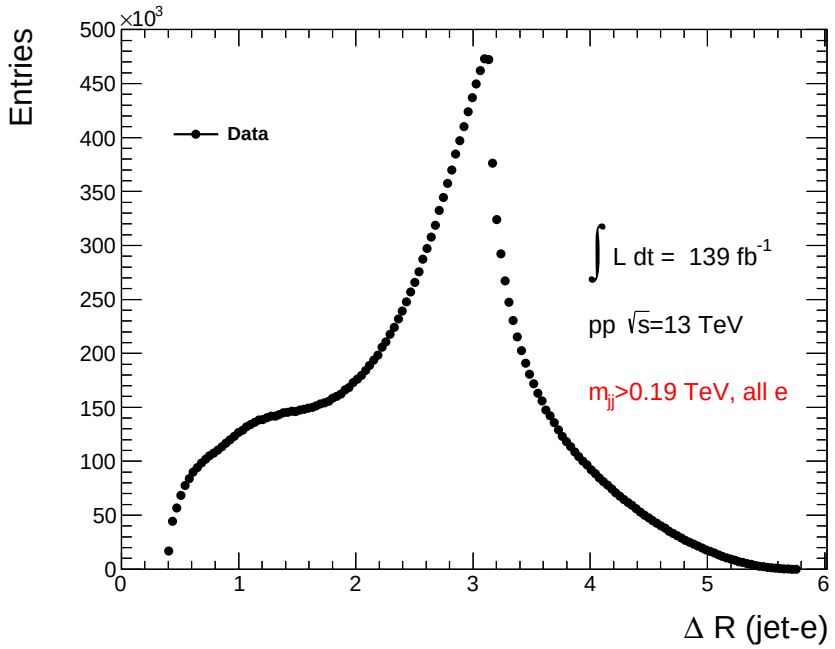


Figure V.11: The distributions of $\Delta R(jet, electron)$ that defines a distance between leading jet and any electron above $p_T^l > 60$ GeV for for $> 190$ GeV (note this cut is lower than for the central analysis).

### V.3.4 Overlap removal

Mis-identification between electron and muon or between leptons and jets are common in detector studies. As a result, strong criteria are needed to remove the overlap for the appropriate identification of jets and leptons. The criteria by which for example an electron is rejected as a muon or a jet is rejected as an electron can be found in Table V.9, where different values with $\Delta R$ represent cone with $\Delta R$ value around the axis of a jet. An example of $\Delta R(jet, electron)$ can be seen in Figure V.11.

| Reject | Against | Criteria |
|---|---|---|
| electron | electron | shared track, $p_{T,1} < p_{T,2}$ |
| muon | electron | is calo-muon and shared ID track |
| electron | muon | shared ID track |
| jet | electron | $\Delta R < 0.2$ |
| electron | jet | $\Delta R < 0.4$ |
| jet | muon | NumTrack $< 3$ and (ghost-associated or $\Delta R < 0.2$) |
| muon | jet | $\Delta R < 0.4$ |

Table V.9: Criteria for overlap removal

The final selection criteria for different objects are summarized in Table V.10.

| Object | Type | $p_T$ | $\eta$ | Cleaning/ID/isolation |
|---|---|---|---|---|
| Jet selection | Anti-$k_T$ 0.4 EMTopo jets | $p_T > 20$ GeV | $\|\eta\| < 2.47$ | "LooseBad" Cleaning |
| Muon selection | | $p_T > 60$ GeV | $\|\eta\| < 2.7$ | "Medium" ID, "FCTight" isolation |
| Electron selection | | $p_T > 60$ GeV | $\|\eta\| < 1.37$ , $1.52 < \|\eta\| < 2.47$ | "TightLH" ID, "FCTight" isolation |

Table V.10: Final selection cuts for objects

### V.3.5 Minimum $m_{jj}$

Jets are not directly affected by triggers and it is also assumed that if leptons are misidentified as jets, $p_T > 60$ GeV cuts for leptons may affect the jet reconstruction. Also at the low region of $m_{jj}$ near 100 GeV, there are possibilities that production of W or Z boson may contribute in distorting the smooth distribution of $m_{jj}$. Figure V.12 provides a comparison among different values for minimum $p_T$ of lepton. For different values of $p_T^{lepton}$, the distributions of $p_T^{jet}$ can be observed. For the cut of $p_T^{lepton} > 60$ GeV, $p_T^{jet}$ starting from 216 GeV provides a smooth distribution.

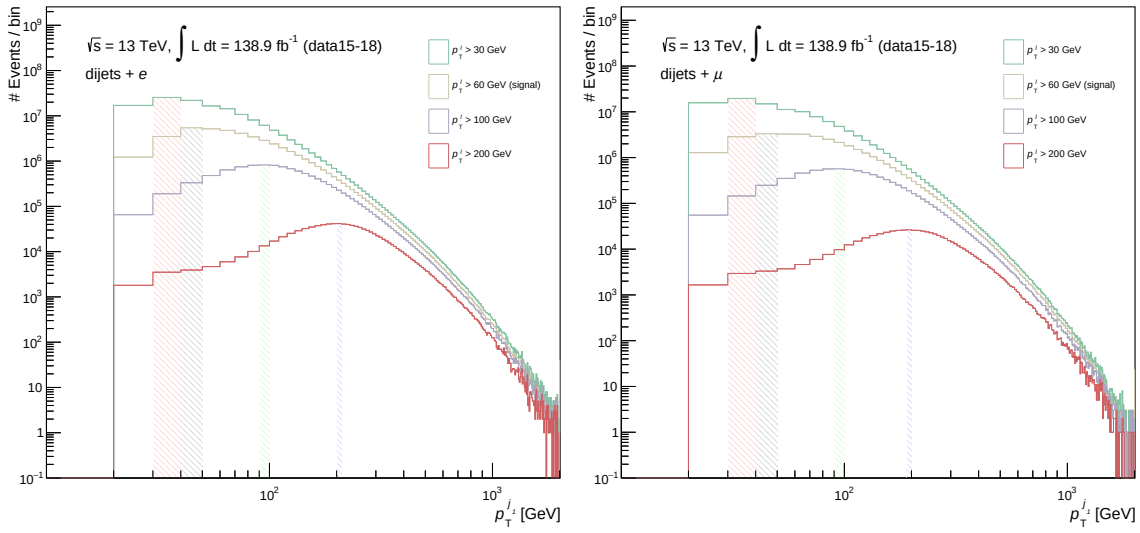


Figure V.12: Studies of the leading jet $p_T$ for different cuts of $p_T^{lepton}$ on electrons (top) and muons (bottom) respectively.

Some past studies [145] also suggests the minimum $m_{jj}$ value above 216 GeV. So, for this analysis, minimum $m_{jj}$ value has been selected as 216 GeV. So the analysis searches for the excess of events as a sign of resonance in the smooth, monotonically decreasing distribution of dijet invariant masses between 216 GeV to 6.3 TeV. To avoid the possibilities of $edgeeffects$, if exclusion limits are calculated, they will be calculated within the mass range of 250 GeV to 6 TeV.

## V.4 Data-Monte Carlo comparison

It is important for any analysis to compare the data and Monte Carlo simulations to see to what extent they match. For that purpose data collected in Run 2 during 2015-2017 and simulations of MC16a-d campaigns have been compared to check the different kinematic distributions.

Figure V.13 shows the the $p_T$ distributions for the selected objects such as electrons, muons and jets.

Figure V.14 provides an example of preliminary data-mc comparison for Dijet invariant mass $m_{jj}$ distributions with leptons. Similarly, Figure V.15 provides a preliminary comparison of data and Monte Carlo for the leading and sub-leading jet $p_T$.

## V.5 Analytic functions and statistical tests

Since the analysis looks for excess in events in dijet invariant mass $m_{jj}$ distributions, it is important that the distribution is optimized. Jet Energy resolution of the ATLAS detector is used for that purpose and the bins of the distribution is selected as if that is almost equal to the resolution at a given mass.

To define the shape of estimated background, the following 5 parameter fit function is used :

$$f(x) = p_1(1-x)^{p_2}x^{p_3+p_4\ln x+p_5\ln^2 x}, \tag{V.5.1}$$

where $x \equiv /\sqrt{s}$ and the $p_i$ represent 5 free parameters, which should be estimated. As in this analysis, the $m_{jj}$ is very wide and more parameters, bring more degree of freedom, so 5 parameter function has been considered. Though it should be noted that more parameters may also have the possibilities that it can make the fits unstable and complicated. To ensure that is not the case, different statistical tests are conducted.

At the same time, to calculate the systematic uncertainty due to the above function, an alternative fit function has been used to provide an alternative prediction about the tail of the distribution:

$$f(x)^{alt} = p_1(1-x)^{p_2}x^{p_3+p_4\ln x+p_5/\sqrt{x}}, \tag{V.5.2}$$

While performing fits, its important to cross check the minimization for the fit functions. For that purpose Minuit/ROOT program which use inputs from "MigradImproved" fits using random parameters. To define the appropriate parameter space, fit with the smallest $\chi^2$ are chosen. For example, five parameter fits can have multiple solutions, among them the solution with lowest $\chi^2$ value is selected. In general any fit which has $\chi^2/ndf > 2$ is not selected.

The residual distribution is also studied in details to ensure good fit quality. In idea case, the tails of residual distribution should be perfectly symmetric while following Normal distribution with $\sigma = 1$.

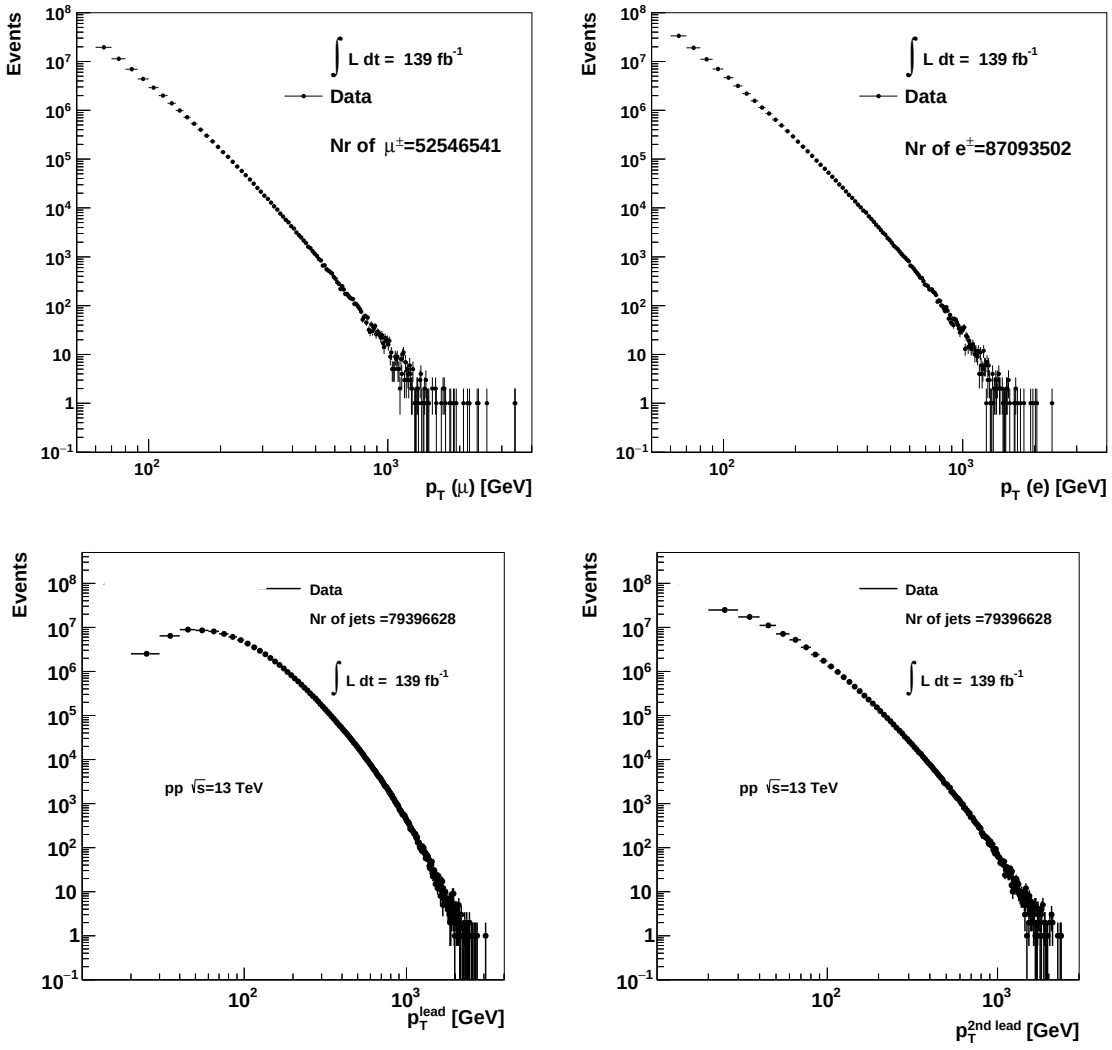


Figure V.13: The distribution of transverse momentum distribution for selected muons(top left), electrons (top right), leading jets(bottom left) and sub-leading jets(bottom right)

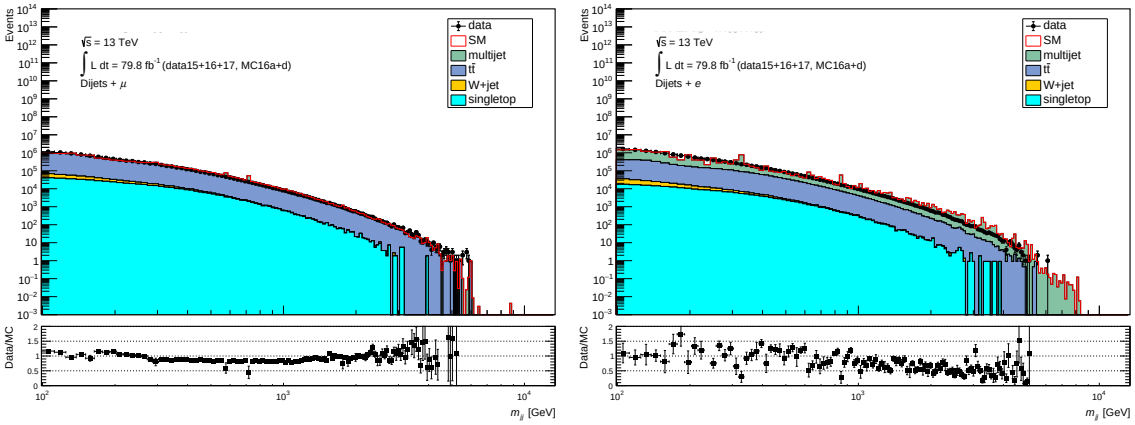


Figure V.14: Dijet invariant mass $m_{jj}$ distributions comparing data and MC. Large differences of over 50% between data and MC appear due to limited statistics in multijet samples. These statistical fluctuations makes quantitative comparisons inappropriate.The left plot is for muons and the right plot is for electrons.Final analysis was done using a data-driven method, without relying on the background MC presented in this figure.

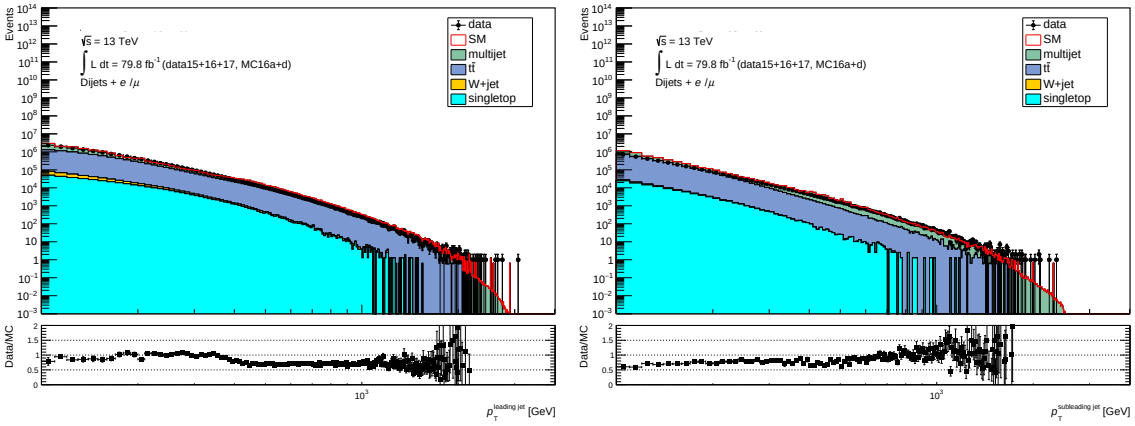


Figure V.15: Jet $P_t$ distributions comparing data and MC. Differences of over 50% also appear here. Final analysis was done using a data-driven method, without relying on the background MC presented in this figure.

Different statistical tests which are performed for ensuring fit quality are the following :

Gaussian Fit : On the residuals, Gaussian fits are implements and it is ensured that the peak position of the fitted Gaussian is at zero and it has width = 1. To check this, $\chi^2/ndf$ test is used.

Shapiro-Wilk's test : The residual distributions are also tried with Shapiro-Wilk's test which checks the extent to which the distribution follows normality with the help of $p$-values. For $p$-value $> 0.05$, the Shapiro-Wilk's test certifies for the normality condition. Though for the analysis, Shapiro Wilk test has been done, but while talking decisions of fit quality, they have not been used.

Kolmogorov-Smirnov (KS) test : The residual distribution is also used for the Kolmogorov-Smirnov (KS) test which investigates if the distribution has a normal distribution with mean equals 0 and the width $\sigma = 1$.The test fails for normality if $KS < 0.5$ where $KS$ is the results from the KS test.

Skewness and Kurtosis checks : Skewness and Kurtosis of the residual distributions can also check whether it is normally distributed. For such distributions, skewness is measured by checking the relative size of the tails and kurtosis checks for possibilities of data being light-tailed or heavy-tailed. For normal distributions, the kurtosis generally has the value of 3 and skewness should be zero. With the help of ROOT program, both of these checks are done on the residual distributions.

While comparing fits with data, the bin-by-bin significance is calculated using fit residuals with the help of the following formula :

$$S_i = \frac{D_i - F_i}{\Delta D_i}, \tag{V.5.3}$$

where $D_i$ represents data point, $F_i$ represents value of the function after the minimization, and $\Delta D_i$ is the uncertainty for the bin (For counting experiments, it is $\sqrt{D_i}$). During likelihood fits, the inclusion of uncertainties coming from the fit function in the definition of significance improves the results.

BumpHunter test : BumpHunter[146] (BH) test has been used extensively for this analysis to find the deviation from the hypothesis that describes only the background. While scanning over the dijet invariant mass $m_{jj}$ distributions, for a fixed number of possible intervals, BumpHunter calculates local $p$ values using unique hypothesis test statistic while it uses the look elsewhere effect [147]. BumpHunter gradually combines each of those different hypothesis tests and forms a new hypothesis test and calculates the minimum $p$ value from different sets. While assuming the fact that the bin-by-bin data follows a Poisson distribution, a global $p$ value and significance values are also calculated. The same procedure as a Pseudo experiment is repeated over 100 times or of for any fixed number of times. The purpose of using multiple pseudo experiment is to find the local excess of most significance. The corresponding global significance is also calculated.

Figure V.16 shows that the five parameter fit describes Monte Carlo simulation description as the $\chi^2/ndf < 2$.

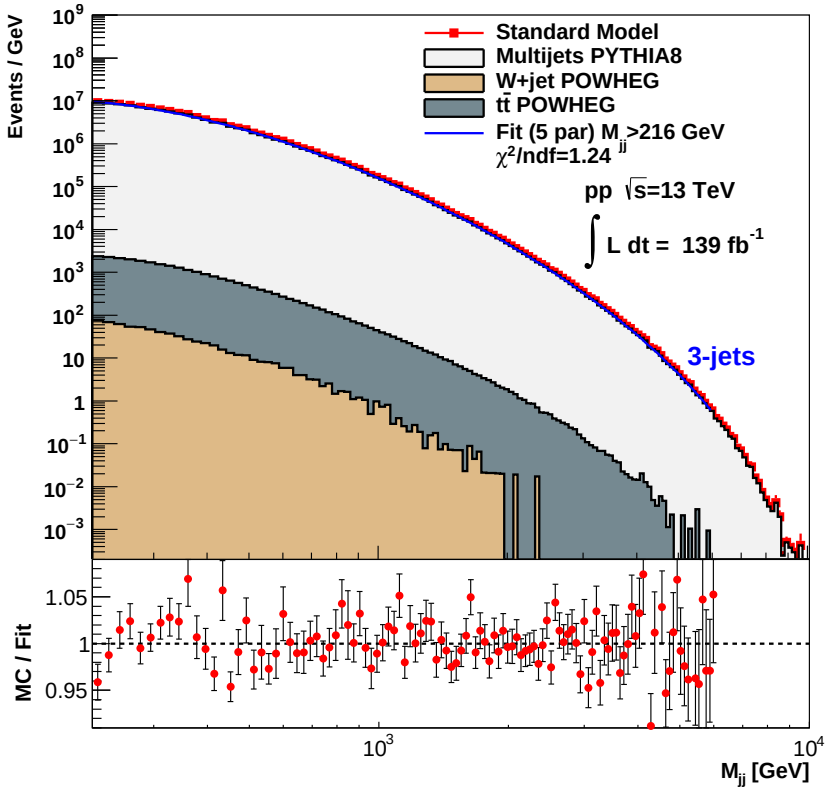


Figure V.16: Example of using 5p fit hypothesis with different Monte Carlo simulations of background samples. The red line denotes the combined contribution of of all Standard Model backgrounds. Each contribution is also shown separately, without stacking the histograms. The observed large spikes in the MC is due to small statistics of the JZ0-JZ12 dijet samples after the lepton requirement.

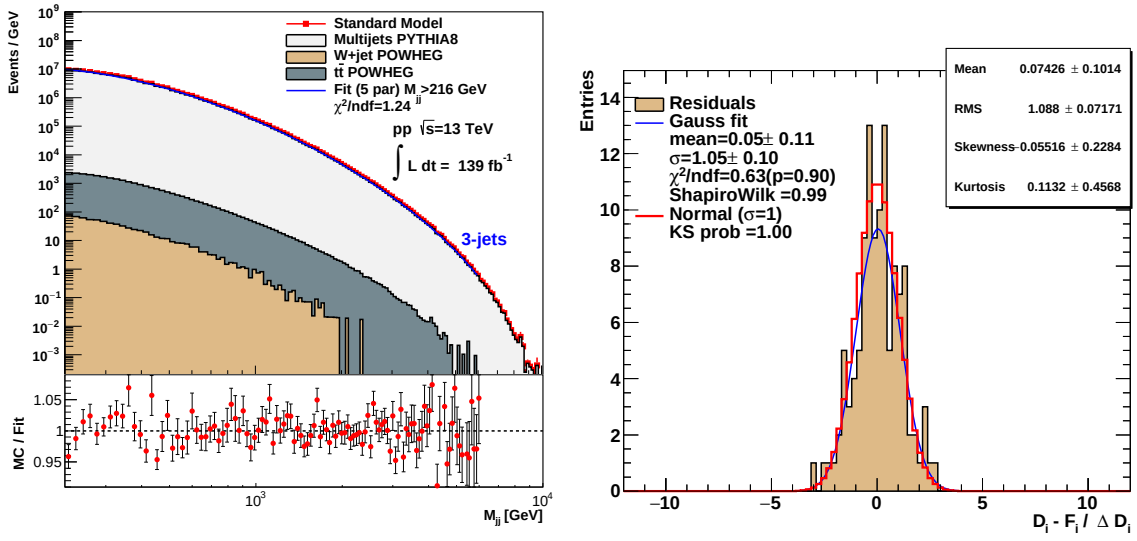


Figure V.17: The left plot shows the 5 parameter(Eq. V.5.1) fit in the 2+1 jet control region and the right plot shows the residuals of the 5p fit of the same MC based control region along with the statistical tests. The 3rd jet has $p_T(jet) > 60$ GeV.

## V.6 Control region studies

Control region studies are important to set strategies to deal with the signal regions and t set different parameters for it as well. The control regions are generally selected in such a way so that the physics signatures and kinematics from signal regions in data are matched. For this analysis there has not been a control region which matches exactly with the signal regions, though two control regions have been used for the analysis are: 1. MC based control region and 2. Loose electron control regions. In the following sections, they are discussed very briefly.

### V.6.1 MC based Control region

This control region using the MC simulations has been constructed with the main purpose of of jet reconstruction effects, jet calibrations and other instrumental effects which can contribute to the possibility that a lepton is misidentified as jet and resulting a signal event.

As the analysis looks for resonance by 2 jets in the presence of an isolated charged lepton, this control region forms a "2+1 jets" or 3 jet control region and uses 5 parameter fit function for description. Since in the signal region, the lepton is required to have transverse momenta $p_T > 60$ GeV, in case of 3rd jet also the same $p_T$ requirement of $> 60$ GeV is applied. This control region has more statistics than the signal region in Monte Carlo simulations. For background contributor multijets also, the statistics increases while using a 3rd jet instead of lepton.

The figures V.17, V.18 show the fit with 5 parameter and the alternative 5 parameter fit functions for the control region respectively. It can be concluded that the Eq. V.5.1 described the Monte Carlo simulations well and also it can be noticed,

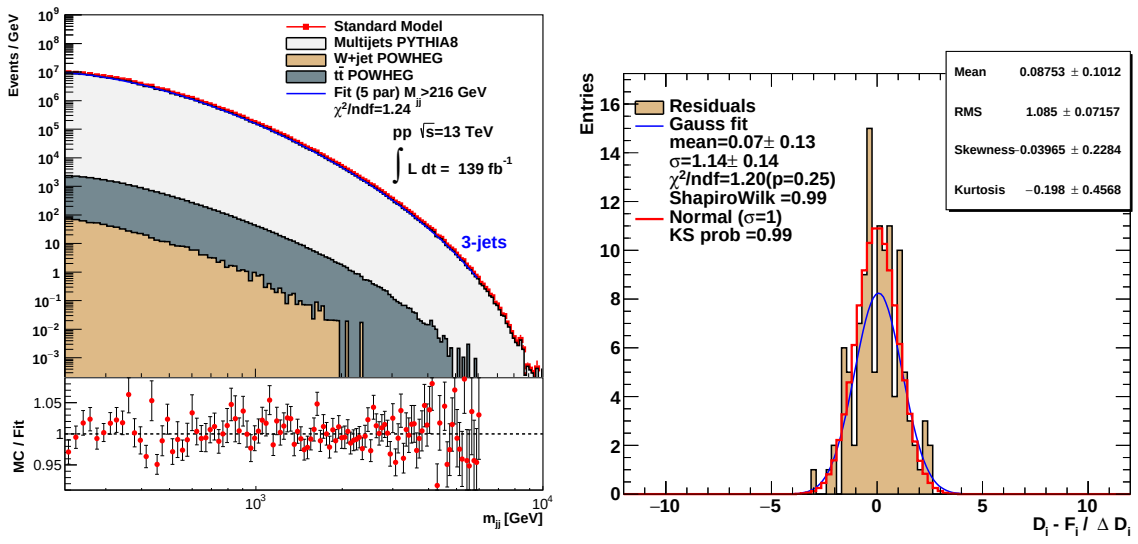


Figure V.18: The left plot shows the alternative 5p fit (Eq. V.5.2) fit in the 2+1 jet control region and the right plot shows the residuals of the 5p fit of the same MC based control region along with the statistical tests. The 3rd jet has $p_T(jet) > 60$ GeV.

among the different background sources, for 3-jet region, W+jet process and $t\bar{t}$ processes contribute very less around 0.01% of the contributions coming from multi-jets.

### V.6.2 Loose electron Control region(LE-CR)

To ensure that no spurious bumps are contributed by jet reconstruction effects, or $m_{jj}$ distributions don't have any biases due to object and event selections, another control region has been constructed by requiring the 2 jets + an isolated charged lepton but with loose lepton identification criteria. The identification criteria for lepton is such that, it fails medium or tight identification conditions , but passes the loosest cuts. In this region, mostly loose electrons are found where only 3% muons can also be observed.

This control region has way more larger statistics than the previously described MC based 2+1 jet region. Loose electron identification criteria provides was more events for the QCD multi-jet events as well.

The figures V.19, V.20 show that Eq. V.5.1 provides good description for the LE-control region as the $\chi^2/ndf < 2$ and the Shapiro wilk test, KS tests provides good results along with Normal distribution having $\sigma = 1$.

Some additional alternative studies have been done on LE-CR region while using a sliding-window fit or "Swift" method [148, 149] which also confirmed the good descriptions by 5 parameter fit function in constructing hypothesis.

So, it can be concluded that based on the studies of both the the control regions of 2+1 jets and LE-CR, the background-only hypothesis for the signal region is constructed over the range of 216 GeV to 6.3 TeV.

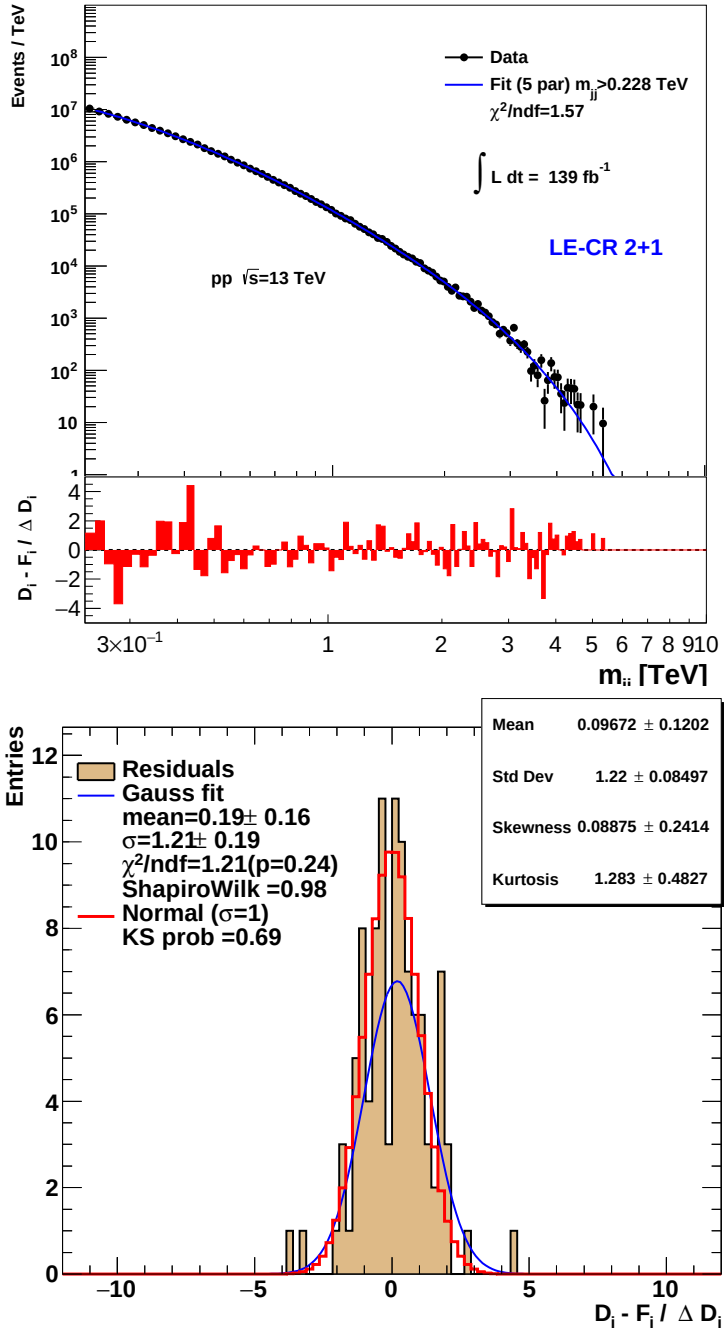


Figure V.19: The top plot shows the 5 parameter(Eq. V.5.1) fit of dijet mass spectra for $>$ 216 GeV in the Loose electron control region and the bottom plot shows the residuals of the 5p fit of the same LE control region along with the statistical tests.

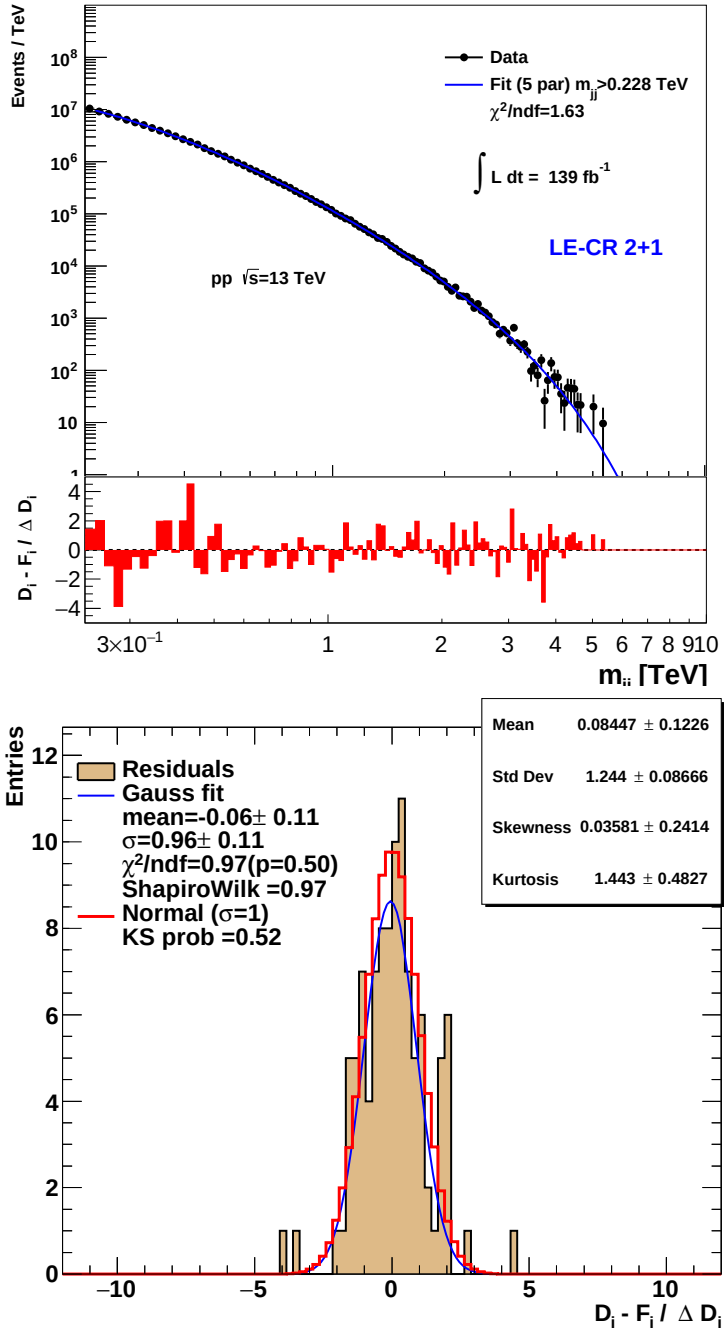


Figure V.20: The top plot shows the alternative function Eq. V.5.2 fit of dijet mass spectra for $>$ 216 GeV in the Loose electron control region and the bottom plot shows the residuals of the 5p fit of the same LE control region along with the statistical tests.

## V.7 Tests on signals

### V.7.1 Signal injection test

While performing searches in the detector, it is possible to have some "spurious signals" which are accidentally produced from the background fits or from the pseudo data whose patterns are similar to real data. To reduce such possibilities, signal injection tests are done. The process involves some steps including : with the help of Gaussian distributions, signal events are modelled and such signals are added to the background distributions to see whether signal plus background fit is able to estimate the correct number of events while considering knows Gaussian shapes for the signal.

For the studies, Loose electron (LE) control region has been used. The detailed steps of the general signal injection process includes the following steps [150] :

1. Creating a set of random histograms using the 5 parameter fit of the LE-CR, scaled to the total number of expected events in the signal region.

2. Calculating the number $N$ of events around a given mass assuming some width (5, 10, 15%) and then calculating 5 $\sqrt{N}$ that approximates the number of events for a 5-sigma sensitivity. Create a Gaussian histogram with 5 $\sqrt{N}$ events and the width (5, 10, 15%), and adding it to the background histogram based on 5p from the first step.

3. Fitting the background+signal histogram from 2nd Step with the 5p background function (using background-only hypothesis), 5p+Gaussian (using the background+signal hypothesis). Alternatively, the Swift method for background can be used.

4. Calculating the numbers of events above the 5p background fit. First assumption is the background-only hypothesis which is the most conservative for the estimates of the number of events. The numbers of events were calculated in the range $\pm 1.5 \times \sigma$ around the known peak position. A wider region was found to be too sensitive to statistical fluctuations for the small signal amplitude considered. In the case of the 5p+Gaussian fit, the numbers of events are calculated by integrating the Gaussian part of the fit.

5. Calculating the efficiency, which is the observed number of events divided by the 5 $\sqrt{N}$.

For the studies of this analysis, both background only hypothesis and signal plus background hypothesis has been used.

The figure V.21 shows the sensitivity of injected signals (which were injected assuming 5 sigma) while using signal plus background hypothesis from the 100 pseudo-experiments. It can also be concluded from the plot that injected signals are well observed.

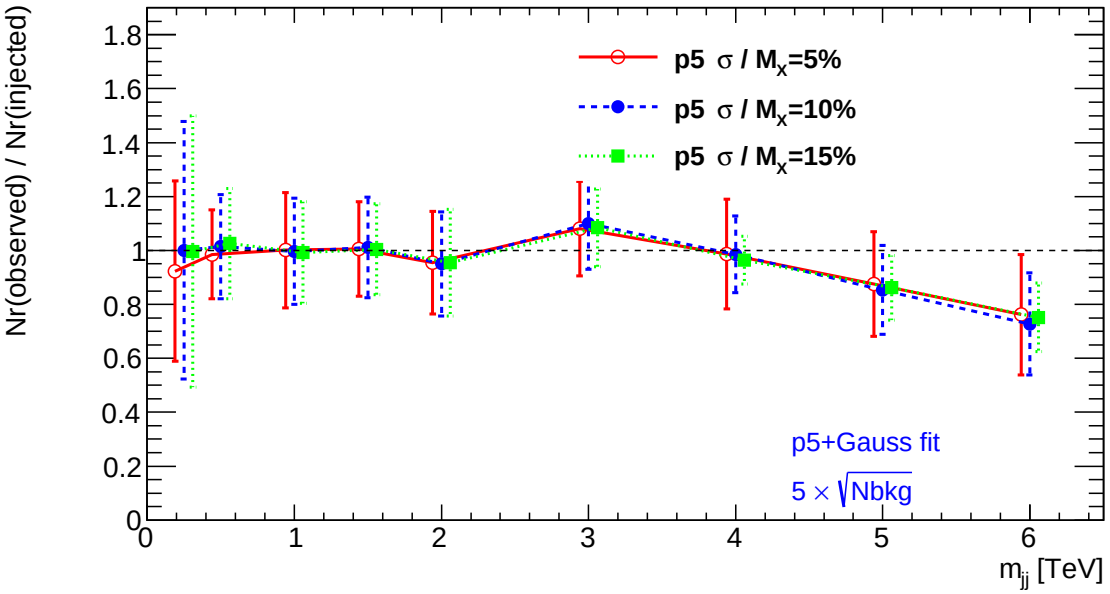


Figure V.21: The plot shows calculated signal reconstruction efficiency using the 5p+Gaussian description while using different widths of the injected Gaussian signals. The number of observed events was calculated from the Gaussian component of the global 5p+Gauss fit using 100 pseudo-experiments. The uncertainties on the data points are the RMS values on the ratios. The peak and the width of the Gaussian function were fixed to the expected values to avoid instabilities in the 8-parameter fit.

### V.7.2 Spurious signal tests

Spurious signal tests are done to detect the possible presence of spurious signals which are not originated from any injected signals. For the studies, templates from Loose Electron control region are created for 100 pseudo experiments and 5p+Gaussian fits have been used to find the fluctuation from Gaussian amplitude.

Figure V.22 is for Gaussian width of 15% only, but during studies other different background templates of different widths are also studied.

It can concluded from the spurious signal studies, it was found that significant deviation from the Gaussian amplitude of zero has not been statistically observed, that signifies absence of spurious signals for the analysis.

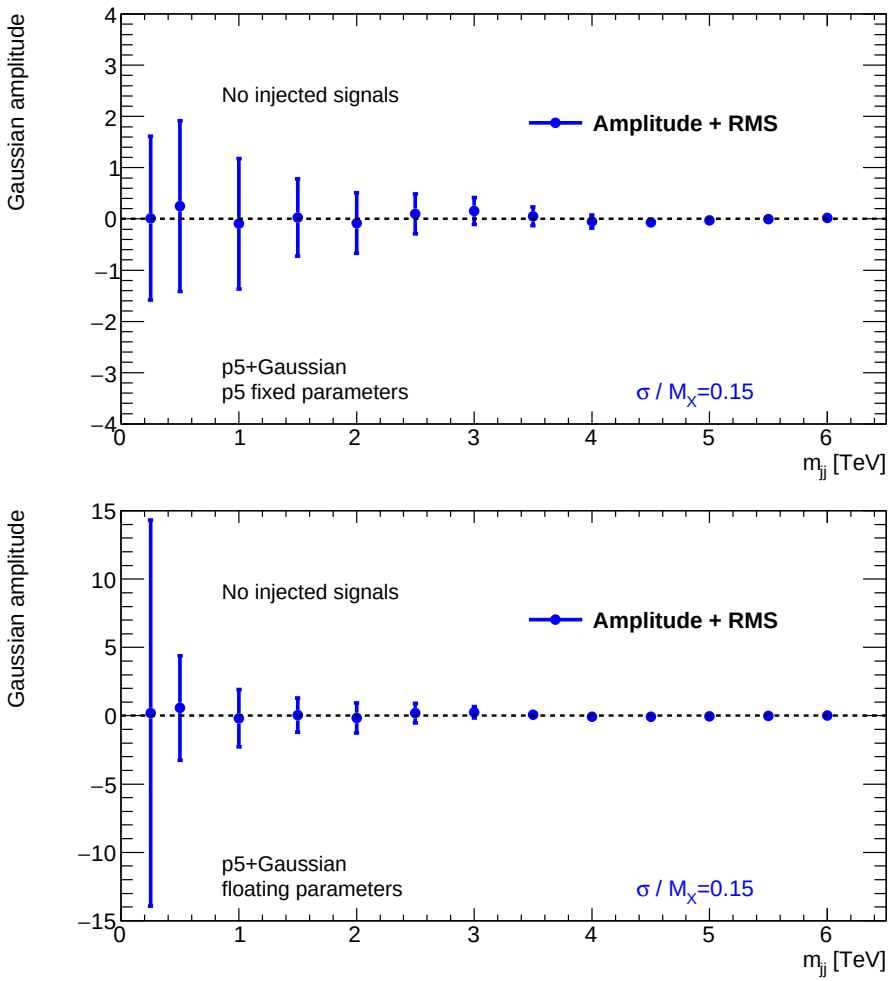


Figure V.22: The average values of events from the Gaussian amplitude (for 15% width) using the 5p+Gaussian fits applied to 100 random templates constructed using background-only hypothesis. For the top plot, the parameters of the 5p fit for 5p+Gaussian were fixed to the 5p-fit only. And for the bottom plot, parameters of the 5p fit were allowed to float (not fixed), though width of Gaussian and peak position are fixed.The vertical error bars shows the RMS values, which are used as additional contribution to systematic uncertainty.

### V.7.3 Tests for Charged Higgs signals

Though the signal and background shapes from detector level can be used for studies with any signal shape, for specific BSM models or resonances corrections on the shapes may be required. Also, there can be difference between the Loose Electron Control region templates and the actual signal templates.

Charged Higgs is a special example as Charged Higgs provide broad signals. If the $H^+$ detector-level limits are needed to correct to the truth level, then it is important to calculate the signal reconstruction efficiency for the 5p background in the case if the signal is broad and asymmetric.

Therefore, the signal injection tests were repeated considered broad signals, $20\%/M$ and $40\%/M$. The latter is a good representation of the $m_{jj}$ from the $H^+$ signal model, which typically has $RMS/M$ close to 40% for masses above 600 GeV. Such signals are typically asymmetric and cannot be well approximated with the standard Gaussian distribution. Thus, the signal injection and signal extraction should be done with the asymmetric Gaussian ("AGaus") keeping the same mean value for each arm of such Gaussian.

The parameters of the AGaus function were determined from the fits of the $H^+$ MC signals. Figure V.25 shows the fits of the $H^+$ signals using the "AGaus" function. The asymmetric Gaussian function describes the $m_{jj}$ masses well, thus it can be used to represent the signal templates for this model during the signal injection tests.

Note that the lowest $H^+$ masses do not show a well defined peak above the $m_{jj}$ cut used in this analysis. Therefore, efficiency of the signal reconstruction is lower compared to other masses. Signal injections also show significant spread of the RMS. Therefore, to reduce the uncertainty in determination of limits, the 300 GeV mass point is excluded from the limits.

After injecting signals using the AGaus shapes (random histograms were created from the AGaus function with the fit parameters determined from the fits of the $H^+$ signals), the signal extraction was done with the 5p+AGaus fit, where "AGaus" is an asymmetric Gaussian. As before, the width of the left and right arm of AGaus was fixed to the expected values during the fit, since this is how the limits are calculated using the known signal templates.

Figure V.24 shows the efficiency of the signal reconstruction of the $H^+$ signals. The signal injection shows a good recovery rate, with some bias at low $m_{jj}$, end increased RMS for the lowest mass. This bias should be taken into account when converting the detector-level limits to "truth" level limits. It can be checked how the typical extraction looks like for $3\sigma$ and $5\sigma$ injected tests. The injected signals (especially in the tail) do not have a significant impact on the background shape during the injection of small signals.

The figure V.25 shows the signal injection test for Charged Higgs boson at different masses while injecting signals at 5 $\sigma$ and using 5p+AGaus fits. In the lower panels, the ratios of simulations to 5p+AGauss fit, 5p part of the 5p+AGauss fit and 5p fit only are also shown.

Figure V.26 shows the spurious signal test with floating fit parameters assuming that the background template was created using the signal region of the data. These plots show a similar behavior as for the LE-CR region (scaled to the data in the signal region). The number of events from the spurious signal test (after dividing by the luminosity), assuming the upper bound on the RMS, show that contribution from this test the limits is negligible. A general trend is a widening RMS as the signal shape becomes wider.

Figure V.26(c) also shows the spurious tests for wide signals, with the width as large as $40 - 60\%/M$, after modeling asymmetric tails that correspond to the $H^+$ signals. Even in this scenario, expected systematic uncertainties at lowest $m_{jj}$ is about 25 events divided by the integrated luminosity, which is a small effect on the calculation limits.

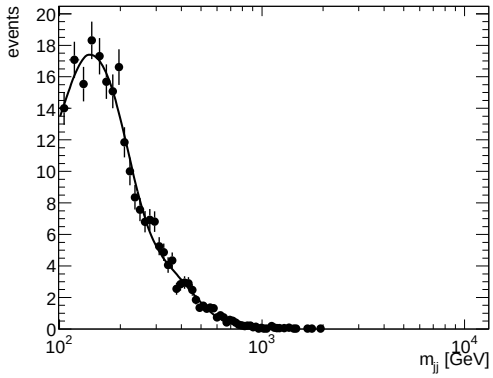


(a) $H^+$ at 300 GeV

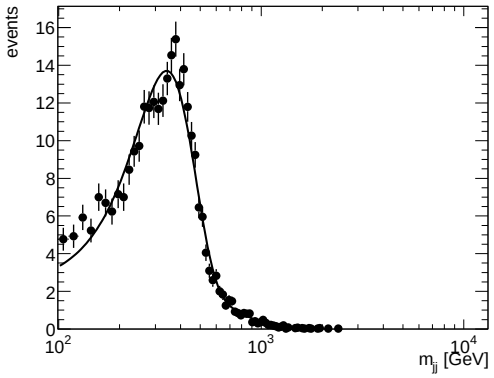


(b) $H^+$ at 600 GeV

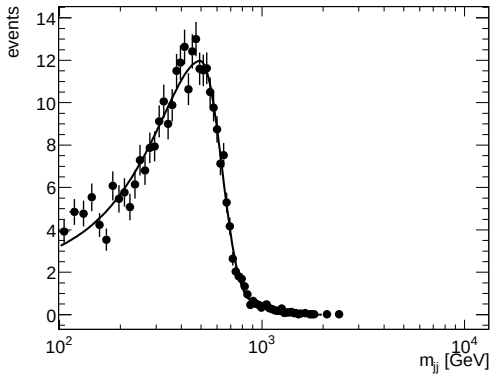


(c) $H^+$ at 800 GeV

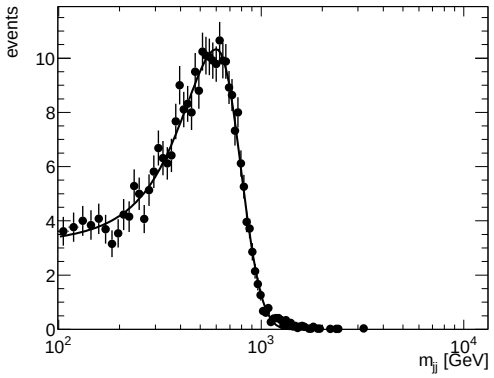


(d) $H^+$ at 1000 GeV

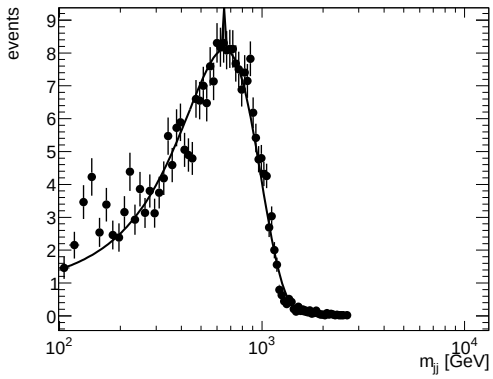


(e) $H^+$ at 1200 GeV

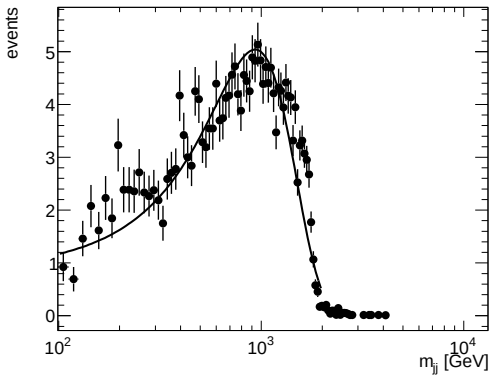


(f) $H^+$ at 1800 GeV

Figure V.23: Examples of the fit of the $m_{jj}$ distributions of the $H^+$ model (for two representative masses) using an asymmetric Gaussian function ("AGaus") for $H^+$ at 300 GeV, 600 GeV, 800 GeV, 1000 GeV, 1200 GeV and 1800 GeV respectively. The dots are the signal $H^+$ Monte Carlo, the solid lines are the fits of using the AGaus function used for the signal recovery. The fits have $\chi^2/ndf = 1 - 1.2$.

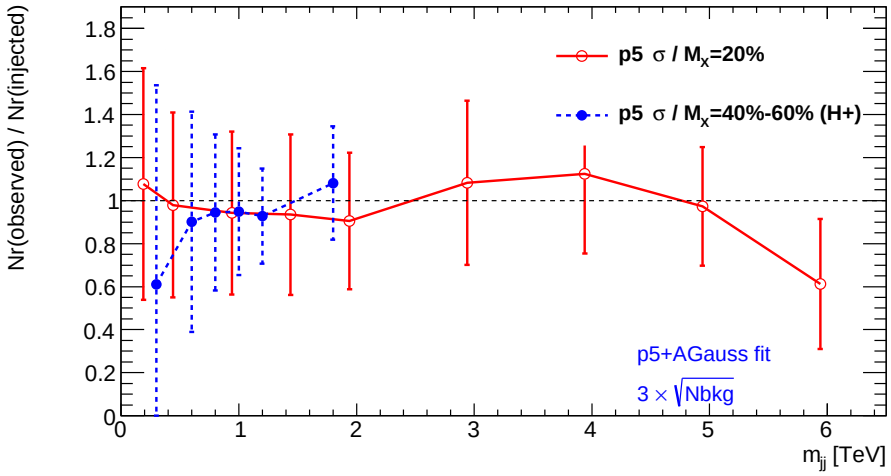


(a) $3\sigma$ injected signals

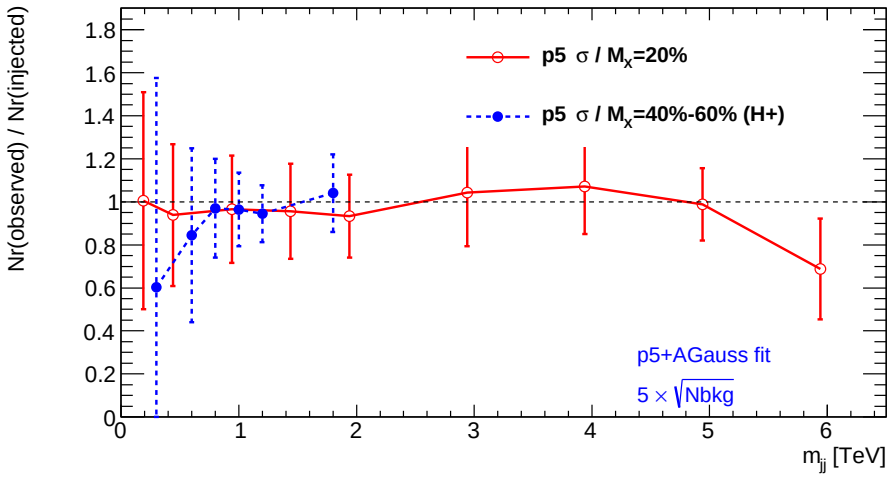


(b) $5\sigma$ injected signals

Figure V.24: Signal reconstruction efficiency calculated using the 5p+AGauss description of the wide Gaussian signals, with $20\%/M$ symmetric Gaussian and $40-60\%/M$ (assuming the $H^+$ signal template). The number of observed events was calculated from the Gaussian component of the global 5p+AGauss fit using 100 pseudo-experiments. The number of injected events corresponds to the 3 for $5\sigma$ amplitudes The pseudo-data were created using the signal region of the data. The uncertainties on the data points are the RMS values on the ratios. The peak and the widths of the asymmetric Gaussian function were fixed to the expected values to avoid instabilities in the 9-parameter fit.

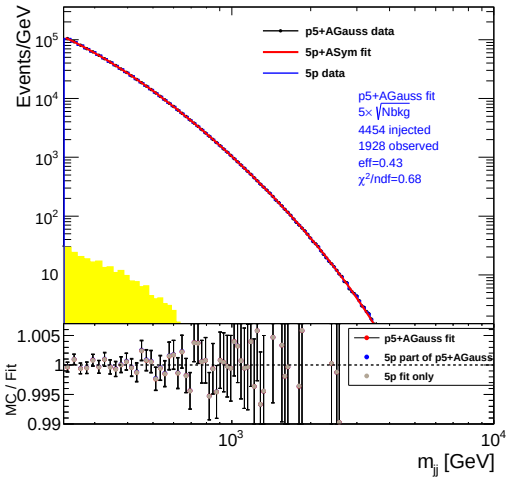


(a) $H^+$ at 300 GeV

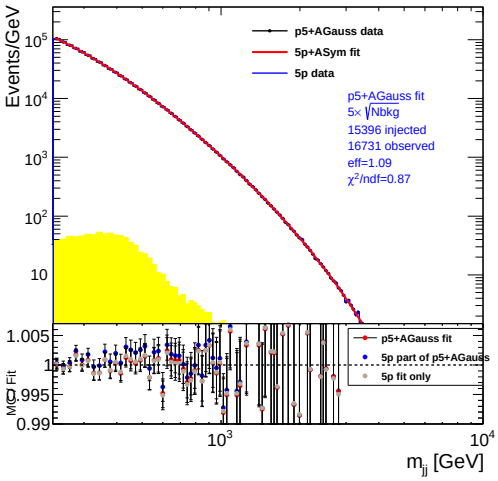


(b) $H^+$ at 600 GeV

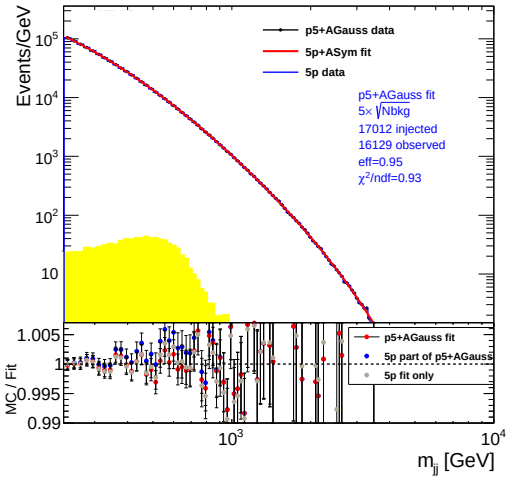


(c) $H^+$ at 800 GeV

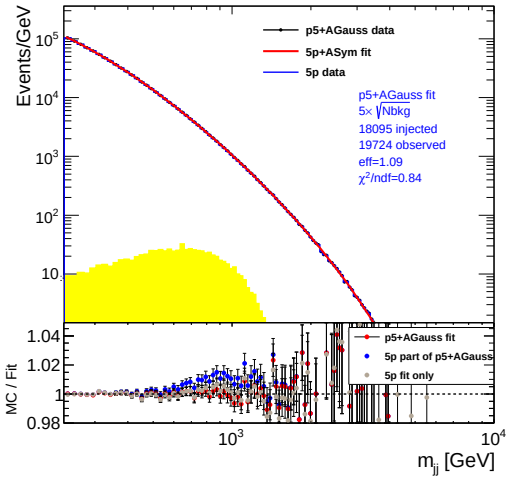


(d) $H^+$ at 1200 GeV

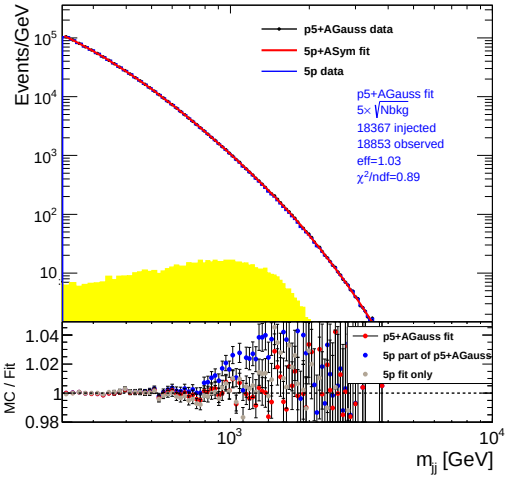


(e) $H^+$ at 1800 GeV

Figure V.25: Signal injection test for $H^+$ signal at different masses for 5 $\sigma$ injected signals.

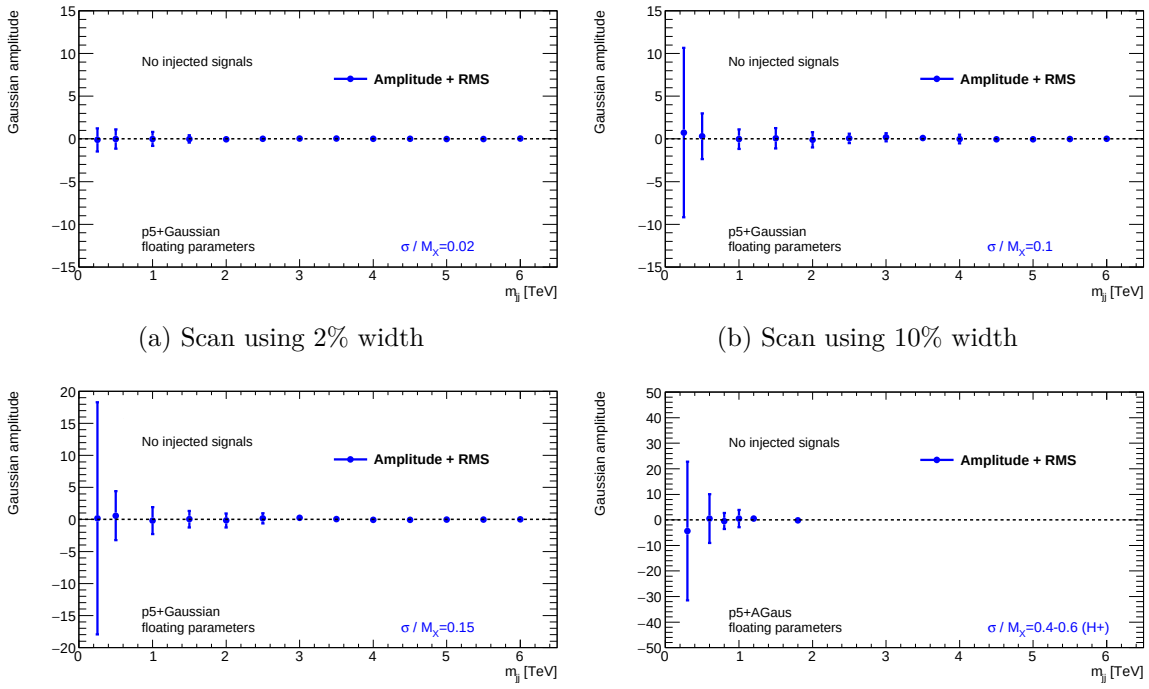


(a) Scan using 2% width

(b) Scan using 10% width

(c) Scan using 15% width

(d) Scan using 40-60% width (H+)

Figure V.26: The average values of events from the Gaussian amplitude using the 5p+Gaussian fits applied to 100 random templates constructed using background-only hypothesis. The parameters of the 5p fit were allowed to float (not fixed to the parameters from background-fit only). The vertical error bars shows the RMS values. The pseudo-data were created using the signal region of the data.

## V.8 Studies of signal region

From the different studies of fit function and control regions, it was finalized that 5 parameter fit function and minimum $m_{jj}$ value of 216 GeV would be used for the signal region studies.

The likelihood fit for dijet along with electron, dijet along with muon and also dijet along with combined lepton (electron or muon) have been performed with such assumptions while using 5 parameter description.

From the combined channel for lepton (electron or muon), the following fit parameters have been obtained :

p0 = 26.4009; p1 = 13.7774; p2 = 0.374297; p3 = 1.31082; p4 = 0.171283;

ndf = 109; logL of fit to data = 628; logL pval = 0.0196 $\pm$ 0.00098;

$\chi^2$ of fit to data = 99.8149; $\chi^2/ndf$ = 0.915; and $\chi^2$ pval = 0.0349 $\pm$ 0.0012,

where p0, p1, p2, p3, p4 are the parameters of Equation V.5.1 and *ndf* represents the number of bins in the $m_{jj}$ spectrum.

Figures V.27, V.28, V.29 represent results from the likelihood fits for three cases: with muon, with electron, and with electron or muon, respectively. Each figure also shows the residual distributions. The fact that the statistical tests including $\chi^2/ndf$ value, Shapiro-Wilk test, KS tests etc. provide good results of normality for the residuals speak of the goodness of the fits for the signal regions.

At the same time, using BumpHunter method, local significance from the background fit and corresponding local $p$ values have also been calculated. While the local p values and region of maximum local excess has been shown in the bottom panels of the top plots, the third(bottom) plots show the distributions of observed local p values corresponding to the observed number of events while scanning over the dijet invariant mass spectrum.

Also some studies have been made with alternative background function and with 3 parameter, 4 parameter and 6 parameter fit functions and after the studies, performance with 5 parameter fit was found to be most useful. At the same time, the contribution from the alternative fit function have been considered for systematic uncertainty.

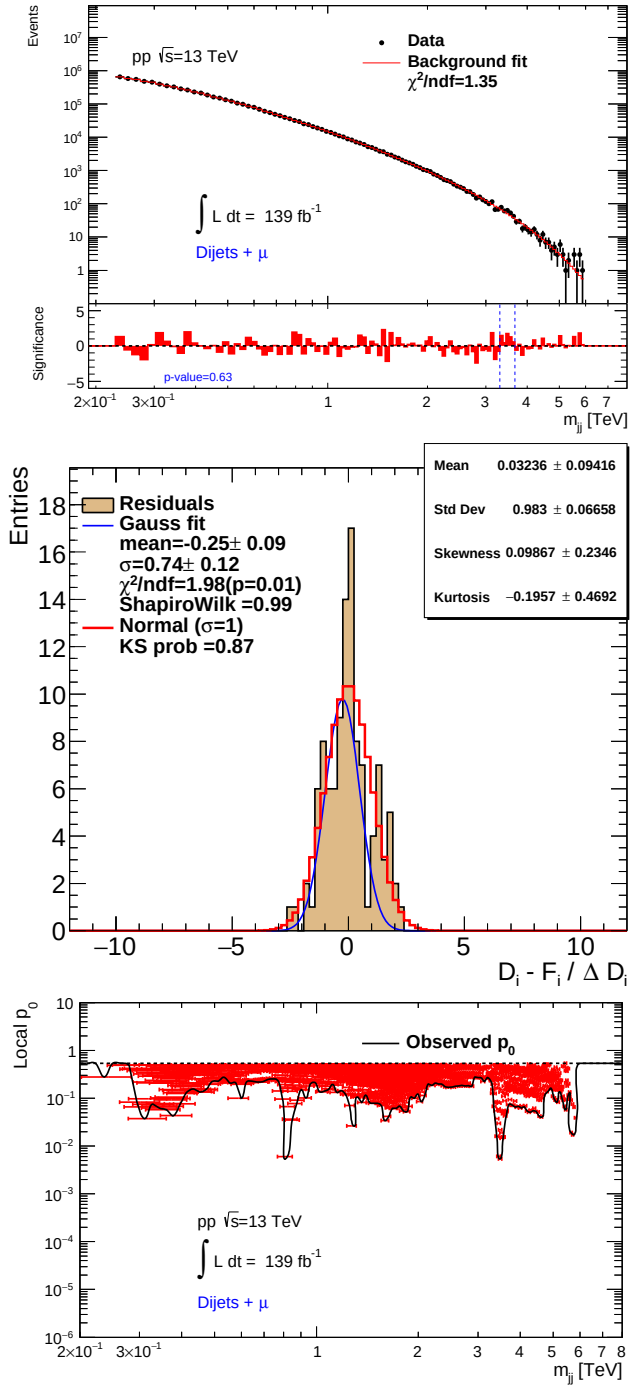


Figure V.27: With the presence of an isolated muon, dijet mass spectra data for $m_{jj} > 216$ GeV after the fit with the 5p background function using the Likelihood method can be found in the top plot. The corresponding distribution of residuals from the same fit can be found in the second plot. Local statistical significance in each mass interval showing the local probability that the background fluctuates to the observed number of events (or higher) can be seen in the bottom plot. The positions of the local excesses indicated using the solid (smoothed) lines.

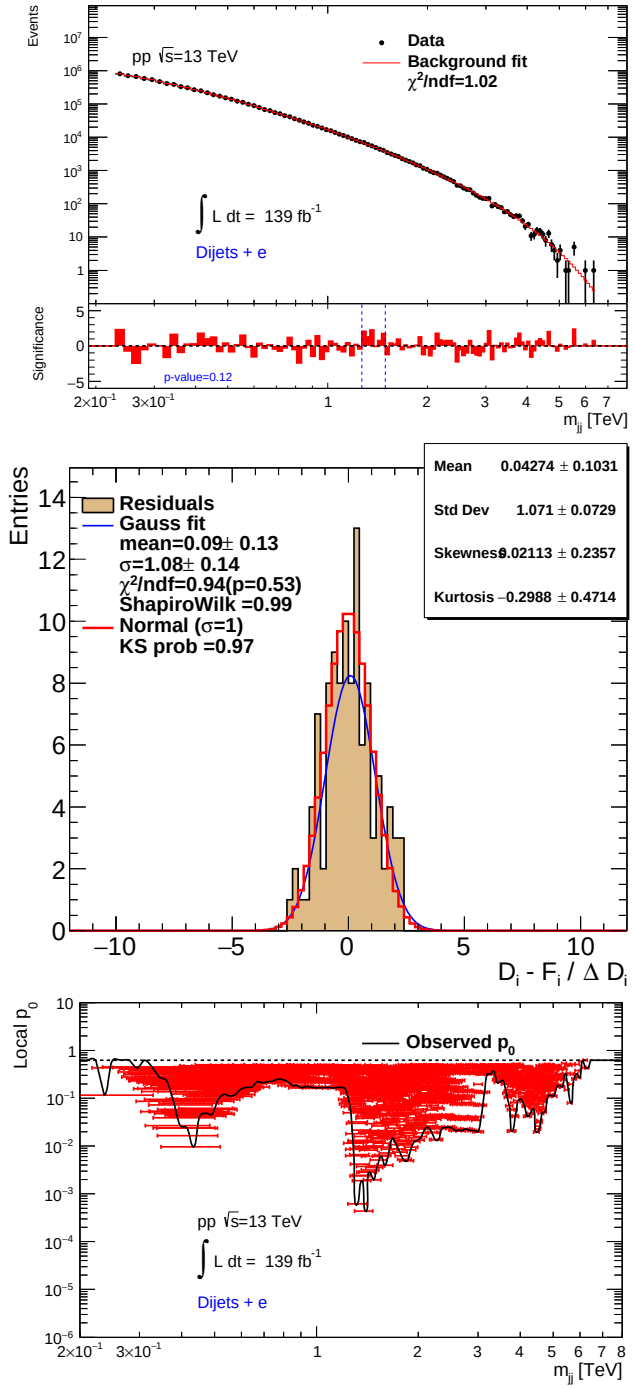


Figure V.28: With the presence of an isolated electron, dijet mass spectra data for $> 216$ GeV after the fit with the 5p background function using the Likelihood method can be found in the top plot. The corresponding distribution of residuals from the same fit can be found in the second plot. Local statistical significance in each mass interval showing the local probability that the background fluctuates to the observed number of events (or higher) can be seen in the bottom plot. The positions of the local excesses indicated using the solid (smoothed) lines.

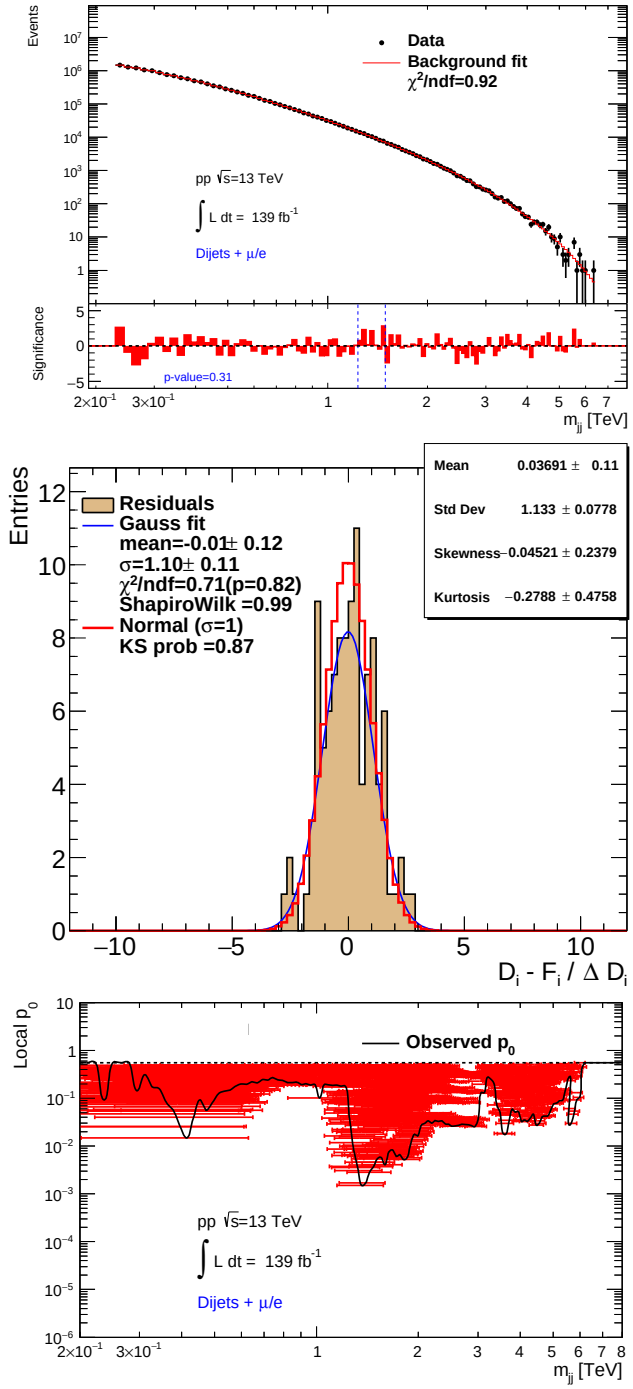


Figure V.29: With the presence of an isolated electron or muon, dijet mass spectra data for $> 216$ GeV after the fit with the 5p background function using the Likelihood method can be found in the top plot. The corresponding distribution of residuals from the same fit can be found in the second plot. Local statistical significance in each mass interval showing the local probability that the background fluctuates to the observed number of events (or higher) can be seen in the bottom plot. The positions of the local excesses indicated using the solid (smoothed) lines.

## V.9 Additional studies for the Charged Higgs boson model

For the Charged Higgs boson model, a set of dedicated studies have been performed. Some of the results from those studies are highlighted in the following sections.

### V.9.1 Mass scan using likelihood fits

Mass scan refers to changing the Charged Higgs boson mass (with the step equal to the width of the bins times two) and performing the global likelihood fits with the 5p function (background only) and background+signal, where signal was given by the $H^+$ shape or, alternatively, by a Gaussian with the width fixed at 30% of its mass. The Gaussian signal allows to look at large $m_{jj}$ for which the $H^+$ Monte Carlo is missing.

For a given mass, the $H^+$ shape was fixed to the MC simulation, but the normalisation (amplitude) was relaxed. Similarly, for Gaussian-like signals, the width was fixed width to 5% and 30% of their masses (i.e. two extreme cases). The normalisation parameter for the signal component was not limited to positive values.

The parameters of the 5p background were floating (but the initial parameters were set for the background-only hypothesis). The test statistics $q_0$ [151, 152] for Neyman-Pearson (NP) method was defined by

$$q_0 = -2 \ln \frac{L(0)}{L(1)},$$

where $L(0)$ and $L(1)$ are the likelihoods of the null (5p) and alternative (5p+signal) hypotheses from the global likelihood fits of the data. Providing the conditions for the asymptotic approximation [153] holds, the significance of the observation is given by $Z = \sqrt{q_0}$ (when $q_0 > 0$), while $Z = 0$ was for negative $q_0$. This estimator should be very close to the true significance.

Figure V.30 shows the $Z$ values for different masses of the signals. One can see that the mass region close to 1.0-1.5 TeV has the local significance of about 2 $\sigma$ or less. It is lower than for for the "measurement of the excess" test discussed in the previous section, and lower than 2.8 $\sigma$ for the null hypothesis from the BumpHunter which does not assume any specific signal shape.

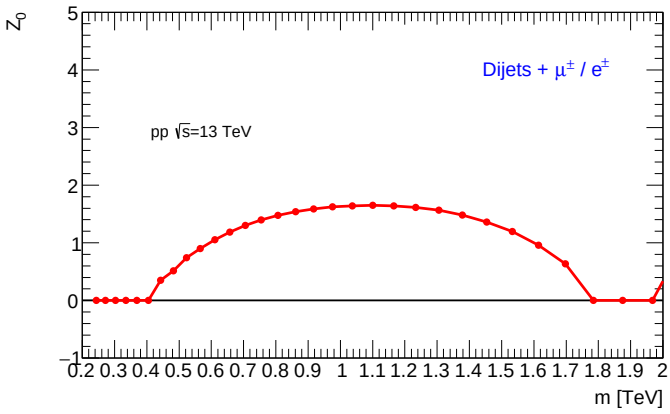


(a) Scan using the $H^+$ signal shape

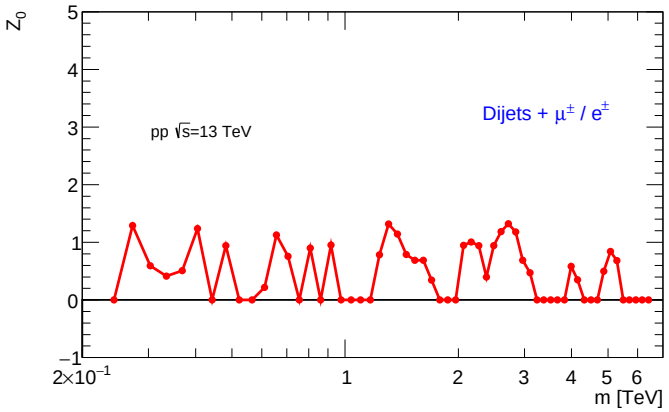


(b) Scan using the Gaussian signal with 5% width of its mass

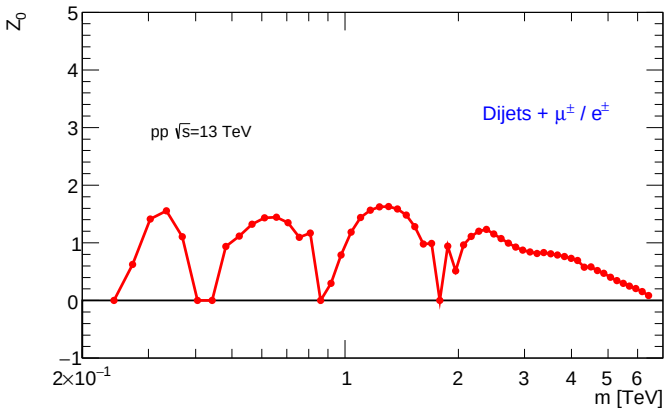


(c) Scan using the Gaussian signal with 30% width of its mass

Figure V.30: $Z$ values from the global likelihood fits of the $m_{jj}$ distribution assuming the 5p function (background only) and 5p+signal, where signal was either the $H^+$ shape or a Gaussian with the widths of 5% and 30%.

### V.9.2 Angle and $p_T$ for leading jet and top quarks

Distributions of the angle between the leading jet and the top quarks from the $H^+$ were calculated. Figure V.31 shows the opening angle between the leading jet that forms $m_{jj}$ and the direction of the highest-$p_T$ jet and the top quarks from the $H^+$ decays. It can be seen that the angle becomes smaller as the top mass increases.

Figure V.32 shows the transverse momentum of the leading jet vs the transverse momentum of the top quark. The plots indicate a correlation between these momenta.

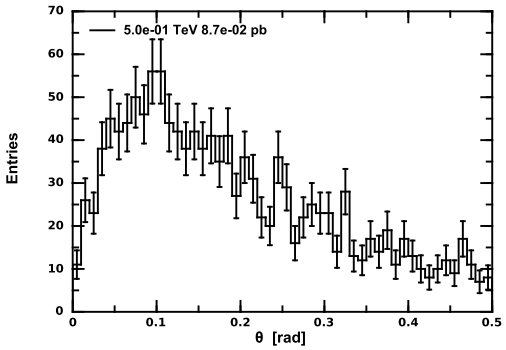


(a) $H^+$ mass 600 GeV

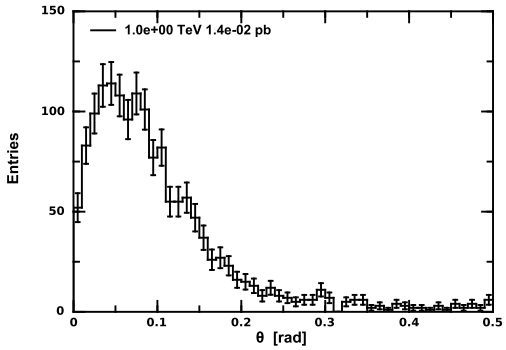


(b) $H^+$ mass 1000 GeV

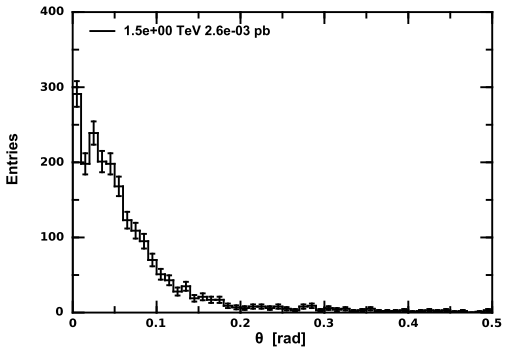


(c) $H^+$ mass 1500 GeV

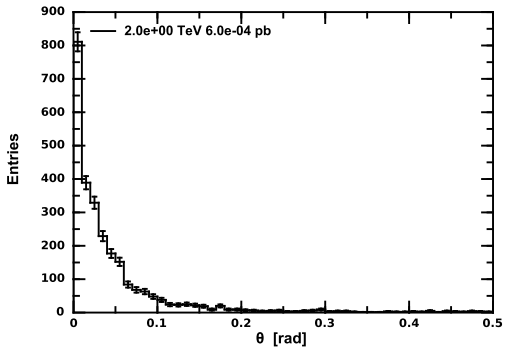


(d) $H^+$ mass 2000 GeV

Figure V.31: The distributions of the opening angle between the leading jet that forms $m_{jj}$ and the direction of the top quark from the $H^+$ decays. The plots show the distributions for different $H^+$ masses.

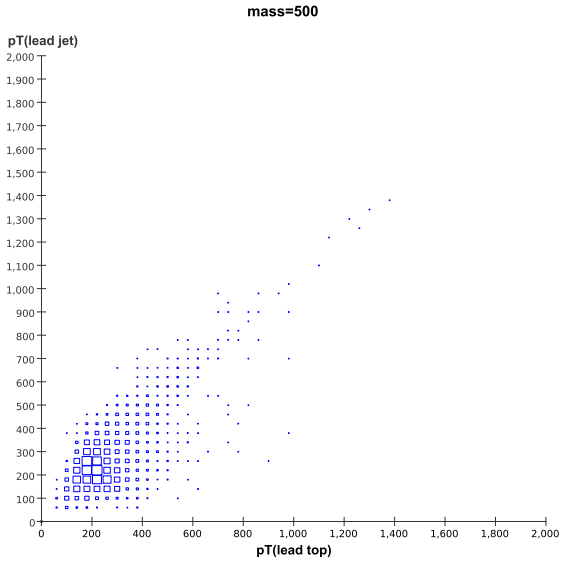


(a) $H^+$ mass 600 GeV

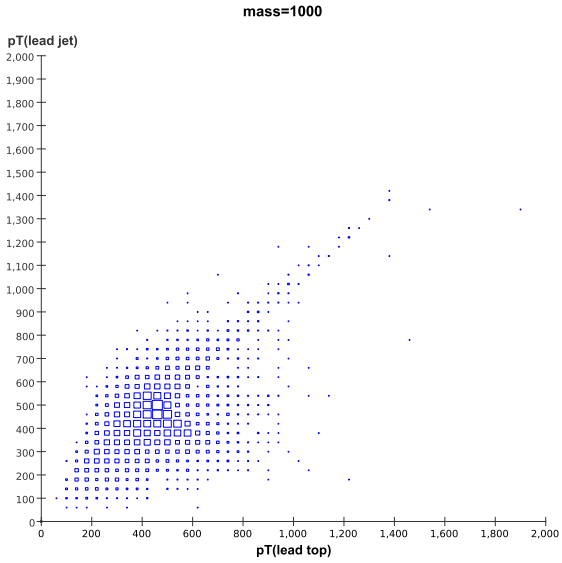


(b) $H^+$ mass 1000 GeV

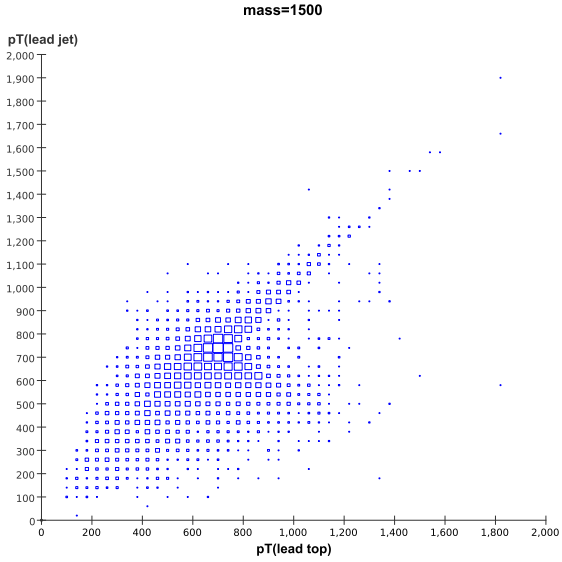


(c) $H^+$ mass 1500 GeV

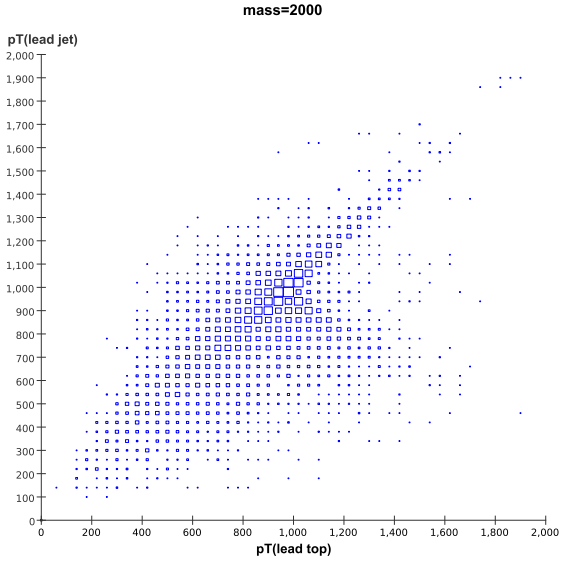


(d) $H^+$ mass 2000 GeV

Figure V.32: Correlation between the $p_T$ of the leading jet and the the top quark from the $H^+$ decays. The plots show the distributions for different $H^+$ masses.

### V.9.3 Boosted topology for $H^+$

According to Fig. V.2, the truth level $m_{jj}$ distribution for 1.8-2 TeV massed of $H^+$ shows a small peak near the $H^+$ due the fully boosted topology. The number of events in this peak is about 9% of the total number. At the detector level (which was used to set the limits), this peak is smeared out. While checking whether the boosted topology somewhat breaks reconstruction of jets for jets close to 1 TeV, it was found that if the detector reconstruction moves 9% of truth-level events from the 1.8-2 TeV region outside the acceptance region of 216 GeV, then there should be some ( 9%) correction to the acceptance.

To verify this, correlations between the $m_{jj}$ mass at the reconstructed and truth level was studied. Figure V.33 shows a strong correlation between the reconstructed and truth $m_{jj}$ values, which is totally expected. No truth-level events have been migrated from the 1.8-2 TeV outside the 216 GeV region.

From this study it was concluded that the chances of migration of events from the region of 1.8-2 TeV outside 216 GeV region that defines the acceptance are very unlikely.

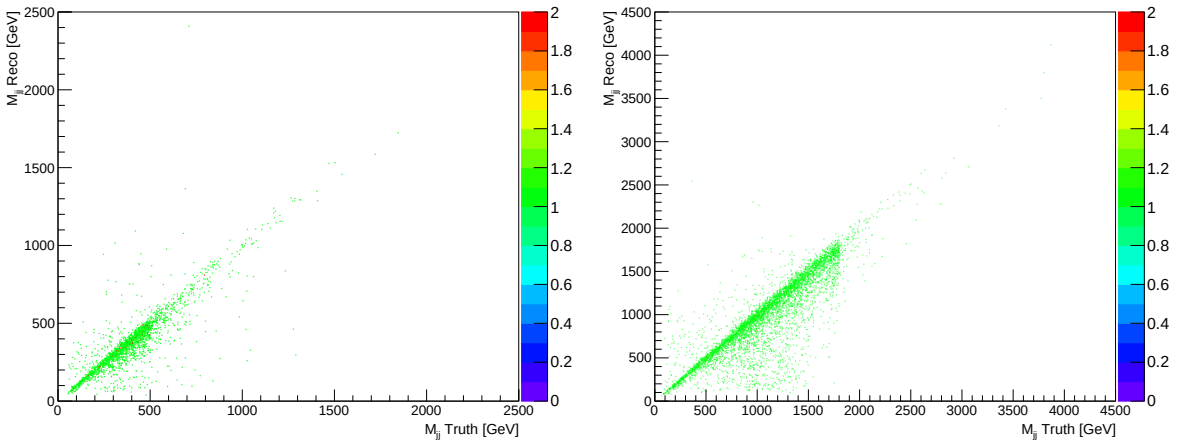


(a) $H^+$ mass 600 GeV (b) $H^+$ mass 1800 GeV

Figure V.33: Correlations between $m_{jj}$ masses at the reconstructed and truth levels for two representative $H^+$ mass points (lowest and where the largest deviations by BumpHunter is reported).

### Theoretical $H^+$ uncertainties

Theoretical uncertainties on the production of $H^+$ were checked. If Charged Higgs boson exists, the following possible uncertainties might be considered:

- Non-zero width of $H^+$;
- Polarisation effect that may modify angular distribution of $W$;
- PDF uncertainties that may affect $m_{jj}$;

It should be mentioned that the modern state-of-the-art Monte Carlo generators (such as NLO MG5) do not include non-zero widths and polarisation effects. All previous ATLAS and CMS papers did not include such effects [21, 76]. According to a discussion with $H^+$ theorists (Carlos Wagner, Wang, Xiaoping and others), experiments should exclude specific Monte Carlo implementations, and make clear what assumptions are used in such implementations. If some BSM model is not available, this does not invalidate the experimental results for the models in hand.

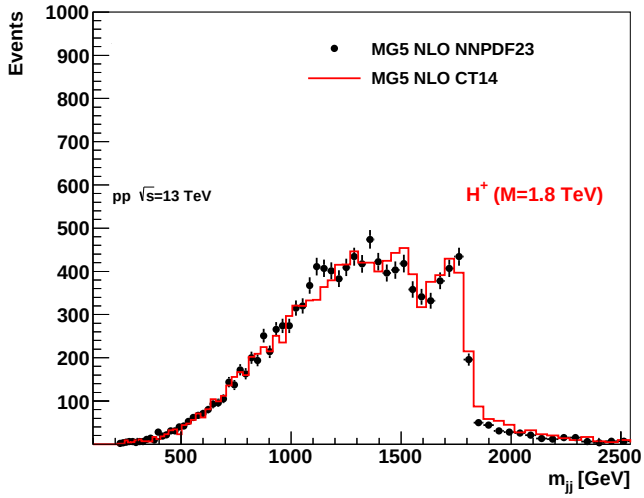


(a) $H^+$ mass 1800 GeV

Figure V.34: Comparisons between $m_{jj}$ generated with MG5 at NLO QCD using the default PDF (NNPDF23NLO) and the alternative PDF (CT10nlo).

It was also important to check for uncertainties due to Monte Carlo modeling. The model uncertainties for LO QCD models were extensively discussed in another section. Figure V.34 shows the comparison of the $m_{jj}$ mass between the default PDF (NNPDF23NLO) with CT14NLO which is recommended by the PMG group to test the sensitivity to PDF. The $m_{jj}$ distributions are shown at the truth level. I used the $H^+$ mass at 1.8 TeV, in the region of the largest deviation. No statistically significant difference in the shapes was observed. The calculated limits using these two shapes

did not indicate statistical difference between these two PDF's. It was found that the acceptance is the same, 0.601, for NNPDF23NLO and CT14NLO.

The polarisation effect can be included in MG5 for the process $tbH^+$ at LO QCD (but not at NLO QCD used in this paper). Therefore, the effect from polarisation can only be checked at LO QCD. Several samples with LO MG5 were created using MadSpin on and off, and showering the partons using Pythia8 A14 tune. Only samples for 2 TeV Higgs mass were created, where the PDF uncertainty is expected to be largest. The events were simulated using the official ATLAS production by applying PYTHIA8 showering with the recommended AZ tune for the shower. Then the EVNT files were transformed to the DAOD TRUTH3, and analysed using the standard analysis code. In total, 5,000 events were created for each variation of the settings.

Figure V.35 shows that the $m_{jj}$ distributions at LO QCD do not have sensitivity to the spin. It was checked that the effect from the inclusion of the spin effect is 0.86% on the acceptance, and is well below the statistical precision with which the acceptance can be calculated. It should also noted that the main effect on the acceptance comes from the lepton cut, not $m_{jj}$. The limits are typically have uncertainty of 40% (for the 1-2 $\sigma$ band). Therefore, effects such as polarisation or are well beyond the experimental sensitivity for the presented limits.

Figure V.35 also shows that the $m_{jj}$ distribution, for two representative masses, does not have the sensitivity to the PDF change (from NNPDF to CTEQ6L) for LO QCD MG5.

A similar plot created using the HepSim outside the ATLAS simulation was discussed with several theorists (Carlos Wagner and others). They have concluded that the fact that such effects are beyond the experimental sensitivity is fully expected. Also, they do not expect that NLO calculation can be sensitive to such effects, especially for the limit setting.

Note that 1% PDF systematics has already been applied to cover possible differences related to PDF.

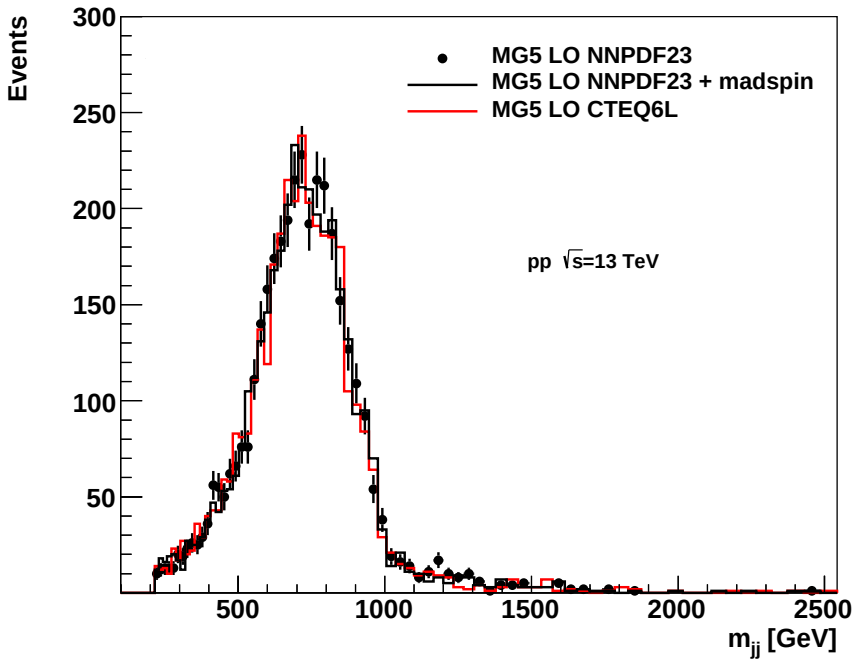


(a) 1000 GeV mass of $H^+$

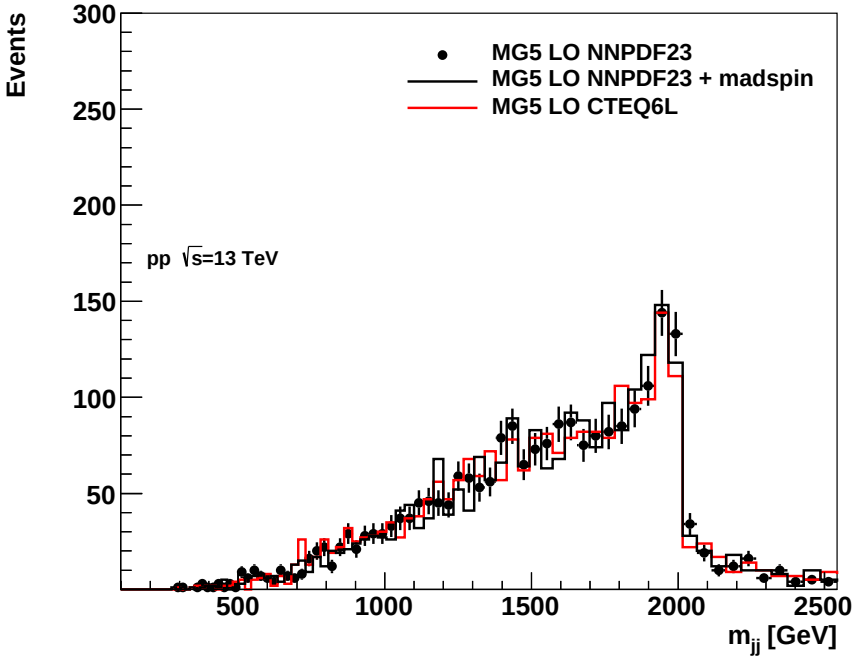


(b) 2000 GeV mass of $H^+$

Figure V.35: Comparisons between $m_{jj}$ (at the truth level) generated with MG5 at LO QCD with and without including MadSpin. Also, comparison with an alternative PDF (CTEQ6L) is shown.

### V.9.4 Zero-width approximation

Here I evaluated theoretical uncertainties of the Charged Higgs boson production limits related to the "zero-width" approximation used by MG5. Modern state-of-the-art Monte Carlo generators (such as MG5) do not model the width of $H^+$. Previous ATLAS [21] and CMS [76] measurements excluded $H^+$ models assuming the narrow-width assumption, for all $\tan\beta$ values.

It was checked that $H^+$ for $\tan\beta = 1$ has a width of about 4% in HMSSM benchmark scenario, and about 18% for $\tan\beta = 0.5$ .

This analysis uses $\tan\beta = 1$ for the limit calculations. A convolution of a wide $m_{jj}$ distribution (which is about 30% broad) with $\sim 4\%$ natural Breit-Wigner width makes a negligible impact on the $m_{jj}$ shape. If one uses a Gaussian approximation analytically, inclusion of the 4% widths leads to $\sqrt{0.3^2 + 0.04^2} = 0.302$, i.e. 30.2% expected width. This change is significantly below the detection level for the $m_{jj}$ distribution.

The case $\tan\beta = 0.5$ is more complex, since 18% width is a non-negligible for any measurement. Therefore, $\tan\beta = 0.5$ theory line, in principle, should be compared with the limits that include the realistic width. However, there is no a MG5 implementation for this width. According to a discussion with $H^+$ theorists (Carlos Wagner, Wang, Xiaoping and others), theorists are fully aware the fact that the experiments assume the narrow widths approximation, and they do not think this assumption invalidates the experimental limits.

Note that convoluting the truth-level with detector resolution, and adding the Breit-Wigner, cannot be realistically accomplished since there are too many other effects beyond the detector two-jet resolution which need to be taken into account. The original $m_{jj}$ (with the zero width approximation) before and after the convolution with 4% and 18% Breit-Wigner shape was compared and it was verified using a dedicated calculation (feynhiggs) that the relative width of the Breit-Wigner does not change with the mass, so 4% and 18% values are reasonable approximation for any $H^+$ mass.

Figure V.36 shows the $m_{jj}$ at the truth level before and after the Breit-Wigner convolution. The figure shows that the 4% width effect cannot be statistically separated from MG5. However, 18% affect the shape indeed.

It should be noted that such changes in the $m_{jj}$ shape do not affect the acceptance correction which is determined by the minimum $p_T$ cut on leptons and the minimum $m_{jj}$ cut at 216 GeV. The limits, however, may change, due to a wider shape of the $m_{jj}$ when no zero approximation is used.

To verify the effect from the zero-width approximation, the shapes presented in Fig V.36 have been used for the limit calculations. No effect was found for the 4% smearing ($\tan\beta = 1$) used for the acceptance corrections in this paper. For the $\tan\beta = 0.5$, the effect was at the level of 2% (for truth-level shapes), which is significantly below the 1 $\sigma$ band for the expected limits (which is about 40% effect). This study does not apply this 2% correction since it is impossible to include such effect exactly in the MC. Instead, this study indicates that the analysis was obtained

using $\tan\beta = 1$ (for which the zero width approximation does not play any role), while the zero width approximation for $\tan\beta = 0.5$ was checked, with the conclusion that such effect cannot make an effect that has a potential to invalidate the results.

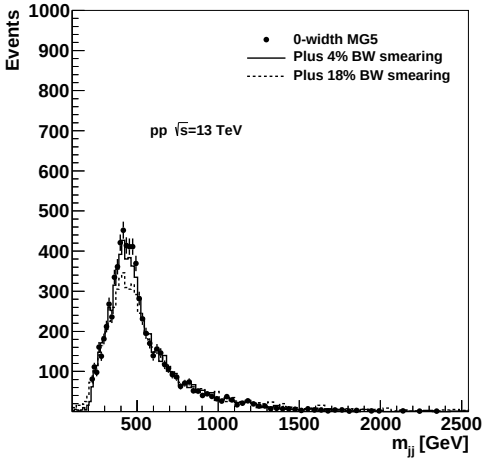


(a) $H^+$ mass 600 GeV

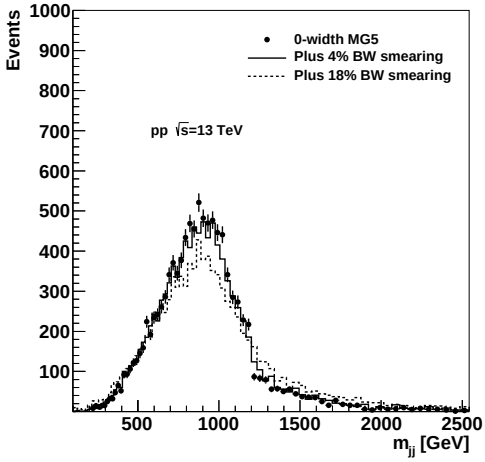


(b) $H^+$ mass 1200 GeV

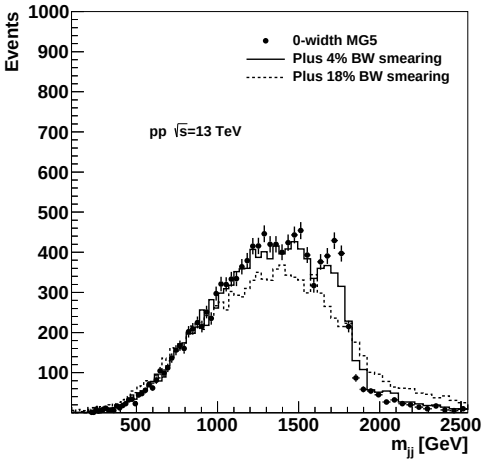


(c) $H^+$ mass 1800 GeV

Figure V.36: Comparisons between $m_{jj}$ shapes before and after 4% ($\tan\beta = 1$) and 18% ($\tan\beta = 0.5$) Breit-Wigner smearing of the original MG5 distribution that assumes the zero-width approximation.

## V.10 Systematic uncertainties

Calculations of systematic uncertainties are very important for any analysis. Systematic uncertainties can come from both signal and backgrounds and are generally derived from the MC simulations and are treated as nuisance parameters during limit calculations. In the following sections, different kinds of systematic uncertainties are described briefly.

### V.10.1 Background estimate uncertainties

Dominant contributions to systematic uncertainties in background comes from the fit functions and the choices of fit parameters. The uncertainty associated with the choice of 5 parameter fit, is calculated by using alternative 5 parameter fit function. By fitting the pseudo-experiments with Poisson distribution, the parameter uncertainties are extracted.

Fits with the default and with the alternative 5p fit hypothesis are compared in the figure V.37. In the figure, yellow band represents the $\pm 1\sigma$ statistical uncertainties on the default 5p function. The alternative function has the largest deviation which is represented by the red line from the default function in the tail of the $m_{jj}$ distribution. The contribution from the alternative background function is about 50% of $\pm 1\sigma$ statistical uncertainty of the default function at 3 TeV and increases in the tail.

All systematic uncertainties, including the uncertainty that comes from the alternative function, are combined using the StatisticalFramework.

### V.10.2 Systematic uncertainties on signal

Some of the different possible systematic uncertainties are described below :

**Jet energy scale and resolution:**

The prominent sources of systematic uncertainties for jets include the Jet Energy Resolution (JER) and Jet energy Scale (JES). As recommended by the ATLAS JetEtMiss group's recommendations, the uncertainties for full Run2 have been used.

There has been total 8 JER uncertainty components and as a result strongly-reduced 8 nuisance parameter are used due to them. Similarly there have been 6 JES uncertainty components.

For the Bayesian limit calculation procedure, the following JER/JES uncertainties are used as nuisance parameters,

- JET_GroupNP_1 (one sigma variation up and down);
- JET_GroupNP_2 (one sigma variation up and down);
- JET_GroupNP_3 (one sigma variation up and down);
- JET_EtaIntercalibration_NonClosure, for "highE", negEta, "posEta" (one sigma variation up and down);
- JET_Flavor_Response, (one sigma variation up and down);
- JET_JER_DataVsMC (one sigma variation up and down);

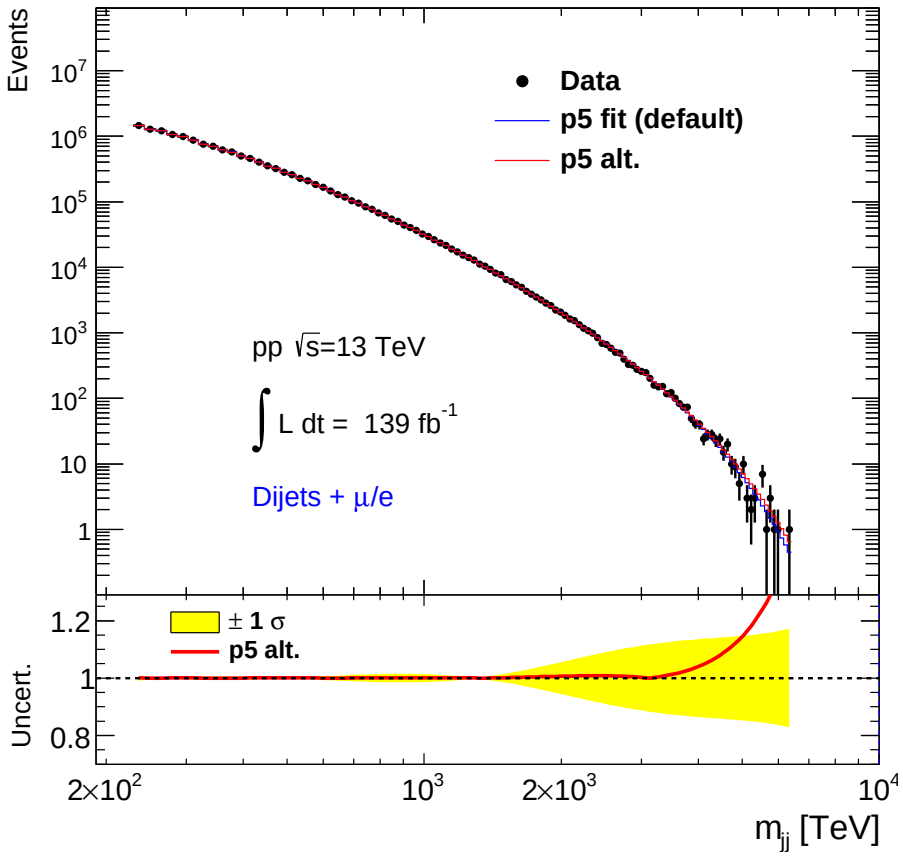


Figure V.37: Comparison of the default 5p and the alternative fit function given by Eq. V.5.2. The yellow area on the ratio shows $\pm 1\sigma$ statistical uncertainties on the default function, while the red curve shows the behaviour of the alternative fit function.

- JET_JER_EffectiveNP_1, (one sigma variation up and down);
- JET_JER_EffectiveNP_2, (one sigma variation up and down);
- JET_JER_EffectiveNP_3, (one sigma variation up and down);
- JET_JER_EffectiveNP_4, (one sigma variation up and down);
- JET_JER_EffectiveNP_5, (one sigma variation up and down);
- JET_JER_EffectiveNP_6, (one sigma variation up and down);
- JET_JER_EffectiveNP_7, (one sigma variation up and down);
- JET_JER_EffectiveNP_8, (one sigma variation up and down);

Depending on the masses of the jets, the systematic uncertainties also vary. The table V.11 shows that variation.

**Lepton uncertainties:**

Lepton identification, energy scale and resolution uncertainty etc. contribute to the systematic uncertainties associated with lepton. The choice of $\ell > 60$ GeV also

| Name | 250 GeV | 1000 GeV | 3000 GeV | 6000 GeV |
|---|---|---|---|---|
| JET_GroupNP_1 | 1% | 0.8% | 0.4% | 0.3% |
| JET_GroupNP_2 | 0.2% | 0.4% | 0.6% | 0.9% |
| JET_GroupNP_3 | 0.2% | 0.3% | 0.3% | 1.4% |
| JET_NonClosure (3 shifts) | 0.1% | 0.1% | 0.1% | 0.2% |
| JET_JER* (8 shifts) | 0.1% | 0.1% | 0.1% | 0.1% |
| Lepton $p_T$ scale | $< 0.05\%$ | $< 0.05\%$ | $< 0.05\%$ | $< 0.05\%$ |
| Lepton $p_T$ resol* | $< 0.05\%$ | $< 0.05\%$ | $< 0.05\%$ | $< 0.05\%$ |

Table V.11: Absolute values of mass shifts for different systematic uncertainties for several mass points. The systematic shifts marked with (*) are shown for the signal width.

contribute to the systematic uncertainties. To study the uncertainty due to $p_T$ , different $p_T$ values have been studied in the previous sections.

The uncertainties associated with the lepton selection were found to have a very negligible effect on the limits.

**Systematic uncertainties from triggers:**

Choices of triggers can contribute to the systematic uncertainties as with different triggers, the event rates change. For broad signals like $H^+$, no effects of the triggers in uncertainties have been observed. Only 1% (flat) uncertainty for the limit calculations was applied.

**Luminosity uncertainty:**

The luminosity also contribute to some systematic uncertainties. With the help of the luminosity measurement system in ATLAS and special LUCID-2 detector, luminosity is calculated and its corresponding uncertainties are also measured. For Run 2 data, the combined systematic uncertainty due to luminosity has been found to be 1.7%.

**PDF uncertainties:**

Since this analysis deals with two jets and the angular distribution between two jets depends on the parton-density-function (PDF). The choice of PDF contribute to 1% systematic uncertainties [154, 155] to specific beyond the standard model signal shapes modelled using specific PDF choices.

### V.10.3 Systematic uncertainties for Gaussian limits (Gaussian signal shape uncertainties)

Calculating systematic uncertainties due to Gaussian shapes is also important as the Gaussian shapes are not created from Monte Carlo simulations, but while using different Gaussian distributions with varying widths and peak positions. Figure V.38 shows the shifts due to different systematic uncertainties in the Gaussian distributions.

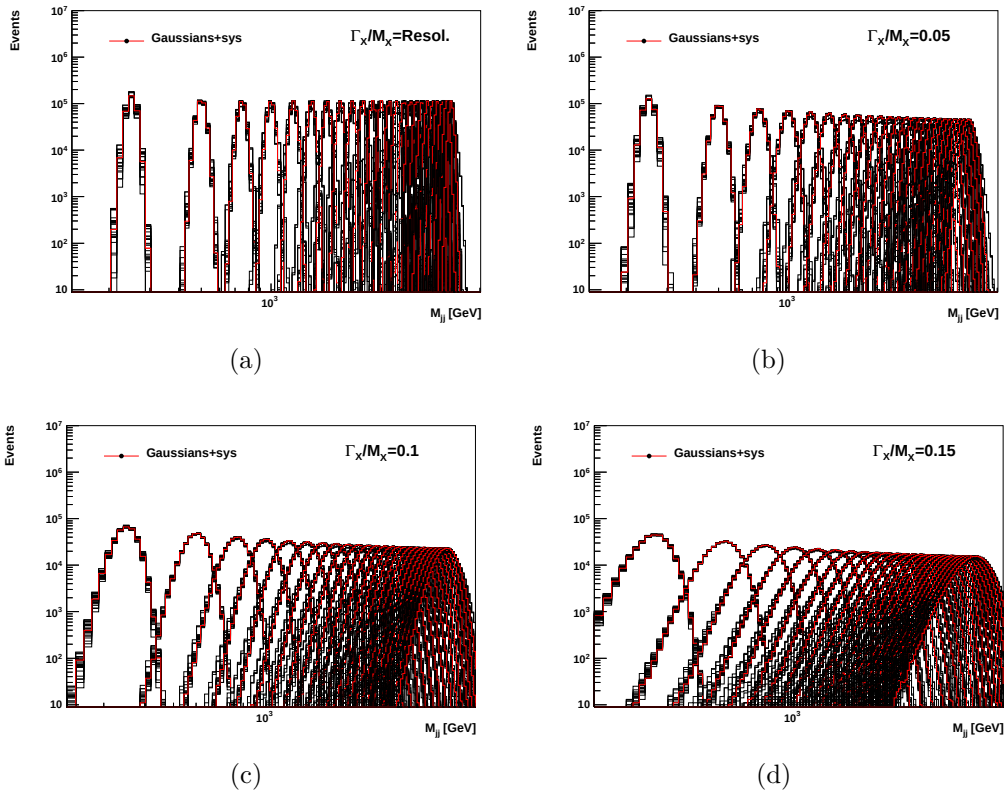


Figure V.38: Shapes of the Gaussian "signals" with different values of the width (detector resolution, 5%, 10%, 15%) together with systematic uncertainties after using the second order polynomials that parameterize shifts for the peaks and widths. The red color shows the nominal values, the black histogram shows signals due to systematic variation.

### V.10.4 Model uncertainty

The $H^+$ model is the only model in this analysis used Next-to-Leading-Order (NLO) QCD, thus scale variations are not as trivial as for the leading order matrix elements. But the variations are expected to be smaller than for the LO QCD. The uncertainty due to different scale choices for the $H^+$ model was estimated previously by varying the renormalisation and factorisation scales up and down by a factor of two. It was found that the uncertainty ranges from 7% at low masses to 15% at masses above 1300 GeV for the lepton+jets final state [21]. The dedicated ATLAS papers on Charged Higgs boson searches do not show theoretical uncertainties for the $H^+$ model on the limit plots (see Fig.8 in Ref. [21], which states that this figure does not consider such uncertainties). It was checked with the $H^+$ analysis team that the limit plot does not include scale uncertainties for the acceptance corrections, though there can be possibilities of truth-level interpretation containing such uncertainties.

## V.11 Results

### V.11.1 Limit calculation for Charged Higgs

Before calculating limits, some studies were conducted on the final selection cuts. For example, for the lepton $p_T$, assuming possibilities of both higher and lower trigger efficiency, 30 GeV and 70 GeV cuts of $p_T^{lepton}$ cases were considered for study. But the 5 parameter fit function didn't provide good description for that $p_T^{lepton}$ values. So, $p_T^{lepton} > 60GeV$ has remained unchanged condition for the isolated charged leptons.

As discussed in the analysis strategy, if significant deviation from the background hypothesis is not found, exclusion limits was supposed to be calculated. Figures V.27, V.28, V.29 shows, there has not been significant deviation, so using Bayesian method [156] at 95% C.L. upper limits have been calculated on cross sections. To calculate upper limits on number of possible signal events in data for a specific mass point, 95% quantile of the posterior is used. And if the number of events is divided by luminosity, the values of cross sections multiplied by branching ratio and acceptance correction for that mass point.

50000 pseudo-experiments are repeated on the basis of best fits from all nuisance parameters while signal is fixed to 0 value for the purpose of calculating C.Ls. For each of those pseudo-experiments, 95% quantile in the signal strength posterior is recorded and considered as the upper limit on probable number of signal events in data for the mass point. 1 $\sigma$ and 2 $\sigma$ bands are also calculated for expected limits. Similarly for observed limits also, 50000 pseudo-experiments are used. For the 1 $\sigma$ and 2 $\sigma$ bands, less number of pseudo-experiments can be used. For example, for calculation of 1 $\sigma$ and 2 $\sigma$ on the observed limits, for the Charged Higgs boson 300 pseudo-experiments were utilized.

To convert the detector level limits into truth level limits, many different correction factors need to be considered. Reconstruction efficiency of the jets or lepton, signal reconstruction efficiency in the detector are the prominent ones. Trigger efficiency in data and Monte Carlo simulations are also checked. For the dijet+ lepton studies, the trigger efficiency for MC has been 90.4% and the trigger efficiency for data has been 88%. The weighted average of lepton reconstruction efficiency, identification and isolation efficiency, in addition to the trigger efficiency has been 84%.

The efficiency $\epsilon$ is calculated using the signal reconstruction efficiency and the event reconstruction efficiency.

Table V.12 provides the truth level upper limits for Charged Higgs model while applying acceptance and efficiency corrections. The uncertainty values mentioned in the table are statistical uncertainties. $\sigma$ represents the cross section of the MC process (in pb), $N_{acc}^{lep}$ represents the number of truth-level events passed the lepton $p_T^l > 60$ GeV with the eta region and $N_{acc}^{full}$ represents the total number truth-level events after the additional requirements on jets. This step requires at least two jets with $m_{jj} > 216$ GeV and $|\eta(jet)| < 2.4$.

$N_{rec}$ represents the number of events after the full event reconstruction, including the trigger efficiencies, final selection cuts and object reconstruction.

| $M$ [GeV] | $N_{gen}$ | $\sigma$ [pb] | $N_{acc}^{lep}$ | $N_{acc}^{full}$ | $A$ | $N_{rec}$ | $\sigma^{vis}$ [pb] | $\epsilon$ |
|---|---|---|---|---|---|---|---|---|
| 300 | 20000 | 2.763E+00 | 5125 | 3300 | $0.165 \pm 0.003$ | 1660 | 2.294E-01 | $0.503 \pm 0.015$ |
| 600 | 20000 | 2.901E-01 | 7402 | 7126 | $0.356 \pm 0.005$ | 4056 | 5.884E-02 | $0.569 \pm 0.011$ |
| 800 | 20000 | 9.005E-02 | 8334 | 8165 | $0.408 \pm 0.005$ | 4841 | 2.180E-02 | $0.593 \pm 0.011$ |
| 1000 | 20000 | 3.237E-02 | 9397 | 9299 | $0.465 \pm 0.006$ | 5372 | 8.695E-03 | $0.578 \pm 0.010$ |
| 1200 | 20000 | 1.288E-02 | 10443 | 10406 | $0.520 \pm 0.006$ | 5514 | 3.550E-03 | $0.530 \pm 0.009$ |
| 1400 | 20000 | 5.516E-03 | 10876 | 10836 | $0.542 \pm 0.004$ | 5333 | 1.471E-03 | $0.492 \pm 0.005$ |
| 1600 | 20000 | 2.509E-03 | 11382 | 11353 | $0.568 \pm 0.007$ | 5395 | 6.768E-04 | $0.475 \pm 0.008$ |
| 1800 | 20000 | 1.188E-03 | 12036 | 12015 | $0.601 \pm 0.007$ | 5775 | 3.431E-04 | $0.481 \pm 0.008$ |
| 2000 | 20000 | 5.483E-04 | 12191 | 12176 | $0.609 \pm 0.007$ | 5254 | 1.441E-04 | $0.432 \pm 0.007$ |

Table V.12: Numbers of $H^+$ events generated, passed the acceptance cuts, fully reconstructed, and the visible cross sections. The final efficiency is given in the last column. Only statistically uncertainties on the acceptance and efficiencies are shown.

$\sigma^{vis}$ represents the visible cross section as reconstructed by the detector which will be compared with the calculated limits at the detector level. These cross sections include acceptance effects and efficiency.

### V.11.2 Results on Charged Higgs

The applicability of the $m_{jj}$ data without signal optimization to complex particle decay topologies can be illustrated using the signal $H^+t$ have been discussed in previous sections. According to the MC simulations, the $m_{jj}$ distributions of the two leading jets from the $H^+t$ process have well-developed peaks near the expected $H^+$ mass for the masses above 300 GeV, thus the usual limit setting procedure can be applied to exclude the complex $H^+t$ process.

The limits on the signal $H^+t$ discussed in previous section are shown in V.39 using the $m_h^{\text{mod}-}$ benchmark model [20]. The non-optimized to the $H^+$ model data exclude the Charged Higgs boson in two-Higgs-doublet model (2HDM) using a four-flavour scheme (4FS) in the $m_h^{\text{mod}-}$ scenario [20] at around 1.2 TeV assuming $\tan(\beta) = 0.5$ and the $t\bar{b}$ decay channel. This exclusion is better by 150 GeV compared to the the published results [21]. For the hMSSM scenario [5], the exclusion is better as the cross section is larger by a few percent as seen in the tables V.1 and V.2.

The difference between the current result and that presented in [21] is that no specific decay channel for Fig. V.39 is assumed, i.e. this limit also includes the decay of $H^+$ to $WH$, as long as the large boost of $H \to b\bar{b}$ and $W \to jj$ results into two jets.

Figure V.40 shows the H+ limits for $\mu$ and $e$ seprately. The limits shows a similar tendencies.

Limits on Charged Higgs model while applying efficiency correction can be found in the figure V.41.

Limits on Charged Higgs model while applying full detector level correction can be found in the figure V.42.

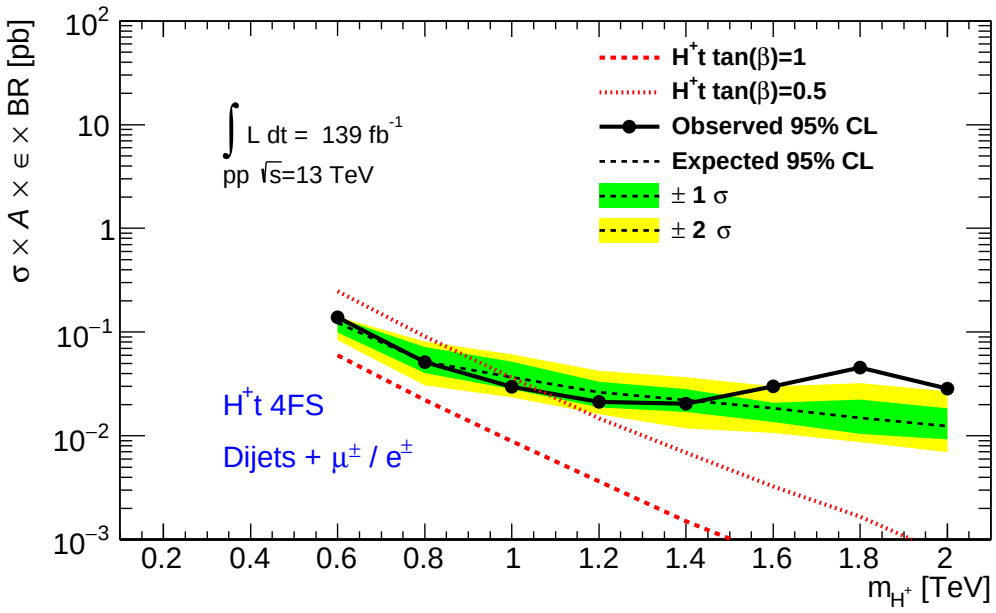


Figure V.39: Observed (filled circles) and expected 95% credibility-level upper limits (dotted line) on the on the cross-section times acceptance ($A$), efficiency ($\epsilon$) and branching ratio (BR) for for the $H^+t$ model for the $m_h^{\text{mod}-}$ benchmark scenario [20].

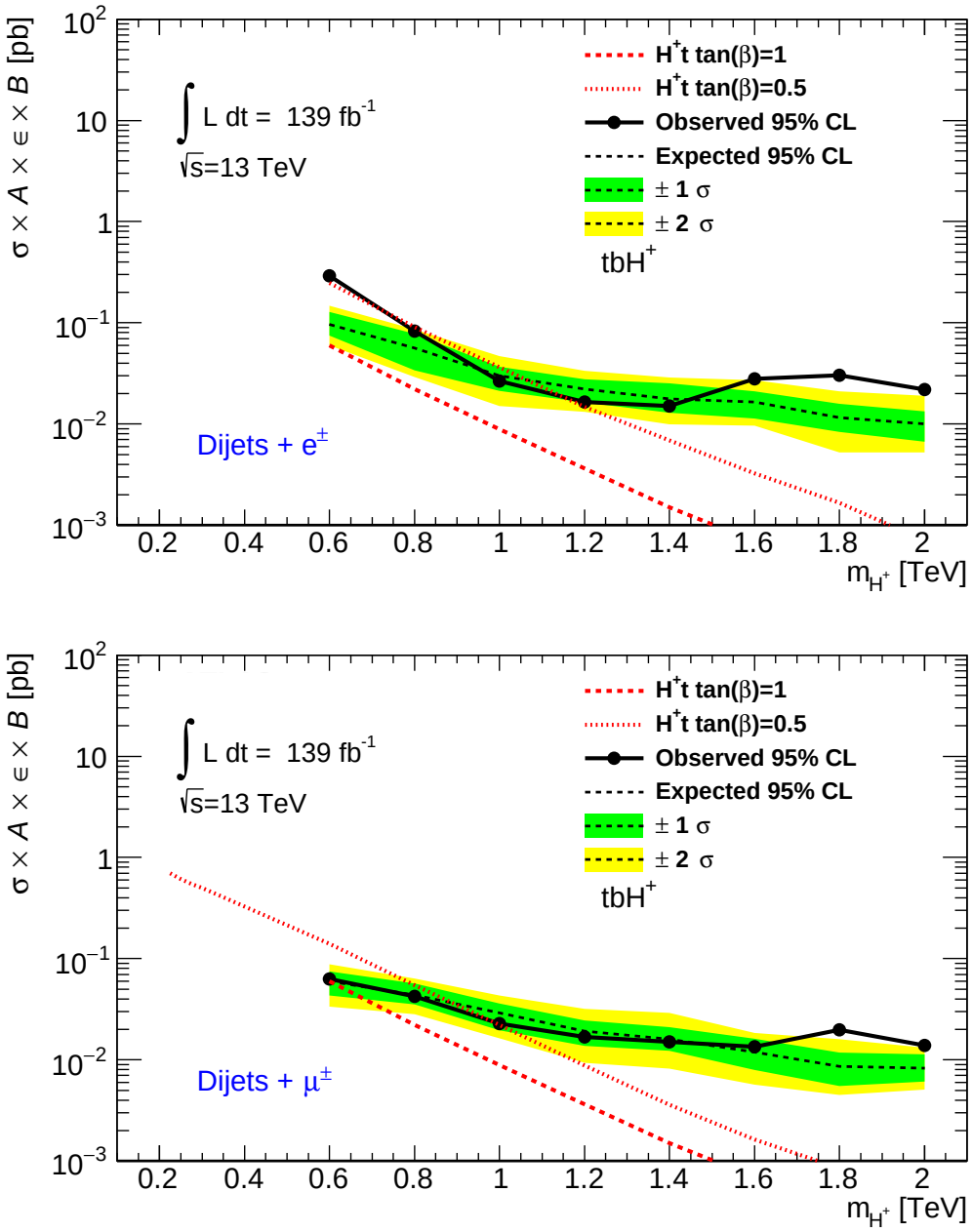


Figure V.40: Observed (filled circles) and expected 95% credibility-level upper limits (dotted line) on the on the cross-section times acceptance ($A$), efficiency ($\epsilon$) and branching ratio (BR) for for the $H^+t$ model for the $m_h^{\text{mod}-}$ benchmark scenario [20]. The limits are shown for $e$ and $\mu$ channels separately.

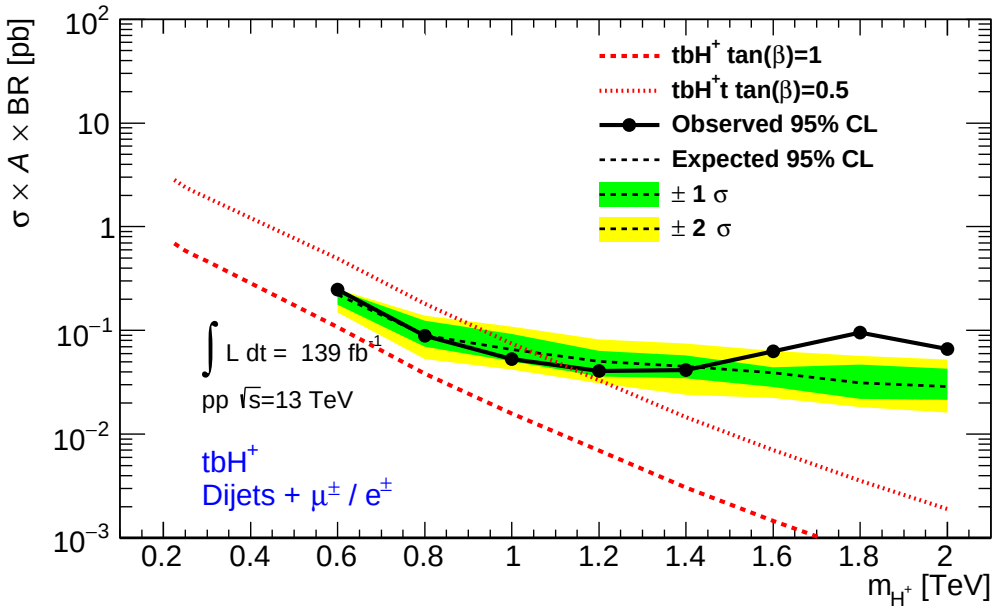


Figure V.41: Observed (filled circles) and expected 95% credibility-level upper limits (dotted line) on the cross-section times acceptance ($A$) and branching ratio (BR) for for the $H^+t$ model for the $m_h^{\text{mod}-}$ benchmark scenario [20].

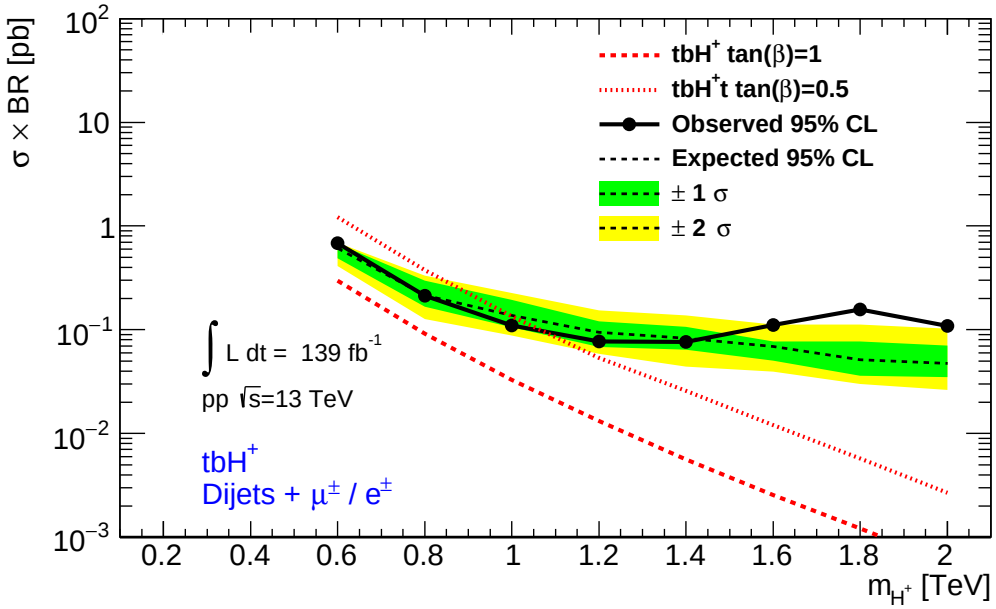


Figure V.42: Observed (filled circles) and expected 95% credibility-level upper limits (dotted line) on the cross-section times branching ratio (BR) for for the $H^+t$ model for the $m_h^{\text{mod}-}$ benchmark scenario [20].

### V.11.3 Comparisons of the $H^+$ limits with published results

The $H^+$ limits are compared with the result [21] based on early Run 2 data, corresponding to about 1/4 of the current dataset, see Fig. V.43 and V.44 On average, the observed and expected limits in the mass range 0.8 TeV – 1.4 TeV are about a factor two better than for the Run 2 data. As the result of this improvement, the excluded $H^+$ mass is 200 GeV higher for $\tan\beta = 0.5$ than for the Run 2 analysis. The excess above the expected limit near the $H^+$ mass of 1.8 TeV corresponds to the excess near 1.3 TeV for the background-only hypothesis, which is also observed in the Gaussian limits. This excess is within the 2 $\sigma$ band of the published limit [21]. The data points for the observed limits correlate since the reconstructed width of the signal is larger than the mass difference between the limit points.

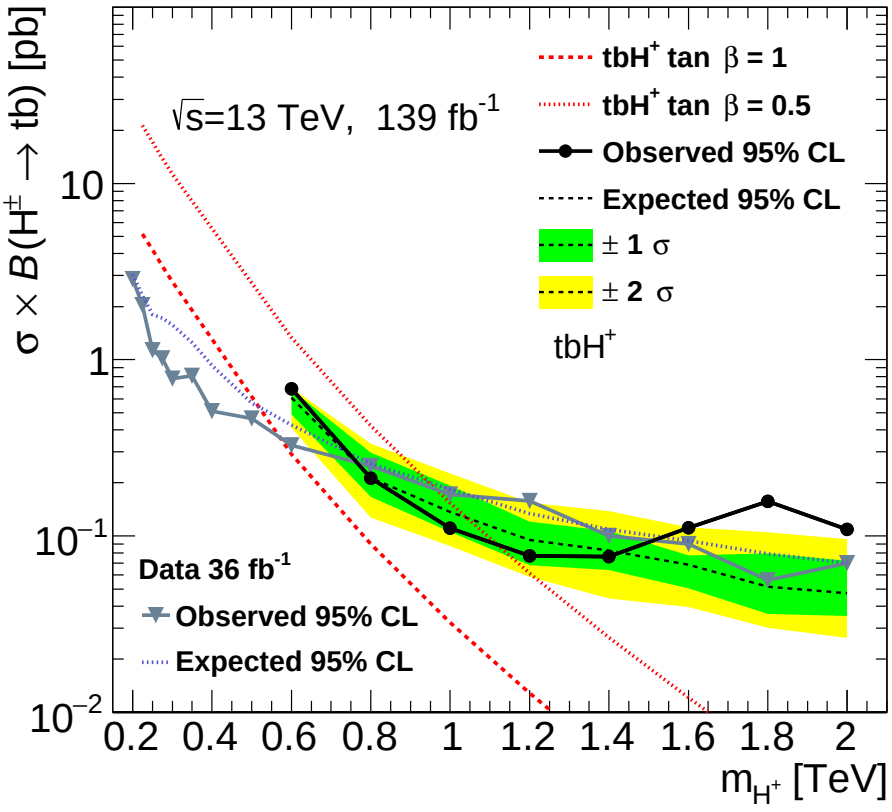


Figure V.43: This figure compares the expected and observed limits from the Run 2 paper [21] (without indicating the 1 and 2 $\sigma$ bands).

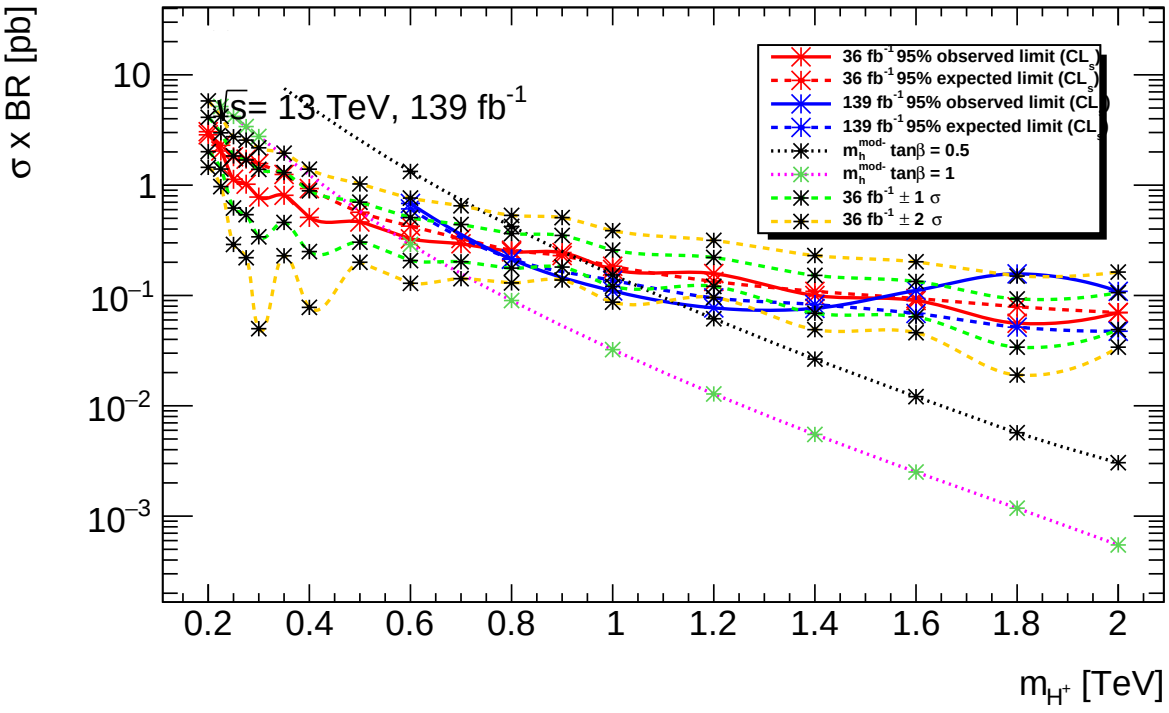


Figure V.44: This figure compares the expected and observed limits from the Run 2 paper [21] with indicating the 1 and 2 $\sigma$ bands.

## V.12 Conclusion from the search

Through this analysis, resonances through dijet invariant masses with the presence of an isolated charged lepton (electron or muon) with $p_T > 60GeV$ have been probed in the mass spectrum in between 216 GeV and 6.3 TeV, where I was interested in the searches for Charged Higgs boson which decays to a top and bottom quarks while providing dijet signature. While using full Run 2 data of pp collision corresponding to 139 $fb^{-1}$ from the ATLAS detector have been used for the studies. High quality object selection and not having any bias towards any BSM model have been part of the strategies for the analysis.

In the entire search range, the maximum deviation from the background hypothesis while including all the systematic uncertainties found was at the dijet invariant mass of 1.3 TeV, which corresponds to $p$ value of 0.3. So, it can be concluded that no significant deviation has been found and the data has been consistent with the standard model background hypothesis and no hints of new physics have been observed.

New upper limits at the 95% credibility-level have been set on Gaussian signals and BSM models including the Charged Higgs boson. Though the analysis was not optimized for dedicated Charged Higgs searches and used conservative approaches on generic dijet resonance searches, the limits found from the analysis exclude Charged Higgs boson below 1.15 TeV assuming $\tan(\beta) = 0.5$ in the $m_h^{mod-}$ scenario of the Minimal Supersymmetric Standard Model (MSSM) Higgs sector. The result has been 150 GeV better than the dedicated Charged Higgs search analysis [21] by ATLAS collaboration.

# CHAPTER VI

## Multi-body searches: Ideas for extension of Dijet resonance searches along with charged lepton

> Nature hides her secret because of her essential loftiness, but not by means of ruse
>
> *Albert Einstein*

In the search of new physics beyond the standard model, many searches are performed in two-body invariant masses of jets which are also known as dijet searches. Dijet resonances are sensitive to many physics processes both in Standard Model and in BSM physics. In different Physics analyses [48, 49, 51, 52, 53] dealing with dijet resonances, various strategies have been used including inclusive searches or using spectator objects to observe the dijet resonance.

For the models where an isolated lepton is present in the final state, dijet resonance searches along with the charged lepton as a spectator object have been described in the previous section in details and also have been published recently by ATLAS [157]. Though the described ATLAS analysis in that section used leptons for triggering purposes only, but for mass reconstructions, leptons have not been used.

The studies of Dijet plus lepton analysis can be extended by having very similar strategy but with the inclusion of lepton and in some cases a lepton and a jet in the mass reconstruction.

Multi-body invariant masses including 2 jets and 1 or 2 leptons are also sensitive to resonances predicted by different BSM models, many of which have not been explored by ATLAS experimental collaboration. A few studies [158, 159] of multi-body (3 body) searches which have been performed at the LHC experiments. In such studies, Monte Carlo descriptions are used to establish the backgrounds hypothesis. An alternative approach is to use data driven control regions without using MC simulations.

This chapter describes some phenomenological investigations which have been performed in the context of dijet plus lepton analysis and motivations of a new approach for searching dijet resonances have been discussed.

### VI.1 Three body invariant masses

The way, dijet plus lepton analysis reconstructed dijet masses, similarly three body mass reconstruction can be done. There have been many beyond the standard model processes where the decay process may look like the following :

$$Particle1 \rightarrow Particle2\ W \rightarrow jjl\nu \tag{VI.1.1}$$

Final state radiation of W or Z boson in the s channel also can contribute to such processes. In dijet plus lepton analysis, while using the lepton for triggering purposes, the two jets were reconstructed to search for the resonance of Particle2. Reconstructing 3 body including 2 jets and the lepton provides opportunities to directly observe Particle1 without dealing with Missing transverse momentum of neutrino if the widths of $m_{jjl}$ is similar or smaller than the width of $m_{jj}$.

For an unknown resonance A, if it decays to two other particles B and C which decay into jets and lepton, 3 body reconstruction can be sensitive to the mass of particle A. If particle B and particle C are unknown and also they are broad in signal widths such that the partial width of the signals is more than 15% of its mass, reconstruction of dijets may not be most appropriate method for identification of events and observation of B may be difficult.

$$A \rightarrow BC \tag{VI.1.2}$$

A representative Feynman diagram can be the following figure VI.1.

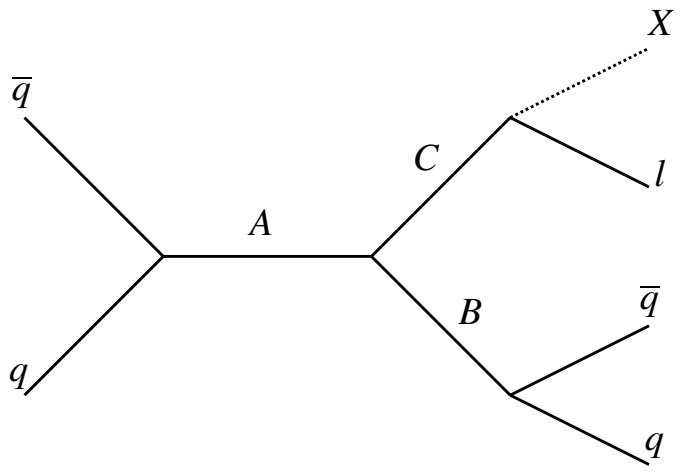


Figure VI.1: A representative diagram of the decay a heavy particle A to two other particles B and C [22].

The process described in figure VI.1 is common in many diboson productions [160]. If particle B and C are known W, Z bosons, they can decay hadronically to $q\bar{q}$ or leptonically to $l^{\pm}\nu$, $l^{+}l^{-}$.

The dijet plus lepton analysis described in the previous section or other similar analysis can have little sensitivity if the width of resonance particle B (which decays

into 2 jets) is very broad, resulting signals being indistinguishable from backgrounds. But the possibilities of particle A having small partial width, can be sufficient for observation of the heavy particle A in such cases. Even if particle B is not directly observable for having larger width, its parent particle can be observed.

The three body reconstruction of two jets and a lepton can be very useful for such decays if the following conditions are fulfilled:

1. The particle B doesn't have significant boost in its transverse momentum and the two jets originating from B is well resolved. In such cases, the angular separation between jets should be approximately equal to $2m_B/p_T^B$.

2. Any constraints on the mass of particle C should not be there due to the presence of at least one lepton. C is allowed to decay both into two leptons C $\rightarrow l^+l^-$ or into a lepton plus neutrino C $\rightarrow l\nu$.

### VI.1.1 Case study : Radion Model

For the studies of 3 body resonance search in our approach, we consider Radion model[57] where Kaluza-Klein excitation of W boson, decays into a radion ($\varphi$) and W boson, and radion decays into two standard model jets, while the W boson results into a lepton and neutrino. It should be also noted, the masses of KK excitation $W_{KK}$ and radion are unknown.

$$Wkk \rightarrow W + \varphi \rightarrow l\nu + gg$$

where $W_{KK}$ denotes the KK boson, and $\varphi$ is a radion which decays into two gluons (jets).

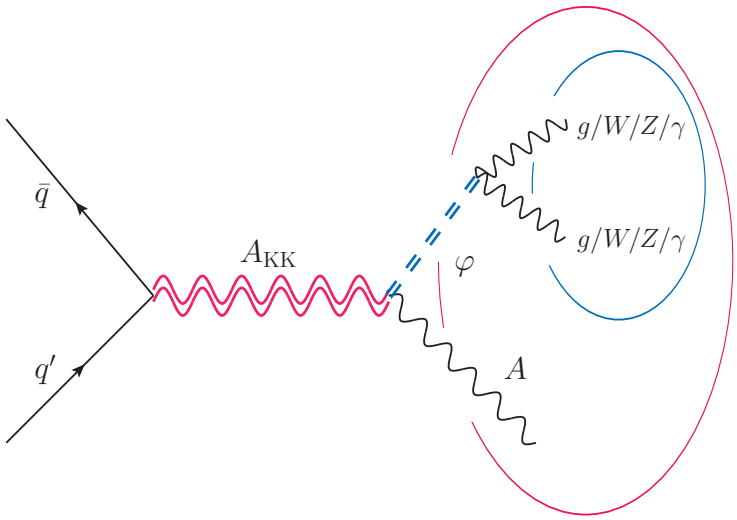


Figure VI.2: A Feynman diagram describing decay in Radion model

Since $W$ decay into $l\nu$, the reconstruction of MET could significantly increase the observed signal width. In our approach, we do not reconstruct MET and after some

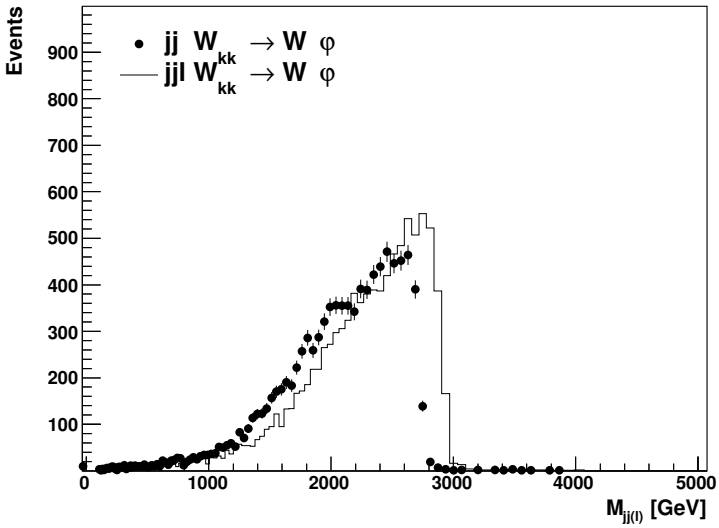


Figure VI.3: Comparisons between $m_{jj}$ and $m_{jjl}$ distributions for the 3 TeV $W_{kk}$ mass for $M_{Wkk} - M_{Rad} = 250$ GeV [22].

investigations on mass difference, 250 GeV mass difference between $W_{KK}$ and $\varphi$ have been considered.

Figure VI.3 shows the 3 body invariant mass distribution has been very similar to 2 body invariant mass distribution. That fulfils the criteria for the observation of parent particle A ($W_{KK}$) in this approach as discussed earlier.

### VI.1.2 A hypothetical scenario

There can be situations when 2-body signal width is larger than 3-body masses and as a result 2-body invariant masses doesn't provide any advantage for the searches.

To explore such scenarios, a study has been done with the simulations generated with Pythia 8 generator. The simulated process has been the following : $W' \rightarrow Z' W*$, where $W'$, $Z'$ and $W*$ are hypothetical bosons and $Z'$ decays to two jets while $W*$ decays to a lepton and a neutrino.

The simulations had the following conditions :

1. Mass of $W'$ : 1 TeV.
2. Width ( $\Gamma$) of $W'$ : 10 GeV.
3. Mass of $Z'$ : 500 GeV.
4. width $\Gamma$) of $Z'$: 250 GeV
5. Ratio of width and mass for both $Z'$ and $W*$ : $\Gamma/m \leq 0.5$

If the conditions described above are analyzed, it can be realized that the observation of particles with large width in $m_{jj}$ distribution is not favourable.

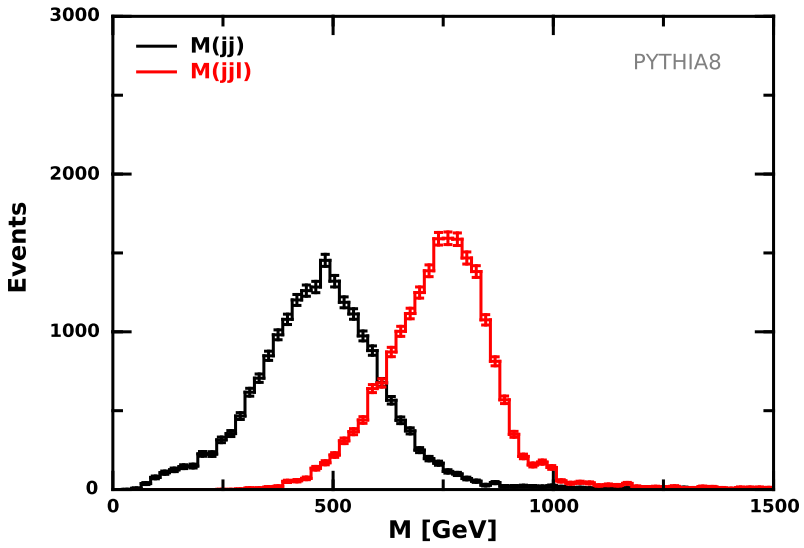


Figure VI.4: The invariant masses of two jets ( $m_{jj}$) and two jets and a lepton ($m_{jjl}$) in events $A \to B\,C$ simulated with Pythia with the settings described earlier.

A comparison of $m_{jj}$ and $m_{jjl}$ distributions in such cases have been made and showed in Figure VI.4.

From figure VI.4, it can be observed that the width of $m_{jjl}$ is smaller than the width of $m_{jj}$. It should be also noted that neutrino's presence contributes to a shift in the invariant mass distributions. The relative width of the $m_{jjl}$ has been close to 15% of masses and that is also acceptable width for experimentally detection on smoothly falling background distribution.

## VI.2 Four-body invariant masses

Four body invariant mass distributions are sensitive to processes where among the final decay products, 4 objects including dijet, lepton and jets are present. Two such cases can be when there are jet-jet-lepton-lepton and jet-jet-jepton-jet.

For figure VI.1, if partial widths of B and C are large such that $\Gamma$ is more than 20% of masses, four body invariant mass distributions should be a better approach than the traditional dijet resonance search.

Such processes are sensitive to quantum black holes scenarios when particle C (of figure VI.4) decays into a lepton and jets [161]. Also, if a very heavy TeV scale particle A decays into two other heavy particles B and C and all decay products are well resolved, four body invariant mass distributions can be a favourable choice.

### VI.2.1 Case study : Composite lepton Model

For the study of 4 body invariant mass reconstruction study, a composite resonance model has been considered. In that composite lepton model[23] , lepton flavour (LF)

universality is broken and has the following decays channel :

$pp \rightarrow V \rightarrow E^{\pm} l^{\mp}$ (where $E \rightarrow Z/h + l$)

where V is a heavy particle $Z'$ boson which decays to composite lepton E and a lepton. E also decays into a lepton and Z boson or Higgs boson while the Z or Higgs decays hadronically into 2 jets.

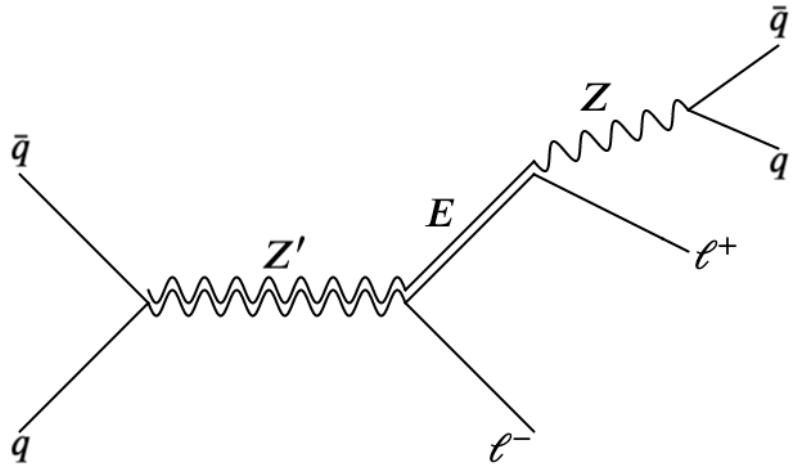


Figure VI.5: A representative Feynman diagram for the composite lepton model[23].

As evident from the decay processes of figure VI.5, masses of 2 jets can be reconstructed to find the mass of Z/h and three body reconstruction of $m_{jjl}$ can be sensitive to composite lepton E and mass of $Z'$ boson can be reconstructed 2jets and 2 leptons using $m_{jjll}$.

The advantage of such process is, even if the composite lepton E is very broad and $m_{jjl}$ is not sensitive to presence of E, if the partial width of $Z'$ boson is narrow, $m_{jjll}$ can be still reconstructed well.

A comparison between three different reconstructions of 2j, 2j+l and 2j+2l at truth level of MC simulations can be found in figure VI.6.

Figure VI.6 shows that both 2jets+lepton and 2jets+2leptons invariant masses can be used for the searches of events originating from the composite resonances [23].

### VI.2.2 A hypothetical scenario

A hypothetical scenario which was considered in the previous section for 3 body reconstruction can also used for 4 body reconstruction as well.

Using Pythia 8 generator, some simulations were produced for the process $W' \rightarrow Z' W*$, where $W'$, $Z'$ and $W*$ are hypothetical bosons and $Z'$ decays to two jets while $W*$ decays to a lepton and a neutrino.

The simulations had the following conditions :

1. Mass of $W'$ : 1 TeV.
2. Width ( $\Gamma$) of $W'$ : 10 GeV.

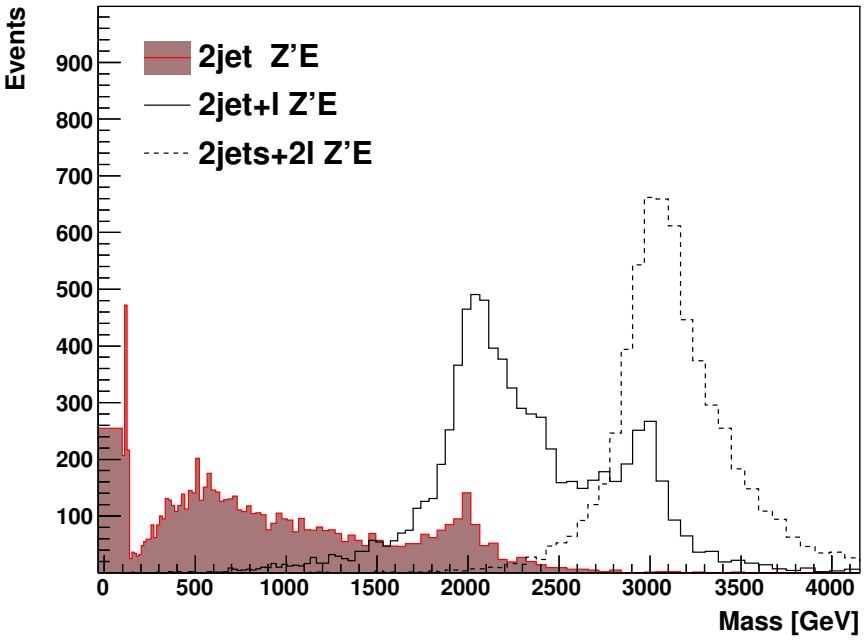


Figure VI.6: Invariant masses for a $Z'E$ model [23] constructed from 2 jets, 2 jets plus a lepton and 2 jets + 2 leptons. The $Z'$ mass was generated at 3 TeV, while $M(E) = 2$ TeV. The simulations are performed using MG5 with Pythia 8 showering.
.

3. Mass of $Z'$ : 500 GeV.

4. width $\Gamma$) of $Z'$: 250 GeV

5. Mass of $W'$ : 300 GeV.

While following the conditions, simulations were produced and jets and leptons were used in the 2-body, 3-body and 4-body invariant mass reconstructions.

A comparison of $m_{jj}$, $m_{jjl}$ and $m_{jjll}$ distributions in such cases have been made and showed in Figure VI.7.

Figure VI.7 illustrates, the relative width for four body invariant mass distribution $m_{jjll}$ is smaller than the traditional dijet invariant masses and also the relative width of $m_{jjll}$ is close to direct detection conditions at the detector.

### VI.3 Exclusion limits

For drawing some upper limits from the studies, proton proton collision events were simulated using Pythia 8 generator[162, 139] and for the parton density function, NNPDF 2.3 LO [163] was chosen. jets were constructed with the help of anti-$k_T$ algorithm [142] with distance parameter of $R = 0.4$ to match with ATLAS FastJet simulation package [143]. In the range of pseudorapidity $|\eta| < 2.5$, jets were required to have minimum transverse energy of 40 GeV. For the isolation of lepton, a cone of

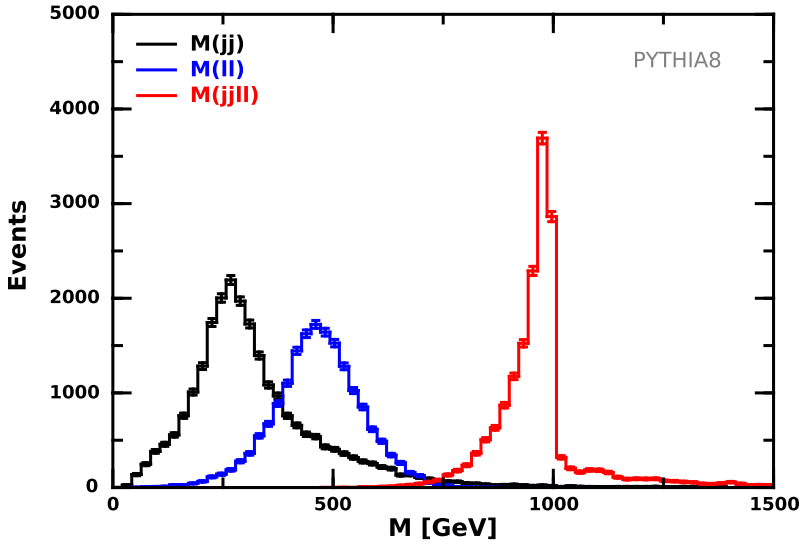


Figure VI.7: The invariant masses of two jets ( $m_{jj}$), two jets and a lepton ($m_{jjl}$) and two jets and two leptons $m_{jjll}$ in events $A \to B\,C$ simulated with Pythia with the settings described earlier.

0.2 in the azimuthal angle and pseudo-rapidity around the direction of the lepton. To ensure lepton's isolation, it had to carry 90% of cone's energy had to be carried by lepton as well.

For background, processes of QCD dijets, W and Z boson process and $t\bar{t}$ events were simulated. Additionally for the leptons $p_T^l > 60$ GeV and for the two jets, $p_T^{jet} > 30$ GeV cuts were used while considering 0.1% misidentification for muons and 1% fake rates for electrons.

$m_{jjl}$ distributions were reconstructed for 140 $fb^{-1}$ luminosity and were also matched to official ATLAS Monte Carlo. And 3 body invariant mass distributions have been made for different luminosities 140 $fb^{-1}$ of LHC Run 2, 440 $fb^{-1}$ for LHC Run 2 and Run 3 and 3 $ab^{-1}$ for HL-LHC.

The distributions of figure VI.8 show a smoothly falling shapes, similar to those for two-body invariant masses studied by ATLAS [48, 49] and CMS [51, 52, 53]. It can be concluded that the $m_{jjl}$ distributions can be examined for local excesses above a data-derived estimate of the smoothly falling predictions, which can be obtained using various smoothing techniques or performing a global fit with an analytic function.

The figure VI.9 shows, limits on the generic Gaussian signal with the width being 15% of the Gaussian peak position have been calculated using the frequentist approach [153] and the asymptotic approximation. The figure shows how the upper limits vary for different luminosities while reconstructing invariant mass of 2 jets and a lepton.

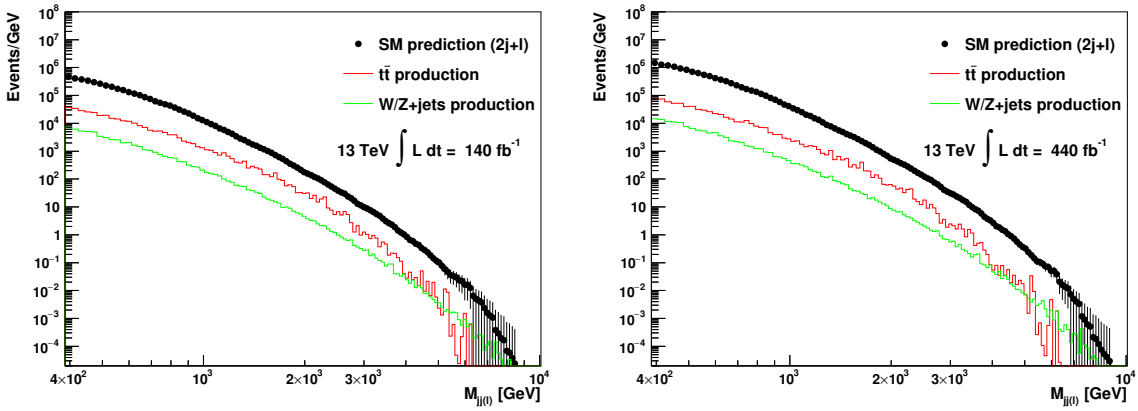


(a) 140




(b) 440

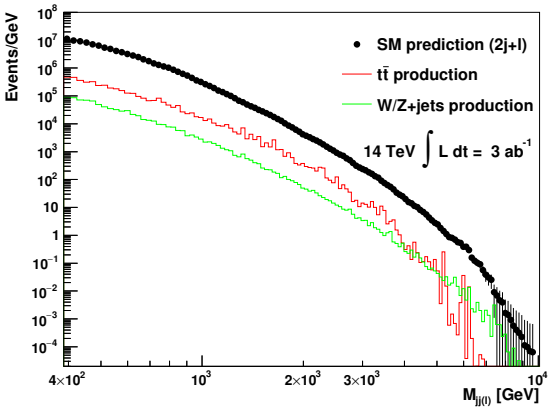


(c) 3

Figure VI.8: Expectations for $m_{jjl}$ invariant mass distributions for 140 $fb^{-1}$, 440 $fb^{-1}$ and 3 $ab^{-1}$(14 TeV) using the Pythia 8 generator for events having at least one isolated lepton with $p_T^l > 60$ GeV. Contributions from $W/Z/H^0$ -boson processes and top-quark processes are shown separately [22].

## VI.4 Conclusion

The discussion presented in this section presents motivation for model independent searches for BSM physics in multi-body final states and also for extending the dijet resonance searches into multi-body invariant mass reconstructions at the detectors which are sensitive to various Physics processes. ATLAS experiment has been investigating many different scenarios of dijet resonances, the study presented in the section may provide new insights for some of the upcoming explorations of model independent resonance searches. The study was submitted as a Snowmass proposal[22].

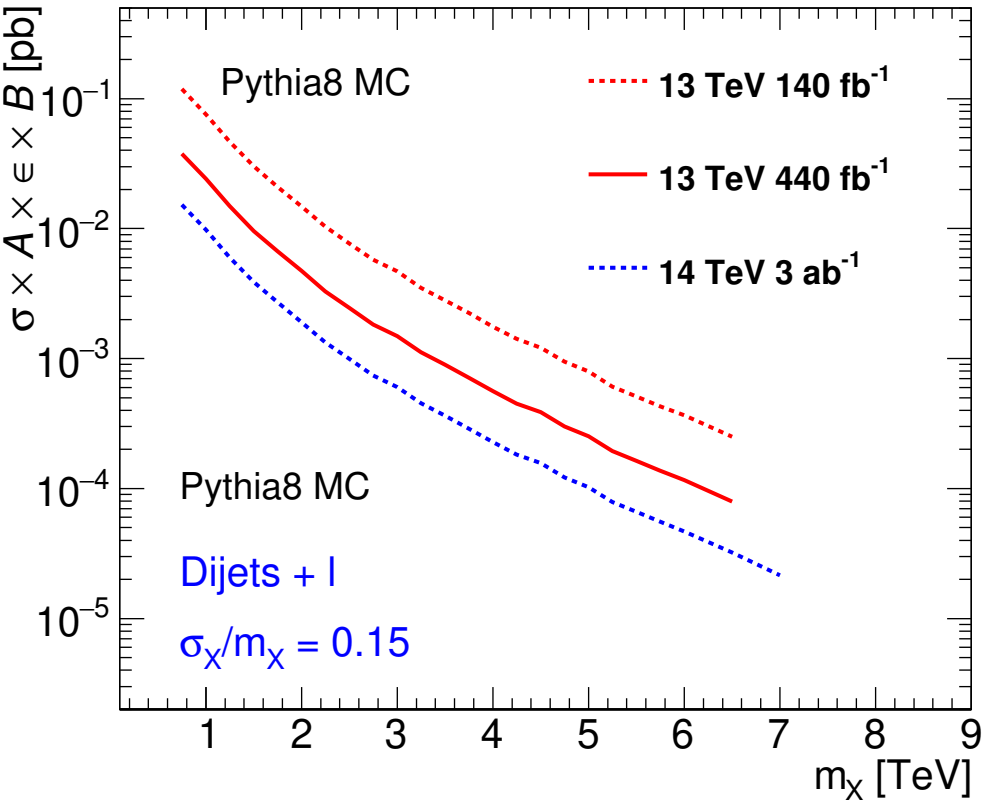


Figure VI.9: The 95% CL upper limits obtained from the $m_{jjl}$ distribution on cross-section times acceptance ($A$), efficiency ($\epsilon$) and branching ratio (BR), for a BSM signal with a cross-section that produces a Gaussian contribution to the particle-level $m_{jjl}$ distribution, as a function of the mean of the Gaussian mass distribution. The limits are calculated assuming 15% width [22].

# CHAPTER VII

## Summary and conclusions

> The deeper we seek, the more is our wonder excited, the more is the dazzlement for our gaze
>
> Abdus Salam at Nobel Prize Banquet speech on 10th December, 1979

In this note, the following studies have been presented: 1. ITk Pixel upgrade studies for HL LHC; 2. Development of Direct tag light jet calibration method; 3. Searches of Charged Higgs boson in the dijet plus lepton channel; 4. Multi-body phenomenology studies. All these studies have been performed with the ATLAS detector except for the Multi-body studies presented in the last chapter.

For the ITK Pixel upgrades, my work at the Argonne National Lab and Fermilab has been part of the long and continuous R&D studies, which are critical for designing and planning detector upgrades for the High Luminosity LHC scheduled to start operation in 2026. Specifically, the Internal Tracker pixel detector upgrades will benefit from the newly installed ATLAS beam telescope at Fermilab and from the studies of pixel sensors, some of which have been described in this thesis.

Development of a new b-tagging calibration method (Direct tag light jet calibration), which I started during my authorship qualification project at ATLAS, provides potential of improvement of b-tagging in general and light jet calibrations in particular specially in the high-$p_T$ regions. With the help of a few collaborators I developed the method further to a working phase. Light jet calibrations and b-tagging are very important for physics results of the ATLAS experiment. It has been shown that the method has good potential of becoming one of the official baseline methods for light jet calibrations in the collaboration.

I have also worked in the Dijet resonance searches along with an isolated charged lepton where I lead the study of the Charged Higgs boson model. Though no significant excess of events above background hypothesis was found, the 95% C.L. exclusion limits reported on Charged Higgs boson production proved to be better than a recent dedicated ATLAS Charged Higgs boson search.

Dijet plus lepton resonance search also provided motivation for multi-body searches while reconstructing 3 or 4 bodies including 2 jets and 1 lepton or 2 jets and 2 leptons. In Chapter 6, I showed that many physics processes are sensitive to the multi-body searches, which will not only help to overcome limitations of dijet resonance searches, but will also provide opportunities to investigate various BSM models by extending the invariant mass reconstruction process while having jets and leptons in the final

state. In the coming days, multi-body search results from ATLAS experiment will be useful to explain if the strategy helps to improve the results previously obtained by dijet resonance searches along with isolated charged lepton.

From historical point of views, it took decades for many particle physics experiments to discover different Standard Model particles. Specially the discovery of the Higgs boson by the ATLAS and CMS experiments took a long time after long explorations by other experiments including the Tevatron experiments. The big collaboration like ATLAS through its joint effort has been trying to explore new beyond the standard model physics in many different channels. The availability of more data, increased luminosity always provide more opportunities to explore something new. While the studies discussed in this thesis didn't find any evidence of new physics, the explorations by the ATLAS experimental collaboration will continue in the search of successful explanations for the discrepancies of the standard model of particle physics and to solve remaining physics problems.

**A few words of hope for LHC Physics through poetry:**

***My dream particle at the LHC***

*For the search of a dream particle of mine,*
*We collided billions of protons, frequently, in a short amount of time.*
*They ran very fast, carrying a lot of my emotions,*
*and collided with its constituent quarks & gluons.*
*While they travelled in speed to sacrifice themselves for my great cause,*
*We wrote complicated algorithms to strategize my search, without pause.*
*We estimated backgrounds, reduced many uncertainties, fakes that would pose,*
*What I ended up so far is excluding more cross sections times branching ratios.*

*It takes decades of efforts, dedicated & continuous,*
*to discover the amazing Tops or Higgs, the gorgeous.*
*Apart from algorithms, they pass through a lot of perseverance,*
*emotions of Physicists, drenched in failures, but with hope & patience.*
*I also hope, someday in a truly magical way,*
*at a new dawn of discovery, as a Sun's bright ray,*
*My dream particle will show up at the Large Hadron Collider,*
*narrating me stories of the exotic world & mysteries of nature.*

(Written by Wasikul Islam)

## REFERENCES


[1] P. A. Zyla et al. Review of Particle Physics. *PTEP*, 2020(8):083C01, 2020.

[2] Jorg Wenninger. Operation and Configuration of the LHC in Run 2. Mar 2019.

[3] G. Aad et al. The ATLAS Experiment at the CERN Large Hadron Collider. *JINST*, 3:S08003, 2008.

[4] D. Frizzell et. al. Systematic Study of Techniques for Assembling a Flex Cable to a Sensor Hybrid for ATLAS ITK Pixel Upgrade.

[5] A. Djouadi, L. Maiani, G. Moreau, A. Polosa, J. Quevillon, and V. Riquer. The post-Higgs MSSM scenario: Habemus MSSM? *Eur. Phys. J.*, C73:2650, 2013.

[6] Vincent Pascuzzi. Looking for Beyond the Standard Model Physics in Dijet-Plus-Lepton Final-State Events Collected with the ATLAS Detector, Oct 2019. Presented 26 Sep 2019.

[7] Abdus Salam. Wikimedia : Standard Model of Elementary Particles. 2018.

[8] CERN. LHC Higgs Working Group report.

[9] CERN. LHC Top Working Group report.

[10] Scott R. Menary. New results on CLEO's heavy quarks bottom and charm. In *23rd Annual SLAC Summer Institute on Particle Physics: The Top Quark and the Electroweak Interaction (SSI 95)*, 1995.

[11] G. Aad et al. Search for dijet resonances in events with an isolated charged lepton using $\sqrt{s} = 13$ tev proton-proton collision data collected by the atlas detector. *Journal of High Energy Physics*, 2020(6), Jun 2020.

[12] Julie Haffner. The CERN accelerator complex. Complexe des accélérateurs du CERN. Oct 2013. General Photo.

[13] *ATLAS magnet system: Technical Design Report, 1.* Technical design report. ATLAS. CERN, Geneva, 1997.

[14] Joao Pequenao. Computer Generated image of the ATLAS calorimeter. Mar 2008.

[15] D. Drakoulakos, E. Gschwendtner, J. M. Maugain, F. Rohrbach, and Yu. Sedykh. The high precision X-ray tomograph for quality control of the ATLAS MDT muon spectrometer. In *7th Asia Pacific Physics Conference*, 7 1997.

[16] ATLAS Collaboration. *Luminosity plots for the 2017 $\sqrt{s}$=13 TeV high-luminosity running period*. CERN.

[17] H. C. Beck. Module development for the HL-LHC ATLAS ITk Pixel upgrade. *JINST*, 14(12):C12008, 2019.

[18] Tetiana Hryn'ova, Fernando Monticelli, Mario Spina, Batool Safarzadeh Samani, and Daniela Maria Koeck. Single electron trigger 2018 performance plots. Technical Report ATL-COM-DAQ-2019-049, CERN, Geneva, Mar 2019.

[19] Muon Trigger Public Results. Twiki.

[20] M. Carena, S. Heinemeyer, O. Stål, C. E. M. Wagner, and G. Weiglein. MSSM Higgs Boson Searches at the LHC: Benchmark Scenarios after the Discovery of a Higgs-like Particle. *Eur. Phys. J.*, C73(9):2552, 2013.

[21] The ATLAS Collaboration. Search for charged Higgs bosons decaying into top and bottom quarks at $\sqrt{s} = 13$ TeV with the ATLAS detector. *JHEP*, 11:085, 2018.

[22] S. V. Chekanov, S. Darmora, W. Islam, C. E. M. Wagner, and J. Zhang. Model-independent searches for new physics in multi-body invariant masses. In *2021 Snowmass Summer Study*, 3 2021.

[23] Mikael Chala and Michael Spannowsky. Behavior of composite resonances breaking lepton flavor universality. *Phys. Rev. D*, 98(3):035010, 2018.

[24] William Wallace. Empedocles. *Cambridge University Press. pp. 344–345*, 9 (11th ed.), 1911.

[25] Emmy Noether. Invariant variation problems. *Transport Theory and Statistical Physics*, 1(3):186–207, Jan 1971.

[26] S.L. Glashow. Partial Symmetries of Weak Interactions. *Nucl. Phys.*, 22:579–588, 1961.

[27] Steven Weinberg. A Model of Leptons. *Phys. Rev. Lett.*, 19:1264–1266, 1967.

[28] Abdus Salam. Weak and Electromagnetic Interactions. *Conf. Proc. C*, 680519:367–377, 1968.

[29] J. J. Aubert et al. Experimental Observation of a Heavy Particle *J*. *Phys. Rev. Lett.*, 33:1404–1406, 1974.

[30] J. E. Augustin, A. M. Boyarski, M. Breidenbach, F. Bulos, J. T. Dakin, G. J. Feldman, G. E. Fischer, D. Fryberger, G. Hanson, B. Jean-Marie, R. R. Larsen, V. Lüth, H. L. Lynch, D. Lyon, C. C. Morehouse, J. M. Paterson, M. L. Perl, B. Richter, P. Rapidis, R. F. Schwitters, W. M. Tanenbaum, F. Vannucci,

G. S. Abrams, D. Briggs, W. Chinowsky, C. E. Friedberg, G. Goldhaber, R. J. Hollebeek, J. A. Kadyk, B. Lulu, F. Pierre, G. H. Trilling, J. S. Whitaker, J. Wiss, and J. E. Zipse. Discovery of a narrow resonance in $e^+e^-$ annihilation. *Phys. Rev. Lett.*, 33:1406–1408, Dec 1974.

[31] M. L. Perl, G. S. Abrams, A. M. Boyarski, M. Breidenbach, D. D. Briggs, F. Bulos, W. Chinowsky, J. T. Dakin, G. J. Feldman, C. E. Friedberg, D. Fryberger, G. Goldhaber, G. Hanson, F. B. Heile, B. Jean-Marie, J. A. Kadyk, R. R. Larsen, A. M. Litke, D. Lüke, B. A. Lulu, V. Lüth, D. Lyon, C. C. Morehouse, J. M. Paterson, F. M. Pierre, T. P. Pun, P. A. Rapidis, B. Richter, B. Sadoulet, R. F. Schwitters, W. Tanenbaum, G. H. Trilling, F. Vannucci, J. S. Whitaker, F. C. Winkelmann, and J. E. Wiss. Evidence for anomalous lepton production in $e^+ - e^-$ annihilation. *Phys. Rev. Lett.*, 35:1489–1492, Dec 1975.

[32] S. W. Herb, D. C. Hom, L. M. Lederman, J. C. Sens, H. D. Snyder, J. K. Yoh, J. A. Appel, B. C. Brown, C. N. Brown, W. R. Innes, K. Ueno, T. Yamanouchi, A. S. Ito, H. Jöstlein, D. M. Kaplan, and R. D. Kephart. Observation of a dimuon resonance at 9.5 gev in 400-gev proton-nucleus collisions. *Phys. Rev. Lett.*, 39:252–255, Aug 1977.

[33] R. Brandelik et al. Evidence for Planar Events in e+ e- Annihilation at High-Energies. *Phys. Lett. B*, 86:243–249, 1979.

[34] G. Arnison et al. Experimental Observation of Isolated Large Transverse Energy Electrons with Associated Missing Energy at $\sqrt{s} = 540$ GeV. *Phys. Lett. B*, 122:103–116, 1983.

[35] S. Abachi et al. Observation of the top quark. *Phys. Rev. Lett.*, 74:2632–2637, 1995.

[36] F. Abe et al. Observation of top quark production in $\bar{p}p$ collisions. *Phys. Rev. Lett.*, 74:2626–2631, 1995.

[37] Serguei Chatrchyan et al. Observation of a New Boson at a Mass of 125 GeV with the CMS Experiment at the LHC. *Phys. Lett. B*, 716:30–61, 2012.

[38] M. Aaboud et al. Observation of Higgs boson production in association with a top quark pair at the LHC with the ATLAS detector. *Phys. Lett. B*, 784:173–191, 2018.

[39] Albert M Sirunyan et al. Observation of Single Top Quark Production in Association with a $Z$ Boson in Proton-Proton Collisions at $\sqrt{s}$ =13 TeV. *Phys. Rev. Lett.*, 122(13):132003, 2019.

[40] G. Aad et al. Observation of the associated production of a top quark and a $Z$ boson in $pp$ collisions at $\sqrt{s} = 13$ TeV with the ATLAS detector. *JHEP*, 07:124, 2020.

[41] M. Aaboud et al. Observation of $H \to b\bar{b}$ decays and $VH$ production with the ATLAS detector. *Phys. Lett. B*, 786:59–86, 2018.

[42] G. W. Bennett, B. Bousquet, H. N. Brown, G. Bunce, R. M. Carey, P. Cushman, G. T. Danby, P. T. Debevec, M. Deile, H. Deng, W. Deninger, S. K. Dhawan, V. P. Druzhinin, L. Duong, E. Efstathiadis, F. J. M. Farley, G. V. Fedotovich, S. Giron, F. E. Gray, D. Grigoriev, M. Grosse-Perdekamp, A. Grossmann, M. F. Hare, D. W. Hertzog, X. Huang, V. W. Hughes, M. Iwasaki, K. Jungmann, D. Kawall, M. Kawamura, B. I. Khazin, J. Kindem, F. Krienen, I. Kronkvist, A. Lam, R. Larsen, Y. Y. Lee, I. Logashenko, R. McNabb, W. Meng, J. Mi, J. P. Miller, Y. Mizumachi, W. M. Morse, D. Nikas, C. J. G. Onderwater, Y. Orlov, C. S. Özben, J. M. Paley, Q. Peng, C. C. Polly, J. Pretz, R. Prigl, G. zu Putlitz, T. Qian, S. I. Redin, O. Rind, B. L. Roberts, N. Ryskulov, S. Sedykh, Y. K. Semertzidis, P. Shagin, Yu. M. Shatunov, E. P. Sichtermann, E. Solodov, M. Sossong, A. Steinmetz, L. R. Sulak, C. Timmermans, A. Trofimov, D. Urner, P. von Walter, D. Warburton, D. Winn, A. Yamamoto, and D. Zimmerman. Final report of the e821 muon anomalous magnetic moment measurement at bnl. *Phys. Rev. D*, 73:072003, Apr 2006.

[43] T. Aoyama et al. The anomalous magnetic moment of the muon in the Standard Model. *Phys. Rept.*, 887:1–166, 2020.

[44] B. Abi et al. Measurement of the Positive Muon Anomalous Magnetic Moment to 0.46 ppm. *Phys. Rev. Lett.*, 126:141801, 2021.

[45] T. Albahri et al. Magnetic Field Measurement and Analysis for the Muon g-2 Experiment at Fermilab. *Phys. Rev. A*, 103:042208, 2021.

[46] T. Albahri et al. Measurement of the anomalous precession frequency of the muon in the Fermilab Muon g-2 experiment. *Phys. Rev. D*, 103:072002, 2021.

[47] Vera C. Rubin and W. Kent Ford, Jr. Rotation of the Andromeda Nebula from a Spectroscopic Survey of Emission Regions. *Astrophys. J.*, 159:379–403, 1970.

[48] ATLAS Collaboration. Search for new phenomena in dijet mass and angular distributions from $pp$ collisions at $\sqrt{s} = 13$ TeV with the ATLAS detector. *Phys. Lett.*, B754:302–322, 2016.

[49] ATLAS Collaboration. Search for new phenomena in dijet events using 37 $\text{fb}^{-1}$ of $pp$ collision data collected at $\sqrt{s}$ =13 TeV with the ATLAS detector. *Phys. Rev.*, D 96(5):052004, 2017.

[50] ATLAS Collaboration. Search for low-mass dijet resonances using trigger-level jets with the atlas detector in $pp$ collisions at $\sqrt{s} = 13$ tev. 2018.

[51] CMS Collaboration. Search for dijet resonances in proton–proton collisions at 13 TeV and constraints on dark matter and other models. *Phys. Lett.*, B769:520–542, 2017. [Erratum: B772 (2017) 882 ].

[52] CMS Collaboration. Search for narrow resonances in dijet final states at $\sqrt{(s)} =$ 8 TeV with the novel CMS technique of data scouting. *Phys. Rev. Lett.*, 117(3):031802, 2016.

[53] CMS Collaboration. Search for narrow resonances in the b-tagged dijet mass spectrum in proton-proton collisions at $\sqrt{s} = 8$ TeV. *Phys. Rev. Lett.*, 120(20):201801, 2018.

[54] Daniel Abercrombie et al. Dark matter benchmark models for early lhc run-2 searches: Report of the atlas/cms dark matter forum. 2015. FERMILAB-PUB-15-282-CD.

[55] B. Mele G. Altarelli and M. Ruiz-Altaba. Searching for new heavy vector bosons in $p\overline{p}$ colliders. *Z. Phys. C*, 45:109, 1989.

[56] A. G. Akeroyd et al. Prospects for charged Higgs searches at the LHC. *Eur. Phys. J.*, C77(5):276, 2017.

[57] Kaustubh S. Agashe, Jack Collins, Peizhi Du, Sungwoo Hong, Doojin Kim, and Rashmish K. Mishra. LHC Signals from Cascade Decays of Warped Vector Resonances. *JHEP*, 05:078, 2017.

[58] G. Aad et al. Observation of a new particle in the search for the Standard Model Higgs boson with the ATLAS detector at the LHC. *Phys. Lett.*, B716:1–29, 2012.

[59] G. Aad et al. Combined Measurement of the Higgs Boson Mass in $pp$ Collisions at $\sqrt{s} = 7$ and 8 TeV with the ATLAS and CMS Experiments. *Phys. Rev. Lett.*, 114:191803, 2015.

[60] Lyndon Evans and Philip Bryant. LHC Machine. *JINST*, 3:S08001, 2008.

[61] T. D. Lee. A Theory of Spontaneous T Violation. *Phys. Rev.*, D8:1226–1239, 1973. [,516(1973)].

[62] John F. Gunion and Howard E. Haber. The CP conserving two Higgs doublet model: The Approach to the decoupling limit. *Phys. Rev.*, D67:075019, 2003.

[63] G. C. Branco, P. M. Ferreira, L. Lavoura, M. N. Rebelo, Marc Sher, and Joao P. Silva. Theory and phenomenology of two-Higgs-doublet models. *Phys. Rept.*, 516:1–102, 2012.

[64] K. S. Babu and Sudip Jana. Enhanced Di-Higgs Production in the Two Higgs Doublet Model. 2018.

[65] T. P. Cheng and Ling-Fong Li. Neutrino Masses, Mixings and Oscillations in SU(2) x U(1) Models of Electroweak Interactions. *Phys. Rev.*, D22:2860, 1980.

[66] J. Schechter and J. W. F. Valle. Neutrino Masses in SU(2) x U(1) Theories. *Phys. Rev.*, D22:2227, 1980.

[67] George Lazarides, Q. Shafi, and C. Wetterich. Proton Lifetime and Fermion Masses in an SO(10) Model. *Nucl. Phys.*, B181:287–300, 1981.

[68] Rabindra N. Mohapatra and Goran Senjanovic. Neutrino Masses and Mixings in Gauge Models with Spontaneous Parity Violation. *Phys. Rev.*, D23:165, 1981.

[69] M. Magg and C. Wetterich. Neutrino Mass Problem and Gauge Hierarchy. *Phys. Lett.*, 94B:61–64, 1980.

[70] J R Andersen et al. Handbook of LHC Higgs Cross Sections: 3. Higgs Properties. 2013.

[71] A. Djouadi, L. Maiani, A. Polosa, J. Quevillon, and V. Riquer. Fully covering the MSSM Higgs sector at the LHC. *JHEP*, 06:168, 2015.

[72] Emanuele Bagnaschi et al. Benchmark scenarios for low $\tan\beta$ in the MSSM. 2015.

[73] G. Abbiendi et al. Search for Charged Higgs bosons: Combined Results Using LEP Data. *Eur. Phys. J.*, C73:2463, 2013.

[74] T. Aaltonen et al. Search for charged Higgs bosons in decays of top quarks in p anti-p collisions at s**(1/2) = 1.96 TeV. *Phys. Rev. Lett.*, 103:101803, 2009.

[75] V. M. Abazov et al. Search for Charged Higgs Bosons in Top Quark Decays. *Phys. Lett.*, B682:278–286, 2009.

[76] Vardan Khachatryan et al. Search for a charged Higgs boson in pp collisions at $\sqrt{s} = 8$ TeV. *JHEP*, 11:018, 2015.

[77] G Aad et al. Search for charged Higgs bosons in the $H^{\pm} \to tb$ decay channel in $pp$ collisions at $\sqrt{s} = 8$ TeV using the ATLAS detector. *JHEP*, 03:127, 2016.

[78] A. Arbey, F. Mahmoudi, O. Stal, and T. Stefaniak. Status of the Charged Higgs Boson in Two Higgs Doublet Models. *Eur. Phys. J.*, C78(3):182, 2018.

[79] Jogesh C. Pati and Abdus Salam. Lepton number as the fourth "color". *Phys. Rev. D*, 10:275–289, Jul 1974.

[80] Guido Altarelli, B. Mele, and M. Ruiz-Altaba. Searching for New Heavy Vector Bosons in $p\bar{p}$ Colliders. *Z. Phys. C*, 45:109, 1989. [Erratum: Z.Phys.C 47, 676 (1990)].

[81] N. Arkani-Hamed, A.G. Cohen, E. Katz, and A.E. Nelson. The Littlest Higgs. *JHEP*, 07:034, 2002.

[82] R.Sekhar Chivukula, Bogdan A. Dobrescu, Howard Georgi, and Christopher T. Hill. Top Quark Seesaw Theory of Electroweak Symmetry Breaking. *Phys. Rev. D*, 59:075003, 1999.

[83] David J. Muller and Satyanarayan Nandi. Top flavor: A Separate SU(2) for the third family. *Phys. Lett. B*, 383:345–350, 1996.

[84] Keith R. Dienes, Emilian Dudas, and Tony Gherghetta. Grand unification at intermediate mass scales through extra dimensions. *Nucl. Phys. B*, 537:47–108, 1999.

[85] Steven Weinberg. Implications of Dynamical Symmetry Breaking. *Phys. Rev. D*, 13:974–996, 1976. [Addendum: Phys.Rev.D 19, 1277–1280 (1979)].

[86] Leonard Susskind. Dynamics of Spontaneous Symmetry Breaking in the Weinberg-Salam Theory. *Phys. Rev. D*, 20:2619–2625, 1979.

[87] Savas Dimopoulos and Leonard Susskind. Mass Without Scalars. 2:930–930, 1979.

[88] Estia Eichten and Kenneth D. Lane. Dynamical Breaking of Weak Interaction Symmetries. *Phys. Lett. B*, 90:125–130, 1980.

[89] Gustavo Burdman, Bogdan A. Dobrescu, and Eduardo Ponton. Resonances from two universal extra dimensions. *Phys. Rev. D*, 74:075008, 2006.

[90] Ehab Malkawi, Timothy M.P. Tait, and C.P. Yuan. A Model of strong flavor dynamics for the top quark. *Phys. Lett. B*, 385:304–310, 1996.

[91] Jogesh C Pati and Abdus Salam. Lepton Number as the Fourth Color. *Phys. Rev. D*, 10:275–289, 1974. [Erratum: Phys.Rev.D 11, 703–703 (1975)].

[92] Christopher T. Hill. Topcolor assisted technicolor. *Phys. Lett. B*, 345:483–489, 1995.

[93] Zack Sullivan. Fully Differential $W'$ Production and Decay at Next-to-Leading Order in QCD. *Phys. Rev. D*, 66:075011, 2002.

[94] Zack Sullivan Daniel Duffty. Model independent reach for W' bosons at the LHC. *Phys. Rev. D*, 86:075018, 2012.

[95] Zack Sullivan. Fully differentialwproduction and decay at next-to-leading order in qcd. *Physical Review D*, 66(7), Oct 2002.

[96] Daniel Duffty and Zack Sullivan. Model independent reach forwbosons at the lhc. *Physical Review D*, 86(7), Oct 2012.

[97] Victor Mukhamedovich Abazov et al. Search for $W' \to tb$ Resonances with Left- and Right-Handed Couplings to Fermions. *Phys. Lett. B*, 699:145–150, 2011.

[98] T. Aaltonen, J. Adelman, T. Akimoto, B. Álvarez González, S. Amerio, D. Amidei, A. Anastassov, A. Annovi, J. Antos, G. Apollinari, and et al. Search for the production of narrowtb¯resonances in1.9fb1ofpp¯collisions ats=1.96tev. *Physical Review Letters*, 103(4), Jul 2009.

[99] A.M. Sirunyan, A. Tumasyan, W. Adam, F. Ambrogi, E. Asilar, T. Bergauer, J. Brandstetter, E. Brondolin, M. Dragicevic, J. Erö, and et al. Search for heavy resonances decaying to a top quark and a bottom quark in the lepton+jets final state in proton–proton collisions at 13tev. *Physics Letters B*, 777:39–63, Feb 2018.

[100] G. Aad, B. Abbott, J. Abdallah, S. Abdel Khalek, O. Abdinov, R. Aben, B. Abi, M. Abolins, O. S. AbouZeid, and et al. Search for $w' \to tb \to qqbb$, $w \to tb \to qqbb$ decays in $pp$ p p collisions at $\sqrt{s}$=8 tev with the atlas detector. *The European Physical Journal C*, 75(4), Apr 2015.

[101] M. Aaboud, G. Aad, B. Abbott, O. Abdinov, B. Abeloos, S.H. Abidi, O.S. AbouZeid, N.L. Abraham, H. Abramowicz, H. Abreu, and et al. Search for w→tb decays in the hadronic final state using pp collisions at s=13tev with the atlas detector. *Physics Letters B*, 781:327–348, Jun 2018.

[102] Kaustubh S. Agashe, Jack H. Collins, Peizhi Du, Sungwoo Hong, Doojin Kim, and Rashmish K. Mishra. Lhc signals from cascade decays of warped vector resonances. *Journal of High Energy Physics*, 2017(5), May 2017.

[103] G. J. Toomer. *Isis*, 55(4):463–465, 1964.

[104] Peter Urbach. *Francis Bacon's Philosophy of Science: An Account and a Reappraisal. La Salle, Ill.* Open Court Publishing Co., 1987.

[105] Francis Bacon and Joseph Devey. *Novum Organum.* New York,Collier,. https://www.biodiversitylibrary.org/bibliography/17510.

[106] Lyndon R Evans and Philip Bryant. LHC Machine. *JINST*, 3:S08001. 164 p, 2008. This report is an abridged version of the LHC Design Report (CERN-2004-003).

[107] C. E. Hill, A. M. Lombardi, W. Pirkl, E. Tanke, and M. Vretenar. Performance of the CERN Linac-2 with a high intensity proton RFQ. 10 1994.

[108] B. Autin et al. Design Study of a Proton-anti-Proton Colliding Beam Facility. 3 1978.

[109] S. Chatrchyan et al. The CMS Experiment at the CERN LHC. *JINST*, 3:S08004, 2008.

[110] A. Augusto Alves, Jr. et al. The LHCb Detector at the LHC. *JINST*, 3:S08005, 2008.

[111] K. Aamodt et al. The ALICE experiment at the CERN LHC. *JINST*, 3:S08002, 2008.

[112] B. Muratori Werner Herr. Concept of luminosity. 2006.

[113] Werner Herr and B Muratori. Beam requirements and fundamental choices, volume 3. chapter 2.

[114] *ATLAS inner detector: Technical Design Report, 1.* Technical design report. ATLAS. CERN, Geneva, 1997.

[115] S Haywood, L Rossi, R Nickerson, and A Romaniouk. *ATLAS inner detector: Technical Design Report, 2.* Technical design report. ATLAS. CERN, Geneva, 1997.

[116] M Capeans et al. ATLAS Insertable B-Layer Technical Design Report. Technical Report CERN-LHCC-2010-013. ATLAS-TDR-19, Sep 2010.

[117] *ATLAS liquid-argon calorimeter: Technical Design Report.* Technical design report. ATLAS. CERN, Geneva, 1996.

[118] *ATLAS muon spectrometer: Technical Design Report.* Technical design report. ATLAS. CERN, Geneva, 1997.

[119] Technical Design Report for the Phase-II Upgrade of the ATLAS Muon Spectrometer. Technical Report CERN-LHCC-2017-017. ATLAS-TDR-026, CERN, Geneva, Sep 2017.

[120] The ATLAS collaboration. Operation of the atlas trigger system in run 2. *Journal of Instrumentation*, 15(10):P10004–P10004, Oct 2020.

[121] Federico Lasagni Manghi. LUCID: The ATLAS Luminosity Detector. *PoS*, ICHEP2018:280, 2019.

[122] Carla Sbarra. The LUCID-2 Detector. Technical Report ATL-FWD-PROC-2018-009, CERN, Geneva, Dec 2018.

[123] M. Aaboud, G. Aad, B. Abbott, J. Abdallah, O. Abdinov, B. Abeloos, R. Aben, O. S. AbouZeid, N. L. Abraham, and et al. Luminosity determination in pp collisions at $\sqrt{s} = 8$ tev using the atlas detector at the lhc. *The European Physical Journal C*, 76(12), Nov 2016.

[124] Luminosity determination in *pp* collisions at $\sqrt{s} = 13$ TeV using the ATLAS detector at the LHC. 6 2019.

[125] M. Garcia-Sciveres et al. The FE-I4 pixel readout integrated circuit. *Nucl. Instrum. Meth. A*, 636:S155–S159, 2011.

[126] Elia Conti et al. Development of a Large Pixel Chip Demonstrator in RD53 for ATLAS and CMS Upgrades. *PoS*, TWEPP-17:005, 2017.

[127] M. Benoit et al. The FE-I4 Telescope for particle tracking in testbeam experiments. *JINST*, 11(07):P07003, 2016.

[128] D. Nelson. HSIO II Developement Platform Users Guide. *JINST*, 14(08), 2015.

[129] M. Kiehn et al. Performance of the ATLASPix1 pixel sensor prototype in ams aH18 CMOS technology for the ATLAS ITk upgrade. *JINST*, 14(08):C08013, 2019.

[130] W. Islam. et al. V.S. Bhopatkar, M. Benoit. Installation and Commissioning of the Argonne Pixel Telescope and Different DAQ systems at Fermilab Test Beam Facility.

[131] M. Rominsky et al. Fermilab Test Beam Facility Annual Report: FY19. 5 2020.

[132] M. Rominsky et al. Fermilab Test Beam Facility Annual Report: FY18. 5 2020.

[133] G. Aad et al. ATLAS b-jet identification performance and efficiency measurement with $t\bar{t}$ events in pp collisions at $\sqrt{s} = 13$ TeV. *Eur. Phys. J. C*, 79(11):970, 2019.

[134] Calibration of light-flavour $b$-jet mistagging rates using ATLAS proton-proton collision data at $\sqrt{s} = 13$ TeV. Technical Report ATLAS-CONF-2018-006, CERN, Geneva, Apr 2018.

[135] Wasikul Islam, Alexander Khanov, Giacinto Piacquadio, David Olivier Jamin, and Andrea Coccaro. Light Jet Calibration using Direct Tag method in pp collision at s=13 TeV with the ATLAS detector. Technical Report ATL-COM-PHYS-2018-246, CERN, Geneva, Mar 2018.

[136] ATLAS Collaboration. Invariant mass distribution of jet pairs produced in association with one lepton and missing transverse energy at the ATLAS experiment. Technical Report ATLAS-CONF-2011-069, CERN, Geneva, May 2011.

[137] Sven Heinemeyer, Wolfgang Hollik, and Georg Weiglein. Constraints on tan in the mssm from the upper bound on the mass of the lightest higgs boson. *Journal of High Energy Physics*, 2000(06):009–009, Jun 2000.

[138] Coll ATLAS, M Beckingham, M Duehrssen, E Schmidt, M Shapiro, M Venturi, J Virzi, I Vivarelli, M Werner, S Yamamoto, and T Yamanaka. The simulation principle and performance of the ATLAS fast calorimeter simulation FastCaloSim. Technical Report ATL-PHYS-PUB-2010-013, CERN, Geneva, Oct 2010.

[139] Stephen Mrenna Torbjorn Sjostrand and Peter Z. Skands. A Brief Introduction to PYTHIA 8.1. *Comput. Phys. Commun.*, 178:852–867, 2008.

[140] Stefano Frixione, Paolo Nason, and Carlo Oleari. Matching nlo qcd computations with parton shower simulations: the powheg method. *Journal of High Energy Physics*, 2007(11):070–070, Nov 2007.

[141] Tetiana Hryn'ova et al. Single electron trigger 2018 performance plots. Technical Report ATL-COM-DAQ-2019-049, CERN, Geneva, Mar 2019.

[142] Matteo Cacciari, Gavin P. Salam, and Gregory Soyez. The anti-$k_t$ jet clustering algorithm. *JHEP*, 04:063, 2008.

[143] Matteo Cacciari, Gavin P. Salam, and Gregory Soyez. FastJet User Manual. *Eur. Phys. J.*, C 72:1896, 2012. http://fastjet.fr/.

[144] ATLAS Collaboration. Tagging and suppression of pileup jets with the ATLAS detector. Technical Report ATLAS-CONF-2014-018, CERN, Geneva, May 2014.

[145] Sergei Chekanov, Jeremy Love, James Proudfoot, Vincent Pascuzzi, Adriana Milic, Dylan Cooper Frizzell, Stephen Sekula, Rui Wang, and Peilong Wang. Search for resonances in the di-jet mass distribution in events with identified leptons in proton-proton collisions at $\sqrt{s}$=13 TeV with the ATLAS detector. Technical Report ATL-COM-PHYS-2017-809, CERN, Geneva, Jun 2017. 251 pages.

[146] G. Choudalakis. On hypothesis testing, trials factor, hypertests and the BumpHunter. Technical report, 2011.

[147] Eilam Gross and Ofer Vitells. Trial factors for the look elsewhere effect in high energy physics. *Eur. Phys. J.*, C70:525–530, 2010.

[148] Matteo Bauce, Benjamin William Allen, Torsten Akesson, Dante Amidei, Harinder Singh Bawa, Iain Alexander Bertram, Caterina Doglioni, Gabriel Facini, Meghan Frate, James Frost, Christopher Grud, Edgar Kellermann, Bogdan Malaescu, Andrea Messina, Katherine Pachal, Trine Poulsen, Jacob Searcy, Karishma Sekhon, David Strom, Marco Vanadia, Venkatesh Veeraraghavan, Ben William Whitmore, Daniel Whiteson, Dengfeng Zhang, Marijus Brazickas, Robert Hankache, Ryan Christopher Edgar, Antonio Boveia, Charles William Kalderon, and Emma Tolley. Search for New Phenomena in Dijet Events with the ATLAS detector at $\sqrt{s}$=13 TeV using 2015 and 2016 data. Technical Report ATL-COM-PHYS-2016-1495, CERN, Geneva, Oct 2016.

[149] Karishma Sekhon, Ryan Christopher Edgar, and Dante Amidei. SWiFt: Sliding Window Fit Method for Resonance Searches. Technical Report ATL-COM-PHYS-2018-161, CERN, Geneva, Feb 2018.

[150] Vincent Pascuzzi, Sergei Chekanov, Dylan Cooper Frizzell, Jeremy Love, Adriana Milic, Wasikul Islam, Alexander Khanov, Huan Yu Meng, James Proudfoot, Rui Wang, Julian Maximilian Volker Glatzer, Max Fredrik Isacson, Jana Schaarschmidt, and Lluisa-Maria Mir. Search for dijet resonances in events with an isolated lepton using $\sqrt{s}$ = 13 TeV proton–proton collision data collected by the ATLAS detector. Technical Report ATL-COM-PHYS-2018-1524, CERN, Geneva, Nov 2018. Supporting material for the Run II paper JDM - dijet+lepton 2018 ANA-EXOT-2018-32. This is early Run II paper without signal optimizations, as agreed with the EXO conveners.

[151] Glen Cowan. Statistics for Searches at the LHC. In *Proceedings, 69th Scottish Universities Summer School in Physics : LHC Phenomenology (SUSSP69): St.Andrews, Scotland, August 19-September 1, 2012*, pages 321–355, 2013.

[152] Eilam Gross. Practical statistics for high energy physics. *CERN Yellow Reports: School Proceedings*, 4(0):165, 2017.

[153] Glen Cowan, Kyle Cranmer, Eilam Gross, and Ofer Vitells. Asymptotic formulae for likelihood-based tests of new physics. *Eur. Phys. J.*, C71:1554, 2011. [Erratum: Eur. Phys. J.C73,2501(2013)].

[154] ATLAS Collaboration. Search for New Phenomena in Dijet Events with the ATLAS detector at $\sqrt{s}$=13 TeV using 2015 and 2016 data. (ATL-COM-PHYS-2016-1495), Oct 2016.

[155] Torsten Paul Ake Åkesson et al. Search for New Phenomena in Dijet Events with the ATLAS Detector at $\sqrt{s}$=13 TeV with the full 2015 dataset. (ATL-COM-PHYS-2015-1205), Sep 2015.

[156] ATLAS Collaboration. Search for New Physics in Dijet Mass and Angular Distributions in pp Collisions at $\sqrt{s} = 7$ TeV Measured with the ATLAS Detector. *New J. Phys.*, 13:053044, 2011.

[157] G. Aad et al. Search for dijet resonances in events with an isolated charged lepton using $\sqrt{s} = 13$ TeV proton-proton collision data collected by the ATLAS detector. *JHEP*, 06:151, 2020.

[158] Serguei Chatrchyan et al. Search for Three-Jet Resonances in *pp* Collisions at $\sqrt{s} = 7$ TeV. *Phys. Lett. B*, 718:329–347, 2012.

[159] The CMS Collaboration. Search for pair-produced three-jet resonances in proton-proton collisions at $\sqrt{s}$ =13 TeV. *Phys. Rev. D*, 99(1):012010, 2019.

[160] Tommaso Dorigo. Hadron Collider Searches for Diboson Resonances. *Prog. Part. Nucl. Phys.*, 100:211–261, 2018.

[161] Georges Aad et al. Search for Quantum Black Hole Production in High-Invariant-Mass Lepton+Jet Final States Using *pp* Collisions at $\sqrt{s} = 8$ TeV and the ATLAS Detector. *Phys. Rev. Lett.*, 112(9):091804, 2014.

[162] Torbjorn Sjostrand, Stephen Mrenna, and Peter Z. Skands. PYTHIA 6.4 Physics and Manual. *JHEP*, 05:026, 2006.

[163] Richard D. Ball et al. Parton distributions for the LHC Run II. *JHEP*, 04:040, 2015.

# APPENDIX

## Direct Tag Light jet calibrations

## A.1 A few additional studies

### A.1.1 Control plots of different reweightings

While working with both ATLAS software reconstruction 20.7 and 21, when results are compared it is also important to look for differences in data. Few distributions describing the transverse momenta and eta regions from both release 20.7 and release 21 are shared below :

**For release 20.7**

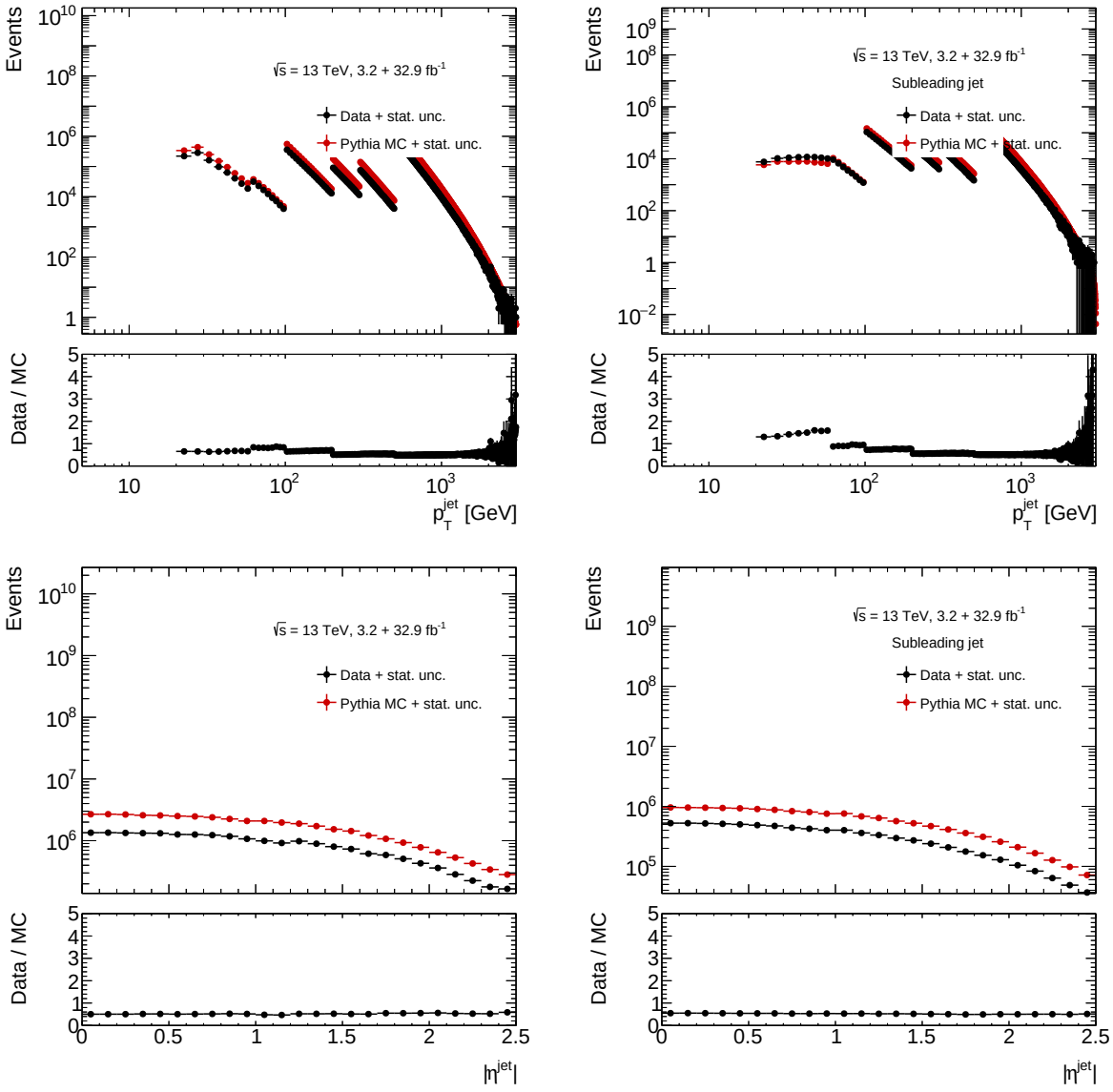


Figure 1: Illustration of the reweighting of the MC to data in each bin of the LF mistag rate measurement ($p_{jet}/|\eta_{jet}|$) for the leading (left) and sub-leading jet (right) as a function of the jet transverse momentum and eta for he Pythia multijet sample in release 20.7 data after pt/$\eta$ reweighting.

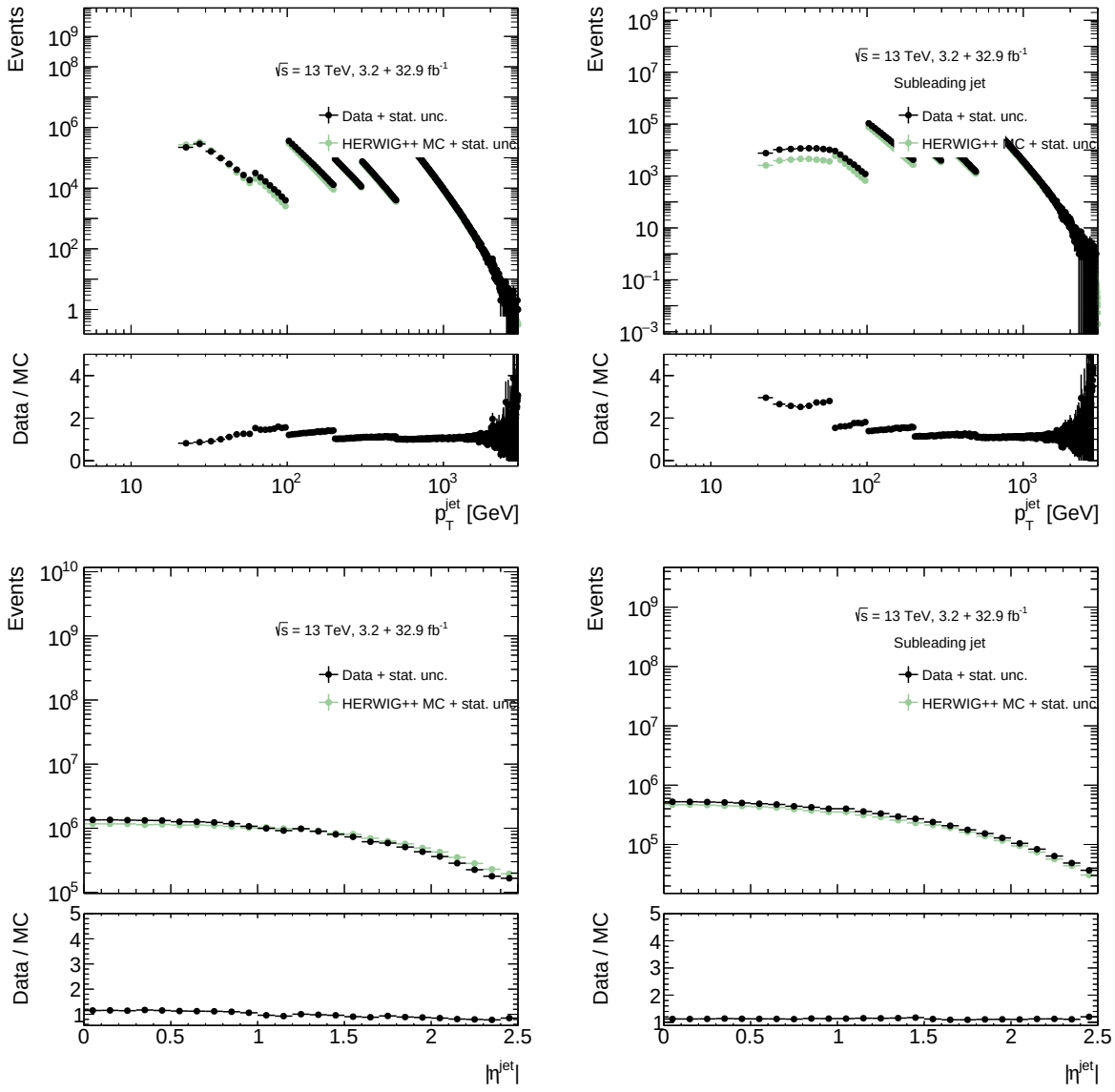


Figure 2: Illustration of the reweighting of the MC to data in each bin of the LF mistag rate measurement ($p_{jet}/|\eta_{jet}|$) for the leading (left) and subleading jet (right) as a function of the jet transverse momentum and eta for HERWIG++ sample in release 20.7 data after pt/$\eta$ reweighting.

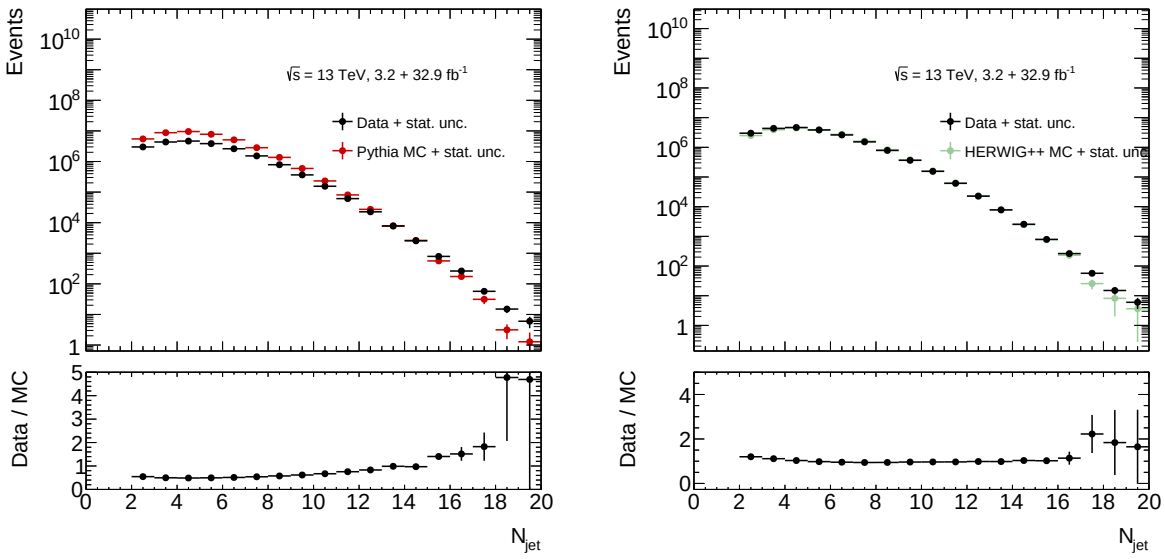


Figure 3: Jet multiplicity distributions in data and in the Pythia and HERWIG++ samples in release 20.7 data after pt/$\eta$ reweighting.

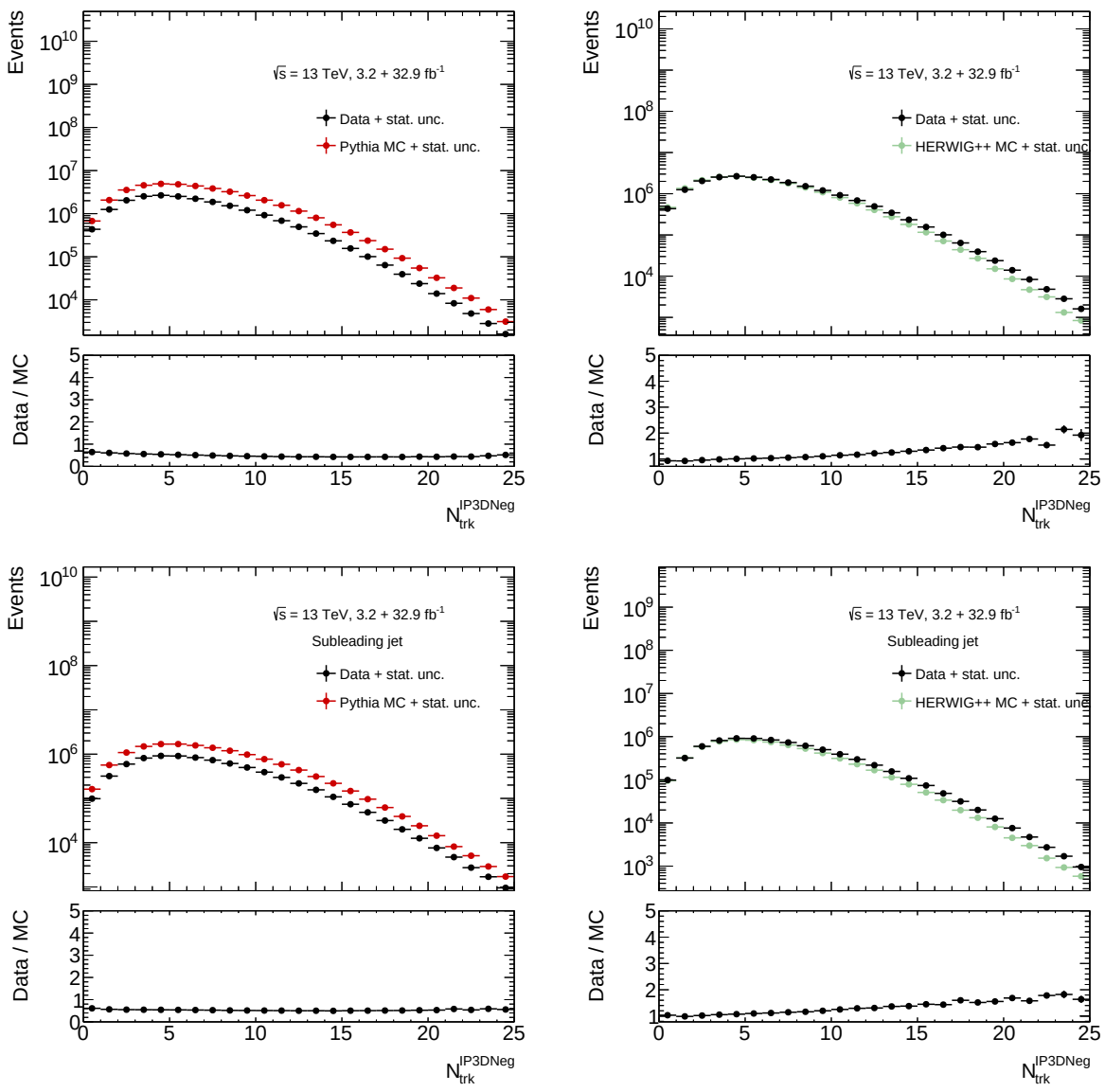


Figure 4: Illustration of the reweighting of the MC to data in each bin of Njet, $\mathrm{IP3D_{Neg}/p_{jet}}$ for the leading (top) subleading (bottom) jet as a function of the jet track multiplicity, Njet, IP3DNeg. The Pythia multijet sample is shown in the left and the HERWIG++ sample is shown in the right in release 20.7 data after pt/$\eta$ reweighting.

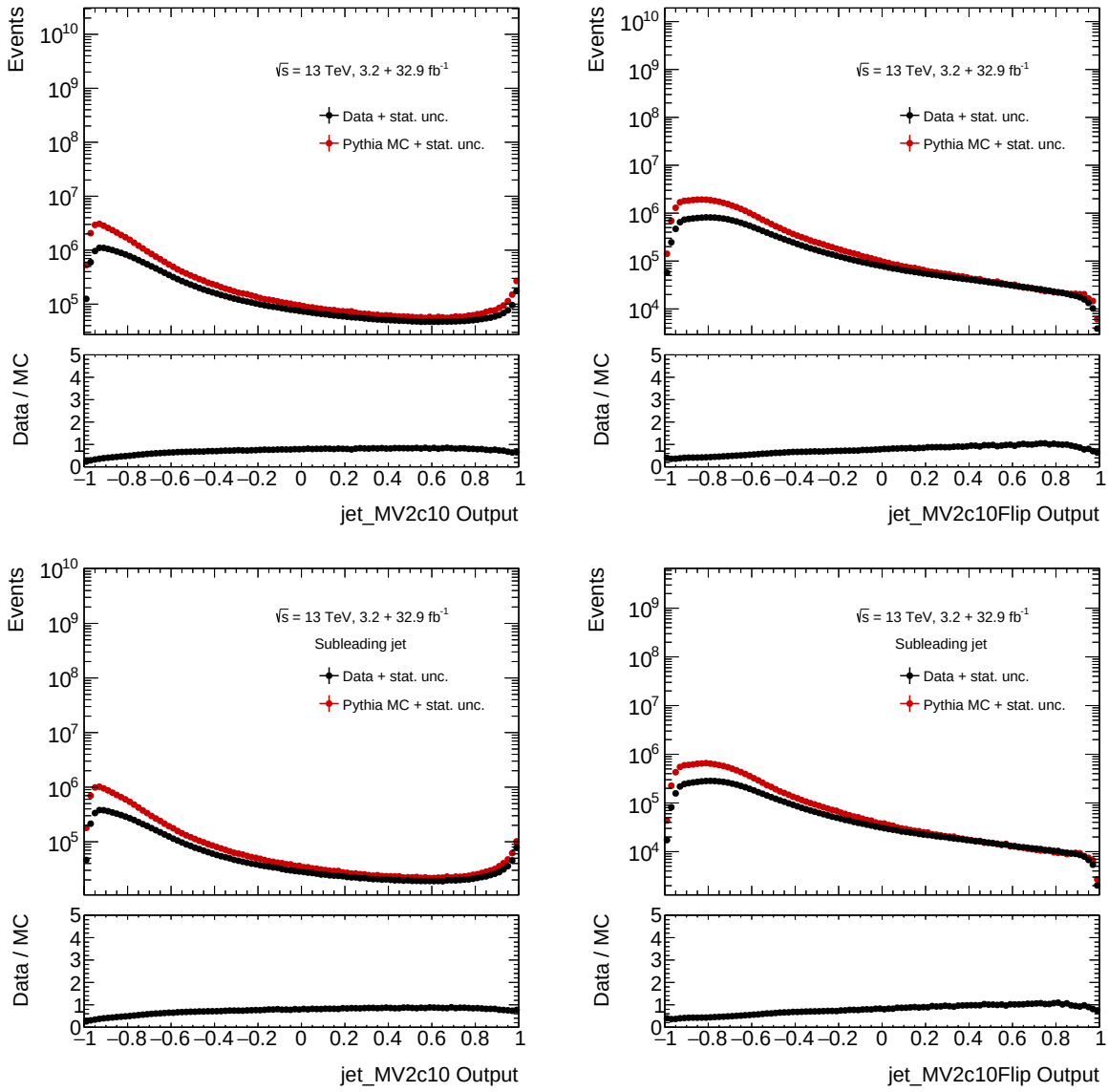


Figure 5: Data/MC comparison in jet MV2c10 Output(left) and in jet MV2c10Flip Output(right) for the leading (left) and subleading jet (right) as a function of the jet transverse momentum and eta for the Pythia multijet sample in release 20.7 data after pt/$\eta$ reweighting.

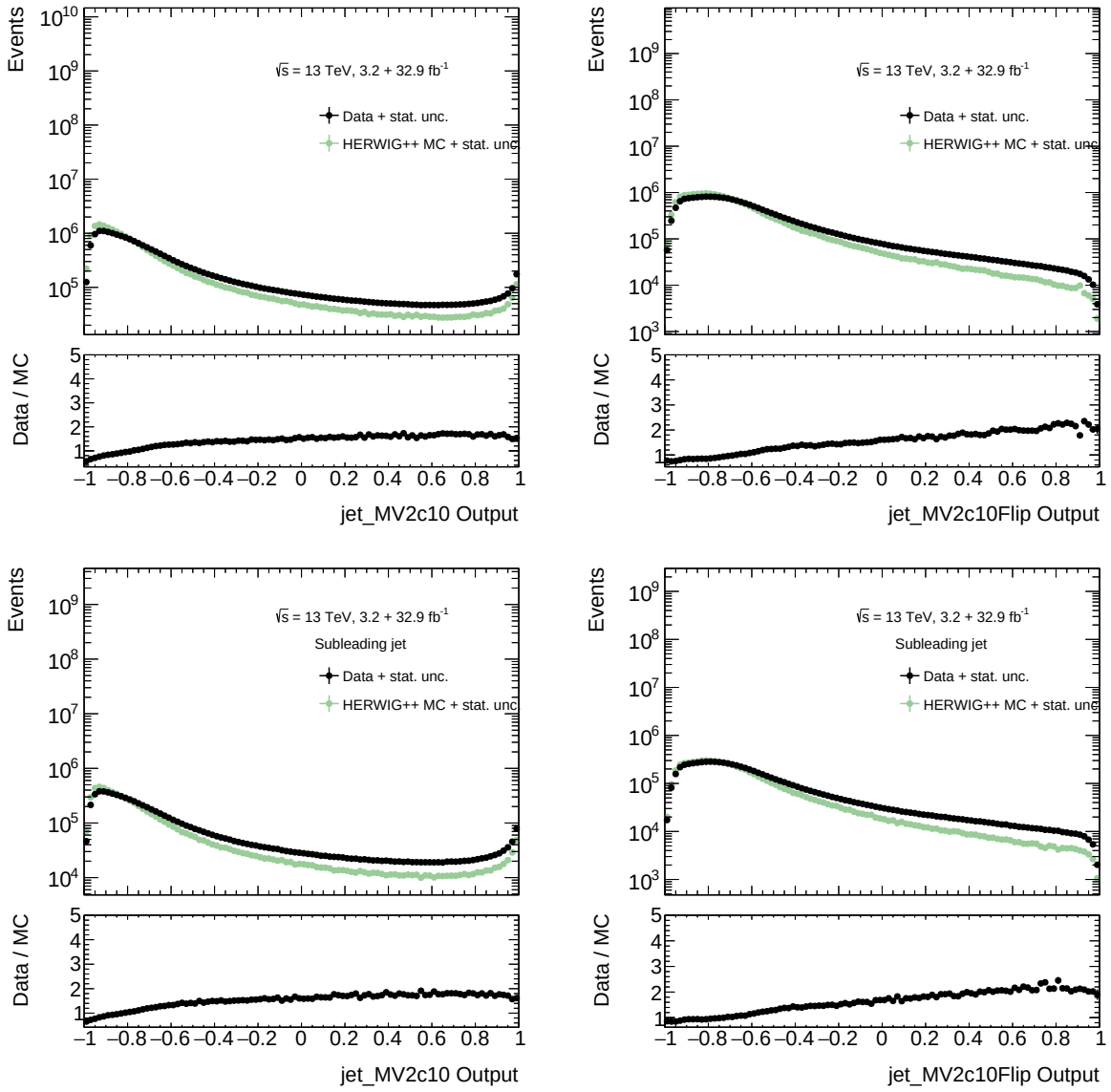


Figure 6: Data/MC comparison in jet MV2c10 Output(left) and in jet MV2c10Flip Output(right) for the leading (left) and subleading jet (right) as a function of the jet transverse momentum and eta for the HERWIG++ multijet sample in release 20.7 data after pt/$\eta$ reweighting.

**For release 21**

The release 21 dataset is full 2015+2016 data with integrated luminosity of 36184.86 $pb^{-1}$. Similar control plots were generated with release 21 data as well while applying pt-$\eta$ reweighting and n-track reweighting. Few control plots are the following :

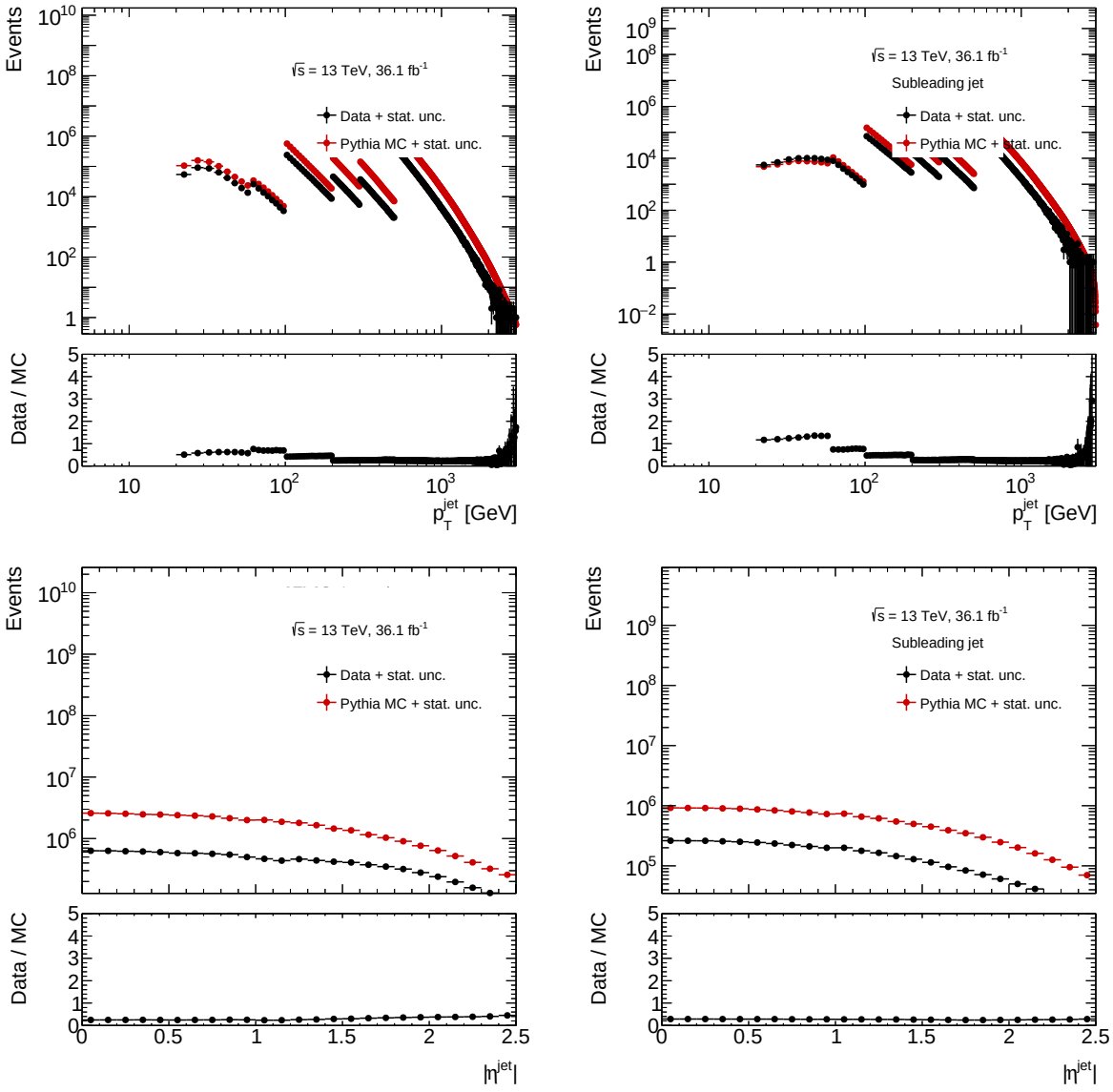


Figure 7: Illustration of the reweighting of the MC to data in each bin of the LF mistag rate measurement ($p_{jet}/|\eta_{jet}|$)for the leading (left) and subleading jet (right) as a function of the jet transverse momentum and eta for he Pythia multijet sample in release 21 data after pt/$\eta$ reweighting.

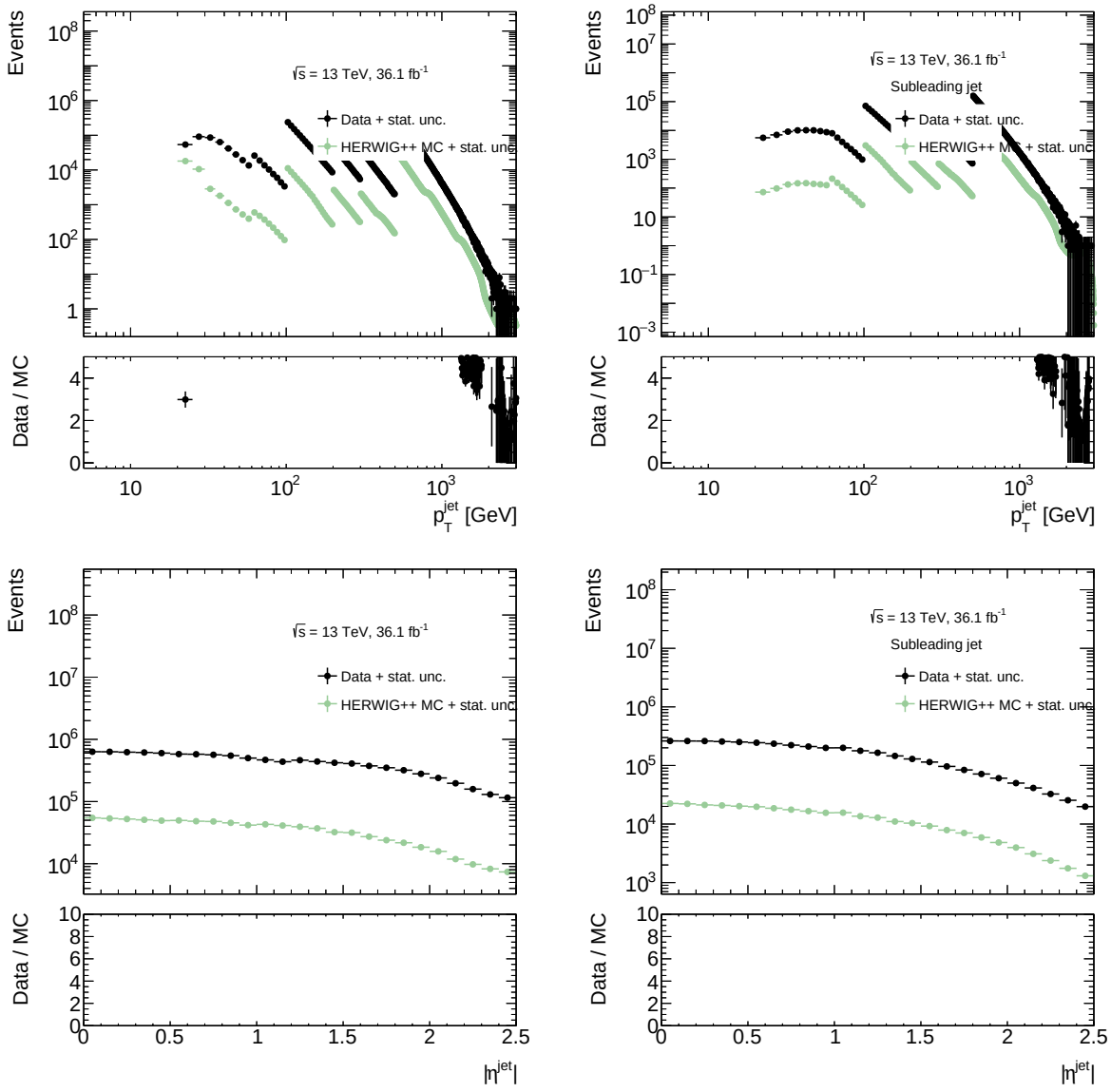


Figure 8: Illustration of the reweighting of the MC to data in each bin of the LF mistag rate measurement ($p_{jet}/|\eta_{jet}|$) for the leading (left) and subleading jet (right) as a function of the jet transverse momentum and eta for HERWIG++ sample in release 21 data after pt/$\eta$ reweighting.

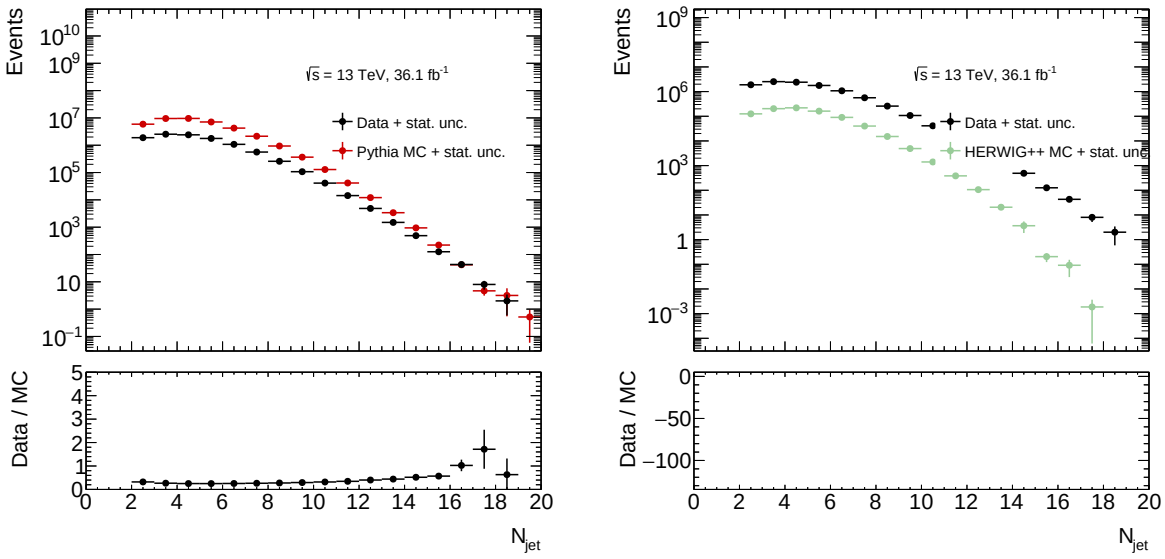


Figure 9: Jet multiplicity distributions in data and in the Pythia and HERWIG++ samples in release 21 data after pt/$\eta$ reweighting.

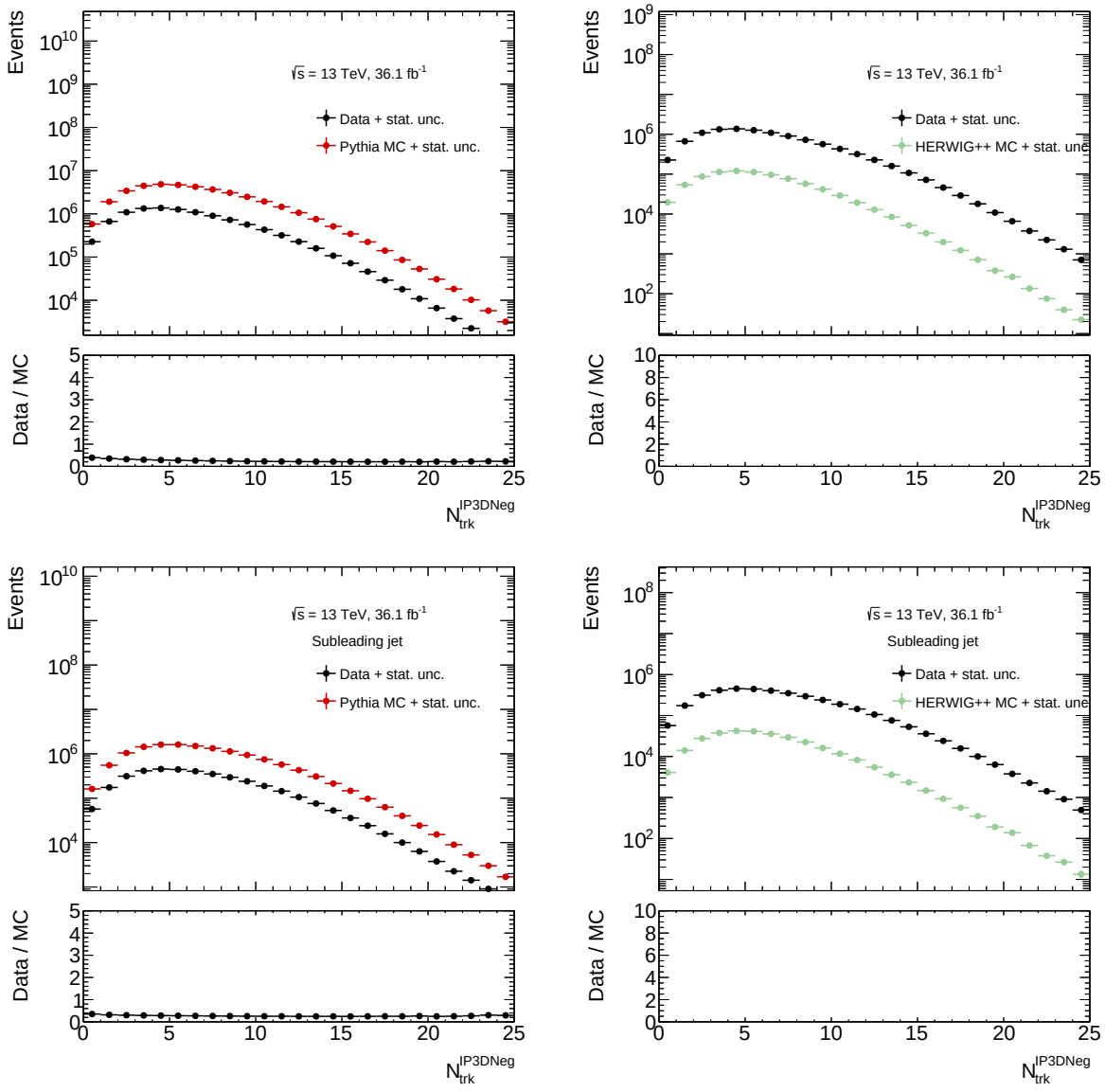


Figure 10: Illustration of the reweighting of the MC to data in each bin of Njet, $IP3D_{Neg}$/pjet for the leading (top) subleading (bottom) jet as a function of the jet track multiplicity, $N_{jet}$, $IP3D_{Neg}$. The Pythia multijet sample is shown in the left and the HERWIG++ sample is shown in the right in release 21 data after pt/$\eta$ reweighting.

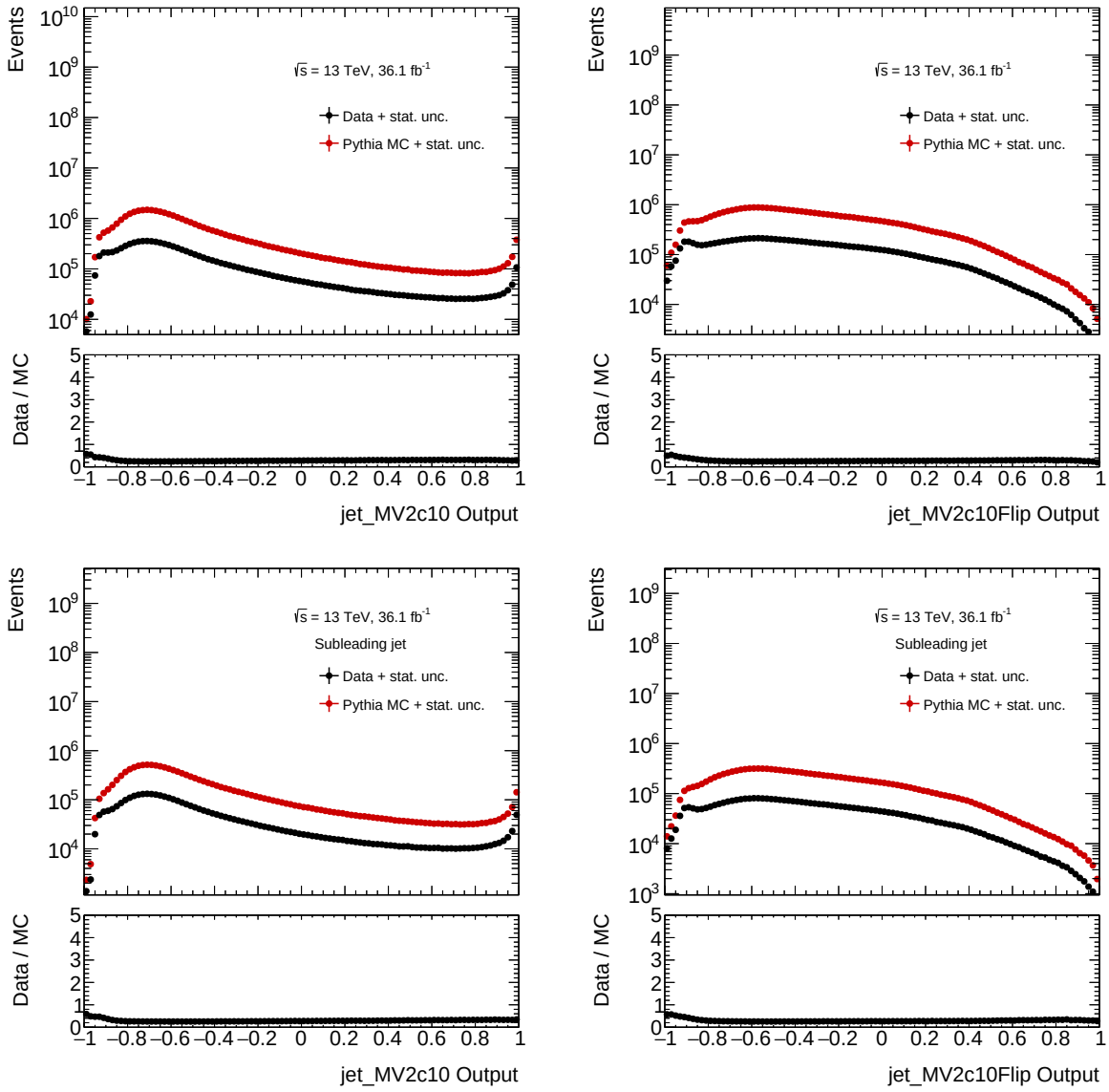


Figure 11: Data/MC comparison in jet MV2c10 Output(left) and in jet MV2c10Flip Output(right) for the leading (left) and subleading jet (right) as a function of the jet transverse momentum and eta for the Pythia multijet sample in release 21 data after pt/$\eta$ reweighting.

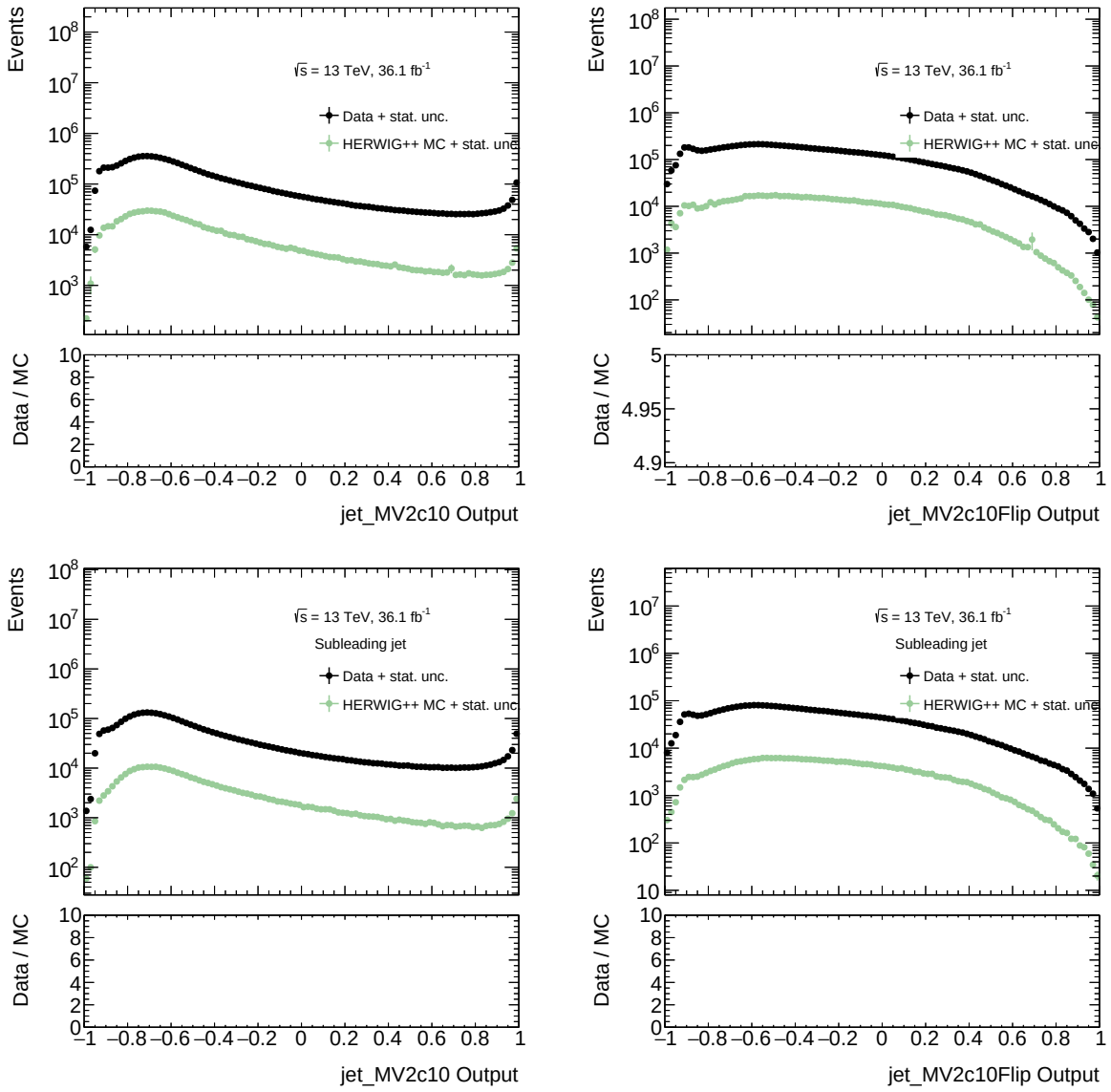


Figure 12: Data/MC comparison in jet MV2c10 Output(left) and in jet MV2c10Flip Output(right) for the leading (left) and subleading jet (right) as a function of the jet transverse momentum and eta for the HERWIG++ multijet sample in release 21 data after pt/$\eta$ reweighting.

### A.1.2 Contribution of each systematic in SF

The following tables provide contributions of different (49) systematic uncertainties for different points in central eta regions. During the studies on Direct tag light jet calibrations, similar values have also been calculated for Forward regions as well.

| Contribution of different systematic uncertainties for pt1 in central eta | | | | | |
|---|---|---|---|---|---|
| Systematic | SF_100% | SF_85% | SF_77% | SF_70% | SF_60% |
| 0 | -0.983166 | 0 | 0 | 0 | 0 |
| 1 | -0.980496 | 0.128463 | 0.315928 | -0.000228782 | -0.000458654 |
| 2 | -0.983995 | -0.0398863 | -0.174729 | 4.10742e-05 | -0.000829083 |
| 3 | -0.982393 | 0.037197 | 0.0554271 | -0.000112912 | -0.000358818 |
| 4 | -0.982295 | 0.0419211 | 0.0940426 | -0.000313888 | -0.000336278 |
| 5 | -0.982083 | 0.0520974 | 0.11191 | -0.000275518 | -0.00050806 |
| 6 | -0.982041 | 0.0541426 | 0.108668 | -0.000275265 | -0.000736078 |
| 7 | -0.981976 | 0.0572557 | 0.122103 | -0.000145619 | -0.000359842 |
| 8 | -0.982235 | 0.0447897 | 0.0887579 | -0.000551882 | -0.000729816 |
| 9 | -0.982296 | 0.0418502 | 0.0787388 | -0.000361892 | -0.000388416 |
| 10 | -0.982095 | 0.051546 | 0.109413 | -0.000221682 | -0.000488024 |
| 11 | -0.982088 | 0.0518623 | 0.106712 | -0.0002969 | -0.000527868 |
| 12 | -0.982104 | 0.0510976 | 0.105489 | -0.000145534 | -0.000359842 |
| 13 | -0.981991 | 0.0565344 | 0.114755 | -0.000275349 | -0.000709098 |
| 14 | -0.982207 | 0.0461478 | 0.0965873 | -0.000359526 | -0.0004105 |
| 15 | -0.982261 | 0.0435329 | 0.0909384 | -0.000362738 | -0.000415054 |
| 16 | -0.982171 | 0.0478881 | 0.0994499 | -0.00038226 | -0.000736533 |
| 17 | -0.982053 | 0.0535237 | 0.109796 | -0.000270616 | -0.00037726 |
| 18 | -0.982041 | 0.0541368 | 0.114239 | -0.000292252 | -0.000397409 |
| 19 | -0.981773 | 0.0669953 | 0.144223 | -0.000255066 | -0.000375666 |
| 20 | -0.982092 | 0.0516514 | 0.10668 | -0.000143929 | -0.000360184 |
| 21 | -0.982076 | 0.0524325 | 0.107958 | -0.000544698 | -0.000701926 |
| 22 | -0.982154 | 0.0487058 | 0.0993771 | -0.00029521 | -0.000392969 |
| 23 | -0.982126 | 0.0500517 | 0.102482 | -0.000144689 | -0.00036007 |
| 24 | -0.982104 | 0.0511002 | 0.105085 | -0.000224894 | -0.000386025 |
| 25 | -0.982081 | 0.052183 | 0.10755 | -0.000258277 | -0.000415851 |
| 26 | -0.98208 | 0.0522597 | 0.107798 | -0.000277378 | -0.000519671 |
| 27 | -0.982108 | 0.0508969 | 0.104515 | -0.000372879 | -0.000479486 |
| 28 | -0.982059 | 0.0532573 | 0.110093 | -0.000118659 | -0.000354492 |
| 29 | -0.982082 | 0.0521613 | 0.107551 | -0.000219231 | -0.000341059 |
| 30 | -0.982159 | 0.0484489 | 0.0972303 | -0.000256333 | -0.000384773 |
| 31 | -0.982195 | 0.0467307 | 0.0926666 | -0.000295717 | -0.000529234 |
| 32 | -0.983075 | 0.00440577 | -0.0263708 | -0.000326481 | -0.000386253 |
| 33 | -0.981963 | 0.0578586 | 0.123147 | -0.000250586 | -0.000390579 |
| 34 | -0.982188 | 0.0470731 | 0.0935634 | -0.000242727 | -0.000387847 |
| 35 | -0.98173 | 0.0690709 | 0.154918 | -0.000416658 | -0.000592072 |

| | | | | | |
|---|---|---|---|---|---|
| 36 | -0.982165 | 0.0481596 | 0.0963411 | -0.000263855 | -0.000391376 |
| 37 | -0.982034 | 0.0544569 | 0.113975 | -0.000523738 | -0.000627362 |
| 38 | -0.982034 | 0.0544667 | 0.114055 | -0.000223373 | -0.000447839 |
| 39 | -0.982211 | 0.0459537 | 0.0903438 | -0.000521456 | -0.000419266 |
| 40 | -0.98214 | 0.0493665 | 0.0998825 | -0.000311522 | -0.000400597 |
| 41 | -0.982112 | 0.0507181 | 0.103679 | -0.000557967 | -0.000754519 |
| 42 | -0.98204 | 0.0541629 | 0.113405 | -0.000231317 | -0.000386594 |
| 43 | -0.982097 | 0.0514501 | 0.105721 | -0.000218302 | -0.000385684 |
| 44 | -0.980172 | 0.144033 | 0.364935 | 0.497494 | -0.00183906 |
| 45 | -0.981637 | 0.0735371 | 0.169402 | -0.000584082 | 0.498132 |
| 46 | -0.982087 | 0.0519113 | 0.110968 | -0.000630988 | -0.000552798 |
| 47 | -0.982278 | 0.042745 | 0.0854807 | -0.000301295 | -0.000728678 |
| 48 | -0.979788 | 0.162491 | 0.427498 | 0.496058 | 0.49518 |

Table 1: Comparing contribution of different systematics for pt1 in central eta

| Contribution of different systematic uncertainties for pt1 in central eta | | | | | |
|---|---|---|---|---|---|
| Systematic | SF_100% | SF_85% | SF_77% | SF_70% | SF_60% |
| 0 | -0.987417 | -0.0756022 | -0.165076 | 3.64976e-05 | 0.000207492 |
| 1 | -0.983287 | 0.103516 | 0.286739 | -0.000182268 | 0.000852408 |
| 2 | -0.988478 | -0.121604 | -0.374074 | -0.000596494 | -9.87764e-05 |
| 3 | -0.986103 | -0.0186032 | -0.0644254 | -0.000251306 | -7.88982e-06 |
| 4 | -0.986 | -0.0141238 | -0.0212175 | 0.000270984 | -0.000531179 |
| 5 | -0.985678 | -0.000194604 | 0.00499837 | -0.000289562 | -0.000362727 |
| 6 | -0.985588 | 0.00374012 | 0.00599546 | 6.42006e-05 | 0.000135561 |
| 7 | -0.985516 | 0.00686519 | 0.0198739 | -0.00013027 | 0.00035453 |
| 8 | -0.985873 | -0.00862054 | -0.0225507 | -0.000147529 | 0.000358731 |
| 9 | -0.985947 | -0.0118272 | -0.0340358 | 0.00021195 | -5.12326e-06 |
| 10 | -0.985695 | -0.00089346 | 0.00185745 | 0.000220415 | -0.000124188 |
| 11 | -0.985667 | 0.000296654 | 0.000614185 | 0.000364206 | 0.000126749 |
| 12 | -0.985696 | -0.000960355 | -0.00179882 | -2.36355e-05 | 0.00016087 |
| 13 | -0.985523 | 0.00656296 | 0.013288 | 2.63838e-05 | 0.000415086 |
| 14 | -0.985861 | -0.00811529 | -0.0159476 | -0.000793383 | -0.000321536 |
| 15 | -0.985913 | -0.0103774 | -0.0200449 | 0.000386523 | 0.0019371 |
| 16 | -0.985724 | -0.00216197 | -0.00211193 | 4.67213e-05 | 0.000298891 |
| 17 | -0.985611 | 0.00271212 | 0.00660039 | -0.000329028 | 0.00138174 |
| 18 | -0.985457 | 0.00939046 | 0.0266405 | -0.000307921 | 0.000614381 |
| 19 | -0.984931 | 0.0322085 | 0.0840417 | -1.05535e-05 | 0.000172654 |
| 20 | -0.985673 | 3.44055e-05 | 0.000510388 | 8.20097e-05 | 0.000169785 |
| 21 | -0.985648 | 0.00113938 | 0.00353576 | -0.000154565 | 0.000174703 |
| 22 | -0.985794 | -0.00521606 | -0.0129295 | -0.000118287 | 0.000365083 |
| 23 | -0.98574 | -0.00286482 | -0.00713732 | 8.16799e-05 | 6.66024e-05 |
| 24 | -0.985699 | -0.00110589 | -0.00271857 | -0.000339911 | 0.000613254 |
| 25 | -0.985657 | 0.000715601 | 0.00170801 | -0.000268455 | 0.000843391 |

| | | | | | |
|---|---|---|---|---|---|
| 26 | -0.985653 | 0.000922118 | 0.00232258 | 5.16683e-05 | 0.000246839 |
| 27 | -0.985707 | -0.00141696 | -0.00358991 | -0.000550432 | 0.000672479 |
| 28 | -0.98562 | 0.00232991 | 0.00662674 | -0.00019535 | -0.000179314 |
| 29 | -0.985658 | 0.000689193 | 0.00170114 | -0.000303634 | 0.000751172 |
| 30 | -0.985788 | -0.00496522 | -0.0138457 | -6.13423e-05 | 8.49436e-05 |
| 31 | -0.985865 | -0.00829789 | -0.0238078 | -0.000110922 | 9.8469e-05 |
| 32 | -0.98754 | -0.0809109 | -0.226797 | -1.75892e-06 | -0.000306678 |
| 33 | -0.98544 | 0.010143 | 0.0280756 | 8.7946e-06 | 0.000321638 |
| 34 | -0.985847 | -0.00749532 | -0.0214531 | 0.000206343 | 9.89814e-05 |
| 35 | -0.984983 | 0.0299654 | 0.0847544 | -0.000189963 | -0.000134639 |
| 36 | -0.985818 | -0.00625114 | -0.0183258 | -0.000334745 | -0.000243047 |
| 37 | -0.98557 | 0.00451779 | 0.0126029 | -0.000251306 | 0.00053702 |
| 38 | -0.985568 | 0.00457327 | 0.0125815 | -0.000135547 | 0.000425026 |
| 39 | -0.985895 | -0.00956565 | -0.0274374 | -0.000102787 | 0.000186487 |
| 40 | -0.985768 | -0.00409676 | -0.0114796 | -2.81427e-05 | -0.000852613 |
| 41 | -0.985711 | -0.00160598 | -0.00458146 | -0.000282966 | 0.000452179 |
| 42 | -0.985573 | 0.00436992 | 0.0124168 | -0.000318914 | 0.00013843 |
| 43 | -0.985686 | -0.000518582 | -0.0012003 | 0.000630463 | -0.000147652 |
| 44 | -0.984184 | 0.0646132 | 0.183411 | 0.497778 | -0.000414267 |
| 45 | -0.985389 | 0.0123529 | 0.0367909 | -0.000359699 | 0.500527 |
| 46 | -0.985643 | 0.00135015 | 0.00471162 | -0.000681582 | -7.92056e-05 |
| 47 | -0.985731 | -0.00248661 | -0.00608589 | -0.000304513 | -0.000149907 |
| 48 | -0.983887 | 0.0775085 | 0.222925 | 0.497198 | 0.497507 |

Table 2: Comparing contribution of different systematics for pt2 in central eta

| Contribution of different systematic uncertainties for pt1 in central eta | | | | | |
|---|---|---|---|---|---|
| Systematic | SF_100% | SF_85% | SF_77% | SF_70% | SF_60% |
| 0 | -0.983336 | -0.0867662 | -0.190924 | -5.20732e-05 | 0.00015288 |
| 1 | -0.978501 | 0.113507 | 0.327888 | 0.000115189 | 7.69789e-05 |
| 2 | -0.984406 | -0.131107 | -0.43318 | -0.00023027 | 5.56318e-05 |
| 3 | -0.981708 | -0.0193415 | -0.0755075 | 8.09787e-05 | 8.9054e-05 |
| 4 | -0.981658 | -0.0172665 | -0.0250794 | 0.000281044 | -0.000152017 |
| 5 | -0.977982 | 0.134992 | 0.410485 | 1.09046 | -0.053671 |
| 6 | -0.98113 | 0.0046017 | 0.00589101 | 0.000183393 | 0.0003008 |
| 7 | -0.981057 | 0.00761531 | 0.0231949 | 0.000143445 | 6.30709e-05 |
| 8 | -0.981475 | -0.00966686 | -0.0260618 | 0.000211216 | 0.000209374 |
| 9 | -0.981559 | -0.0131506 | -0.0396544 | -3.68085e-06 | 0.000323549 |
| 10 | -0.981271 | -0.00122028 | 0.00232282 | 0.000448089 | -2.69534e-06 |
| 11 | -0.981234 | 0.000279641 | 0.000534051 | 0.000181986 | 6.46882e-06 |
| 12 | -0.981268 | -0.00112773 | -0.00210843 | 0.000127855 | -6.72757e-05 |
| 13 | -0.981054 | 0.00777182 | 0.0143028 | -0.000147992 | -0.000358588 |
| 14 | -0.98147 | -0.00947077 | -0.018256 | 0.000117571 | 8.06446e-05 |

| | | | | | |
|---|---|---|---|---|---|
| 15 | -0.981548 | -0.0127144 | -0.0250969 | 0.000171593 | 9.41213e-05 |
| 16 | -0.981323 | -0.00340779 | -0.00430906 | 3.51846e-05 | -9.16415e-05 |
| 17 | -0.981164 | 0.00320739 | 0.00671228 | 0.000168561 | 0.000396646 |
| 18 | -0.981027 | 0.00888481 | 0.0268284 | -0.000189456 | 0.000372388 |
| 19 | -0.980433 | 0.0334763 | 0.0889938 | 0.000139114 | 2.00533e-05 |
| 20 | -0.981242 | -2.35756e-05 | 0.000496278 | 0.000402945 | -0.000184469 |
| 21 | -0.981209 | 0.00134572 | 0.00307911 | 0.000216954 | 8.19383e-06 |
| 22 | -0.981375 | -0.00553564 | -0.0140221 | 0.000448522 | 6.56585e-05 |
| 23 | -0.981316 | -0.00310377 | -0.00799487 | -2.76064e-05 | 5.57396e-05 |
| 24 | -0.981269 | -0.00116978 | -0.00292896 | 0.000143012 | 0.000206894 |
| 25 | -0.981222 | 0.000809853 | 0.00198951 | 0.000167695 | 0.000398695 |
| 26 | -0.981218 | 0.000947085 | 0.00243885 | -9.29956e-05 | -8.19383e-06 |
| 27 | -0.981277 | -0.00147236 | -0.0038067 | 0.00021533 | 0.000100806 |
| 28 | -0.981177 | 0.00265647 | 0.00661047 | 0.000380751 | 8.19383e-06 |
| 29 | -0.981223 | 0.000752348 | 0.00191022 | 4.11389e-06 | 5.2074e-05 |
| 30 | -0.981362 | -0.00502447 | -0.0159083 | -0.00034416 | -0.000135198 |
| 31 | -0.981468 | -0.00938117 | -0.0276613 | -0.000285049 | -0.000396107 |
| 32 | -0.983383 | -0.0887371 | -0.264793 | 1.6239e-06 | 0.000545105 |
| 33 | -0.980979 | 0.0108388 | 0.0313996 | 0.00038519 | -8.19383e-06 |
| 34 | -0.98144 | -0.00825432 | -0.0244837 | 0.000433691 | 5.06724e-05 |
| 35 | -0.980457 | 0.0324695 | 0.0965937 | 0.000152539 | 0.000175736 |
| 36 | -0.981408 | -0.00691457 | -0.020864 | 0.000231136 | -6.73835e-05 |
| 37 | -0.981121 | 0.00496895 | 0.0144714 | 0.000398614 | 0.000258429 |
| 38 | -0.981125 | 0.00480273 | 0.0139867 | -0.000195302 | 0.000101021 |
| 39 | -0.981498 | -0.0106355 | -0.0315903 | 0.00013316 | -6.84616e-05 |
| 40 | -0.981347 | -0.00436491 | -0.0129702 | 2.01364e-05 | 6.60897e-05 |
| 41 | -0.981282 | -0.00170509 | -0.00504973 | 0.000281044 | -0.000116439 |
| 42 | -0.98113 | 0.00461667 | 0.0138855 | -3.68085e-06 | -1.6172e-06 |
| 43 | -0.981253 | -0.000481866 | -0.00144742 | 0.000148208 | 0.000526562 |
| 44 | -0.979705 | 0.063646 | 0.190134 | 0.498574 | -0.0011963 |
| 45 | -0.980983 | 0.0106984 | 0.0328059 | -0.000291978 | 0.498248 |
| 46 | -0.981223 | 0.000751392 | 0.00304639 | 0.000126015 | -0.000142098 |
| 47 | -0.981256 | -0.000631841 | -0.00158673 | -5.00163e-05 | -0.000925256 |
| 48 | -0.979411 | 0.075808 | 0.228767 | 0.497808 | 0.496854 |

Table 3: Comparing contribution of different systematics for pt3 in central eta

| Contribution of different systematic uncertainties for pt1 in central eta | | | | | |
|---|---|---|---|---|---|
| Systematic | SF_100% | SF_85% | SF_77% | SF_70% | SF_60% |
| 0 | -0.980676 | -0.15537 | -0.352965 | 0.000145244 | -0.000126145 |
| 1 | -0.973651 | 0.178231 | 0.506358 | 4.19214e-05 | -4.25167e-05 |
| 2 | -0.981856 | -0.211402 | -0.681302 | 3.07576e-05 | 3.12726e-05 |
| 3 | -0.977995 | -0.0280846 | -0.108408 | -1.70875e-05 | 2.83445e-05 |

| | | | | | |
|---|---|---|---|---|---|
| 4 | -0.978138 | -0.0348675 | -0.0628295 | 2.51756e-05 | -2.67047e-05 |
| 5 | -0.977433 | -0.00138888 | 0.00682982 | -5.35409e-06 | 6.44192e-06 |
| 6 | -0.977211 | 0.00916487 | 0.015014 | -9.22727e-06 | 1.18297e-05 |
| 7 | -0.977093 | 0.0147515 | 0.0429327 | -8.65768e-06 | 1.08927e-05 |
| 8 | -0.977815 | -0.019504 | -0.0519618 | -9.91077e-06 | 1.28838e-05 |
| 9 | -0.977972 | -0.0269964 | -0.0777426 | -9.68294e-06 | 1.25325e-05 |
| 10 | -0.977443 | -0.00186728 | 0.00286708 | 7.06285e-06 | -7.96456e-06 |
| 11 | -0.977393 | 0.000533624 | 0.00109687 | 1.29865e-05 | -1.41722e-05 |
| 12 | -0.977449 | -0.00212121 | -0.00434355 | -3.18967e-06 | 3.74803e-06 |
| 13 | -0.977065 | 0.0160822 | 0.0332937 | -0.000455554 | 0.000376443 |
| 14 | -0.977753 | -0.016589 | -0.0338843 | 3.0188e-05 | -3.13897e-05 |
| 15 | -0.977973 | -0.0270249 | -0.059123 | 3.41751e-07 | -4.68504e-07 |
| 16 | -0.977816 | -0.0195727 | -0.044877 | 1.21891e-05 | -1.34695e-05 |
| 17 | -0.977285 | 0.00565023 | 0.0122227 | -8.42985e-06 | 1.06585e-05 |
| 18 | -0.977623 | -0.0103896 | -0.0221463 | 2.66566e-05 | -2.79931e-05 |
| 19 | -0.977154 | 0.0118464 | 0.0330145 | -7.74635e-06 | 9.60432e-06 |
| 20 | -0.977425 | -0.00101229 | -0.00189389 | -8.31593e-06 | 1.04242e-05 |
| 21 | -0.977359 | 0.00212358 | 0.00480992 | 1.70875e-06 | -1.99114e-06 |
| 22 | -0.977523 | -0.00566652 | -0.014168 | -2.96184e-06 | 3.74803e-06 |
| 23 | -0.977475 | -0.0033546 | -0.00856963 | 1.37839e-05 | -1.49921e-05 |
| 24 | -0.977431 | -0.00130645 | -0.0032222 | -8.65768e-06 | 1.08927e-05 |
| 25 | -0.97738 | 0.00114941 | 0.00280117 | 1.44674e-05 | -1.56949e-05 |
| 26 | -0.977379 | 0.00116688 | 0.00299378 | -1.00247e-05 | 1.3001e-05 |
| 27 | -0.977437 | -0.00158577 | -0.00407951 | 2.17581e-05 | -2.31909e-05 |
| 28 | -0.97733 | 0.00350809 | 0.00855468 | 1.94798e-05 | -2.09655e-05 |
| 29 | -0.977384 | 0.000925586 | 0.00232957 | 1.44674e-05 | -1.56949e-05 |
| 30 | -0.977574 | -0.00809853 | -0.0232767 | -9.91077e-06 | 1.27667e-05 |
| 31 | -0.977622 | -0.0103549 | -0.0296561 | -5.12626e-06 | 6.09055e-06 |
| 32 | -0.9795 | -0.0995278 | -0.289143 | -0.000707538 | 0.000581647 |
| 33 | -0.977099 | 0.0144881 | 0.0410534 | -5.58193e-06 | 6.67618e-06 |
| 34 | -0.977626 | -0.0105279 | -0.0298824 | 3.98709e-06 | -4.45078e-06 |
| 35 | -0.97663 | 0.0367728 | 0.107065 | -6.37935e-06 | 7.84743e-06 |
| 36 | -0.977548 | -0.00685541 | -0.0200029 | 2.26695e-05 | -2.40108e-05 |
| 37 | -0.977265 | 0.00660129 | 0.018565 | 9.11335e-07 | -9.37007e-07 |
| 38 | -0.977266 | 0.00654315 | 0.0184801 | 1.62901e-05 | -1.7686e-05 |
| 39 | -0.97766 | -0.0121598 | -0.0348484 | 1.32144e-05 | -1.44065e-05 |
| 40 | -0.97751 | -0.00504673 | -0.0142536 | -9.56902e-06 | 1.21811e-05 |
| 41 | -0.977446 | -0.00197582 | -0.00576063 | -1.02525e-05 | 1.33524e-05 |
| 42 | -0.9773 | 0.00492436 | 0.0146543 | 4.10101e-06 | -4.56791e-06 |
| 43 | -0.977415 | -0.000534898 | -0.00161712 | 2.31251e-05 | -2.44793e-05 |
| 44 | -0.975769 | 0.0776384 | 0.224313 | 0.504884 | -0.0122342 |
| 45 | -0.977215 | 0.0089749 | 0.0275687 | -0.00117779 | 0.498395 |
| 46 | -0.97743 | -0.00124658 | -0.00264728 | -0.000898918 | 0.000597693 |
| 47 | -0.977406 | -0.000103813 | -0.0003159 | -0.000796393 | 4.62647e-05 |

| | | | | | |
|---|---|---|---|---|---|
| 48 | -0.975613 | 0.0850584 | 0.248327 | 0.4938 | 0.490756 |

Table 4: Comparing contribution of different systematics for pt4 in central eta

| Contribution of different systematic uncertainties for pt1 in central eta | | | | | |
|---|---|---|---|---|---|
| Systematic | SF_100% | SF_85% | SF_77% | SF_70% | SF_60% |
| 0 | -0.974934 | -0.115427 | -0.236899 | 6.2659e-07 | 7.32238e-08 |
| 1 | -0.967683 | 0.141432 | 0.375308 | 1.56648e-07 | 0 |
| 2 | -0.976497 | -0.170791 | -0.514557 | -7.83238e-07 | 3.66119e-07 |
| 3 | -0.972352 | -0.0239595 | -0.0860638 | -1.56648e-07 | 7.32238e-08 |
| 4 | -0.972379 | -0.0249217 | -0.0375711 | 1.56648e-07 | 0 |
| 5 | -0.971687 | -0.000403611 | 0.00740112 | 0 | -7.32238e-08 |
| 6 | -0.971493 | 0.00646401 | 0.00874013 | -7.83238e-08 | 0 |
| 7 | -0.971349 | 0.0115765 | 0.0316376 | -7.83238e-08 | -7.32238e-08 |
| 8 | -0.972098 | -0.0149665 | -0.0369943 | 0 | 0 |
| 9 | -0.97227 | -0.0210665 | -0.0567246 | -7.83238e-08 | 0 |
| 10 | -0.971709 | -0.00119226 | 0.00355857 | 0 | 0 |
| 11 | -0.971665 | 0.000380579 | 0.000696353 | 0 | -7.32238e-08 |
| 12 | -0.971719 | -0.00154398 | -0.00278541 | 7.83238e-08 | -7.32238e-08 |
| 13 | -0.97134 | 0.0118814 | 0.0219749 | -7.83238e-08 | 7.32238e-08 |
| 14 | -0.972017 | -0.0121054 | -0.0217679 | 7.83238e-08 | -7.32238e-08 |
| 15 | -0.972239 | -0.0199562 | -0.0388391 | 7.83238e-08 | -7.32238e-08 |
| 16 | -0.972075 | -0.0141474 | -0.0285212 | 0 | -7.32238e-08 |
| 17 | -0.971558 | 0.00417129 | 0.00826571 | -7.83238e-08 | 0 |
| 18 | -0.971869 | -0.006857 | -0.0117108 | 0 | -7.32238e-08 |
| 19 | -0.971374 | 0.0106866 | 0.028559 | -7.83238e-08 | 0 |
| 20 | -0.971695 | -0.000687948 | -0.00103931 | -7.83238e-08 | 0 |
| 21 | -0.971631 | 0.00158682 | 0.00333575 | -7.83238e-08 | 0 |
| 22 | -0.971802 | -0.0044753 | -0.0104116 | 0 | 0 |
| 23 | -0.97175 | -0.00264739 | -0.00631021 | 7.83238e-08 | -7.32238e-08 |
| 24 | -0.971705 | -0.00102075 | -0.00234178 | -7.83238e-08 | 0 |
| 25 | -0.971651 | 0.000869463 | 0.00196892 | 0 | 0 |
| 26 | -0.97165 | 0.000910249 | 0.00217333 | 0 | 0 |
| 27 | -0.971711 | -0.00125587 | -0.00301509 | 0 | 0 |
| 28 | -0.9716 | 0.00268564 | 0.00614249 | -7.83238e-08 | 0 |
| 29 | -0.971656 | 0.000710706 | 0.00167518 | -7.83238e-08 | 0 |
| 30 | -0.971878 | -0.0071497 | -0.0193543 | -7.83238e-08 | 0 |
| 31 | -0.971953 | -0.00983664 | -0.0265637 | 0 | 0 |
| 32 | -0.974327 | -0.0939033 | -0.254822 | -2.34971e-07 | 7.32238e-08 |
| 33 | -0.971275 | 0.0141923 | 0.0367465 | 0 | 0 |
| 34 | -0.971955 | -0.00989971 | -0.0265006 | -7.83238e-08 | 0 |
| 35 | -0.970708 | 0.0342735 | 0.0931473 | 1.56648e-07 | 0 |
| 36 | -0.971853 | -0.00629511 | -0.0175901 | 0 | -7.32238e-08 |

| | | | | | |
|---|---|---|---|---|---|
| 37 | -0.971499 | 0.00626591 | 0.0165205 | 7.83238e-08 | 0 |
| 38 | -0.9715 | 0.00623801 | 0.016402 | 0 | 0 |
| 39 | -0.971999 | -0.01145 | -0.0309641 | 0 | 0 |
| 40 | -0.97181 | -0.00475518 | -0.0128115 | 0 | 0 |
| 41 | -0.97173 | -0.00190454 | -0.00511146 | 0 | 0 |
| 42 | -0.971545 | 0.0046261 | 0.0127282 | -7.83238e-08 | 7.32238e-08 |
| 43 | -0.971691 | -0.000524461 | -0.00144163 | 7.83238e-08 | 0 |
| 44 | -0.969281 | 0.0848264 | 0.229515 | 0.498183 | -0.00107544 |
| 45 | -0.971368 | 0.0108948 | 0.0321101 | -0.000408224 | 0.49941 |
| 46 | -0.971716 | -0.00143745 | -0.00244566 | -0.000138476 | -5.26479e-05 |
| 47 | -0.971678 | -7.60883e-05 | -0.000171739 | -1.14353e-05 | 3.71977e-05 |
| 48 | -0.968965 | 0.0960378 | 0.26334 | 0.496934 | 0.497585 |

Table 5: Comparing contribution of different systematics for pt5 in central eta

| Contribution of different systematic uncertainties for pt1 in central eta | | | | | |
|---|---|---|---|---|---|
| Systematic | SF_100% | SF_85% | SF_77% | SF_70% | SF_60% |
| 0 | -0.94631 | -0.0804413 | -0.160676 | 0.000610722 | -0.00831031 |
| 1 | -0.936777 | 0.0969629 | 0.253401 | -0.000125186 | -0.000589762 |
| 2 | -0.948511 | -0.121401 | -0.360074 | -0.00417812 | -0.00100329 |
| 3 | -0.942922 | -0.0173865 | -0.0610444 | -0.00280804 | -0.00101101 |
| 4 | -0.942963 | -0.0181461 | -0.0270136 | -0.000471408 | -0.00051962 |
| 5 | -0.942013 | -0.0004674 | 0.00466395 | -0.00221194 | -0.00156501 |
| 6 | -0.941751 | 0.00439535 | 0.00544414 | -0.000701373 | -0.00175209 |
| 7 | -0.941539 | 0.00835443 | 0.022157 | -0.00235184 | -0.00185867 |
| 8 | -0.942606 | -0.0115079 | -0.0277528 | -0.000216524 | -0.0006178 |
| 9 | -0.942924 | -0.0174346 | -0.0454607 | -0.0048431 | -0.00121772 |
| 10 | -0.942091 | -0.0019289 | -0.000562747 | -0.00797421 | -0.00357277 |
| 11 | -0.941944 | 0.000812786 | 0.00193588 | 0.00321853 | -0.00185154 |
| 12 | -0.942073 | -0.00158143 | -0.00314634 | -0.00228111 | -0.00166515 |
| 13 | -0.941549 | 0.00815885 | 0.0142655 | -0.00319616 | -0.00121479 |
| 14 | -0.942468 | -0.00893433 | -0.0161537 | -0.00355239 | -0.00168185 |
| 15 | -0.94284 | -0.0158565 | -0.0311703 | -0.00350176 | -0.00168977 |
| 16 | -0.942756 | -0.0143079 | -0.0298942 | -0.00227434 | -0.0016673 |
| 17 | -0.941857 | 0.00242186 | 0.00428942 | -0.00227444 | -0.0016672 |
| 18 | -0.942671 | -0.0127267 | -0.0264462 | -0.0031424 | -0.00110987 |
| 19 | -0.942298 | -0.00578521 | -0.0108384 | -0.00225972 | -0.00167199 |
| 20 | -0.942039 | -0.000953749 | -0.00183079 | -0.000720897 | -0.00175151 |
| 21 | -0.941941 | 0.000868963 | 0.00163355 | -0.000572852 | -0.00175581 |
| 22 | -0.942127 | -0.00260451 | -0.00609466 | -0.00319812 | -0.00121254 |
| 23 | -0.942085 | -0.00181892 | -0.00439854 | -0.00248478 | -0.00199955 |
| 24 | -0.942041 | -0.00099291 | -0.00240316 | -0.00228621 | -0.00166339 |
| 25 | -0.941984 | 6.9627e-05 | -2.98393e-05 | -0.00227542 | -0.00166691 |

| | | | | | |
|---|---|---|---|---|---|
| 26 | -0.941987 | 8.39686e-06 | -0.000121807 | -0.00227581 | -0.00166681 |
| 27 | -0.942047 | -0.0010991 | -0.00269131 | -0.00227934 | -0.00166564 |
| 28 | -0.941929 | 0.00109241 | 0.00219568 | -0.00228915 | -0.0016631 |
| 29 | -0.942001 | -0.000255695 | -0.00077626 | -0.00315682 | -0.00113068 |
| 30 | -0.942331 | -0.00639499 | -0.0169033 | -0.00608867 | -0.000883325 |
| 31 | -0.942361 | -0.0069474 | -0.0182674 | -0.00228022 | -0.00166544 |
| 32 | -0.945327 | -0.0621458 | -0.165901 | -0.00322932 | -0.00124341 |
| 33 | -0.941442 | 0.0101499 | 0.0254302 | -0.00228209 | -0.00166486 |
| 34 | -0.942399 | -0.00765846 | -0.0198423 | -0.00316251 | -0.00121938 |
| 35 | -0.940779 | 0.0224993 | 0.0595042 | -0.000245073 | -0.00062962 |
| 36 | -0.942202 | -0.00399676 | -0.0111702 | -0.00228532 | -0.00166349 |
| 37 | -0.941768 | 0.00408489 | 0.0102429 | -0.00305498 | -0.0010704 |
| 38 | -0.941783 | 0.00380155 | 0.00949844 | -0.00453033 | -0.00122065 |
| 39 | -0.94244 | -0.00841194 | -0.0222056 | -0.00432352 | -0.00119633 |
| 40 | -0.942191 | -0.00379419 | -0.00994542 | -0.00313523 | -0.00110245 |
| 41 | -0.942105 | -0.0021872 | -0.00570395 | -0.00451865 | -0.00124 |
| 42 | -0.941869 | 0.00221187 | 0.00613858 | -0.00321804 | -0.00124009 |
| 43 | -0.94203 | -0.000787224 | -0.00207213 | -0.00227022 | -0.00166798 |
| 44 | -0.937327 | 0.0867364 | 0.228542 | 0.49326 | -0.00406132 |
| 45 | -0.941515 | 0.00879701 | 0.0266274 | -0.00343132 | 0.496605 |
| 46 | -0.942166 | -0.00332478 | -0.00671804 | -0.00206056 | -0.000815234 |
| 47 | -0.942012 | -0.000457369 | -0.00114641 | -0.00213179 | -0.00170911 |
| 48 | -0.936816 | 0.0962389 | 0.25911 | 0.495724 | 0.496581 |

Table 6: Comparing contribution of different systematics for pt6 in central eta

| Contribution of different systematic uncertainties for pt1 in central eta | | | | | |
|---|---|---|---|---|---|
| Systematic | SF_100% | SF_85% | SF_77% | SF_70% | SF_60% |
| 0 | -0.900735 | -0.0523686 | -0.11094 | 0.00134813 | 0.00253963 |
| 1 | -0.889717 | 0.0590045 | 0.171264 | 0.00114731 | 0.00305061 |
| 2 | -0.903804 | -0.0833952 | -0.273815 | 0.00304283 | -0.000535698 |
| 3 | -0.896652 | -0.0110988 | -0.0440012 | 0.00319537 | 0.00187249 |
| 4 | -0.896698 | -0.0115595 | -0.0176186 | -0.0016846 | 0.00162637 |
| 5 | -0.89549 | 0.000646119 | 0.00637075 | 0.00100625 | 0.00701056 |
| 6 | -0.895272 | 0.00285649 | 0.00385167 | 0.00101386 | 0.00209514 |
| 7 | -0.894881 | 0.00680509 | 0.0198449 | 0.00474981 | 0.00311629 |
| 8 | -0.896238 | -0.00691033 | -0.0178953 | 0.00438277 | 0.00303732 |
| 9 | -0.896632 | -0.0108924 | -0.0308926 | 0.00269765 | -0.000924955 |
| 10 | -0.895511 | 0.000434028 | 0.00453329 | 0.00148282 | 0.00214377 |
| 11 | -0.895511 | 0.000441921 | 0.00113765 | 0.00163565 | 0.00215555 |
| 12 | -0.8956 | -0.000463902 | -0.000509065 | 0.00137498 | 0.00221962 |
| 13 | -0.894993 | 0.00567495 | 0.0111719 | 0.0010849 | 0.00223337 |
| 14 | -0.896027 | -0.00477584 | -0.0081909 | 0.00108973 | 0.00178923 |

| | | | | | |
|---|---|---|---|---|---|
| 15 | -0.896504 | -0.0095958 | -0.0194719 | 0.00133365 | 0.00216724 |
| 16 | -0.896532 | -0.00988241 | -0.0220201 | 0.000594211 | 0.00576123 |
| 17 | -0.895324 | 0.00233173 | 0.00531513 | 0.00347235 | 0.00139221 |
| 18 | -0.896499 | -0.00955396 | -0.0213273 | 0.00131865 | 0.0022207 |
| 19 | -0.896214 | -0.00666446 | -0.0143194 | 0.00171942 | 0.0039645 |
| 20 | -0.895618 | -0.000640603 | -0.00113864 | -0.000455279 | 0.00373266 |
| 21 | -0.895431 | 0.00124573 | 0.00323312 | 0.0038822 | 0.00213083 |
| 22 | -0.895629 | -0.000751783 | -0.00182798 | 0.00101518 | -0.00271891 |
| 23 | -0.895598 | -0.00043946 | -0.00101769 | 0.00134001 | 0.00236812 |
| 24 | -0.895525 | 0.000297896 | 0.00101262 | 0.00311687 | 0.00217518 |
| 25 | -0.895498 | 0.000566171 | 0.00152973 | 0.00154033 | 0.002258 |
| 26 | -0.895507 | 0.000475784 | 0.00135221 | 0.00138764 | 0.0024802 |
| 27 | -0.895559 | -5.03282e-05 | -3.31879e-05 | 0.00152482 | 0.00223622 |
| 28 | -0.895477 | 0.000785137 | 0.0019582 | -0.000228261 | 0.00220196 |
| 29 | -0.89551 | 0.000447607 | 0.00122938 | 0.001388 | 0.00214217 |
| 30 | -0.895918 | -0.00367617 | -0.010324 | 0.00284317 | 0.000460737 |
| 31 | -0.896043 | -0.00493726 | -0.013995 | -0.000495152 | 0.00259344 |
| 32 | -0.900208 | -0.0470413 | -0.135963 | 0.00155423 | 0.00224577 |
| 33 | -0.894696 | 0.00867368 | 0.0235004 | 0.00152386 | 0.00223667 |
| 34 | -0.89612 | -0.0057179 | -0.0154186 | -0.000230603 | 0.00905492 |
| 35 | -0.893851 | 0.0172157 | 0.0492453 | 0.00186333 | 0.00209094 |
| 36 | -0.895773 | -0.00221274 | -0.00681873 | 0.00151765 | 0.00224176 |
| 37 | -0.895139 | 0.00419388 | 0.011581 | 0.00303397 | 0.00105096 |
| 38 | -0.895152 | 0.0040681 | 0.0111386 | 0.0020387 | 0.00193567 |
| 39 | -0.896097 | -0.00548306 | -0.0154403 | 0.00146548 | 0.00222587 |
| 40 | -0.895768 | -0.00216301 | -0.00604626 | 0.00152745 | 0.00223087 |
| 41 | -0.895626 | -0.000725898 | -0.00200395 | 0.00152006 | 0.00223488 |
| 42 | -0.895329 | 0.00227852 | 0.00691598 | 0.00118294 | 0.0099714 |
| 43 | -0.895545 | 9.84498e-05 | 0.000282593 | 0.00189084 | 0.00216751 |
| 44 | -0.886578 | 0.0907397 | 0.256262 | 0.496955 | -0.00704305 |
| 45 | -0.895266 | 0.00291411 | 0.0138515 | 0.00085342 | 0.500686 |
| 46 | -0.895855 | -0.0030376 | -0.00632764 | 0.0012708 | 0.00267064 |
| 47 | -0.895539 | 0.000159302 | 0.000561879 | 0.00115689 | 0.00238409 |
| 48 | -0.886312 | 0.0934245 | 0.272116 | 0.501937 | 0.508168 |

Table 7: Comparing contribution of different systematics for pt7 in central eta

| Contribution of different systematic uncertainties for pt1 in central eta | | | | | |
|---|---|---|---|---|---|
| Systematic | SF_100% | SF_85% | SF_77% | SF_70% | SF_60% |
| 0 | -0.867037 | -0.0369945 | -0.0716432 | -2.19293e-05 | -0.000112094 |
| 1 | -0.857075 | 0.0386559 | 0.112309 | -3.93458e-05 | -0.000195648 |
| 2 | -0.870358 | -0.0622123 | -0.203277 | -0.000148217 | 0.00432948 |
| 3 | -0.863292 | -0.00855902 | -0.0344729 | 1.79806e-05 | 9.77669e-05 |

| | | | | | |
|---|---|---|---|---|---|
| 4 | -0.863109 | -0.00716533 | -0.00751661 | -1.57947e-05 | -8.14915e-05 |
| 5 | -0.862113 | 0.000399025 | 0.00489052 | -1.1282e-06 | -5.96e-06 |
| 6 | -0.861938 | 0.0017261 | 0.00107014 | 1.69229e-06 | 8.82538e-06 |
| 7 | -0.861626 | 0.00409568 | 0.0119013 | -3.4551e-06 | -1.79946e-05 |
| 8 | -0.862855 | -0.00523813 | -0.0137768 | 6.41662e-06 | 3.41554e-05 |
| 9 | -0.863219 | -0.00800588 | -0.0225764 | 1.10704e-05 | 5.92561e-05 |
| 10 | -0.862142 | 0.000176254 | 0.00327999 | -7.05123e-07 | -3.78231e-06 |
| 11 | -0.86215 | 0.000117678 | 0.00017701 | -4.65381e-06 | -2.45277e-05 |
| 12 | -0.862228 | -0.000480662 | -0.000716667 | -3.31408e-06 | -1.75361e-05 |
| 13 | -0.861675 | 0.00372439 | 0.00601343 | 8.88455e-06 | 4.75654e-05 |
| 14 | -0.862595 | -0.00326778 | -0.00487372 | -4.37176e-06 | -2.28085e-05 |
| 15 | -0.863043 | -0.00666312 | -0.0121534 | 9.87172e-07 | 5.15769e-06 |
| 16 | -0.863083 | -0.00697379 | -0.0145928 | -3.52561e-06 | -1.84531e-05 |
| 17 | -0.862005 | 0.00121421 | 0.00212239 | 1.19871e-06 | 6.41846e-06 |
| 18 | -0.863088 | -0.00700495 | -0.0147734 | -1.90383e-06 | -9.97154e-06 |
| 19 | -0.862872 | -0.0053703 | -0.0107672 | 1.26922e-06 | 6.53307e-06 |
| 20 | -0.862203 | -0.000285828 | -0.000399339 | 0 | 0 |
| 21 | -0.86211 | 0.000419451 | 0.000821474 | 2.82049e-06 | 1.49e-05 |
| 22 | -0.862234 | -0.000525533 | -0.00124733 | 8.10891e-06 | 4.33246e-05 |
| 23 | -0.862219 | -0.000408579 | -0.00102909 | -2.53844e-06 | -1.341e-05 |
| 24 | -0.862186 | -0.000157937 | -0.000354746 | 4.93586e-07 | 2.63615e-06 |
| 25 | -0.862138 | 0.000205838 | 0.000469271 | 4.30125e-06 | 2.28085e-05 |
| 26 | -0.862143 | 0.000170983 | 0.000436667 | -4.23074e-07 | -2.17769e-06 |
| 27 | -0.862191 | -0.000193846 | -0.000488071 | 2.82049e-06 | 1.50146e-05 |
| 28 | -0.862089 | 0.00058167 | 0.00132081 | -4.72432e-06 | -2.47569e-05 |
| 29 | -0.862152 | 0.000101404 | 0.000289174 | 2.04486e-06 | 1.07738e-05 |
| 30 | -0.862757 | -0.0044922 | -0.0120796 | 6.06406e-06 | 3.23215e-05 |
| 31 | -0.862843 | -0.00514892 | -0.0143421 | 3.4551e-06 | 1.84531e-05 |
| 32 | -0.869051 | -0.0522929 | -0.146307 | 3.73715e-06 | 1.95992e-05 |
| 33 | -0.861047 | 0.00848917 | 0.0222172 | -3.87817e-06 | -2.05161e-05 |
| 34 | -0.862927 | -0.00578218 | -0.0156336 | 2.82049e-06 | 1.49e-05 |
| 35 | -0.859857 | 0.0175274 | 0.0486786 | 1.90383e-06 | 9.97154e-06 |
| 36 | -0.862528 | -0.00275259 | -0.00815771 | -7.05123e-08 | -2.29231e-07 |
| 37 | -0.86164 | 0.00399058 | 0.0105766 | 8.46147e-07 | 4.47e-06 |
| 38 | -0.861644 | 0.00395448 | 0.0102376 | 3.24356e-06 | 1.71923e-05 |
| 39 | -0.862965 | -0.00607156 | -0.0167265 | -1.83332e-06 | -9.51307e-06 |
| 40 | -0.862507 | -0.0025988 | -0.00707394 | 7.82686e-06 | 4.16054e-05 |
| 41 | -0.862304 | -0.00105443 | -0.00281908 | -1.76281e-06 | -9.28384e-06 |
| 42 | -0.861874 | 0.00221012 | 0.00626373 | 9.1666e-07 | 4.69923e-06 |
| 43 | -0.862229 | -0.000483166 | -0.00122735 | 5.64098e-07 | 3.09461e-06 |
| 44 | -0.848532 | 0.103525 | 0.276914 | 0.494884 | 0.00101022 |
| 45 | -0.862541 | -0.00285656 | 0.00110992 | -0.000714078 | 0.505241 |
| 46 | -0.862654 | -0.00371049 | -0.00746284 | -0.00018164 | 0.00423721 |
| 47 | -0.862205 | -0.000306715 | -0.000150308 | 1.14935e-05 | 0.0073716 |

| | | | | | |
|---|---|---|---|---|---|
| 48 | -0.849105 | 0.0991722 | 0.276517 | 0.493993 | 0.500736 |

Table 8: Comparing contribution of different systematics for pt8 in central eta

| Contribution of different systematic uncertainties for pt1 in central eta | | | | | |
|---|---|---|---|---|---|
| Systematic | SF_100% | SF_85% | SF_77% | SF_70% | SF_60% |
| 0 | -0.973713 | -0.0275463 | -0.0579 | -9.42883e-07 | -1.32463e-05 |
| 1 | -0.971682 | 0.0462468 | 0.112542 | -1.25718e-07 | -9.1705e-07 |
| 2 | -0.974591 | -0.0594638 | -0.152625 | 4.40012e-06 | 1.51823e-05 |
| 3 | -0.973233 | -0.0101386 | -0.0276472 | 1.19432e-06 | 5.6042e-06 |
| 4 | -0.973073 | -0.00429151 | -0.00690031 | -6.91448e-07 | -6.31746e-06 |
| 5 | -0.972933 | 0.000771189 | 0.00298532 | 3.14294e-07 | 1.63031e-06 |
| 6 | -0.972926 | 0.00103387 | 0.00135305 | 1.25718e-07 | 4.07578e-07 |
| 7 | -0.972858 | 0.00351842 | 0.00867118 | -6.28589e-08 | -5.09472e-07 |
| 8 | -0.973067 | -0.00410312 | -0.00968654 | 0 | -4.07578e-07 |
| 9 | -0.973126 | -0.00623323 | -0.015275 | 1.25718e-07 | 7.13261e-07 |
| 10 | -0.972946 | 0.000296367 | 0.00161428 | -2.51436e-07 | -1.8341e-06 |
| 11 | -0.972952 | 7.80915e-05 | 0.000149651 | 1.25718e-07 | 4.07578e-07 |
| 12 | -0.972963 | -0.000323361 | -0.000621021 | 4.40012e-07 | 2.34357e-06 |
| 13 | -0.972898 | 0.00205829 | 0.00377551 | 1.25718e-07 | 5.09472e-07 |
| 14 | -0.97303 | -0.00272834 | -0.00523198 | 0 | -3.05683e-07 |
| 15 | -0.973073 | -0.00430434 | -0.00865331 | -3.77153e-07 | -2.85305e-06 |
| 16 | -0.973016 | -0.00223745 | -0.00447571 | -4.40012e-07 | -3.15873e-06 |
| 17 | -0.972928 | 0.000977695 | 0.00202086 | 6.28589e-08 | 1.01894e-07 |
| 18 | -0.97293 | 0.000902493 | 0.00272915 | 6.28589e-08 | 3.05683e-07 |
| 19 | -0.972744 | 0.0076579 | 0.0180421 | 2.51436e-07 | 1.12084e-06 |
| 20 | -0.972956 | -4.74329e-05 | -2.90462e-05 | 1.25718e-07 | 7.13261e-07 |
| 21 | -0.972943 | 0.000411884 | 0.000887362 | -1.25718e-07 | -1.12084e-06 |
| 22 | -0.973 | -0.0016493 | -0.00365875 | 2.51436e-07 | 1.32463e-06 |
| 23 | -0.97298 | -0.000921593 | -0.00212467 | -6.28589e-08 | -7.13261e-07 |
| 24 | -0.972964 | -0.000343095 | -0.000777808 | -3.77153e-07 | -2.54736e-06 |
| 25 | -0.972948 | 0.000253234 | 0.000568801 | -6.28589e-08 | -7.13261e-07 |
| 26 | -0.972946 | 0.00030264 | 0.000699699 | -1.88577e-07 | -1.22273e-06 |
| 27 | -0.972967 | -0.000442542 | -0.00102375 | -6.28589e-08 | -5.09472e-07 |
| 28 | -0.972932 | 0.000819256 | 0.00185233 | 6.28589e-08 | 3.05683e-07 |
| 29 | -0.972948 | 0.000233076 | 0.000533882 | 3.14294e-07 | 1.63031e-06 |
| 30 | -0.972998 | -0.00159115 | -0.00397832 | 3.77153e-07 | 1.936e-06 |
| 31 | -0.973018 | -0.00230976 | -0.00570032 | -6.28589e-08 | -4.07578e-07 |
| 32 | -0.973564 | -0.0221486 | -0.0545417 | 6.28589e-08 | 1.01894e-07 |
| 33 | -0.972869 | 0.00309617 | 0.00745964 | -1.88577e-07 | -1.63031e-06 |
| 34 | -0.973015 | -0.00220742 | -0.00546227 | 1.25718e-07 | 4.07578e-07 |
| 35 | -0.972727 | 0.00825973 | 0.0202508 | 6.28589e-08 | 1.01894e-07 |
| 36 | -0.972998 | -0.00156676 | -0.0039285 | -1.88577e-07 | -1.22273e-06 |

| | | | | | |
|---|---|---|---|---|---|
| 37 | -0.972916 | 0.00138302 | 0.0034894 | -1.25718e-07 | -7.13261e-07 |
| 38 | -0.972917 | 0.00137358 | 0.00346465 | 1.25718e-07 | 6.11367e-07 |
| 39 | -0.973029 | -0.00269063 | -0.00665102 | 0 | -1.01894e-07 |
| 40 | -0.972984 | -0.00108877 | -0.00272908 | -6.28589e-08 | -5.09472e-07 |
| 41 | -0.972966 | -0.000423513 | -0.00108481 | 3.77153e-07 | 1.8341e-06 |
| 42 | -0.972922 | 0.00116672 | 0.00289029 | 1.88577e-07 | 1.12084e-06 |
| 43 | -0.972958 | -0.000118054 | -0.000280422 | 6.28589e-08 | 1.01894e-07 |
| 44 | -0.970662 | 0.0833175 | 0.206458 | 0.496974 | -0.00192214 |
| 45 | -0.97251 | 0.016143 | 0.0410291 | -0.00057585 | 0.499009 |
| 46 | -0.972966 | -0.000409981 | 0.000428811 | -0.000225161 | -0.000188199 |
| 47 | -0.973087 | -0.00482842 | -0.0108114 | -5.90245e-05 | -8.99728e-05 |
| 48 | -0.970199 | 0.100149 | 0.252269 | 0.496049 | 0.495708 |

Table 9: Comparing contribution of different systematics for pt1 in Forward eta

### A.1.3 Plots from investigations of different taggers

The following section includes some investigations with different parameters like IP2D, IP3D, SV1 etc. to determine the which can be a good discriminator for light jet calibrations and to see which one provides better fit results. SV1 tagger was found to be best among the choices as can be observed in the following plots.

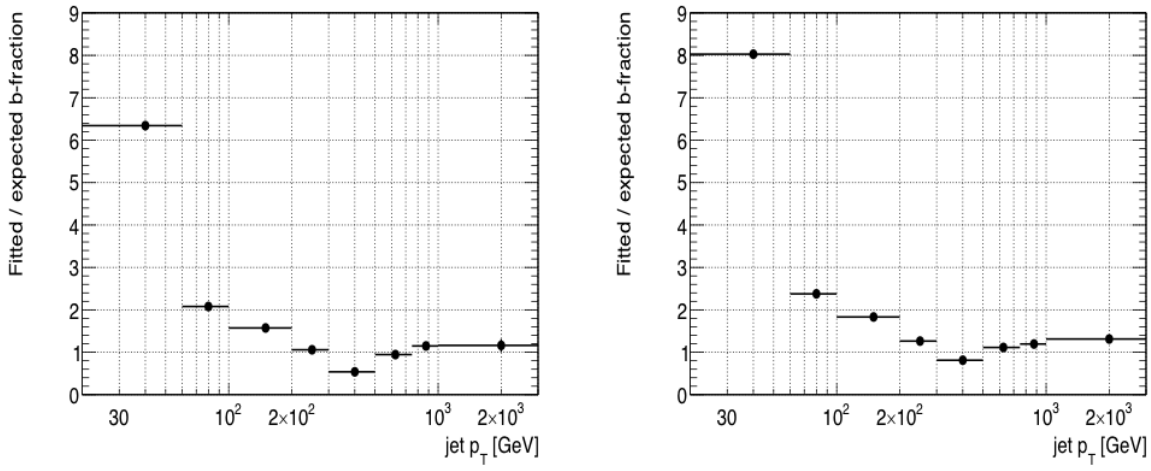


Figure 13: Fit/MC ratio for b jets for central and forward eta using MV2c20 tagger

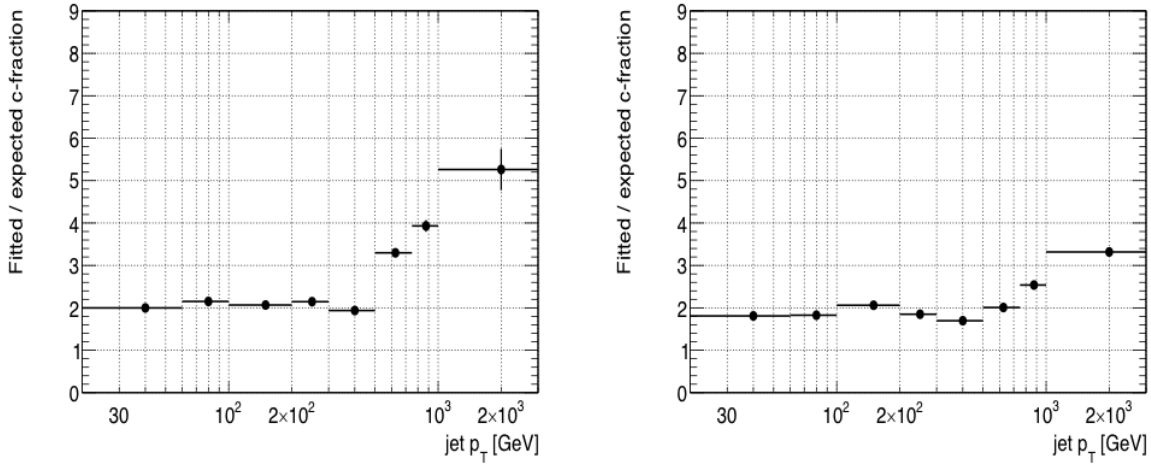


Figure 14: Fit/MC ratio for c jets for central and forward eta using MV2c20 tagger

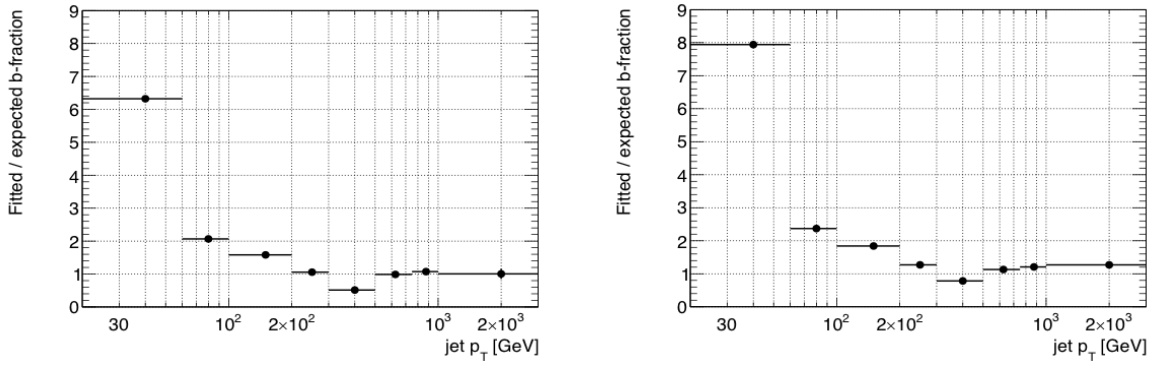


Figure 15: Fit/MC ratio for b jets for central and forward eta using MV2c10 tagger

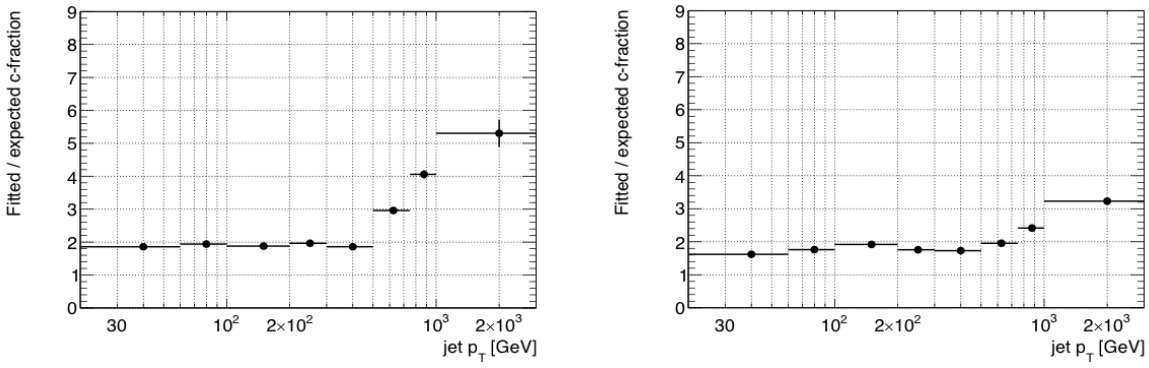


Figure 16: Fit/MC ratio for c jets for central and forward eta using MV2c10 tagger

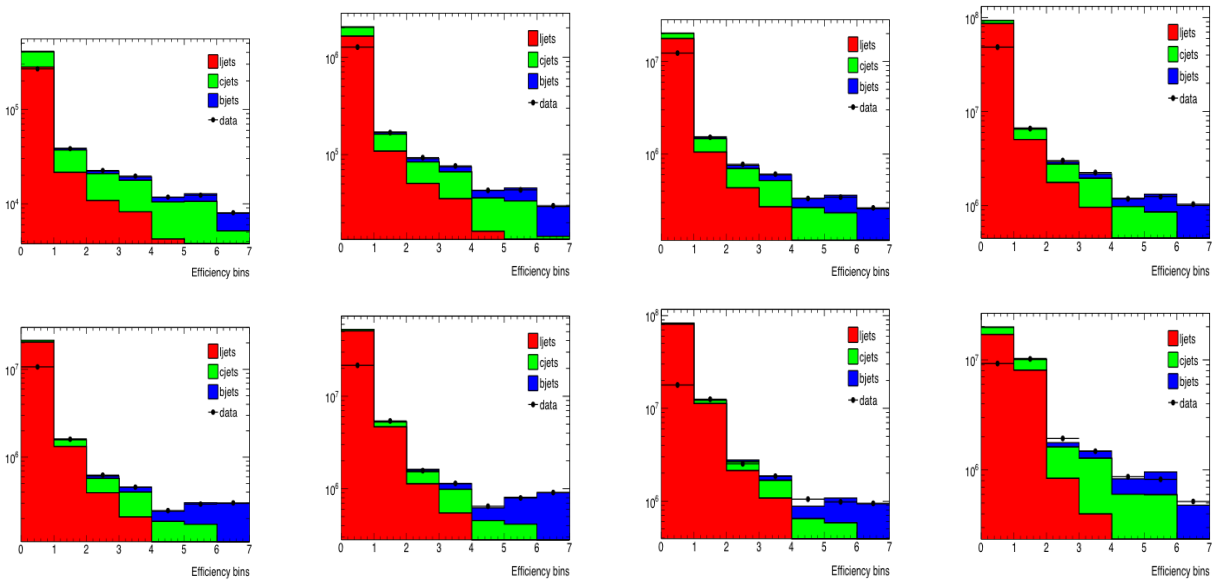


Figure 17: Fitting of b, c and light jet templates for central eta using IP2D tagger

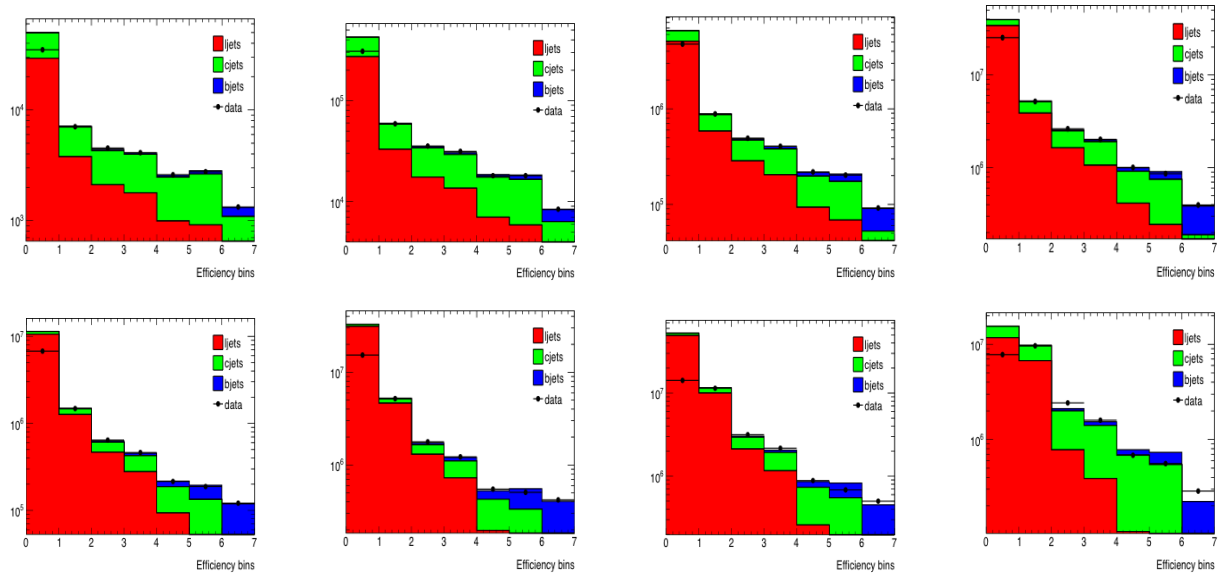


Figure 18: Fitting of b, c and light jet templates for forward eta using IP2D tagger

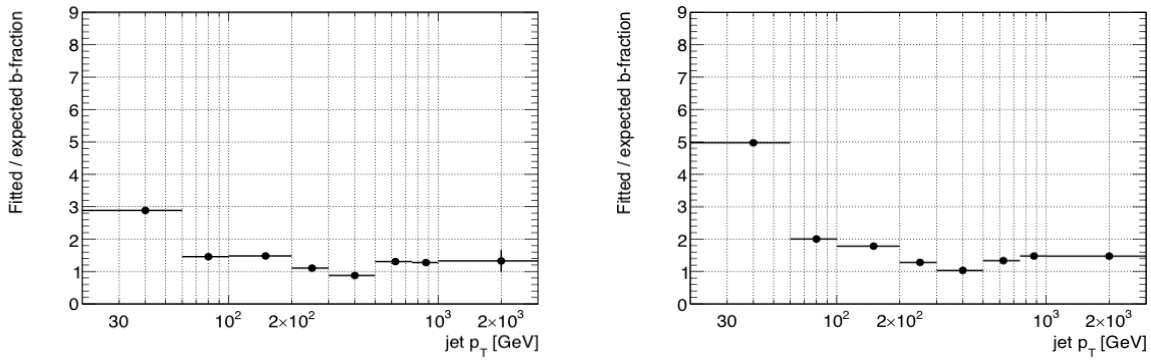


Figure 19: Fit/MC ratio for b jets for central and forward eta using IP2D tagger

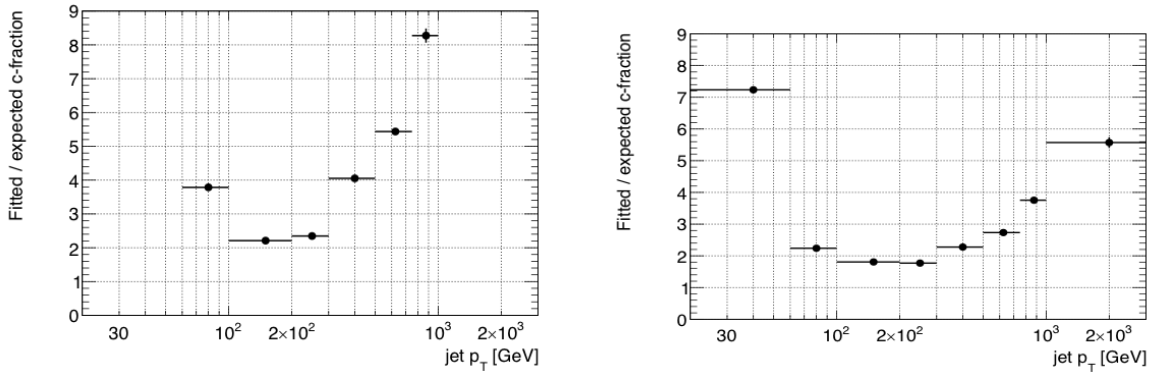


Figure 20: Fit/MC ratio for c jets for central and forward eta using IP2D tagger

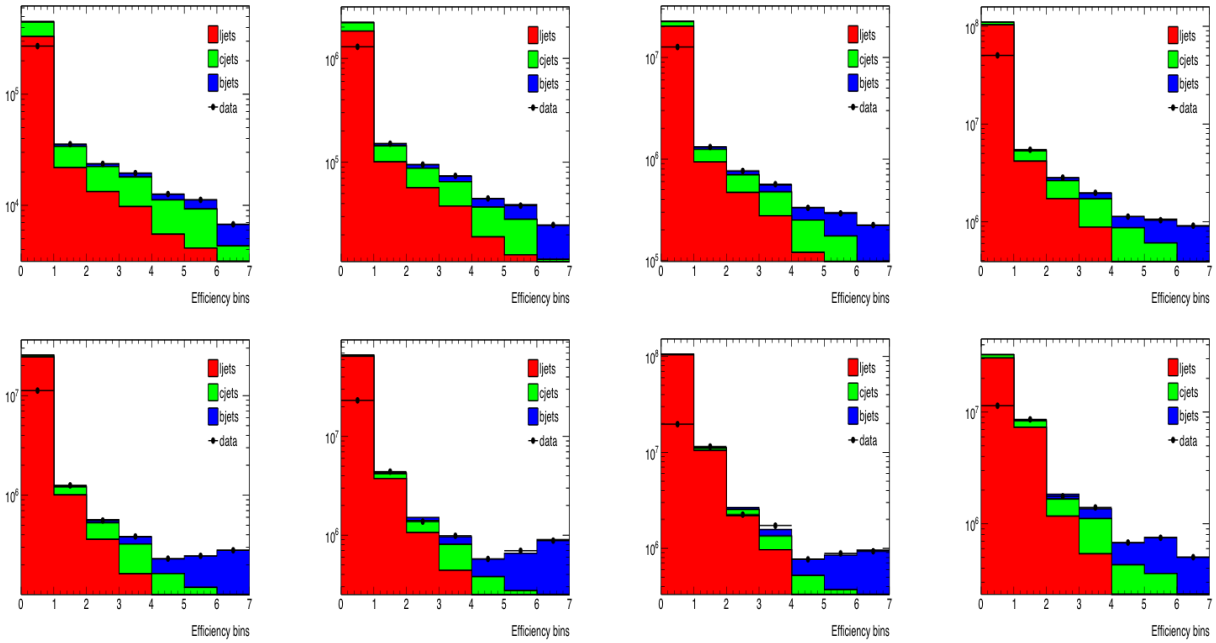


Figure 21: Fitting of b, c and light jet templates for central eta using IP3D tagger

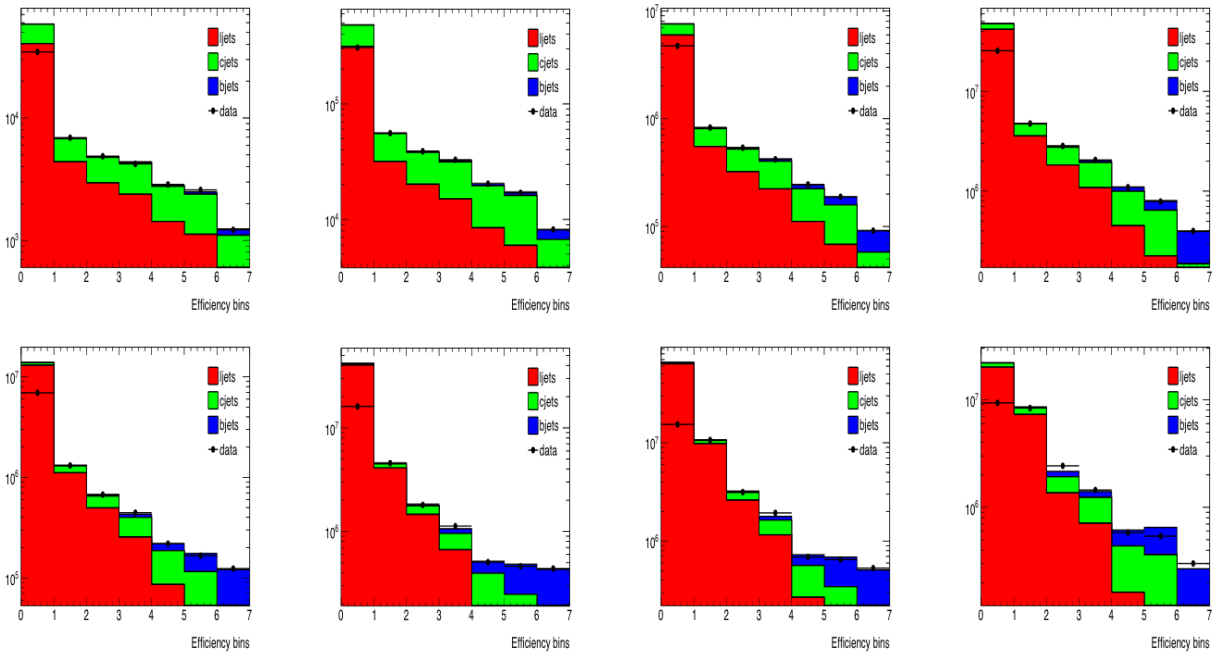


Figure 22: Fitting of b, c and light jet templates for forward eta using IP3D tagger

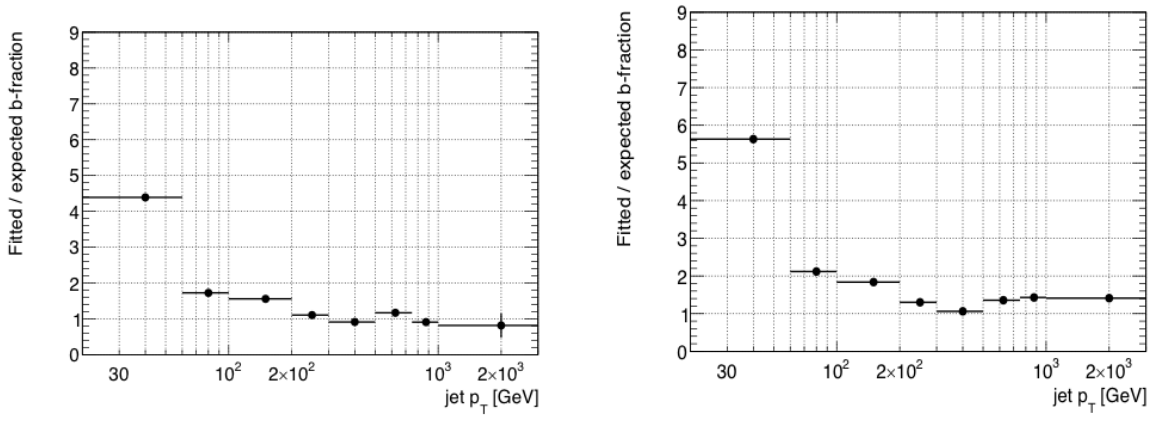


Figure 23: Fit/MC ratio for b jets for central and forward eta using IP3D tagger

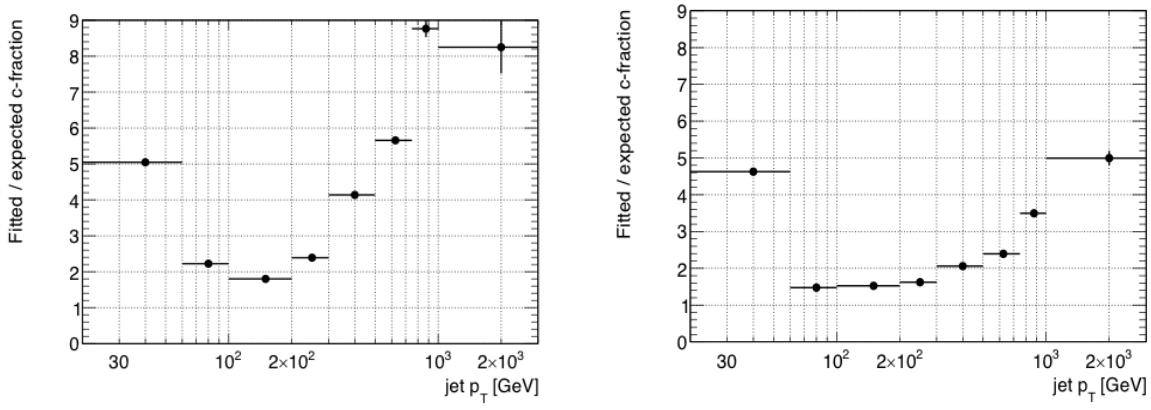


Figure 24: Fit/MC ratio for c jets for central and forward eta using IP3D tagger

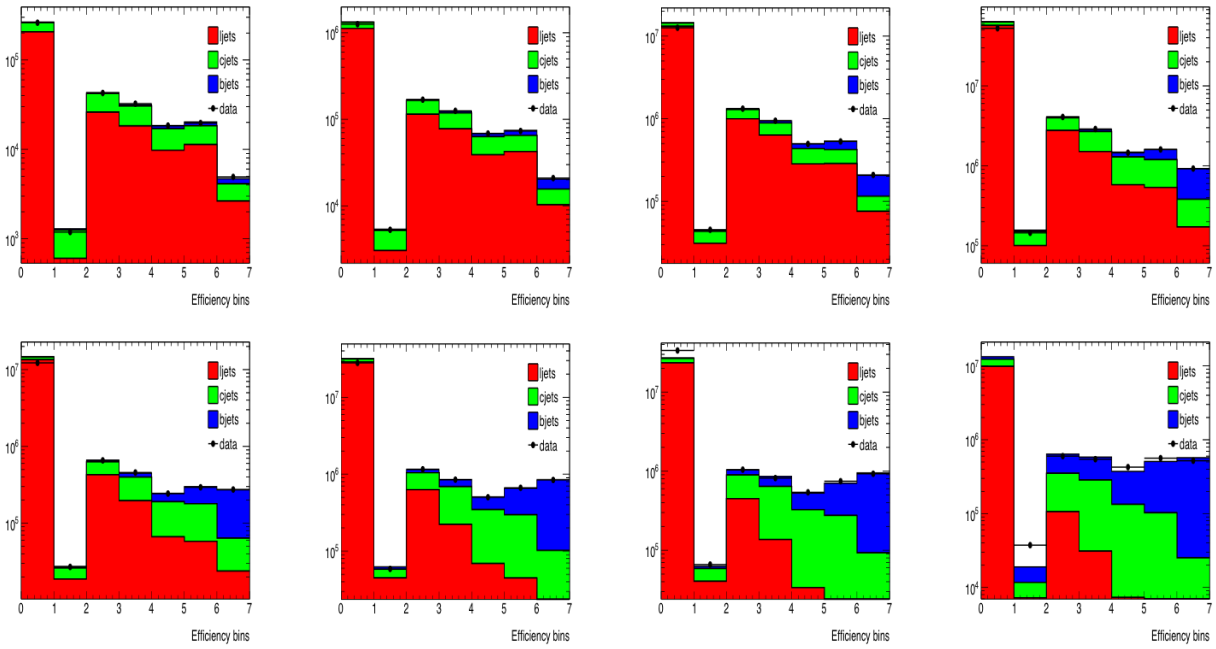


Figure 25: Fitting of b, c and light jet templates for central eta using SV1 tagger

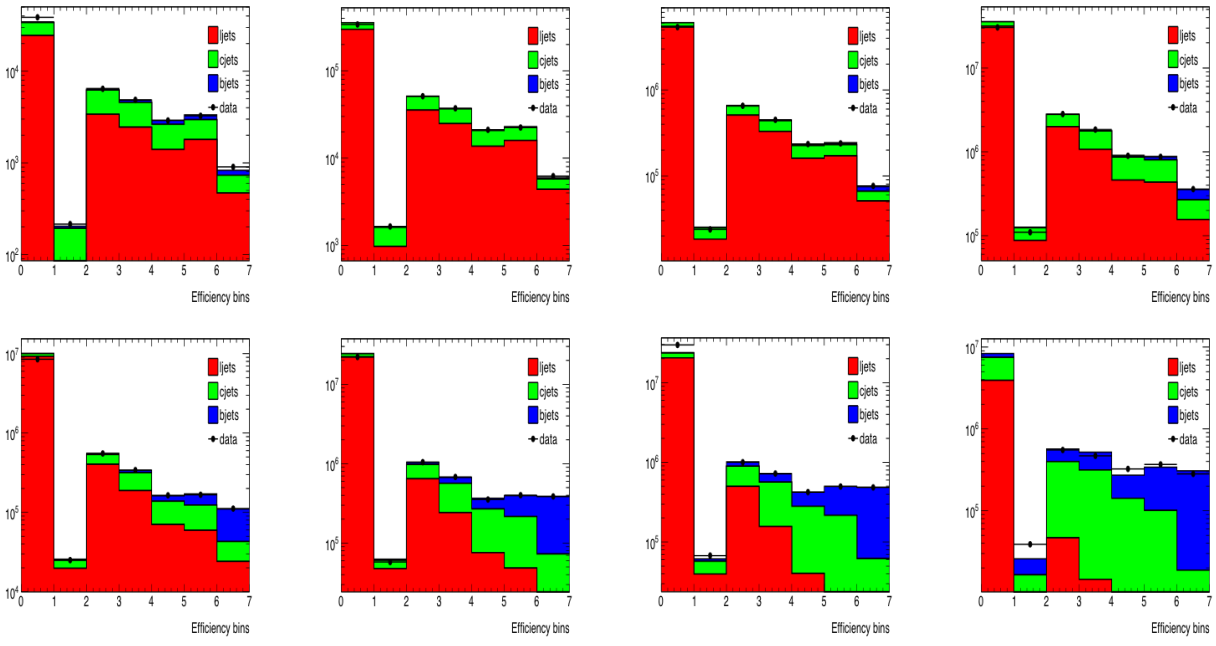


Figure 26: Fitting of b, c and light jet templates for forward eta using SV1 tagger

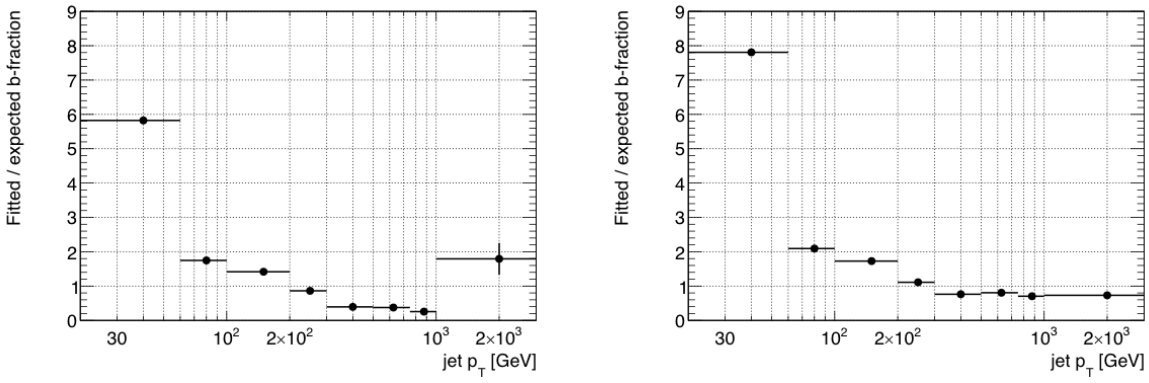


Figure 27: Fit/MC ratio for b jets for central and forward eta using SV1 tagger

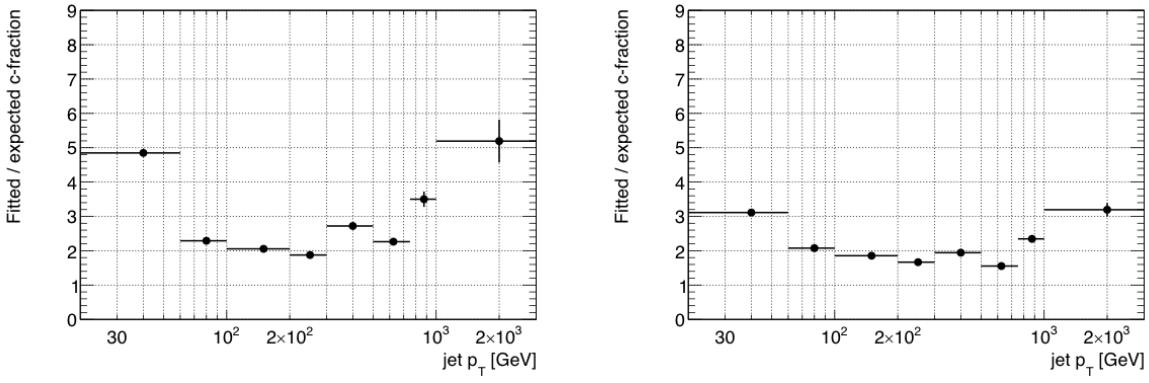


Figure 28: Fit/MC ratio for c jets for central and forward eta using SV1 tagger

### A.1.4 Plots from investigations of discriminators unaffected by track IP resolution

In this section the variables associated with JetFitter algorithm and few other variables associated with mass of secondary vertex which are used as inputs for the multivariate algorithm are investigated and the b, c and light jet tagging efficiencies have been compared.

The variables which have been studied are the following: JetFitter_N2Tpair , JetFitter_dRFlightDir, JetFitter_energyFraction, JetFitter_mass, JetFitter_nSingleTracks, JetFitter_nTracksAtVtx, JetFitter_nVTX, JetFitter_significance3d, SV1_N2Tpair, SV1_L3d, SV1_Lxy, SV1_NGTinSvx, SV1_deltaR, SV1_efracsvx, SV1_masssvx etc.

Figures 29, 30 shows the comparisons of discriminators in two different cases of including the underflow bins and excluding the underflow bins. Figures 33, 34 show similar investigations with data of different reconstruction versions 20.7 and 21. It was found that SV1_masssvx provides very good performance compared to others.

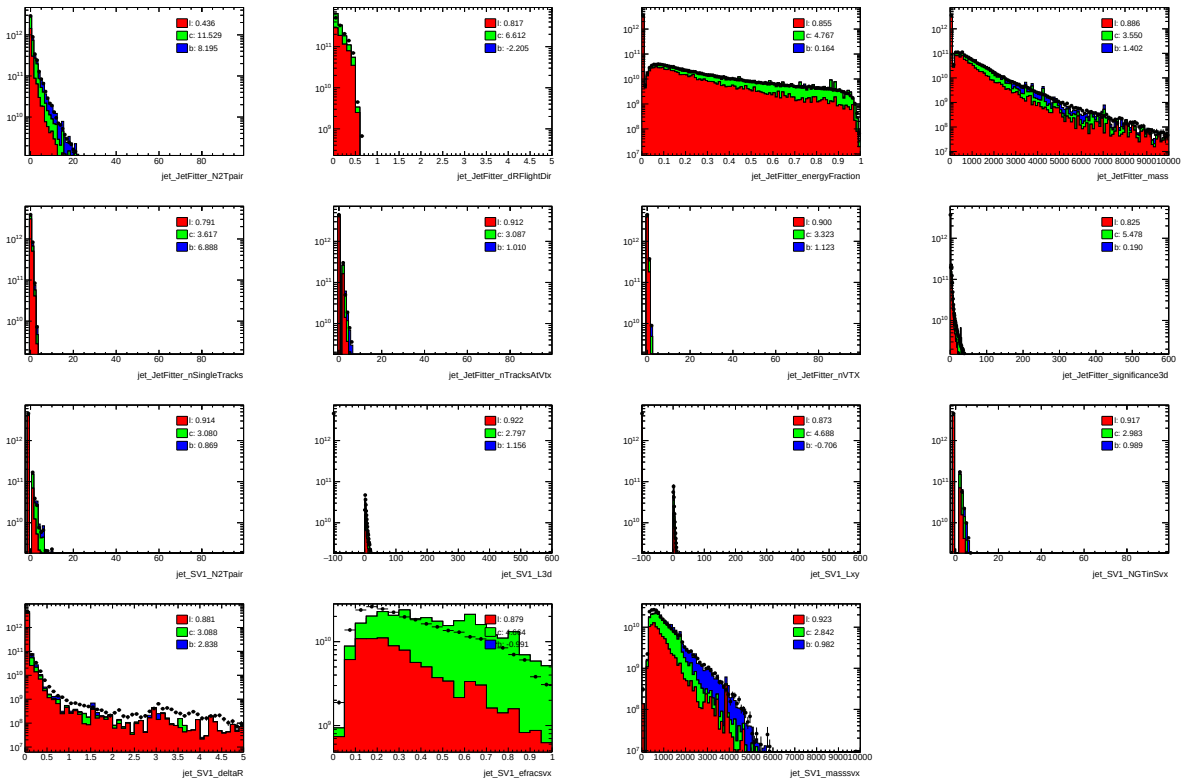


Figure 29: b, c and light jet efficiencies using different discriminators including underflow bins. b, c and light jet tagging efficiencies are calculated for each discriminator.

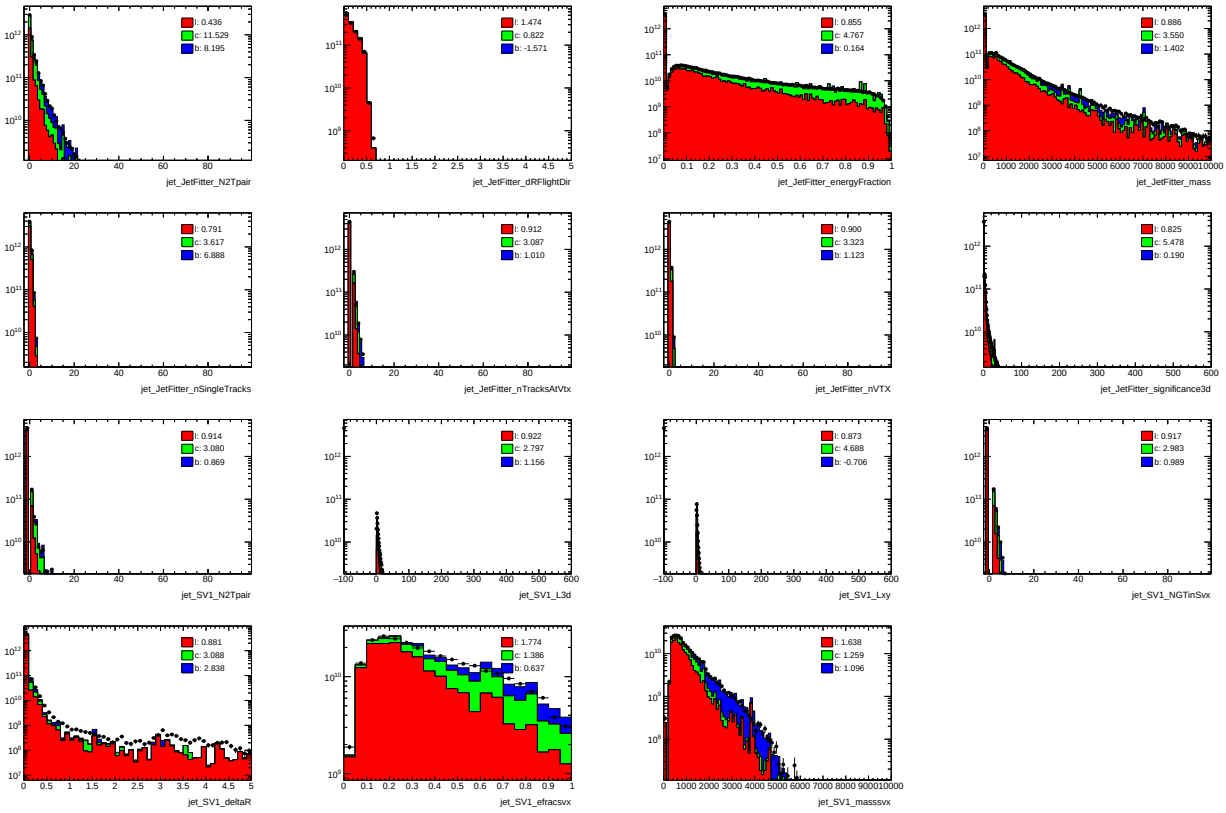


Figure 30: b, c and light jet efficiencies using different discriminators excluding underflow bins. b, c and light jet tagging efficiencies are calculated for each discriminator.

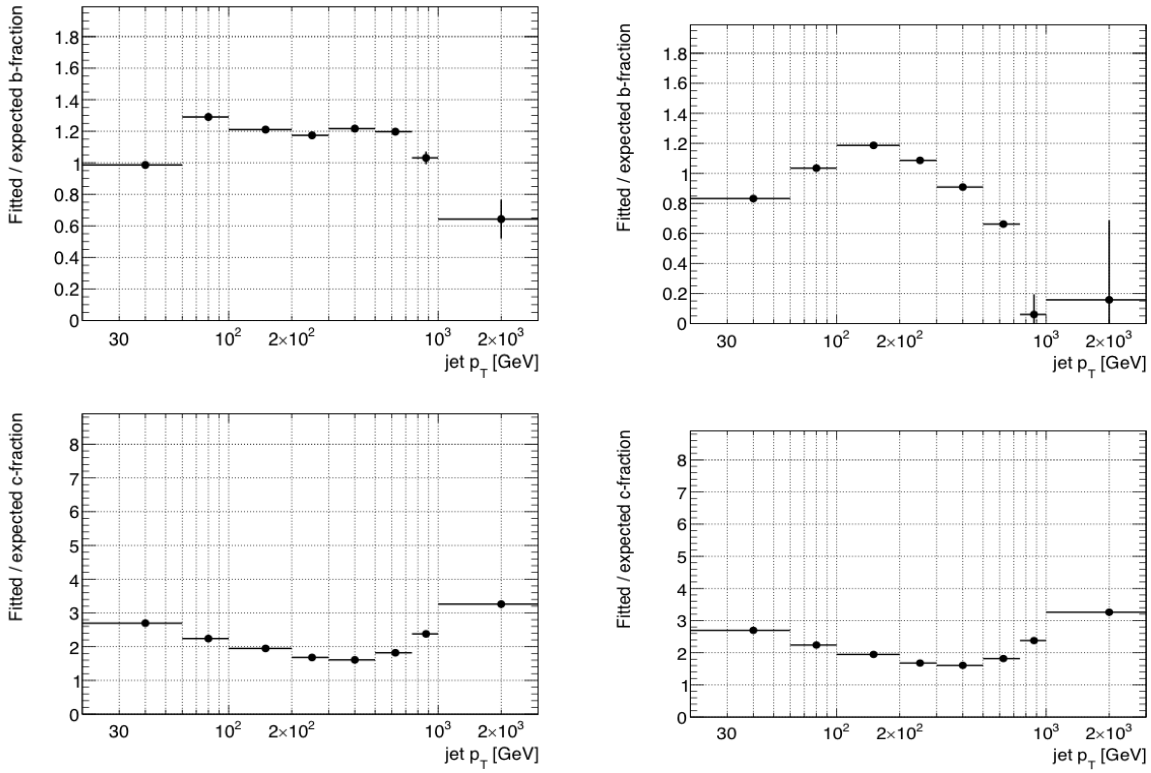


Figure 31: fit/MC ratio for b, c jets with masssvx discriminator including the underflow bins

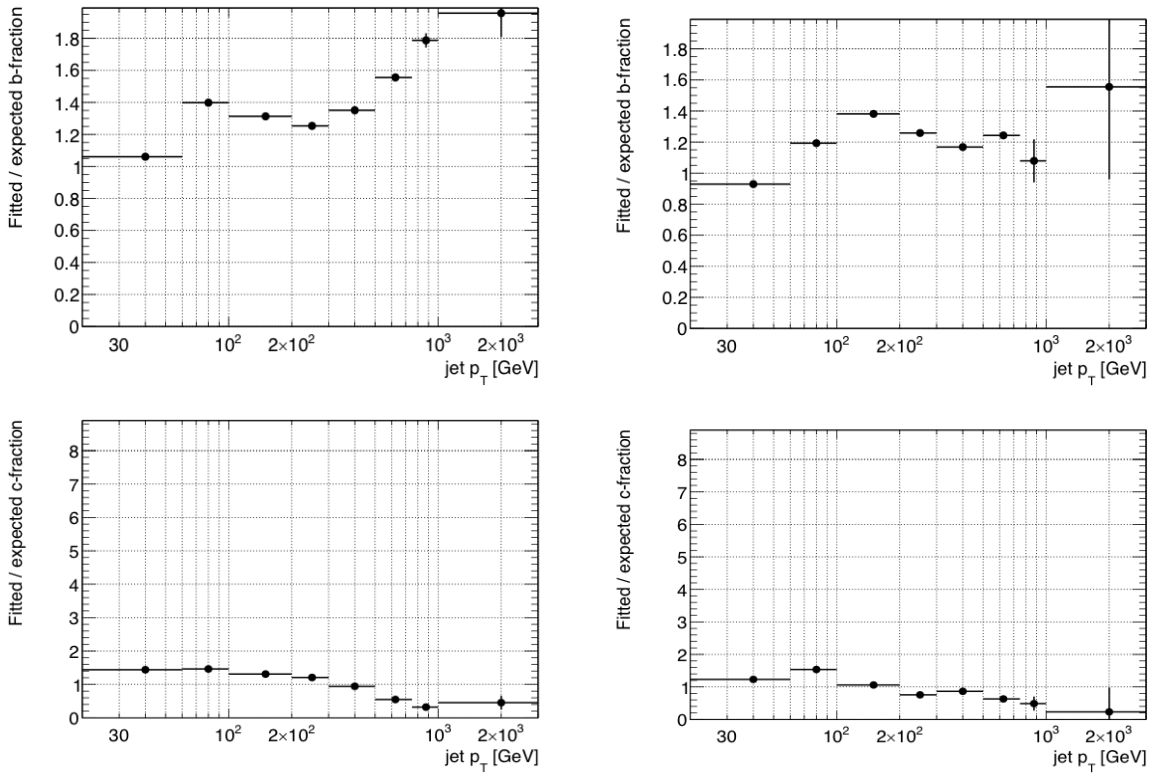


Figure 32: fit/MC ratio for b, c jets with masssvx discriminator excluding the underflow bins

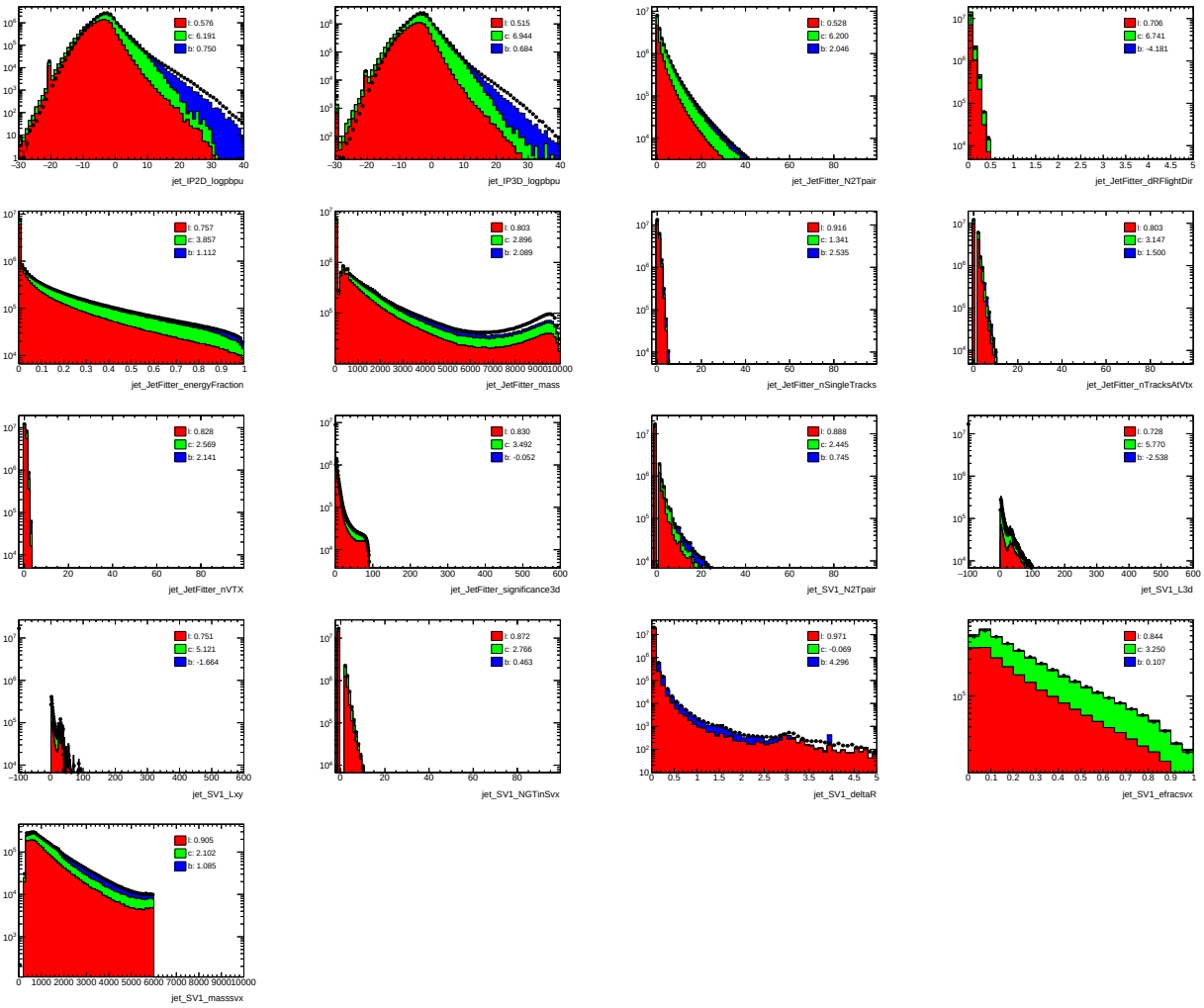


Figure 33: b, c and light jet efficiencies using different discriminators in release 20.7 data with reweighting.

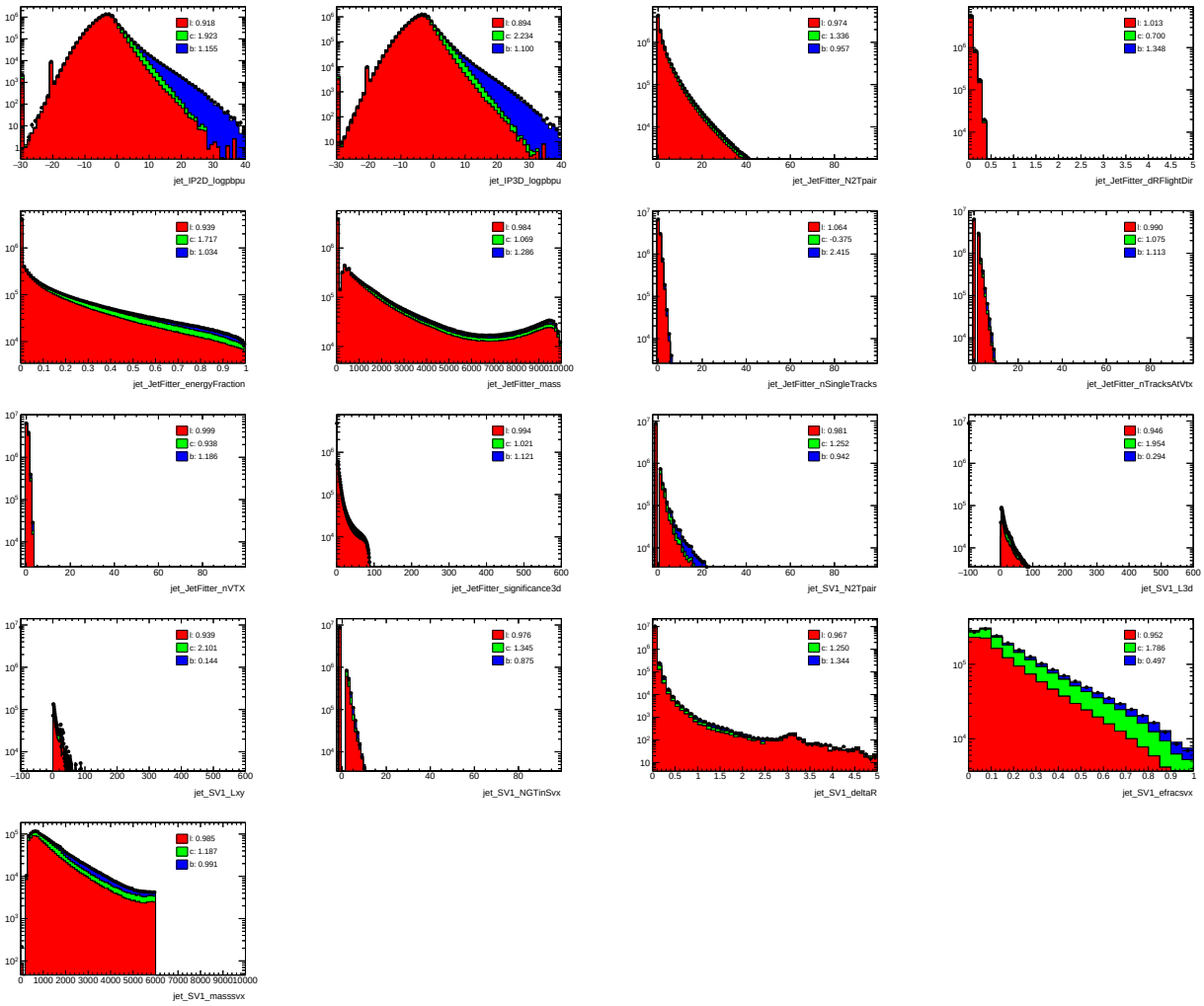


Figure 34: b, c and light jet efficiencies using different discriminators in release 21 data.

### A.1.5 Alternative Fit/MC method

An alternative fitting method has developed to cross check the results of Direct tag light jet calibration method and the following plots shows the template fits and corresponding ratios of fits and monte carlo simulation along the Jet $p_T$ spectrum.

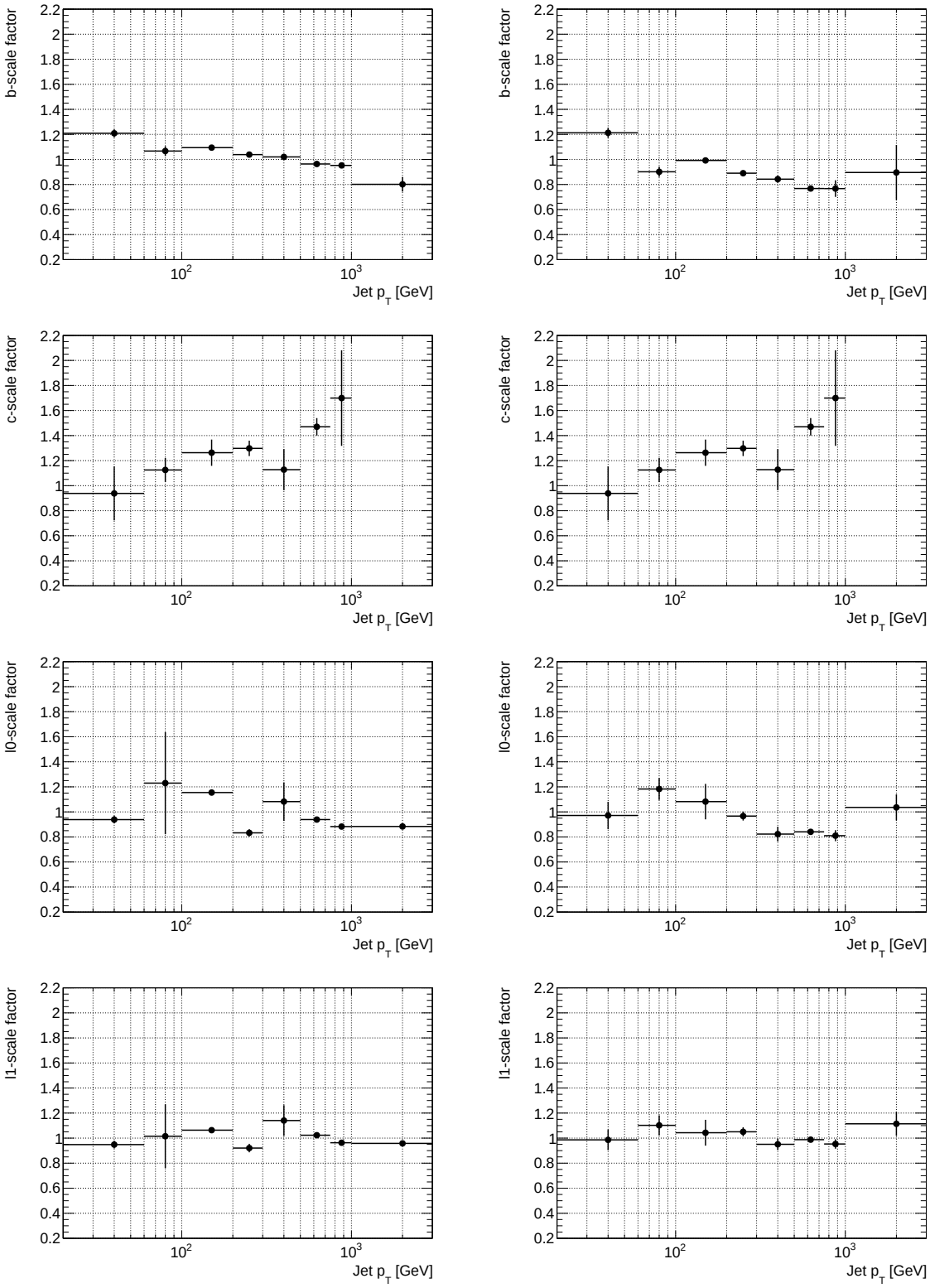


Figure 35: Alternative fit/MC procedure for Pythia in 7 bin template fit.

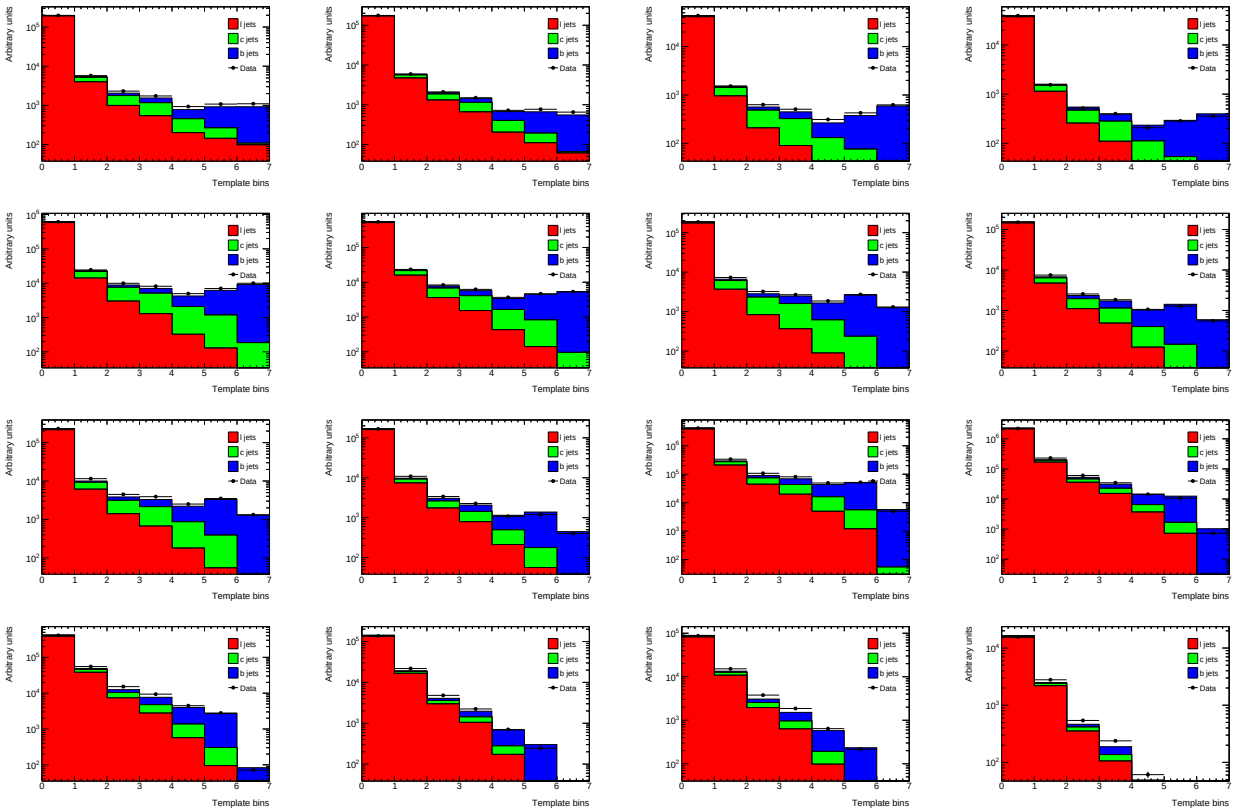


Figure 36: Prefit plots by Alternative fit/MC procedure for Pythia in 7 bin template fit.In the top row: leftmost plot is for pt bin 1 in central eta, second plot is for pt bin 1 for forward eta, third plot is for pt bin 2 in central eta and rightmost plot is for pt bin 2 for forward eta. In the Second row: leftmost plot is for pt bin 3 in central eta, second plot is for pt bin 3 for forward eta, third plot is for pt bin 4 in central eta and rightmost plot is for pt bin 4 for forward eta.In the third row: leftmost plot is for pt bin 5 in central eta, second plot is for pt bin 5 for forward eta, third plot is for pt bin 6 in central eta and rightmost plot is for pt bin 6 for forward eta. In the 4th/bottom row: leftmost plot is for pt bin 7 in central eta, second plot is for pt bin 7 for forward eta, third plot is for pt bin 8 in central eta and rightmost plot is for pt bin 8 for forward eta.

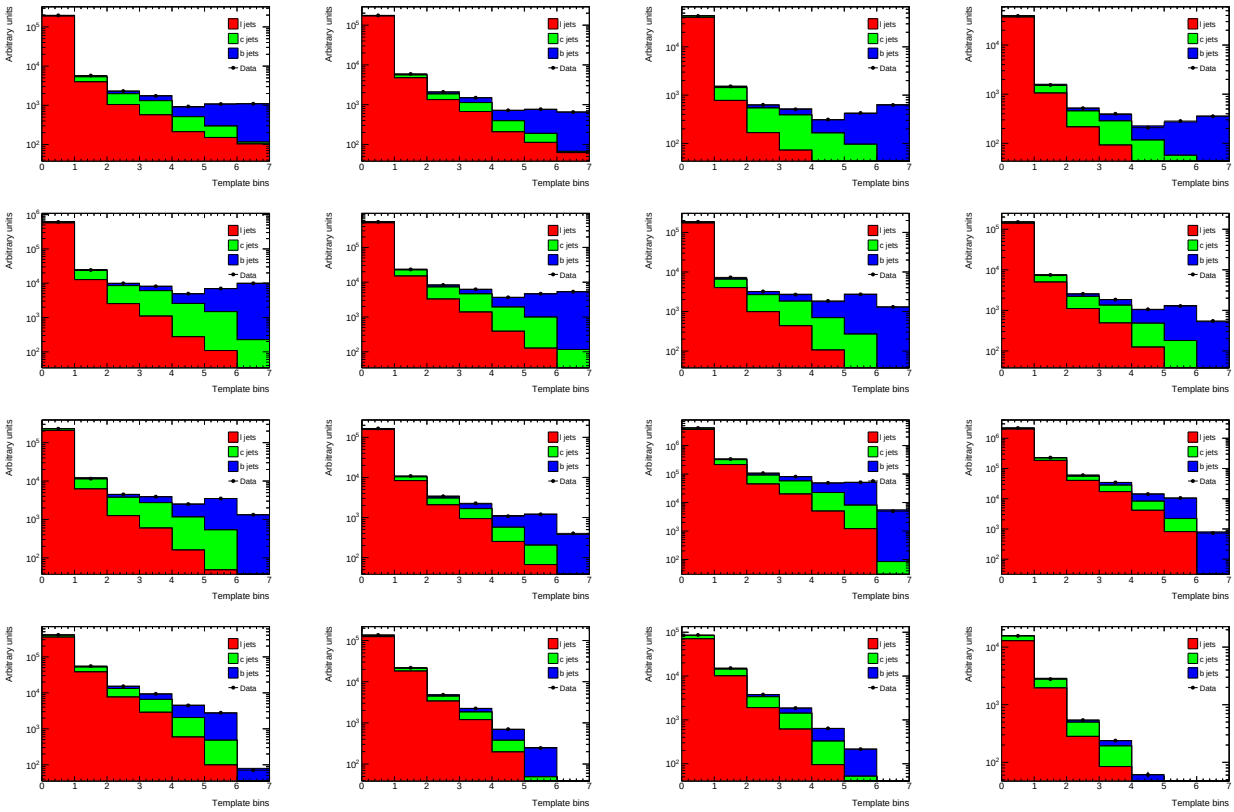


Figure 37: Postfit plots after Alternative fit/MC procedure for Pythia in 7 bin template fit.In the top row: leftmost plot is for pt bin 1 in central eta, second plot is for pt bin 1 for forward eta, third plot is for pt bin 2 in central eta and rightmost plot is for pt bin 2 for forward eta. In the Second row: leftmost plot is for pt bin 3 in central eta, second plot is for pt bin 3 for forward eta, third plot is for pt bin 4 in central eta and rightmost plot is for pt bin 4 for forward eta.In the third row: leftmost plot is for pt bin 5 in central eta, second plot is for pt bin 5 for forward eta, third plot is for pt bin 6 in central eta and rightmost plot is for pt bin 6 for forward eta. In the 4th/bottom row: leftmost plot is for pt bin 7 in central eta, second plot is for pt bin 7 for forward eta, third plot is for pt bin 8 in central eta and rightmost plot is for pt bin 8 for forward eta.

VITA

Wasikul Islam

Candidate for the Degree of

Doctor of Philosophy

Thesis: SEARCHES FOR BEYOND THE STANDARD MODEL PHYSICS IN DI-JET RESONANCES AND DEVELOPMENT OF A NEW B-TAGGING CALIBRATION ALGORITHM AT THE ATLAS EXPERIMENT AT CERN

Major Field: Physics

Biographical:

Education:
Completed the requirements for the Doctor of Philosophy in Physics at Oklahoma State University, Stillwater, Oklahoma in May, 2021.
Completed Master of Science in Physics at Aligarh Muslim University, Aligarh, UP, India in 2015.
Completed Bachelor of Science (B.Sc.) in Physics at Aligarh Muslim University, Aligarh, UP, India in 2013.

Experiences:
1. Researcher, ATLAS Collaboration of CERN (2016-2021), 2. Graduate Research Assistant, Oklahoma State University, USA (2015 - 2021), 3. Resident Associate, Argonne National Laboratory, USA (ANL-ATLAS Graduate Fellow; Jan. - Dec. 2018), 4. Visitor, Fermi National Accelerator Laboratory, USA (Jan. - Dec. 2018), 5. Graduate Research Aide, HEP-CCE of Argonne National Laboratory, USA (June - Aug. 2017), 6. Summer Intern, European Organization for Nuclear Research(CERN), Switzerland (Summer 2015)

Professional Membership:
American Physical Society, Oklahoma Center for High Energy Physics (OCHEP), USA, ATLAS Experiment of CERN, Geneva, Switzerland.